

Department of Precision and Microsystems Engineering

Improving a Fiber Optic Interferometer for the SAFARI Instrument

Finn van Rij

Report no : ME 12.001
Coach : Ir. J.W.Spronck
Professor : Prof. Dr. R.H.Munnig Schmidt
Specialisation : Mechatronic System Design
Type of report : Master Thesis
Date : 11 January 2012

This report is company confidential

Date: 11 January 2012

Title: Improving a fiber optic interferometer for the SAFARI instrument

Graduate student: Finn van Rij
Student number: 1152904
Email: Finnvanrij@gmail.com
Phone: 06-11879710

University: Delft University of Technology
Department: Precision and Microsystems Engineering
Specialization: Mechatronic System Design

Company: Technobis TFT-FOS

Graduate Commission: Prof. Ir. R.H Munnig-Schmidt
Ir. J.W. Spronck
Ing. R. Evenblij
Dr. J.J. van den Dobbelsteen

Type of report: Master Thesis
Report no.: ME 12.001

Preface

This thesis is part of the Mechatronic System Design MSc program at the faculty of Mechanical Engineering of the Technical University of Delft (TUDelft). It has been performed in cooperation and under the supervision of Technobis TFT-FOS. The subject of this thesis deals with the design of a fiber optic interferometer that has to be used inside an instrument called SAFARI. The SAFARI instrument is used to detect light with very small intensities in the infrared spectrum in space.

In this preface I would like to take the opportunity to thank all the people that have helped me with the realization of this thesis report.

First of all from the TUDelft I would like to thank my supervisor Jo Spronck. Also from the TUDelft I would like to thank Daniel Rixen, Urs Staufer and Merlijn van Spengen. They have been incredibly helpful.

From Technobis I would like to thank Rolf Evenblij and all other employees that have helped me out. I would like to take the effort to mention them one by one, these are Arjan de Koning, Michael Haverdings, Vincent Docter, Alex de Leth, Mar van der Hoek, Pim Kat, Iskander Deerenberg, Raymond Pietersen, Corrie van der Zon, Serge Sonneborn, Cor Omta, Joyce Ijdema, Ellen Schipper, Mark Wokke.

From SRON, the company with who I have closely worked together on the fiber optic interferometer, I would like to thank Dennis van Loon, Martin Grim, Ad van Nieuwenhuizen, Jelle Tasma and Geert Keizer for their help and support. Special thanks go out to Dennis and Martin with who I had the pleasure to work together during this project.

From TNO I thank Teun van den Dool.

Furthermore from Baas BV I would like to thank Luuk van Belt, Michiel van Dam, Eddy and Mustapha.

Last but not least I would like to thank my friends and family who have helped me out in several ways. They all know how much they have meant for me, so I won't mention them all in person. All I would like to say to them is; "Bedankt voor al jullie hulp door de jaren heen en alle bijdragen, in elke vorm, die hebben geresulteerd in de totstandkoming van dit Msc verslag. Mijn onvoorwaardelijke dank, respect en liefde hiervoor".



Executive summary

In this thesis report it has been researched if LUNASYS is operational for the SAFARI instrument. The requirements for LUNASYS were not clear yet. It was my task to gather, determine and check these requirements. It became clear that the initial system configuration of LUNASYS does not meet the requirements as specified in the table below. The maximal required electrical power of LUNASYS surprisingly doesn't meet the requirements either.

Type of parameter	Required value	Specified value	Meets requirements?
Stroke	34.5 (mm)	34.5 (mm)	Yes
Accuracy	10 (nm) over 200(s)	1100 (nm) over 1 (hr)	No
Resolution	1 (nm)	0.19 (nm)	Yes
Sample frequency	439 (Hz)	781 (Hz)	Yes
Heat load	100 (μW)	20.9 (μW)	Yes
Stray light power	0.89 (μW)	2.4E-12 (μW)	Yes
Space qualified	No	No	No
Maximal required electrical power	1.0 (W)	6.67 (W)	No
Functionality at cryogenic temperature	Yes	No	No
Relative displacement measurement	Yes	Yes	Yes
Laser + electronics placed in room of 293 (K)	Yes	Yes	Yes
Sensor head placed near the ODL	Yes	Yes	Yes

In order to make the system space qualified, the exact requirements for space qualification need to be known. The most important ones are: vacuum tolerance, the maximum radiation dose and the maximum radiation dose rate. Also very important is the reliability about the origin of the batch of the component and the test results of the batch. For space qualification there exist clear rules. It is best to use the expertise of SRON for this.

A lot of research was performed in order to determine what requirements LUNASYS did not meet and to what extent. From this it became apparent that the accuracy due to drift was the bottleneck of the design. This is why more research was done to determine the cause of the drift.

The possible causes for the drift have been stated, and after further analysis it has been shown using experiments that temperature disturbances acting on the reference and measurement arm are the dominant factor causing the measurement drift.

Reduction of the drift or compensation of the drift is possible; however it would be wiser to prevent the drift from happening. For this it would be better to come up with a completely new concept which is based on minimizing the drift.

New concepts indeed have been developed, where the drift has a negligible effect on the accuracy of the measurement system. In these concepts the measurement drift due to temperature disturbances has now been minimized to an error of $e_{Temp}=0.75$ (pm).

Besides the problems with the accuracy, it also enables less strict demands regarding functionality of the optical components at cryogenic temperatures. This is because for the new concept fewer components need to be placed at a temperature of 4.5 (K). Also, a possible solution has been worked out to reduce the stray light power to acceptable levels. This concept needs to be built and worked out in detail in order to validate its functionality.

Table of contents

Preface	iv
Executive summary.....	v
Table of contents.....	vi
1 Introduction.....	0
1.1 Problem setting	3
1.1.1 Research questions	3
1.1.2 Scope	4
1.1.3 Method	4
2 Initial system configuration OPD metrology.....	8
2.1 Sensing	9
2.2 Signal conditioning and processing.....	14
3 System requirements	16
3.1 SPICA requirements.....	16
3.2 Focal plane array requirements.....	18
3.3 Heat shields and cryogenic cooling requirements.....	19
3.4 FTS mechanism requirements.....	21
3.5 ODL requirements	22
3.6 OPD actuator requirements	24
3.7 OPD metrology requirements.....	25
3.8 LUNASYS requirements	27
4 System specifications.....	30
4.1 Component location.....	30
4.2 Relative displacement measurement	30
4.3 Fiber optic interferometer resolution.....	31
4.4 Sample frequency.....	33
4.5 Heat load and stray light.....	34
4.6 Total required electrical power.....	40
4.7 Space qualification.....	40
4.8 Functionality at 4.5 (K)	41
4.9 Accuracy and precision.....	42
4.9.1 Intensity noise.....	44
4.9.2 Optical disturbance signals.....	47
4.9.3 Laser	48
4.9.3.1 Frequency stability	49
4.9.3.2 Spectral linewidth	50
4.9.4 Temperature	51
4.9.5 Alignment.....	55
4.9.6 Photodiode.....	57
4.9.7 ADC quantization error	59
4.9.8 Mechanical vibrations	59
4.9.9 Error budgeting	60
4.10 Specifications overview	61
5 Drift	62
5.1 Causes of drift.....	62
5.2 Experiments.....	66

6	System specifications after improvements.....	86
6.1	AR coating grin lens.....	86
6.2	Reduce the laser power.....	87
6.3	Stray light maze	89
6.4	Thermal coefficient of expansion at 4.5 (K).....	92
6.5	Drift improvements.....	94
6.6	Lens and mirror choice.....	95
6.7	New system specifications	98
7	New interferometer concepts.....	99
8	Conclusion and recommendations	109
8.1	Conclusions.....	109
8.2	Recommendations	111
	Appendix A Background information.....	114
A.1	MCU diode readout.....	114
A.2	Baseline configuration of SPICA.....	115
A.3	Drawing of the FTS mechanism	117
A.4	Quadrature	118
	Appendix B Power calculations.....	122
B.1	Standard heat load calculation.....	122
B.2	Laser power loss	136
	Appendix C Algorithm.....	142
C.1	Wave superposition	142
C.2	Clarke transform	144
C.3	Detector signal.....	147
C.4	Interference signal	154
	Appendix D Errors.....	158
D.1	Intensity noise	158
D.2	Optical disturbance signals.....	177
D.3	Laser frequency deviations.....	181
D.4	Mirror and lens alignment	185
	Appendix E Experimental data	190
E.1	Specifications of the experimental setup.....	190
E.2	Drift measurement 1.....	192
E.3	Drift measurement 2.....	195
E.4	Drift measurement 3.....	198
	Appendix F System improvements.....	202
F.1	Stray light maze	202
F.2	Stray light maze dimensions	203
	Appendix G Datasheets	204
G.1	Laser datasheets.....	204
G.2	Laser test report	209
G.3	Datasheet circulator	212
G.4	Test datasheet circulator	214
G.5	Datasheet 3x3 splitter	215
G.6	Test datasheet 3x3 splitter.....	217
G.7	Datasheet Grin lens.....	219
G.8	Datasheet connector	220
G.9	Datasheet optical fiber.....	221

G.10 Datasheet photodiode.....	225
Bibliography	228
Nomenclature and abbreviations	232



[Page intentionally left blank]

1 Introduction

This master thesis was requested by Pim Kat, director of the Technobis Group, on the 4th of April 2011.

In Figure 1-1 a schematic overview of the architecture of all the relevant systems and subsystems for the design of the fiber optic interferometer is shown. The name of the companies responsible for the design of each system is also included in the diagram. The system is arranged from top to bottom respectively from system, to sub system, sub-sub system etc.

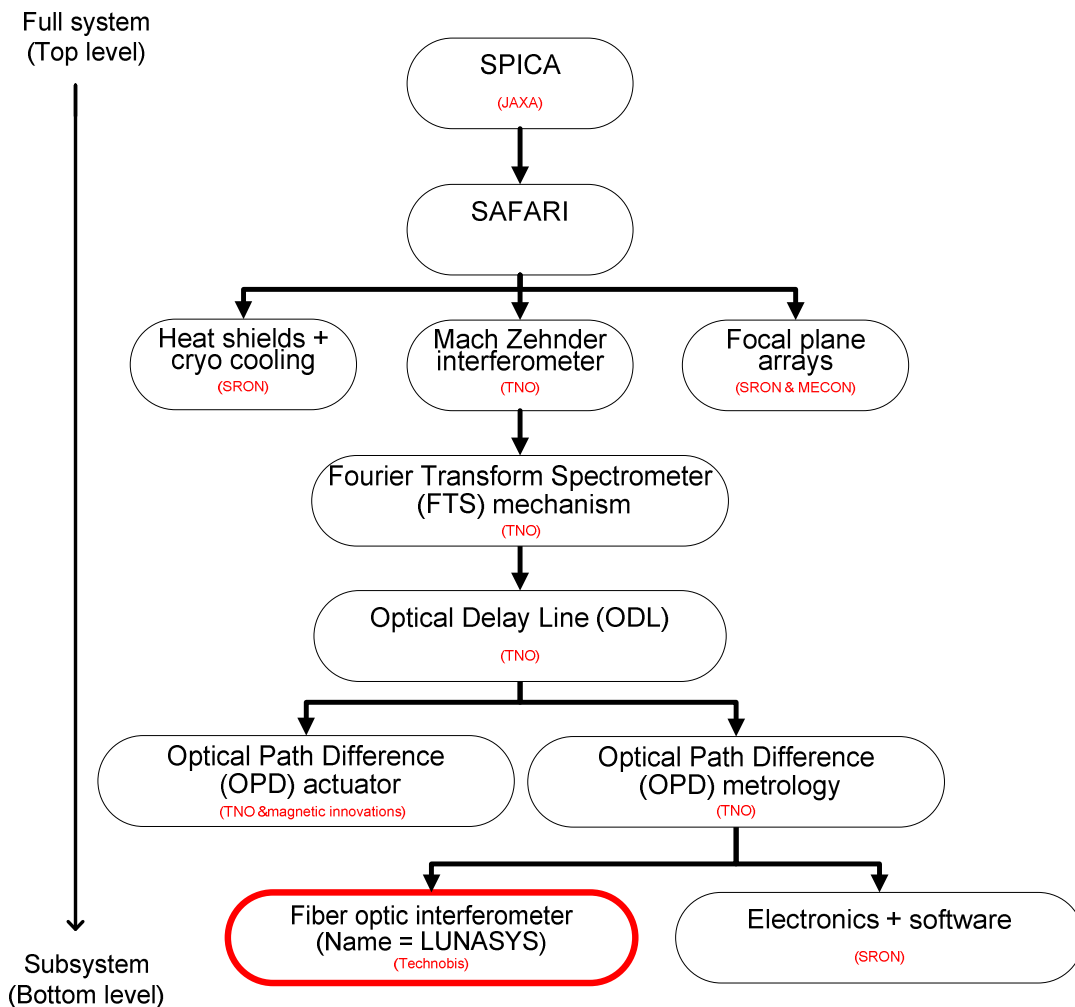


Figure 1-1 Diagram of the system architecture including the systems and subsystems directly influencing the design of the fiber optic interferometer. The non-specified systems are not included in this diagram

In order to do observations in space in the far infrared light spectrum the SPICA/SAFARI project is started (SPICA = Space Infrared telescope for Cosmology and Astrophysics,

SAFARI = SpiCA far infrared Instrument). Its high spatial resolution and unprecedented sensitivity in the mid- and far-infrared makes it possible to perform the desired observations in this spectrum. With this information it will be possible to determine the composition of the gasses surrounding a celestial body. This telescope is equipped with three instruments; SAFARI is one of these instruments. SAFARI can be subdivided into multiple components. Three of these components are the heat shields with cryogenic cooling, the focal plane arrays and the Mach Zehnder interferometer.

Because SAFARI has to detect very small signals, undesired radiation, which could disturb the measurement signal, has to be reduced. Thermal radiation decreases with temperature, so for this reason SPICA has cryogenically cooled zones within telescope. To keep the thermal radiation minimal, the focal plane arrays are cooled by mechanical and passive cooling. The heat shields and cryogenic cooling are necessary to keep the temperature low at the focal plane arrays. In Figure A-1a the basic configuration of SPICA is displayed. It can be seen that the main structure consists of multiple layers; in Figure A-1b a schematic conceptual view of the cryogenic system is shown. The cryogenic cooling system uses radiators with mechanical coolers to transfer heat to the surroundings.

The focal plane arrays are built up out of several charge coupled devices (CCDs). They are used to measure the very low light intensities.

The baseline optical configuration of SAFARI is a Mach-Zehnder imaging Fourier Transform Spectrometer (MZFTS). Because this instrument also suffers from thermal noise this instrument is placed in the cryogenic cooled region of SPICA. The MZFTS is shown in Figure 1-2.

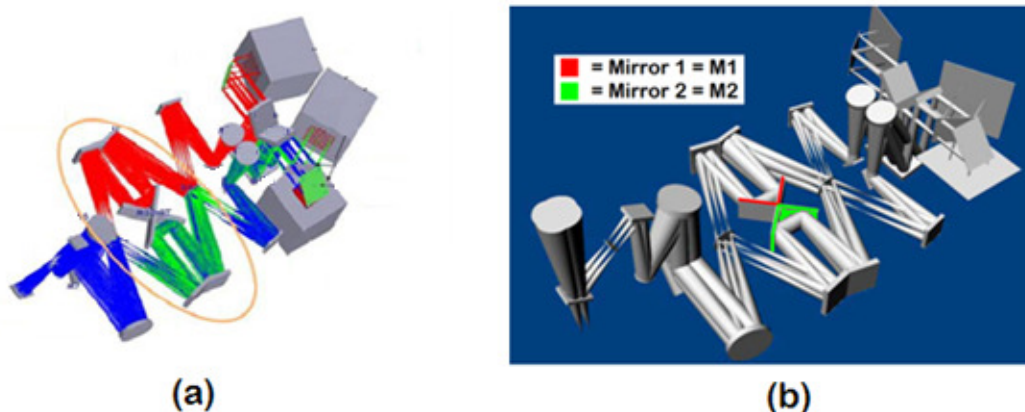


Figure 1-2 (a) Mach Zehnder imaging Fourier Transform Spectrometer (MZ-FTS) used in SAFARI. The red circle indicates the FTS mechanism. (b) Indication of the mirrors that are positioned with a feedback mechanism [17]

As the name implies, a Fourier Transform Spectrometer (FTS) mechanism can be found within the MZFTS. The FTS mechanism scans an auto-correlation function of light correlated with a time-delayed version of itself. The wavelength spectrum of the measured light is equal to the FFT of this auto-correlation function. This process is called a spectral deconvolution.

In order to measure the intensity of a certain wavelength the velocities of the mirrors M1 and M2 in Figure 1-2b need to be controlled. For this reason the Optical Delay Line (ODL) is designed.

As shown in Figure 1-3 the mirrors are attached to this mechanism and by the Optical Path Difference (OPD) actuator the translational motion is generated. This actuator is basically a linear motor with magnetic bearings that moves the mirrors over a certain stroke. During launch the actuator is mechanically fixed by the launch lock actuator shown in yellow in Figure 1-3.

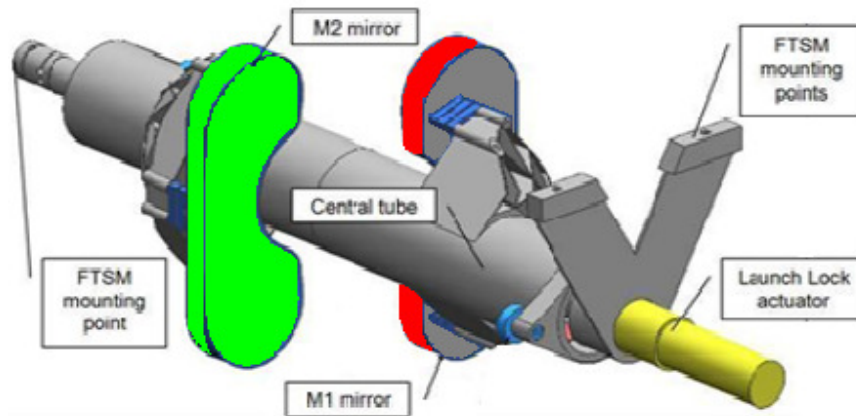


Figure 1-3 A concept of the cryogenic ODL on a magnetic bearing with the attached mirrors that need to be positioned [17]

In order to apply feedback, a measurement system (OPD metrology) is needed to measure the position of the mirrors.

This measurement system consists of a sensor; a fiber optic interferometer called LUNASYS. This fiber optic interferometer is made by Technobis and SRON.

Furthermore, LUNASYS uses electronics and software to readout the output of the fiber optic interferometer, apply the feedback and control the actuator.

Technobis would like to know if the current setup of LUNASYS is operational for the SAFARI application or not. In the content of this report by operational there is meant, that it functions according to the SAFARI requirements. And if not, they would like to know what needs to be improved in order to make it operational for the SAFARI instrument.

In the second chapter of this report the working principle of the fiber optic interferometer is explained. In chapter 3 the requirements for the fiber optic interferometer are determined and clarified. After this a specification of the current design is made in chapter 4, in order to see if the initial setup of the fiber optic interferometer meets the requirements. As a result of this research it seemed that the accuracy will be the limiting factor on the design. The system suffers from drift that highly influences the accuracy of the fiber optic interferometer. Drift is a small continuous change in the measurement value of a measurement instrument over time, while the value that should be measured remains constant. For this reason the most important factors that influence the drift of the fiber optic interferometer will be

researched in chapter 5. Improvements on the system are made in chapter 6. When it seemed that these improvements were not good enough to meet the requirements, a new concept for the fiber optic interferometer is introduced in chapter 7. Finally the conclusions of this thesis will be presented and recommendations will be made in chapter 8.

1.1 Problem setting

The problem setting of this thesis consists of three parts; definition of the main problem, the goal and the scope of this thesis. In the scope of this thesis report it is determined what parts of the SAFARI instrument are of importance for this research and finally the research method will be treated. In the research method there is briefly described what, why and how certain things are researched.

1.1.1 Research questions

As mentioned in the introduction, the main goal of Technobis is to build a system that is operational for the SAFARI instrument. The main goal of this thesis is to determine whether the current system that is built by Technobis is ready for this task or not. Therefore, the following research question with its corresponding sub questions has been formulated.

1) Is the current setup of LUNASYS operational for the SAFARI instrument?

- a) What are the requirements for LUNASYS for the SAFARI application?
- b) What are the specifications of the current setup of LUNASYS?

When it seemed that the current setup of LUNASYS was not yet operational for the SAFARI instrument, a second main goal for this thesis was formulated. If LUNASYS is not operational for the SAFARI instrument yet, insight should be gained about the limiting factors that cause that LUNASYS is not operational for the SAFARI instrument. If possible the issues should be solved. This leads to the second main question and its sub questions.

2) What needs to be improved on the current setup of LUNASYS to make the system operational for the SAFARI application?

- c) Is temperature the dominant factor causing the position drift of LUNASYS?
- d) What needs to be improved on the current setup of LUNASYS in order to reach the targeted requirements?

1.1.2 Scope

In the introduction a brief description of all systems, subsystems, sub-subsystems etc. is given. Without going into further detail on all systems within the SAFARI instrument, Figure 1-1 shows that the fiber optic interferometer is a small subsystem of a larger system. Also there is some interaction with some of the other subsystems within SAFARI. In this thesis only the systems within SPICA that interact with the fiber optic interferometer are shown in Figure 1-1. There are more systems on board of SPICA that interact with the fiber optic interferometer. Because these systems are not specified yet, the interaction with the fiber optic interferometer is not mentioned in Figure 1-1. Consequently it is assumed that the systems that are not displayed in Figure 1-1 are beyond the scope of this thesis.

1.1.3 Method

In the content of this report sometimes there is referred to a fiber optic interferometer and sometimes to LUNASYS, note that as stated in the introduction, LUNASYS is the name of the fiber optic interferometer.

In order to answer the first research question the functional requirements for the system should be known. Unfortunately the requirements for the fiber optic interferometer aren't precisely known. The requirements known about the interferometer are spread over several documents and most of these requirements are not well formulated or even incorrect. On top of this, the entire SAFARI instrument is still in conceptual phase and the design of different parts of this instrument is continuously changed. Therefore, the requirements for the fiber optic interferometer also change.

The design process of the fiber optic interferometer is done according to the V-model of systems engineering. The applied model is displayed in Figure 1-4.

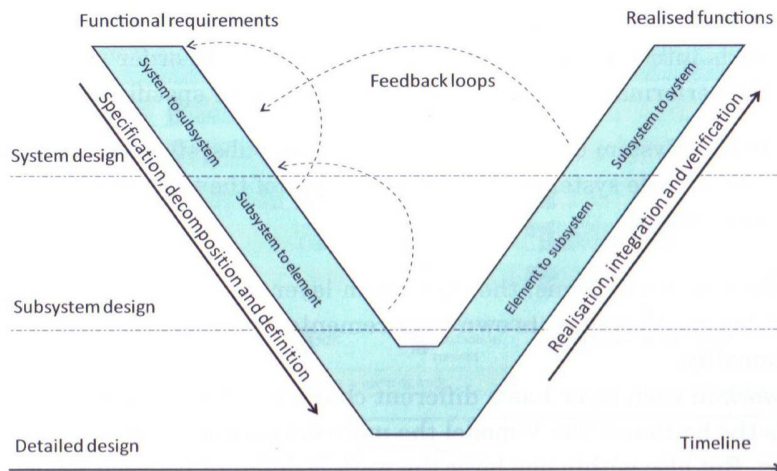


Figure 1-4 The V-model of systems engineering divides the design process of a complex system both in time and in levels of complexity [4]

Applying the V-model organizes the design. It gives better insight to where certain requirements come from and why certain design decisions are made. This is especially true for complex systems like the SAFARI instrument and its subsystems. Another benefit of applying the V-model is that it organizes the way of working.

After determining the functional requirements on top level of the V-model, these requirements can be translated to lower level requirements. If this process is repeated from top to bottom, the requirements for the fiber optic interferometer can be determined. This is followed by determining the specifications of the current setup of the fiber optic interferometer. These obtained specifications result in the answers to the first two research sub questions. With these answers the first main research question can be answered. When the specifications are determined some starting points are used to calculate lower level specifications. These starting points are treated in chapter 4. Because not all specifications of the interferometer are known, certain detail analyses are simplified or not even made at all.

During the design phase of the V-model (left side of the V-model) it sometimes happens that the specifications of sub-system can't meet the requirements. If a certain requirement is not feasible at a lower subsystem, then perhaps the requirement could be changed at a higher level of the design. This process could also be used during the realization phase of the design (right side of the V-model). During the realization, each sub system will be verified with the sub system requirements. Finally the total system will be verified with the full system requirements.

During this research it is concluded that the current system doesn't meet the set requirements. The precision of the measurement system seemed to be the bottleneck of the design. The biggest impact on the total precision of the system seemed to be the drift of the position signal.

In order to find all possible causes of the drift a global model of the interferometer has been made and analyzed. The main cause of the drift of the position signal seemed to be related to the temperature. This supposition has been confirmed during the first integration test of the optical setup of the fiber optic interferometer from Technobis and the detector electronics and software from SRON. When a heat source came nearer to

the reference arm or the measurement arm, the position signal clearly increased drifting. The result of this measurement is shown in chapter 5.

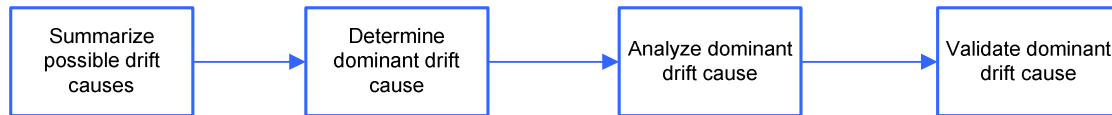


Figure 1-5 Block schedule representing the analysis of the cause of the drift

The cause of the drift is analyzed according to Figure 1-5. First the possible causes of the drift are summarized and each cause is analyzed. It seemed that temperature is a dominant factor causing the position drift. Hereafter, a model is made to determine where the impact of a temperature disturbance on the fiber optic interferometer will be greatest. It seemed that the biggest impact of a temperature disturbance is on the reference arm and the measurement arm of the fiber optic interferometer. For this reason drift measurements are performed while the temperature in the measurement arm and the reference arm is measured, in order to see if the position drift and the temperature are related to each other.

In order to exclude as much external influences on the drift as possible, the measurements need to be performed with certain improvements on the fiber optic interferometer. However, not all improvements have been applied to the fiber optic interferometer during the experiments. This is because the measurements had to be performed before a certain time. The reason for this is that the needed people and facilities were not available on a later date. So as a consequence of this not all improvements were applied to the experimental setup when the measurements were performed at SRON. For this reason the measurement setup is partially conform the initial specifications and partially conform the new system specifications that are given in chapter 6. As a result from these measurements, it was concluded that temperature disturbances on the measurement- and the reference arm were the dominant factors for the position drift.

Due to the little amount of time left, the decision has been made to think of some new concepts that suffered less from position drift as a consequence of temperature fluctuations. This is done instead of continuing with the old setup. These new concepts are treated in chapter 7. There it is shown why each setup is more beneficial than the initial system setup.

Finally the conclusions and recommendations of all obtained results are summarized in chapter 8.

This report follows the following layout:

- Introduction
- Assumptions
- Modeling
- Result
- Validation
- Discussion



Not all points mentioned above are necessarily added to each paragraph. Some paragraphs may deviate from this layout. The points added to a paragraph depend on what points are applicable to the subject.

2 Initial system configuration OPD metrology

In this chapter the working principle of the initial system configuration of the Optical Path Difference (OPD) metrology will be explained. In order to find out if the current setup of the fiber optic interferometer is operational for the SAFARI instrument it needs to be understood how this interferometer works.

First it is explained how the OPD metrology functions within the Optical Delay Line (ODL). Then the OPD metrology is split into the three main subsystems of a measurement system defined in [4] as the structure of a measurement system.

The fiber optic interferometer is part of the ODL. The OPD metrology is used as the sensor for the control loop of the (ODL). Schematically the control loop of the ODL and its components are displayed in Figure 2-1. The goal of the ODL is to move a mirror with high precision and accuracy over a certain stroke in the Fourier Transform Spectrometer (FTS). In the introduction this system is described in more detail.

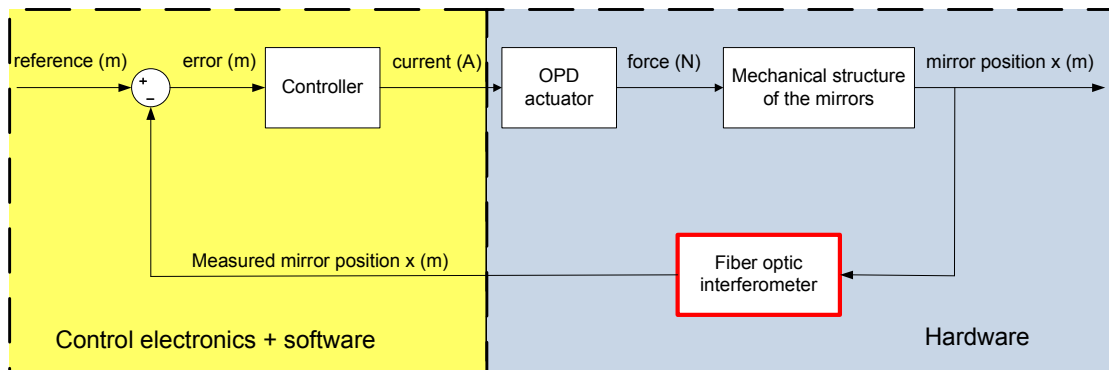


Figure 2-1 Control loop of the ODL used for positioning of the mirrors used in the FTS

Now that it is known how the ODL is built up and where and for what reason the OPD metrology is used, it will be made clear how the different components in the OPD metrology interact with each other. This in order to make sure that this total system works. The OPD metrology is basically built up as shown in Figure 2-2.

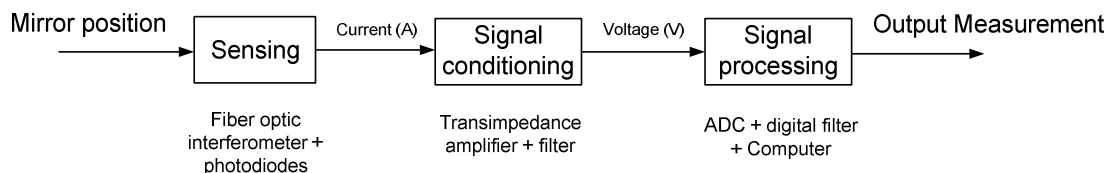


Figure 2-2 Blok schedule of the OPD metrology

The position of the mirror is sensed by the fiber optic interferometer and the physical input is transduced to an electric current. The analog output signal of the sensor is manipulated to fit the Analogue to Digital Converter (ADC) range for further processing. After the conditioning of the signal, the signal is converted to a digital signal and the digital signal is analyzed and processed to a useable quantity that indicates the measured mirror position. The output of the measurement system can then be used to compared to the reference position in order to determine the position error.

2.1 Sensing

Referring to Figure 2-2, an important part of the OPD metrology is sensing. Sensing is done by a fiber optic interferometer. The principle of interference between two light waves and the working principle of a Michelson homodyne interferometer are described in reference [30] and [37] respectively. The configuration of the main parts of this sensor is shown in Figure 2-3. A more detailed description of the sensing part of the OPD metrology is shown in Figure B-9.

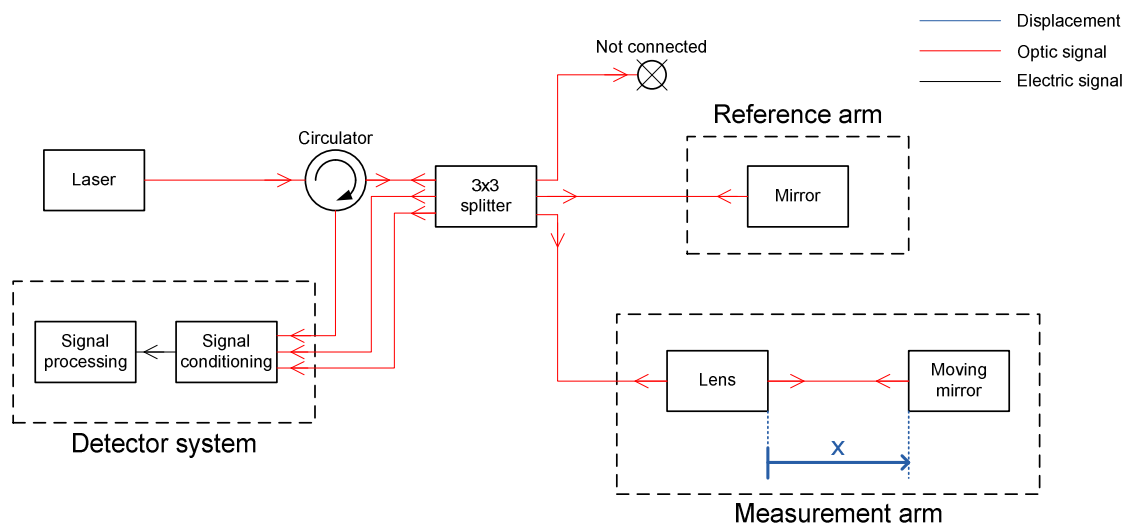


Figure 2-3 System model for the initial system configuration of the fiber optic interferometer

A detailed indication of the optical power in all the components shown in Figure 2-3 can be found in appendix B.2 (Figure B-9 and Table B-2). The configuration of the fiber optic interferometer shown in Figure 2-3 differs from a Michelson homodyne interferometer in two main aspects: a circulator is used to guide the reflected light to the detector and the main beam splitter is replaced by the 3x3 splitter.

Now it will be briefly explained how the initial system configuration of the fiber optic interferometer is built up. A laser creates a monochromatic light bundle with a wavelength of 1550 (nm). This light is guided through FC APC SM cables (fixed connection angled physical contact single mode). In order to connect the cables FC APC type connectors are used. After the light leaves the laser and passes through the cable

and the connector the light arrives at the circulator. A circulator is an optical component that consists of 3 optical connections. In Figure 2-4 the optic symbol for a circulator is shown.

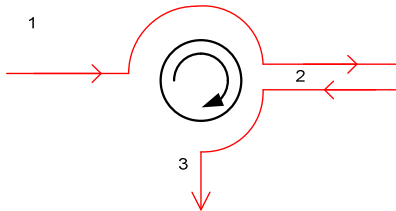


Figure 2-4 Schematic symbol for a circulator

A circulator basically works as an optical diode. Referring to Figure 2-4 the light enters at 1 and then exits the circulator at 2. When the light enters the circulator in 2 it exits at 3. So basically there are only two different paths possible for the light to travel along, path 1-2 and path 2-3. Lasers become quickly unstable when a small part of the exiting light gets reflected back into the laser. So the circulator prevents instability of the laser due to back reflections of light from individual parts of the system. After the light passes through the circulator it reaches the 3x3 splitter.

The 3x3 splitter, also called the splitter or the coupler, ideally splits the entering optical power equally over the three outputs. A 3x3 splitter basically consists of three fiber claddings twisted around each other. After twisting, the fibers are stretched out while they are heated. Due to the geometry of the twisted claddings, cross talk of the evanescent field around the fiber occurs. If the intensity is equally distributed over the three exiting fibers, then as a consequence of conservation of energy, the phases of the three exiting fibers have a 120 degree phase difference with respect to each other [26]. This is explained in equation (2.3) where a function is described. The optic symbol for a 3x3 splitter is shown in Figure 2-5.

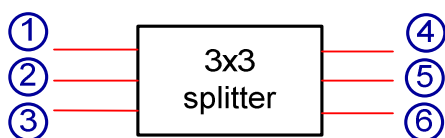


Figure 2-5 Schematic symbol for a 3x3 splitter

According to reference [17] and [18], the three output powers can be written as a function of the three input powers.

$$P_{sp,out} = T_p P_{sp,in} \quad (2.1)$$

Where:

$P_{sp,out}(W)$ = Power of the splitter on the output

$P_{sp,in}(W)$ = Power of the splitter on the input

$T_p(-)$ = Splitter power transformation matrix

Now consider the model of the 3x3 splitter in Figure 2-5. Ideally the output is coupled in three equal powers. In this case the corresponding powers of fiber 4, 5 and 6 can be calculated when the laser light with a unity input only enters the splitter in fiber 1. Applying equation (2.1) results in the next output powers of the exiting fibers:

$$P_{sp,out} = \begin{bmatrix} P_4 \\ P_5 \\ P_6 \end{bmatrix} = \begin{bmatrix} T_{11} & T_{12} & T_{13} \\ T_{21} & T_{22} & T_{23} \\ T_{31} & T_{32} & T_{33} \end{bmatrix} \begin{bmatrix} P_1 \\ P_2 \\ P_3 \end{bmatrix} = \begin{bmatrix} 1/3 & 1/3 & 1/3 \\ 1/3 & 1/3 & 1/3 \\ 1/3 & 1/3 & 1/3 \end{bmatrix} \begin{bmatrix} 1 \\ 0 \\ 0 \end{bmatrix} = \begin{bmatrix} 1/3 \\ 1/3 \\ 1/3 \end{bmatrix}$$

The phase is also changed by the splitter and can be written in a general form as a phase transformation function.

$$f_{in} \xrightarrow{\varphi \text{ transform}} f_{out} \quad (2.2)$$

For three different input signals on the splitter the result of (2.2) for the exiting signals is as followed:

$$\begin{bmatrix} f_{in,1}(t, \varphi_1) \\ f_{in,2}(t, \varphi_2) \\ f_{in,3}(t, \varphi_3) \end{bmatrix} \xrightarrow{\varphi \text{ transform}} \begin{bmatrix} f_{in,1}(t, \varphi_1) + f_{in,2}(t, \varphi_2 - 120^\circ) + f_{in,3}(t, \varphi_3 + 120^\circ) \\ f_{in,1}(t, \varphi_1 + 120^\circ) + f_{in,2}(t, \varphi_2) + f_{in,3}(t, \varphi_3 - 120^\circ) \\ f_{in,1}(t, \varphi_1 - 120^\circ) + f_{in,2}(t, \varphi_2 + 120^\circ) + f_{in,3}(t, \varphi_3) \end{bmatrix} \quad (2.3)$$

Where:

$f_{in}(-)$ = Optic wave function entering the splitter

$f_{out}(-)$ = Optic wave function exiting the splitter

Adding the effect of the splitter power transformation matrix T_p to this function, gives the following result for the total relation between the input and the output of the splitter.

$$\begin{bmatrix} f_{in,1}(t, \varphi_1) \\ f_{in,2}(t, \varphi_2) \\ f_{in,3}(t, \varphi_3) \end{bmatrix} \xrightarrow{\varphi \text{ trans.}} \begin{bmatrix} T_{11}f_{in,1}(t, \varphi_1) + T_{12}f_{in,2}(t, \varphi_2 - 120^\circ) + T_{13}f_{in,3}(t, \varphi_3 + 120^\circ) \\ T_{21}f_{in,1}(t, \varphi_1 + 120^\circ) + T_{22}f_{in,2}(t, \varphi_2) + T_{23}f_{in,3}(t, \varphi_3 - 120^\circ) \\ T_{31}f_{in,1}(t, \varphi_1 - 120^\circ) + T_{32}f_{in,2}(t, \varphi_2 + 120^\circ) + T_{33}f_{in,3}(t, \varphi_3) \end{bmatrix} \quad (2.4)$$

The function from equation (2.4) is applied to the configuration of Figure 2-5. If light enters the splitter only at input 1, the output of the splitter can be obtained using equation (2.4).

$$f_{in} = \begin{bmatrix} f_1(t, \varphi_1) \\ 0 \\ 0 \end{bmatrix} \xrightarrow{\text{phase transform}} f_{out} = \begin{bmatrix} T_{11}f_1(t, \varphi_1) \\ T_{21}f_1(t, \varphi_1 + 120^\circ) \\ T_{31}f_1(t, \varphi_1 - 120^\circ) \end{bmatrix}$$

The initial functional model of the fiber optic interferometer that is currently used, including all the fiber connectors, fiber optic cables, photodiodes and all other parts is shown in Figure 2-6.

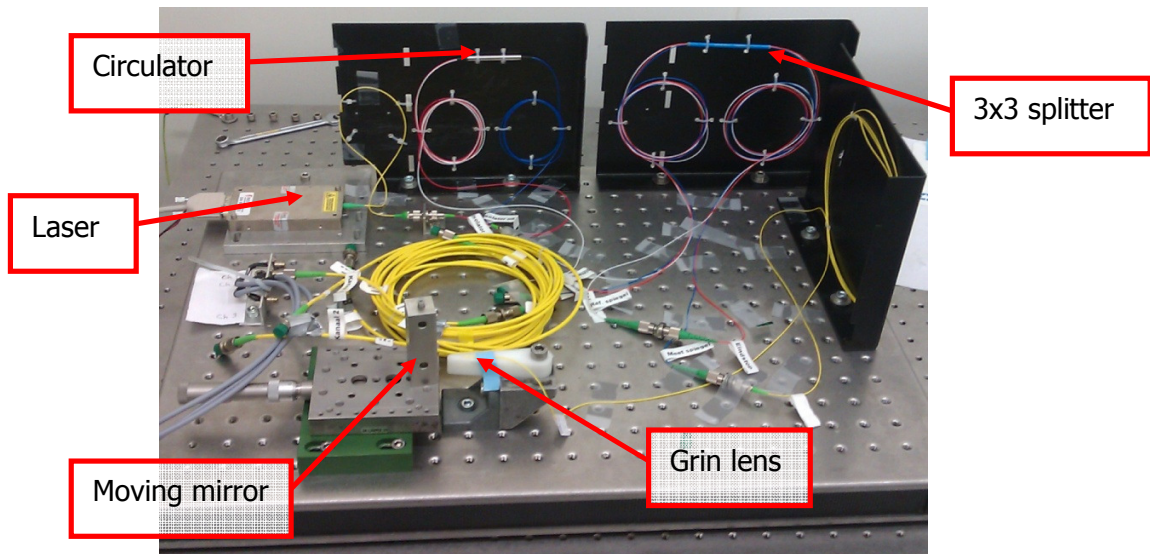


Figure 2-6 Photo of the initial functional model of the fiber optic interferometer built up by Finn van Rij

One output of the 3x3 splitter is not connected as can be seen in Figure 2-3. Because it is undesirable to let the light exit the system uncontrolled, the end of this fiber is connected to a connector with a closed end. This closed end prevents light from reflecting back into the fiber optic cable. In order to create a fixed reference point, relative from which the optical path difference is measured, a reference mirror is used like in a Michelson interferometer [30] and [37].

Grin lens

A GRAdient INdex lens or a grin lens is used to collimate the beam that exits the fiber. The grin lens directs the collimated light to the moving mirror to which the distance needs to be measured and after reflection on the measurement arm, it couples the light back into the fiber. The lens is built up from different layers of material with a different refractive index, such that the refraction of the light is dependent on the vertical position of the incident light. In the optical center of the lens the refractive index has the highest value and further away from the center the refractive index becomes lower. In this way the outer rays of the bundle leaving the fiber core are refracted most. A schematic view of the light passing through the grin lens and the refractive index profile over the fiber diameter is shown in Figure 2-7.

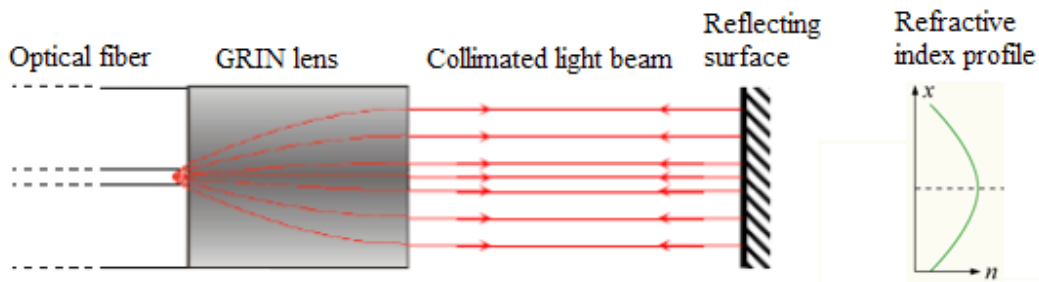


Figure 2-7 Schematic view of light beams collimated by a grin lens reflecting on a mirror [20]

The distance from a fixed point to the moving mirror on the FTS mechanism needs to be measured. The light exiting the grin lens needs to be reflected back into the fiber. For this purpose a reflecting surface (mirror) is used to attach on the moving mirror of the FTS mechanism. In the content of this report when there is referred to the moving mirror, the mirror of the fiber optic interferometer that is attached to the moving mirror for the FTS mechanism is meant.

In the initial setup of the fiber optic interferometer a block of metal is used. This metal block is placed on a linear optic stage as shown in Figure 2-8. In order to create a manual controlled displacement that represents a displacement actuated by the FTS mechanism.

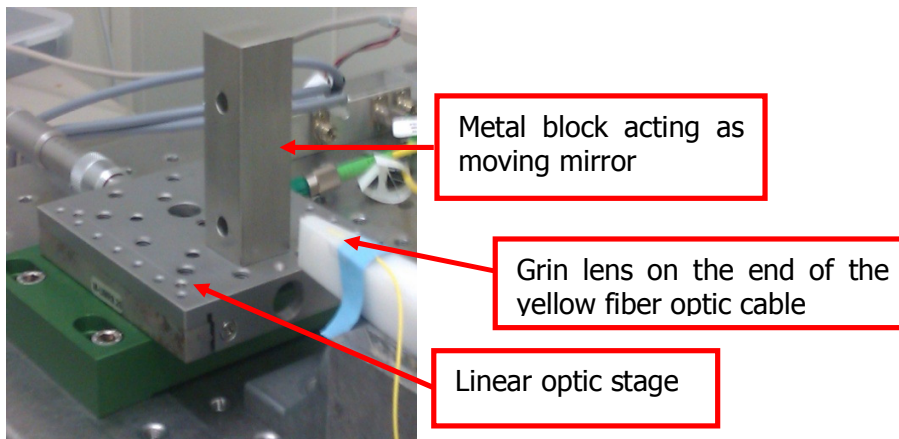


Figure 2-8 Photo of the metal block used as a mirror on a linear optic stage. In the lower right corner the grin lens is taped on a piece of polymer

Finally the measured irradiance of the optic signal or the electromagnetic power representing the displacement of the FTS mechanism should be converted to a useable electrical signal for further processing. For this purpose a FD100 photodiode is used. The photodiode creates a current proportional to the incident light. Three photodiodes are used, one for every output signal of the interferometer.

2.2 Signal conditioning and processing

The output signal of the photodiode needs to be converted to a useable signal in order to be sampled properly by the ADC. The analog signal of the photodiode is a small current in the order of microamperes. The necessary signal for the ADC should be given in voltages. The value of the ADC voltage should be spread over the biggest part of the total range of the ADC. For the ADC128S102 this is 3 Volt. This ADC is a 12 bits multiplexed ADC with 8 inputs and a maximum sample rate of 1(MHz). After sampling, the signal can be analyzed and processed by the computer algorithm. These steps are schematically shown in Figure 2-9 [7].

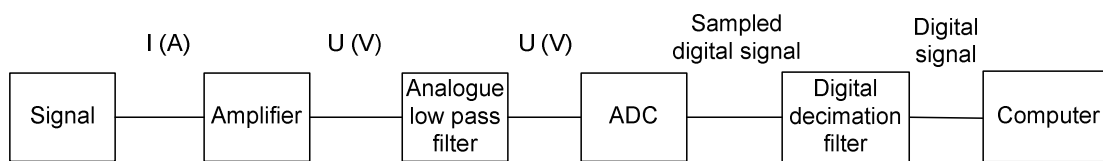


Figure 2-9 Block schedule of the signal conditioning and the signal processing for the OPD metrology



3 System requirements

The first research question of this thesis report was: "Is the current setup of LUNASYS operational for the SAFARI instrument?" In order to answer this question the requirements for LUNASYS for the SAFARI application need to be determined.

As described in the research method, the functional requirements need to be determined from the top level downwards to the bottom level of the system architecture. If it is known why certain requirements are formed, then this facilitates the design of the fiber optic interferometer. So in order to gain insight in how these requirements are formed, the requirements are written down for each subsystem of the system architecture shown in Figure 1-1. In the next paragraphs these requirements will be stated for each subsystem.

3.1 SPICA requirements

The many different components of SAFARI can't be placed randomly in SPICA. There are several main components that are restricted from certain regions due to temperature requirements. To explain where these requirements come from, a few things need to be explained about thermal radiation.

Two main features about thermal radiation are that all bodies at temperatures above absolute zero, radiate electromagnetic waves. Secondly an ideal thermal radiator, a black body, radiates at all wavelengths. The spectral emissive power of a thermal radiator is wavelength dependent. The emissive power of a thermal radiator is shown in the Planck curve of Figure 3-1.

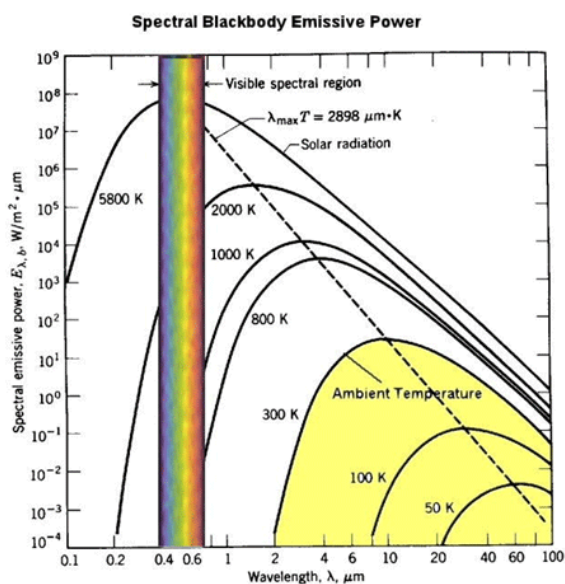


Figure 3-1 Planck curve [32]

In order to prevent stray light in the sensitive measurement system of SAFARI most optical components are cooled to cryogenic temperatures. For this reason there are different temperature regions in SAFARI. Most components of the Mach Zehnder interferometer are cooled to a temperature of 4.5 (K). The focal plane array is even cooled to 50 (mK)! From the relationship described in equation (3.1) [19], it can be seen that the spectral emissive power for a fixed wavelength decreases with decreasing temperature. The same can be concluded when looking at the famous Planck curve represented in Figure 3-1. The curve is plotted for different temperatures.

$$I(\lambda, T) = \frac{2hc^2}{\lambda^5} \frac{1}{e^{\frac{hc}{\lambda k_B T}} - 1} \quad (3.1)$$

Where:

$I(W)$ = Emissive power

$\lambda(m)$ = Wavelength of the electromagnetic wave

$T(K)$ = Temperature

$h(m^2 kg / s)$ = Planck's constant

$k_B(m^2 kg / s^2 K)$ = Boltzmann's constant

Several components of the OPD metrology, like the electronics, don't function at very low temperatures. Therefore, they need to be placed in a region with a higher temperature. The electrical conductivity of semiconductors decreases with temperature, in contrast to normal electrical conducting materials. At temperatures of 4.5 (K) semiconductors can't function anymore.

This fundamental physical problem forces the designer to place the electronics for the laser, the photodiodes, signal conditioning and signal processing in a "warmer" region of 253 (K). Furthermore, the external cavity laser performance deteriorates at low temperature. This will result in a less stable laser. So some parts of the sensor need to stay in the high temperature region and the sensor head (the measurement arm) needs to be placed in the cryogenic cooled zone near the positioned mirror on the FTS mechanism. A schematic configuration of this is given in Figure 3-2. In this figure two fiber optic cables are passing through the heat shield to the cryogenic side.

Another reason for the placement of the electronics is that the heat dissipation is too large. This heat would cause temperature disturbances in the cryogenic cooled zone that are too high.

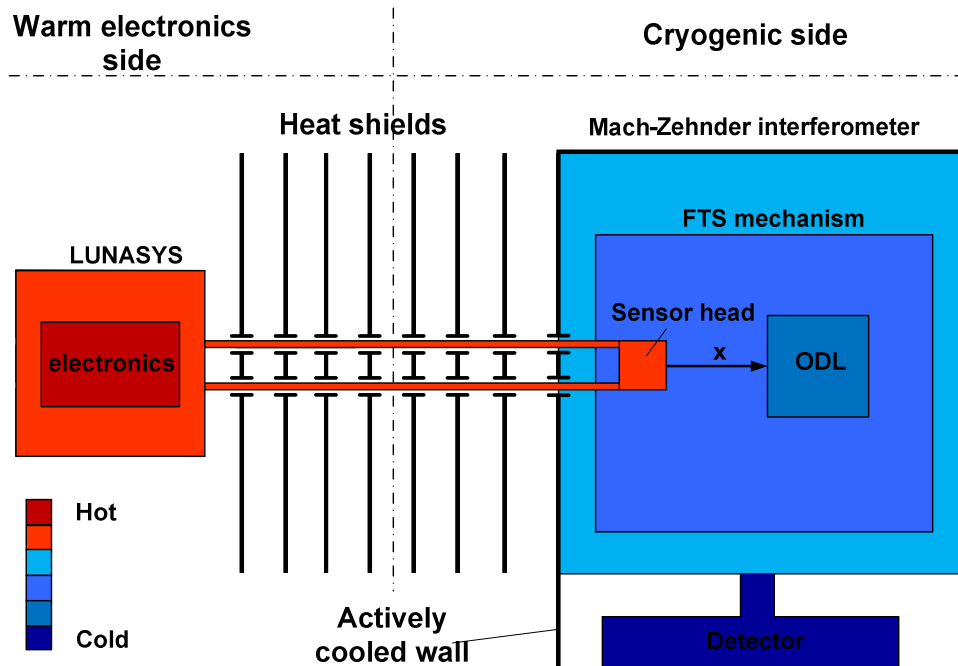


Figure 3-2 Schematic view of component placement of the OPD metrology in the satellite SPICA

As mentioned before, the telescope needs to measure infrared light of a very low intensity. The measurements need to be performed in space. Therefore, the following requirement needs to be fulfilled.

Space qualification requirement:

All parts in this system need to be space qualified. In the content of this report space qualified is defined as able to function in vacuum.

Component location requirements:

- The laser and the electronics for signal conditioning and signal processing can't be placed in cryogenic temperatures. For good functionality they must be placed at 293 (K).
- The sensor head needs to be placed in the cryogenic cooled zone near the positioned mirror on the FTS mechanism.

3.2 Focal plane array requirements

The focal plane array of SAFARI has a high sensitivity because it needs to detect very small signals. In order to measure with a high precision the Signal to Noise Ratio (SNR)

needs to be as high as possible. Since the signal can't be influenced (we can't say to the stars: shine a little brighter) the noise floor needs to be lowered.

There are three focal plane arrays within SAFARI, each with a different wavelength range [23].

Focal plane array requirements:

From [23] it follows that the allowable noise equivalent power at the focal plane array NEP_{detector} needs to be:

$$NEP_{\text{det}} \leq 2 \cdot 10^{-19} \left(W / \sqrt{Hz} \right) \text{ @ 50 (mK) operating temperature}$$

Where:

$NEP_{\text{det}} \left(W / \sqrt{Hz} \right)$ = Noise equivalent power of the focal plane array

Table 3-1 Detector wavelength ranges for the three focal plane arrays

Focal plane array	Wavelength range (μm)
short-wave band	34 - 60
mid-wave band	60 - 100
long-wave band	110 - 210

3.3 Heat shields and cryogenic cooling requirements

The spectral emissive power of all matter increases with increasing temperature, as mentioned in equation (3.1).

All emissive power due to rising of temperature is considered to be stray light. In order to prevent too much stray light from entering the focal plane array the maximum allowable temperature in the room for the Mack Zehnder interferometer is restricted. As a consequence the desired temperature of all the parts in the cryogenically cooled room is given [23].

Cryogenic cooling requirements:

$$T_{FTS} = 4.5 (K)$$

$$T_{\text{max},FTS} = 6 (K)$$

Where:

$T_{FTS} (K)$ = Desired reference temperature in the Mach Zehner interferometer

$T_{\text{max},FTS} (K)$ = Maximum allowable temperature in the Mach Zehner interferometer

The temperature in the FTS is passively and actively cooled. The active cooling consists of a mechanical cooling system with Helium used as a refrigerant. The mechanical coolers operate at set speeds to control the temperature in the cryogenic cooled space of the FTS [6].

Cryogenic cooling specifications:

15 (Hz) and 45 (Hz) cooler frequencies
--

Because the total design of SPICA is still in the conceptual phase it is not yet known exactly how the connection of the laser to the sensor head will be implemented through the satellite. For system integration of the fiber optic interferometer with the rest of the satellite, it would be preferable to build up the sensor out of several modules connected with optical connectors. The exact amount of connectors that have to be used is still unknown. In Figure 3-3 a possible configuration of the path of the optical fiber within SPICA is shown.

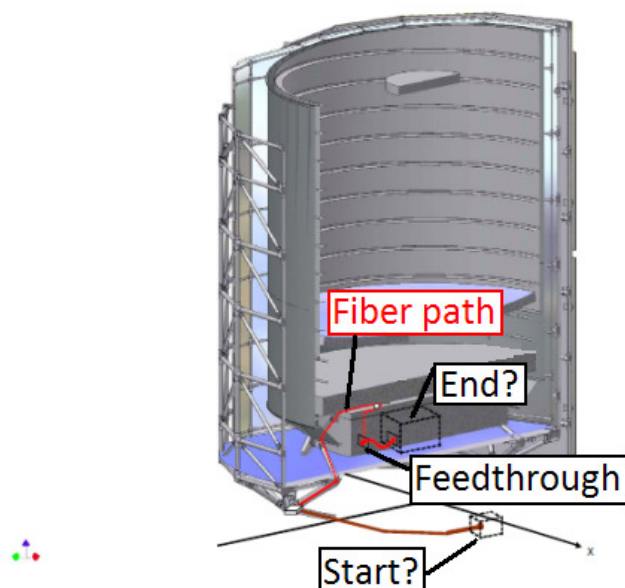


Figure 3-3 A cross section of SPICA, with a proposed possible path indicated by a red line for the fiber optic cable from the heated electronics to the cryogenic cooled zone. This picture is obtained from [17]

The old configuration of the setup for the fiber optic interferometer LUNASYS is displayed in Figure 3-4. In this configuration it was chosen to place the laser, detector, electronics, circulator and the 3x3 splitter in the warm electronics side of 293 (K). The reference and the measurement arm are placed in the cryogenic cooled zone of the FTS mechanism.

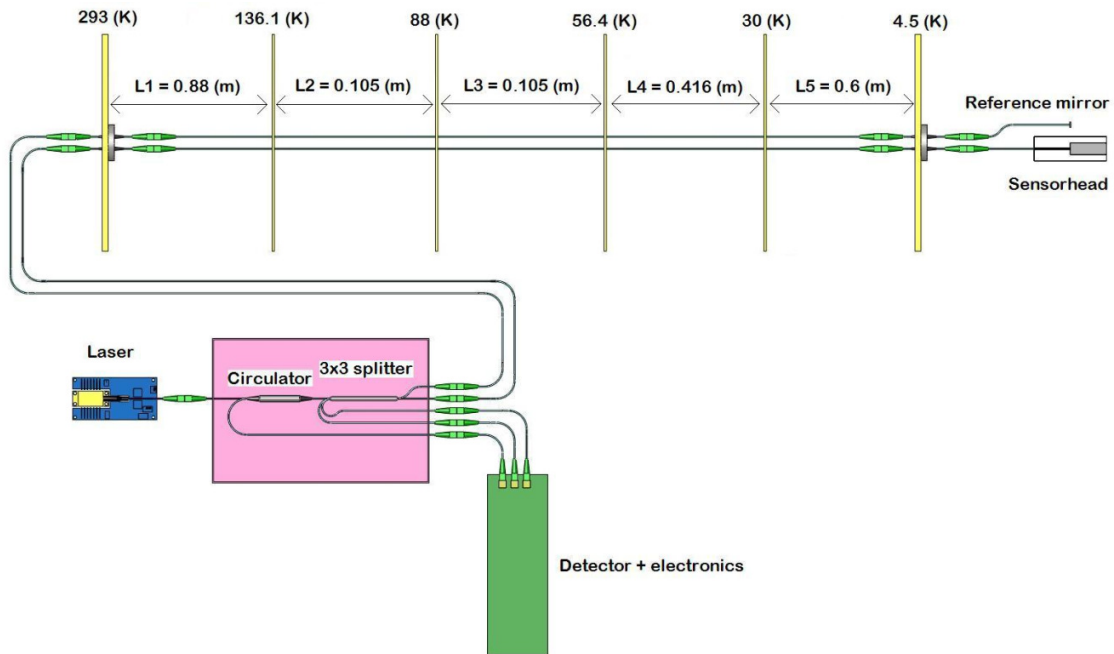


Figure 3-4 Initial system configuration of the setup for LUNASYS

As mentioned in section 3.1 there are several heat shields, all of different temperatures and all at a certain distance from each other. In Figure 3-4 it can be seen that two fiber optic cables have to pass through the heatshields to get to the cryogenic side. The temperatures of all the heat shields have been added to this picture.

Heat shields specification:

- Aluminium material is used for the heat shields [23].
- Heat shields temperature and interspatial dimensions are given in Table 3-2 [23].

Table 3-2 Heat shield temperature and spatial dimensions between the heat shields

Heat shield	1	2	3	4	5	6
Temperature (K)	293	136.1	88	56.4	30	4.5
Fiber length between the shields (m)		0.88	0.105	0.105	0.416	0.6

3.4 FTS mechanism requirements

The purpose of the FTS mechanism is to measure the infrared light of a certain spectrum and determine the intensity of each wavelength within this spectrum.

FTS mechanism requirements:

Scan time of the detector [23]	$t_{\text{scan}} = 200 \text{ (s)}$
--------------------------------	-------------------------------------

Where:

$t_{scan} (s)$ = Scan time of the FTS mechanism

The total power requirement for all the electronics that are used for the FTS mechanism is 7(W) [23]. All the power required for LUNASYS is included in this requirement.

Maximal available power FTS	$P_{max,FTS} = 7 (W)$
-----------------------------	-----------------------

Where:

$P_{max,FTS} (W)$ = Maximal available power for the FTS

Other requirements for the FTS are given below.

FTS mirror rotation tilt [6]	$< \pm 30$ (arcsec)
FTS mirror lateral displacement [6]	< 100 (μm)
Parasitic heat load [6]	< 300 (μW)

3.5 ODL requirements

The accuracy of the movement of the ODL is a measure for the spectral intensity of the detected light of the SAFARI instrument. For this reason the velocity of the moving mirrors by the ODL needs to be controlled.

Relative displacement measurement:

In order to apply the feedback in the correct direction, the direction and the magnitude of the displacement need to be measured. Therefore a relative and not an absolute displacement need to be measured.

ODL requirements:

Mirror location accuracy [6]	< 15 (nm)
Mirror location resolution [6]	< 5 (nm)
Linear stroke [6]	34.5 (mm)
Maximum stroke velocity [6]	170 ($\mu\text{m/s}$)

Stray light power requirement:

There are three focal plane arrays, each with a different wavelength detection area. The optical filters in the mid wave band and the long wave band will have a higher attenuation on the 1.5 (μm) wavelength caused by the laser of the fiber optic interferometer than the short wave band. So the limiting factor for the stray light caused by the fiber optic interferometer is the short wave band.

When the FTS mechanism scans, it moves with a constant velocity. If a FFT of the optical signal in the focal plane array is made while the FTS mechanism scans, a cosine signal, which is a measure for the light intensity for a certain wavelength, is obtained. This process is called a spectral deconvolution as mentioned in the introduction. The frequency of this cosine signal is proportional to the velocity of the FTS mechanism. The minimal sample frequency of the focal plane array system follows from the Nyquist-Shannon sampling criterion.

$$f_{sample} \geq 2f_{signal} \quad (3.2)$$

Where:

$f_{sample} (Hz)$ = Sample frequency

$f_{signal} (Hz)$ = Signal frequency

Similar to the optical path difference for the fiber optic interferometer, the sample frequency has to be twice as high for the focal plane array. The formula for the maximal sample frequency is given by [23]:

$$f_{fpa} = \frac{4v_{max}}{\lambda_{min}} \quad (3.3)$$

Where:

$f_{fpa} (Hz)$ = Maximal required sample frequency of the focal plane array

$v_{max} (m/s)$ = Maximal stroke velocity of the moving mirror

A calculation of the maximal required sample frequency of the focal plane array is performed for the smallest wavelength in the short wave band 34 (μm) and a maximal stroke velocity of the moving mirror of 170 ($\mu m/s$) and then applied to (3.3).

$$f_{fpa} = 20(Hz)$$

There is a 120 (dB) power attenuation of the light between the FTS and the focal plane array [23]. For the power attenuation there can be written:

$$P_{dB} = 10 \log(P) \quad (3.4)$$

Where:

$P_{dB} (dB)$ = Power in units of dB

$P(W)$ = Power in units of Watts

For the allowable noise equivalent power at the ODL equation (3.5) applies.

$$NEP_{ODL} = Att_{ODL-detector} \cdot NEP_{detector} \quad (3.5)$$

Where:

$Att_{ODL-foc} (-)$ = Light attenuation for 1550(nm) wavelength, from the ODL to the focal plane array

$NEP_{ODL} (W / \sqrt{Hz})$ = Allowable noise equivalent power at the ODL

If it is assumed that the noise equivalent power is constant over the spectrum of 0-20 (Hz), then with this data and equation (3.5) the allowable noise equivalent power at the ODL can be calculated.

$$NEP_{ODL} = 2 \cdot 10^{-7} (W / \sqrt{Hz})$$

With NEP_{ODL} the stray light power or the noise level at the ODL can be determined. This value is maximal when the sample frequency is at its maximum.

$$N_{ODL} = NEP_{ODL} \sqrt{f_{fpa}} \quad (3.6)$$

Where:

$N_{ODL} (W)$ = Noise level or stray light power at the ODL

The maximal noise level at the ODL can be calculated for the maximal sample frequency of the focal plane array of 20 (Hz) by using equation (3.6).

$$N_{ODL} = 8.9 \cdot 10^{-7} (W)$$

Maximal stray light in ODL	$< 8.9 \cdot 10^{-7} (W)$
----------------------------	---------------------------

3.6 OPD actuator requirements

The control bandwidth for the actuator is a requirement that is still To Be Considered (TBC).

OPD actuator requirements:

Moving actuator mass [24]	<100 (g)
Control bandwidth [6]	1 (kHz) ¹

¹ The bandwidth value has been assumed.



3.7 OPD metrology requirements

The ODL consists of the OPD metrology and the OPD actuator. The next requirements for the OPD metrology are necessary.

OPD metrology additional requirements:

Maximal extra mass on moving actuator [6]	48 (g)
Maximal acceleration in stroke direction [23]	30 ($\mu\text{m}/\text{s}^2$)
Outer length between the magnetic bearings [24]	250 (mm)
(See appendix A.2)	

OPD metrology requirements:

A relative displacement measurement needs to be made with respect to the fixed point of the moving mirror of the ODL. This happens when it is released after being clamped in by a launch lock mechanism. The launch lock mechanism is used to keep the moving actuator in its place in order to prevent damage on the magnetic bearings of the moving actuator during launch.

In this context space qualified means; photon resistance and functionality at vacuum. The stroke velocity of the mirror has the following requirements:

Minimal stroke velocity [6]	30 ($\mu\text{m}/\text{s}$)
Maximal stroke velocity [6]	170 ($\mu\text{m}/\text{s}$) - 500($\mu\text{m}/\text{s}$) ²

The stroke velocity needs to be translated to another design requirement, namely the sample frequency of the detector system of the fiber optic interferometer. The fringe frequency is the signal frequency. The frequency of the fringes that are detected at the photodiodes is described in equation (3.7).

$$f_{\text{fringe}} = \frac{v_{\text{max}}}{x} \tag{3.7}$$

Where:

$x(m)$ = Displacement of the moving mirror

$f_{\text{fringe}}(Hz)$ = Fringe signal frequency at the photodiode

$v_{\text{max}}(m/s)$ = Maximal stroke velocity of the moving mirror

Combining this relation with equation (3.2) and equation (4.3) gives the relation for the minimal required sample frequency of the ADC.

² The maximal required stroke velocity is still uncertain, for this thesis report the maximal required stroke velocity will be assumed to be 170 ($\mu\text{m}/\text{s}$).

$$f_{sample,adc} = \frac{4v_{max}}{\lambda_{laser}} \quad (3.8)$$

Where:

$f_{sample,adc}$ (Hz) = Sample frequency of the ADC

λ_{laser} (m) = Laser wavelength

Note that this obtained formula has the same relation as for the minimal sample frequency of the focal plane array that is described by equation (3.3). In order to prevent aliasing the minimal required sample frequency of the ADC will be determined. For a laser wavelength of 1550 (nm) and a maximal stroke velocity of the moving mirror of 170 ($\mu\text{m/s}$) the required sample frequency of the ADC can be calculated.

$$f_{sample,adc} = 439 \text{ (Hz)}$$

Where:

$f_{sample,adc}$ (Hz) = Sample frequency of the ADC

The maximal available power for the FTS is 7(W), from this power budget 2(W) are reserved for the OPD metrology [23]. This power budget is equally distributed over the electronics and LUNASYS.

The fiber optic interferometer will also be used in photometric mode. In this mode the FTS mechanism doesn't move with a constant velocity, but remains in a constant position. The exact static position of the FTS is still unknown however.

If the fiber optic interferometer can be reset and recalibrated the stability of the fiber optic interferometer is determined by the scan time of the FTS mechanism. Then the error of the measured position of the moving mirror is time limited. To be precise, it is limited by the scan time of the FTS mechanism. This gives the following requirements for the OPD metrology:

Total error [6]	~10 (nm)	over 200 (s)
Resolution [6]	<1 (nm)	
Stroke [6]	34,5 (mm)	
Sample frequency	439 (Hz)	
Parasitic heat load [6]	<100 (μW)	
Stray light	<0.89 (W)	
Control bandwidth [6]	1 (kHz)	(TBC)
P_{diss} electronics [6]	<1 (mW)	
Total required electrical power	<2 (W)	
Relative displacement measurement		
Space qualified [6]		
Functionality at low temperatures [6]		



The minimal operating temperature for the different components of the OPD metrology is given below in Table 3-3.

Table 3-3 Minimal operating temperature of all the different components for the OPD metrology

Component	Minimal temp. (K)
Laser	263
Circulator	263
3x3 splitter	263
Reference mirror	4.5
Measurement mirror	4.5
Grin lens	4.5
Fiber	4.5
Connector	4.5
Electronics	263

3.8 LUNASYS requirements

LUNASYS is part of the OPD metrology as can be seen in the system architecture shown in Figure 1-1. Some requirements overlap with the requirements for the electronics of the OPD metrology. These requirements are also stated for LUNASYS.

The secondary conditions for LUNASYS are described below in Table 3-4

Table 3-4 Secondary conditions for LUNASYS

Secondary condition	Description
Weight	As low as possible
Volume	As small as possible
Development time	Launch of SPICA in 2020
Costs	As low as possible
Lifetime expectancy	Several years

From the previous sections it became clear what the requirements for LUNASYS are for the SAFARI application. These requirements are summarized in Table 3-5.

Table 3-5 Requirements overview for LUNASYS

Type of requirement	Quantity
Total error	10 (nm) over 200(s)
Resolution	1 (nm)
Stroke	34.5 (mm)
Sample frequency	439 (Hz)
Heat load	100 (μ W)
Stray light power	890 (nW)
Control bandwidth	1 (kHz)
Space qualified	
Functionality at cryogenic temperature	4.5 ± 1.5 (K)
Maximum required electrical power for the laser	1 (W)
Relative displacement measurement	
Laser and electronics placed in room of 293 (K)	
Sensor head placed near the ODL	

Some system specifications are needed for the specifications of the OPD metrology. These specifications can be used for future detail engineering and are given in Table 3-6.

Table 3-6 System specifications necessary for the specifications of the OPD metrology

Type of specification	Quantity
Heat shield temperatures and spatial dimensions	See Table 3-1
Mechanical disturbance frequencies	15 (Hz) and 45 (Hz)
extra mass on moving actuator	48 (g)
Maximal acceleration on stroke direction	$30 (\mu\text{m}/\text{s}^2)$
Outer length between the magnetic bearings	250 (mm)

In sub question a) of the first research question there is asked what the requirements for LUNASYS for the SAFARI application are. These requirements are displayed in Table 3-5.



4 System specifications

Now that the requirements for the current setup of LUNASYS to be operational for the SAFARI instrument are known, the answer to the sub question 1b) needs to be determined. This question is: "What are the specifications of the current setup of LUNASYS". Taking the requirements formed in chapter 3 into account, it can be determined if the current setup will be operational for the SAFARI instrument. This can be done by validating the initial specifications of LUNASYS with the requirements.

In the next sections different models are used to estimate the specifications of the old OPD metrology. The requirements given in Table 3-5 will be validated one by one in the sections of this chapter. Finally in the last section of this chapter an overview of the system specifications will be given. These specifications will show that the current setup of LUNASYS is not yet operational for the SAFARI application.

4.1 Component location

Introduction

For reasons of functionality certain components of the fiber optic interferometers are required to be positioned in regions with a certain temperature.

Result

In Figure 3-4 where the old system configuration of LUNASYS is displayed, it can be seen that the electronics for the detector and the laser are placed before the heat shield of 253 (K). So the requirement for the placement of the laser and the electronics is met. Furthermore, the sensor head is placed behind the heat shield of 4.5 (K) within the cryogenic cooled zone for the FTS mechanism and is pointed towards the moving mirror. Clearly the two requirements for positioning the sensor head, the laser and the electronics are met.

4.2 Relative displacement measurement

Introduction

When the mirror moves, it is desired to know how much and in what direction the mirror moves. In other words a relative displacement of the mirror needs to be measured.

Result

A fiber optic interferometer is an absolute measurement system if it only has one interference signal. If a quadrature phased signal is added to the signal of the measurement system then a change of direction can be measured. The fiber optic interferometer based on a 3x3 splitter has a quadrature phased signal. For this reason

the measurement system is able to detect a change of direction in the displacement. If the system is calibrated, by setting the zero position when the moving mirror is still clamped in by the launch lock mechanism, then the moving mirror can only move into one direction and consequently a relative displacement with respect to the fixed position of the mirror when it's clamped in by the launch lock mechanism is obtained.

Another possibility is to introduce an end stop for the OPD actuator, which can be used as a fixed reference instead of the launch lock mechanism. In this way it is prevented that the launch lock mechanism is a Single Point Of Failure (SPOF) for the fiber optic interferometer. A SPOF is a part of a system, which causes the entire system to stop working in case of failure of this part.

4.3 Fiber optic interferometer resolution

Introduction

The smallest detectable change in position of the moving mirror is called the resolution of this measurement system. The required resolution for this measurement system is 1 (nm). This resolution is required in order to measure very small displacements of the moving mirror.

Assumptions

- Light with a wavelength of 1550 (nm) has to be used
- The voltage signal range is equal to the input range of the ADC

Modeling

The smallest detectable change that can be detected is a function of two things.

- The wavelength of the monochromatic light source
- The ADC that samples the signal.

The exact relation for the resolution of a measurement is given below [34].

$$\text{res} = \frac{U_{\text{range}} E}{U_{\text{signal}} 2^{n_{\text{bits}} - 1}} \quad (4.1)$$

Where:

$\text{res} (nm)$ = Resolution of the measurement system

$n_{\text{bits}} (-)$ = Number of bits in the ADC

$U_{\text{range}} (V)$ = Total voltage range of the ADC

$U_{\text{signal}} (V)$ = Total peak to peak voltage range of the signal

$E (nm)$ = Measure to what displacement U_{signal} corresponds

The optical path difference between the light travelling in the reference arm to the fixed mirror and back, and the light in the measurement arm travelling to the moving mirror and back is equal to twice the displacement of the moving mirror if the refractive index of the waveguide is assumed to be equal to one.

$$OPD = 2x \quad (4.2)$$

Where:

$x(nm)$ = Displacement of the moving mirror

$OPD(nm)$ = Optical Path Difference

It can also be stated that one fringe has the wavelength of the laser and is measured at the detector system. This fringe corresponds to a displacement of the moving mirror equal to half a wavelength of the laser light. This is explained in more detail in chapter 5.

$$x_{fringe} = \frac{\lambda_{laser}}{2} \quad (4.3)$$

Where:

$\lambda_{laser}(nm)$ = Laser wavelength

A full scale voltage range of the signal corresponds to half a fringe measured and this is equal to a quarter of a wavelength displacement. This gives:

$$E = \frac{\lambda_{laser}}{4}$$

Assuming that the voltage signal range is equal to the ADC input range, the following formula gives the resolution for the fiber optic interferometer.

$$res = \frac{\lambda_{laser}}{2^{n_{bits}+1}} \quad (4.4)$$

Result

A 12 bit ADC and a laser wavelength of 1550 (nm) is used. Using (4.4) gives:

$$res = \frac{1550(nm)}{2^{12+1}} = 0.19(nm)$$

The given wavelength and number of bits of the ADC are sufficient to meet the requirement for the resolution of 1 (nm).

Discussion

In reality the voltage signal will be chosen lower than the ADC input range in order to prevent clipping of the signal. This will result in a higher value for the resolution than calculated, depending on the ratio of the signal range and the ADC input range.

The use of light with a wavelength of 1550 (nm) is not a requirement. Preferably the wavelength should be chosen as far as possible outside of the spectral bandwidth of the detector system, because this slightly increases the effectivity of the focal plane array. This is due to the fact that the optical filters between the ODL and the detectors filter more effective at this wavelength (a bandpass filter is used). The lowest wavelength that needs to be detected for the short wave focal plane array is 34 (μm). For this reason the wavelength of the laser light should be chosen as low as possible.

When choosing the wavelength of the laser several factors such as availability of the optical components, filter efficiency and the resolution of the measurement system need to be taken into account.

4.4 Sample frequency

Introduction

If no clever techniques software techniques are used to prevent aliasing. Then the velocity, of which the moving mirror moves, is a measure for the frequency of the fringes and therefore a measure for the minimal required sample frequency. In this case the minimal sampling frequency in order to prevent aliasing is 439 (Hz).

Assumptions

- The velocity of the moving mirror is constant
- The electronics other than the ADC are not limiting the bandwidth of the measurement system
- The control bandwidth of the ODL is not defining for the minimal required sample frequency

Modeling

The sample frequency of the ADC128S102 is set at 100 (kHz) [7]. The average is determined over the last 128 samples³. Then the averaged value is saved and the other 127 samples are discarded. So the effective sample frequency during signal processing is:

$$f_{eff} = \frac{100(kHz)}{128} = 781(Hz)$$

Where:

$$f_{eff} (Hz) = \text{Effective sample frequency}$$

³ This value is arbitrarily chosen for testing purposes.

Result

From this calculation it can be concluded that the sample frequency is high enough to detect the moving mirror with the desired stroke velocity without aliasing.

Validation

The bandwidth of the used photodiodes is about 1 (MHz) as can be seen from the datasheet. From the datasheets of the OPA656 and OP2177 the following specifications are obtained:

- The gain bandwidth product (GBW) of the opamp that is used in the transimpedance amplifier is 230 (MHz)
- The active low pass filter that is used during signal conditioning has a GBW of 1.3 (MHz) and a gain of 3 is set for this filter.

So the assumption that the electronics were not limiting the bandwidth of the system was correct.

Discussion

The minimal required sample frequency can be determined by two things: The maximal signal frequency and the bandwidth of the control loop. The control bandwidth for the OPD actuator is higher than the minimal calculated sample frequency for the ADC. Therefore the limiting factor for the minimal sample frequency will be the control bandwidth and not the maximal stroke velocity of the ODL. For this design, it is assumed that the control bandwidth of the ODL is not defining for the minimal required sample frequency.

4.5 Heat load and stray light

Introduction

For this application stray light is defined as light that exits the interferometer, and leaks into the cryogenic cooled zone of the ODL without going back into the fiber optic interferometer. In order to prevent too much stray light from entering the detector, a maximum temperature for the room of the Mach Zehnder interferometer is defined. In order to prevent a raise of temperature the maximal amount of heat entering the cryogenic cooled zone around the Mach Zehnder interferometer is restricted. This can be seen in Figure 3-2. LUNASYS is thermally connected to the warm electronics side so heat is transferred into the cryogenic cooled zone by conduction. Also, the optical components inside the cryogenic cooled zone dissipate optical power that is strayed into the cryogenic room or is absorbed and transferred into heat.

Assumptions

- LUNASYS is in steady state or in other words in thermal equilibrium with its surroundings.
- The change of internal energy is zero and the work done by and on the system is zero.
- Heat transfer by convection can be neglected.

- Heat transfer out of the cryogenic cooled system boundary through the fiber optic cable is zero.
- Heat transfer by radiation within the fiber optic cable besides the laser power can be neglected.
- The feed through on the wall of the cryogenic cooled zone blocks all thermal radiation from entering the cryogenic cooled zone outside the optic fiber.
- Power losses in the cables, the connectors and splitter are completely absorbed by a tube shield surrounding these components.
- Power losses in the moving measurement mirror, the reference mirror and the grin lens are completely scattered to the surroundings.

Modeling

The first law of thermodynamics states [33]:

$$dU = dQ - dW \quad (4.5)$$

Where:

$dU (J)$ = Change of internal energy

$dQ (J)$ = Heat added to the system

$dW (J)$ = Work done by the system

Rewriting (4.5) gives:

$$d\dot{U} = d\dot{Q} - d\dot{W} \quad (4.6)$$

In Figure 4-1 a thermal model of LUNASYS inside the cryogenic cooled zone is given based on Figure 3-2. The total heat load on the cryogenic cooled zone can be determined by making a power balance on the system boundary of LUNASYS.

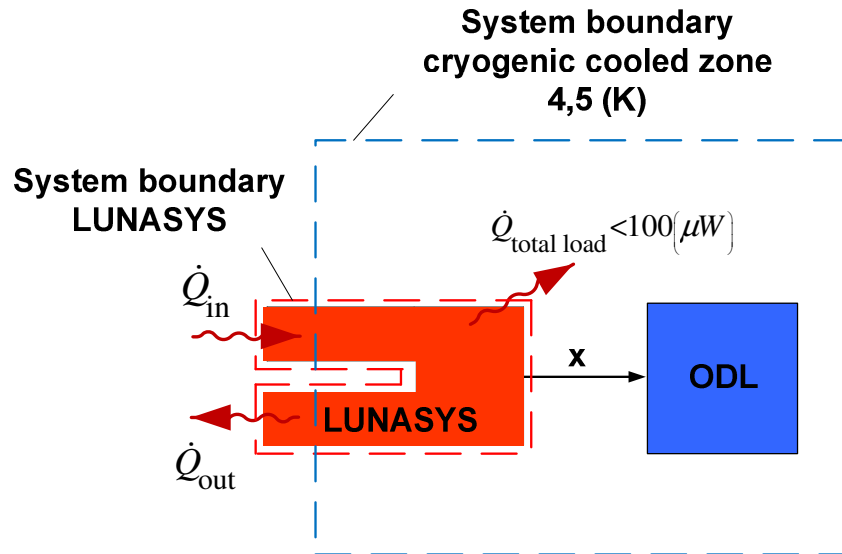


Figure 4-1 Thermal model of LUNASYS within the cryogenic cooled zone

It is assumed that LUNASYS is in thermal equilibrium with its surroundings and the work done by the system and on the system is equal to zero. These assumptions are used to fill into equation (4.6). The resulting equation is given below.

$$d\dot{Q} = 0 \quad (4.7)$$

Now consider a power balance on the system boundary of LUNASYS (the red dotted line) in Figure 4-1:

$$d\dot{Q} = 0 \text{ or } \sum \dot{Q} = 0$$

$$\dot{Q}_{in} - \dot{Q}_{out} - \dot{Q}_{total\ load} = 0 \quad (4.8)$$

Where:

$\dot{Q}_{in} (W)$ = Power entering the cryogenic cooled zone

$\dot{Q}_{out} (W)$ = Power exiting the cryogenic cooled zone

$\dot{Q}_{total\ load} (W)$ = Total heat load on the cryogenic cooled zone

The total heat load can be subdivided into two main heat components. One heat component consists of the power lost by the laser and the other heat component consists of the heat transferred at the end of the fiber optic cable to the cryogenic cooled wall.

$$\dot{Q}_{total\ load} = \dot{Q}_{standard\ load} + \dot{Q}_{laser\ load} \quad (4.9)$$

Where:

$\dot{Q}_{\text{laser load}} (W)$ = Heat load on the cryogenic cooled zone caused by the laser

$\dot{Q}_{\text{standard load}} (W)$ = Standard heat load on the system

If the power entering into the system boundary of the cryogenic cooled zone is considered, then this power consists of two components. This is written in the equation below.

$$\dot{Q}_{\text{in}} = \dot{Q}_{\text{standard load}} + \dot{Q}_{\text{laser, in}} \quad (4.10)$$

Where:

$\dot{Q}_{\text{standard load}} (W)$ = Standard heat load on the system

$\dot{Q}_{\text{laser, in}} (W)$ = Laser power entering the cryogenic cooled zone

Now consider Figure 4-2. If it assumed that the thermal resistance from the fiber to the active cooled wall R_{wall} is much higher than the thermal resistance of the fiber R_{fiber} , then most heat going through the fiber enters the cryogenic cooled zone. This assumption can't be validated because the exact dimensions of the cryogenic cooled wall are not known yet. Consider a worst case scenario when all the heat that reaches the cryogenic cooled wall through conduction of the fiber optic cable enters the cryogenic cooled space.

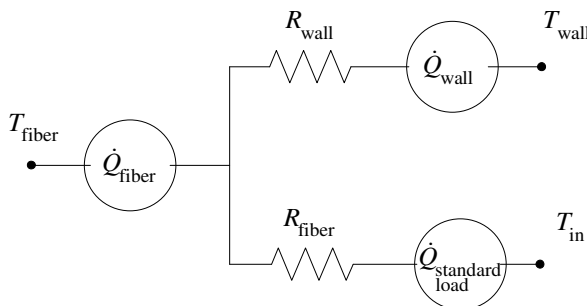


Figure 4-2 Thermal resistor network of a fiber that passes through the active cooled cryogenic wall

As a result of this assumption the next equation applies.

$$\dot{Q}_{\text{fiber}} = \dot{Q}_{\text{standard load}} \quad (4.11)$$

Where:

$\dot{Q}_{\text{fiber}} (W)$ = Heat reaching the cryogenic cooled wall by conduction of the fiber

It is assumed that the heat transfer from LUNASYS going out of the cryogenic cooled system boundary through the fiber optic cable is zero. Also, the mechanical cooling

power is disregarded. Therefore, all power exiting the system boundary of the cryogenic cooled space is the returning laser power.

$$\dot{Q}_{\text{out}} = \dot{Q}_{\text{laser, out}} \quad (4.12)$$

Where:

$\dot{Q}_{\text{laser, out}}$ (W) = Laser power exiting the cryogenic cooled zone

Equation (4.13) is used to define how much of the laser power lost out of the system boundary of LUNASYS into the cryogenic cooled zone is transferred to heat and how much laser power is unleashed into the cryogenic cooled space.

$$\dot{Q}_{\text{laser load}} + P_{\text{stray light}} = \dot{Q}_{\text{laser, in}} - \dot{Q}_{\text{laser, out}} \quad (4.13)$$

Where:

$P_{\text{stray light}}$ (W) = Stray light power within the cryogenic cooled zone

Result

The standard heat load for a single fiber optic cable entering the cryogenic cooled space is modeled and numerically determined in Appendix B.1. The result is given below.

$$\dot{Q}_{\text{fiber}} = 0.3(\mu W)$$

For the old system configuration two fiber optic cables enter the cryogenic cooled space. This means that the standard heat load on the system becomes:

$$\dot{Q}_{\text{standard load}} = 2\dot{Q}_{\text{fiber}} = 0.6(\mu W)$$

The laser power loss within the cryogenic cooled zone can be determined with the model and the calculation in Appendix B.2. The result is given in Figure 4-3. The contribution of all optical components to the total laser power loss is expressed as a percentage of the total laser power loss.

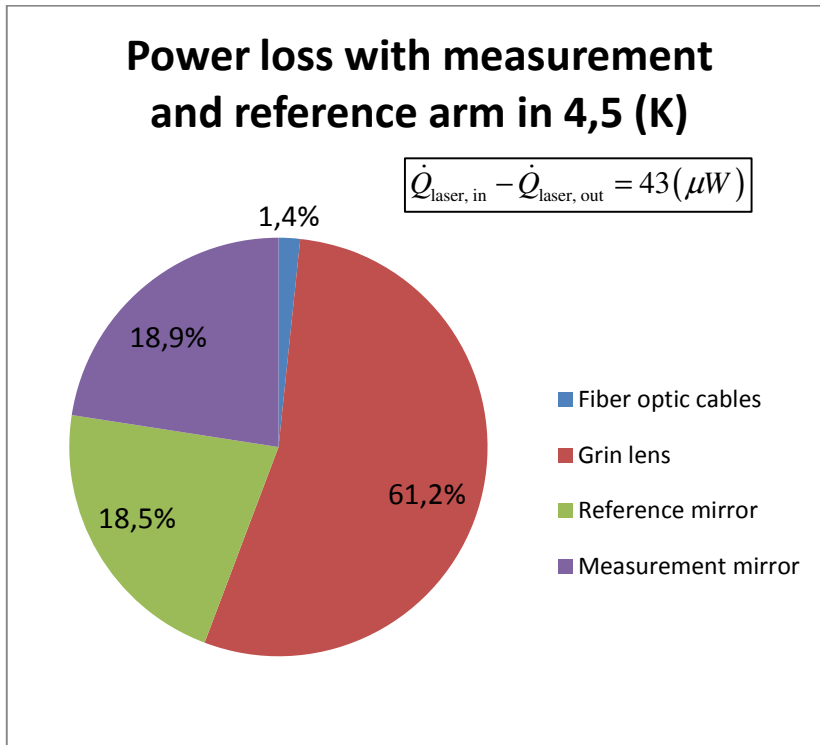


Figure 4-3 Distribution of the laser power loss of the components within the measurement arm and the reference arm placed within the cryogenic cooled zone of 4.5 (K)

Now there needs to be considered what happens with all this laser power that is lost in all the different optical components.

From equation (4.13) it can be seen that the total heat load on the cryogenic cooled zone and the stray light power within the cryogenic cooled zone are related to each other. If it is assumed that an ideal opaque tube shield is surrounding the fiber optic cables, the connectors and the splitter, then all laser power lost in these components is absorbed by the shield and transferred to heat. However, the lost power in the moving measurement mirror, the reference mirror and the grin lens are assumed to completely scatter into the surroundings as stray light. With these assumptions the heat load on the cryogenic cooled zone caused by the laser can be calculated and thereby also the total heat load on the cryogenic cooled zone. Furthermore, the amount of stray light can also be calculated.

$$\dot{Q}_{\text{laser load}} = P_{\text{cables}} = 0.7 (\mu W)$$

The total heat load can be calculated by applying equation (4.9).

$$\dot{Q}_{\text{total load}} = 0.6 (\mu W) + 0.7 (\mu W) = 1.3 (\mu W)$$

The amount of stray light from each part can be calculated with the result from Appendix B.2.

$$P_{\text{stray light}} = P_{\text{grin lens}} + P_{\text{measurement mirror}} + P_{\text{reference mirror}} = 22.3(\mu\text{W}) + 9.7(\mu\text{W}) + 9.3(\mu\text{W}) = 42.3(\mu\text{W})$$

4.6 Total required electrical power

The total required electrical power in order to make the fiber optic interferometer operate is determined by two main power consumers:

- Electronics
- Laser

The total required electrical power for the electronics is at the moment estimated to be 670 (mW) [7].

The total required electrical power for the laser is specified on the datasheet of the laser given in appendix G.1. The required power for the laser is 4-6 (W). The maximal available power for the OPD metrology was determined in section 3.7 and is 2 (W).

From these results it can be concluded that the required electrical power for the OPD metrology is too high and it doesn't meet the requirement. More specifically the maximum electrical power for the laser is too high and therefore LUNASYS doesn't meet the requirement for the total required electrical power.

The functionality of the laser is specified for a maximal temperature fluctuation of the laser casing of 0.1 (K). In order to maintain this temperature stability, possibly a temperature control unit is required for the laser and this temperature control unit would require extra electrical power. However it is still unknown if a temperature control unit is really necessary. Therefore this temperature control unit is not taken into account for this specification.

4.7 Space qualification

It is required for all components to function in vacuum. In Table 4-1 a summary of the status of the space qualification of all used components is given.



Table 4-1 Status summary for the space qualification of the components for the fiber optic interferometer [21]

Device	Type	Space qualified?	Remarks
Laser	RIO Orion laser module	no	NASA, in progress
Circulator	Optolink circulator	no	
3x3 splitter	Gould 3x3 coupler	no	
Grin lens	Grintech	no	
Fiber	IX-fiber IXF-CUST-SiO2/F	yes	Optical identical to SMF28+ fiber.
Connector	Diamond mini-AVIM	no	Never tested at 4 (K) (min -150 °C), ESA qualification in progress. Contact Diamond for this.
Detector	Fermionics FD100	no	SRON, in progress

Clearly not all components are space qualified yet.

4.8 Functionality at 4.5 (K)

Introduction

A big problem for designing mechanical constructions in cryogenic temperatures is the occurrence of undesired mechanical stresses or even fracture of components due to the use of different materials with different coefficients of thermal expansion that are rigidly attached together. Depending on the location of the components, certain functionality requirements are posed on the components.

Result

The lowest required operating temperature for each component of the fiber optic interferometer is given below. Operating ranges are specified by the suppliers of the components.

Table 4-2 Required minimal temperature and specified operating range for the optical components used in the fiber optic interferometer

Component	Minimal temp. (K)	Specified operating temp. range (K)
Laser	253	283-328
Circulator	253	233-343
3x3 splitter	253	233-358
Reference mirror	4.5	???
Measurement mirror	4.5	???
Grin lens	4.5	???
Fiber	4.5	???
Connector	4.5	???
Electronics	253	248-298

For components with an unknown operating temperature range, functionality can't be guaranteed. So it is assumed that these components won't function at the desired minimal temperature at all.

If a grin lens is designed for a certain temperature range, say -10 degrees Celsius to 60 degrees Celsius. Then for lower temperatures the lens will shrink in all directions. As a consequence the outer layer of the lens will come closer to the optical center of the lens and this will result in too much refraction of the outer rays of the light that passes through the lens. The exiting light bundle won't be collimated anymore and the light rays will converge. When the light bundle is reflected by the moving mirror and come back onto the grin lens, the light rays are not perpendicular to the lens surface. As a consequence not all the light will couple back into the fiber core and the amount of light that couples back into the fiber is dependent on the position of the moving mirror. In appendix D.4 it is shown that this will result in an error of the measured position of the moving mirror.

Discussion

If the fibers are welded together the use of connectors won't be necessary. This will result in less power loss, and the connectors don't have to be used at cryogenic temperatures. However, integration of the fiber optic interferometer with the harness and the other mechanical structures on SPICA could become a problem.

4.9 Accuracy and precision

There are many factors that influence the accuracy and the precision of the measurement system. In the next paragraphs the error caused by many of these different factors will be calculated in order to determine the accuracy and precision. First the relation between the displacement of the moving mirror and the phase of the interference pattern is given. The superposition of waves of the same frequency is explained in Appendix C.1. The result of this wave addition gives the relation between the displacement of the moving mirror and the phase of the interference pattern. Then

the basic algorithm used for signal processing is explained. Finally an estimation of the signals on the three photodiodes is made, since these signals are needed for certain error calculations.

The relation between the displacement of the moving mirror and the phase of the interference pattern is written in equation (4.14). This equation is obtained in Appendix C.1 and is equal to equation (C.8).

$$x = \frac{\lambda\phi}{4\pi n} \quad (4.14)$$

Equation (4.14) will be used very frequently in this report to calculate the displacement. When it is approximated that the refractive index of the waveguide is equal to one, equation (4.14) simplifies to:

$$x = \frac{\lambda\phi}{4\pi} \quad (4.15)$$

The basic algorithm used for signal processing is explained in Appendix C.2. A Clarke transformation of the three signals measured on the photodiode is performed.

Consider three signals at the photodiodes of the detector system of LUNASYS.

$$I_1(OPD) = A_1 \left(1 + V_1 \cos \left(\frac{2\pi}{\lambda} OPD \right) \right) \quad (4.16)$$

$$I_2(OPD) = A_2 \left(1 + V_2 \cos \left(\frac{2\pi}{\lambda} OPD + \frac{2\pi}{3} \right) \right) \quad (4.17)$$

$$I_3(OPD) = A_3 \left(1 + V_3 \cos \left(\frac{2\pi}{\lambda} OPD + \frac{4\pi}{3} \right) \right) \quad (4.18)$$

Where:

$I(A)$ = Current signal

$A(A)$ = Current offset

$V(-)$ = Visibility or contrast

The three signals are not calibrated and have a phase difference with respect to each other of 120 degrees. If calibration is performed like described in Appendix C.2, then the three signals on the photodiodes can be used to calculate the displacement. The phase of the projection on the complex plane of the calibrated three intensities that are measured on the different photodiodes can be calculated with the next formula.

$$\theta = \left| \arctan \left(\sqrt{3} \frac{I_+ - I_-}{2I_s - (I_+ + I_-)} \right) \right| \quad (4.19)$$

For certain calculations on the accuracy of the measurement system it is required to estimate what the laser power and the visibility of the three signals at the photodiodes will be.

From the results displayed in Appendix C.3 the signals from equations (4.16), (4.17) and (4.18) become:

$$I_1(OPD) = 32.4(\mu A) \left(1 + 0.74 \cos \left(\frac{2\pi}{\lambda} OPD \right) \right) \quad (4.20)$$

$$I_2(OPD) = 44.5(\mu A) \left(1 + 0.96 \cos \left(\frac{2\pi}{\lambda} OPD + \frac{2\pi}{3} \right) \right) \quad (4.21)$$

$$I_3(OPD) = 48.3(\mu A) \left(1 + 0.77 \cos \left(\frac{2\pi}{\lambda} OPD + \frac{4\pi}{3} \right) \right) \quad (4.22)$$

The voltage signal at the ADC can be calculated with equation (C.26) that is shown below.

$$V_{\max} = I_{\text{photo}} G_{\text{trans}} G_{\text{filter}} \quad (4.23)$$

4.9.1 Intensity noise

Introduction

The signals used for the algorithm that determine the displacement of the moving mirror, deviate from the mean measured value due to the presence of noise. This causes an uncertainty in the measurement. This uncertainty can be expressed as a factor that influences the precision of the mirror position. In the content of this report by intensity noise there is meant; the noise on the detected signal that seems to be a fluctuation of the intensity of the signal. This includes all different noise sources that have an effect on the value of the processed signal into the algorithm, except for the intensity noise induced by the phase noise of the laser.

Assumptions

The assumptions made are given in appendix D.1.

Modeling

The intensity noise has been modeled in appendix D.1. The electric circuit that is used to qualify the noise sources and to quantify the impact on the precision of the displacement of the moving mirror is shown in Figure D-1 and illustrated again in the figure below.

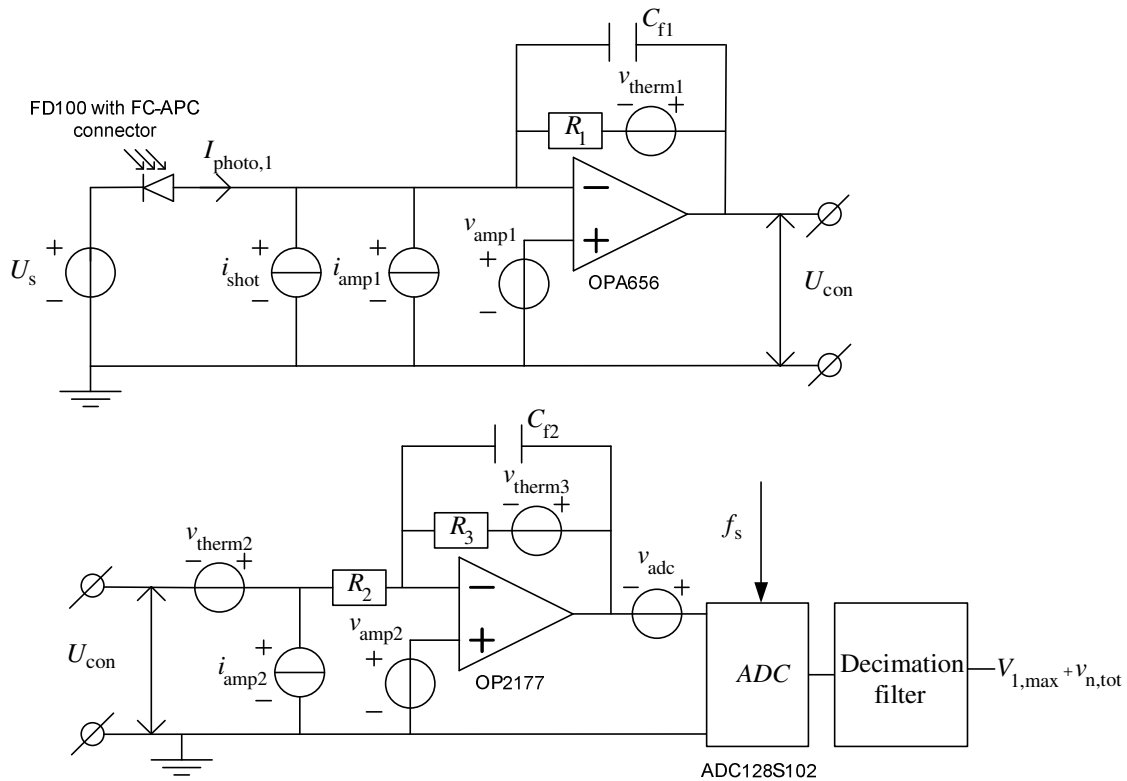


Figure 4-4 Simplified intensity noise model of the analogue electronics based on the electronic circuit shown in Appendix A.1

Result

The different noise sources in Figure 4-4 all have a different influence on the output signal after the decimation filter. The contribution of all noise sources on this output signal is given in Table 4-3.

Table 4-3 Contribution of all the noise sources on the final output signal $v_{n,tot}$ after the decimation filter, modeled for photodiode 1

Noise source	Output noise
$i_{shot} = 5.3(pA / \sqrt{Hz})$	$v_{n1} = 3.1(\mu V_{rms})$
$i_{amp1} = 1.3(fA / \sqrt{Hz})$	$v_{n2} = 0.001(\mu V_{rms})$
$v_{amp1} = 7.0(nV / \sqrt{Hz})$	$v_{n3} = 0.41(\mu V_{rms})$
$v_{therm1} = 14.2(nV / \sqrt{Hz})$	$v_{n4} = 0.84(\mu V_{rms})$
$i_{amp2} = 0.2(pA / \sqrt{Hz})$	$v_{n5} = 0.04(\mu V_{rms})$
$v_{amp2} = 7.9(nV / \sqrt{Hz})$	$v_{n6} = 4.0(\mu V_{rms})$
$v_{therm2} = 7.3(nV / \sqrt{Hz})$	$v_{n7} = 0.43(\mu V_{rms})$
$v_{therm3} = 12.7(nV / \sqrt{Hz})$	$v_{n8} = 0.25(\mu V_{rms})$
$v_{adc} = 725(nV / \sqrt{Hz})$	$v_{n9} = 9.2(\mu V_{rms})$

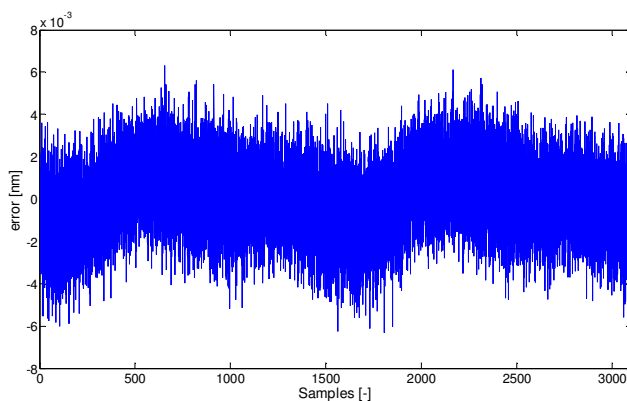
The total noise in the three circuits can be determined by applying equation (D.15) on the results given in Table 4-3. This is performed for all three photodiodes.

$$v_{1,tot} = 11(\mu V_{rms})$$

$$v_{2,tot} = 22(\mu V_{rms})$$

$$v_{3,tot} = 22(\mu V_{rms})$$

With these results, the contribution to the precision of the position of the mirror is simulated. The result of a simulation where the moving mirror moves with constant velocity and makes a displacement of 1550 (nm) is shown in the next figure.

**Figure 4-5 Simulated error signal due to the presence of intensity noise on the three signals**



The standard deviation of this noise signal is equal to the precision of the mirror position caused by the intensity noise, for a mirror moving with constant velocity:

$$e_{\text{int},n} = 1.6 (pm)$$

4.9.2 Optical disturbance signals

Introduction

Reflections and cross talk can create undesired optical signals within the measurement system that interact with the optical signal that's containing the information about the measured position of the moving mirror. The position error caused by these optical disturbance signals is modeled and determined in appendix D.2.

Assumptions and modeling

The applied model and assumptions made are described in appendix D.2.

Result

Two signals on the photodiode have been calculated. One signal arises from the power calculations from Appendix B.2. This is described by the parameters in Table C-1 and equations (C.9), (C.10) and (C.11). The other signal is the optical disturbance signal. The result of the calculation of the power of the optical disturbance signals is displayed as a ratio of the power of optical disturbance signals over the original signal. The ratio of the ideal signal over the sum of all optical disturbance signals (the total disturbance) is also shown in this table for all three photodiodes. The disturbance numbers refer to the disturbances shown in Figure D-19.

Table 4-4 Ratio of the power of each disturbance signal over the ideal calculated signal power that has been calculated in appendix C.3, given for all three photodiodes

Disturbance #	Ratio photodiode 1	Ratio photodiode 2	Ratio photodiode 3
$I_{u,1}$	1.4E-04	0.0E+00	0.0E+00
$I_{u,2}$	2.6E-07	0.0E+00	0.0E+00
$I_{u,3}$	0.0E+00	2.0E-06	2.0E-06
$I_{u,4}$	4.4E-09	3.4E-09	3.5E-09
$I_{u,5}$	6.9E-07	7.0E-07	6.1E-07
$I_{u,6}$	6.2E-07	6.1E-07	7.1E-07
$I_{u,7}$	3.6E-02	3.6E-02	4.2E-02
$I_{u,8}$	3.0E-02	3.0E-02	3.5E-02
Total disturbance	6.7E-02	6.6E-02	7.6E-02

The largest optical disturbance signals are $I_{u,7}$ and $I_{u,8}$. In appendix D.2 it can be seen that these disturbances are caused by the grin lens.

The simulated error due to these optical disturbances for a mirror moving over a distance of 1550 (nm) with constant velocity is shown below.

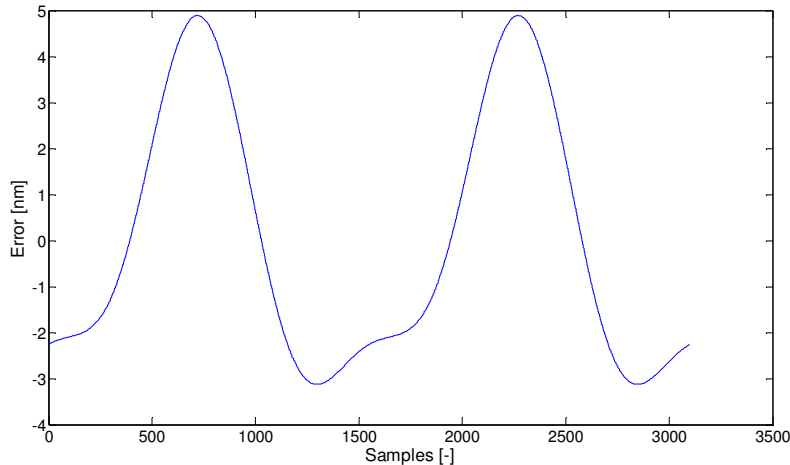


Figure 4-6 Simulated error of the measurement system for two fringe signals due to the influence of optical disturbance signals

The resulting error is a systematic error. The maximal error that can occur is equal to:

$$e_{\text{opt,dis}} = 4.9 \text{ (nm)}$$

4.9.3 Laser

Introduction

Non-ideal behavior of the laser results in errors of the measured position of the moving mirror. In the next three subsections different types of non-ideal behavior of the laser will be treated. Most required information about the specifications of the laser can be found in appendix G.1 and G.2. A grade 1 laser is used for the initial system configuration.

Assumptions

In the datasheets it is not mentioned that the laser has a certain settling time for the power and frequency to become stable. This settling time is in the order of 10 (s) [27]. Also an important fact is that certain specifications are made for a fixed case temperature. The exact wavelength is determined in the laser test report (see appendix G.2) and is 1550.148 (nm).

- It is assumed in this report that the settling time for the laser power has passed and the frequency has become stable
- It is assumed in this report that the laser casing temperature suffices to the made temperature requirements
- In this report it will be assumed that the wavelength of the laser is 1550 (nm)

- The maximal measured OPD of the fiber optic interferometer is assumed to be 0.1 (m)

4.9.3.1 Frequency stability

After one hour of stabilization the frequency stability of the laser, with an assumed constant casing temperature can be obtained from appendix G.1. By correspondence with the supplier of the laser, it became clear that the maximal case temperature fluctuation is allowed to be 0.1 (K) [27]. If the fluctuation is higher than this value, the specifications from the datasheet can't be guaranteed.

The worst case for the measured position error is when the frequency stability has a maximal value. In appendix G.1 two values are given for the frequency stability corresponding with two different running times.

$$\Delta v_1 = 4(MHz) \quad \text{free running over 1 hour}$$

$$\Delta v_8 = 6(MHz) \quad \text{free running over 8 hours}$$

From appendix D.3 the frequency stability is related to the wavelength deviation as described in the formula below.

$$\Delta \lambda = \frac{\Delta v}{v_{\text{laser}}} \lambda_{\text{laser}} = \frac{\Delta v \lambda_{\text{laser}}^2}{c} \quad (4.24)$$

Where:

$\Delta \lambda (m)$ = Wavelength deviation from the center wavelength of the laser

$\Delta v (Hz)$ = Frequency deviation from the center frequency of the laser

For the given frequency stabilities this results to:

$$\Delta \lambda_1 = 3.2 \cdot 10^{-14} (m) \quad \text{free running over 1 hour}$$

$$\Delta \lambda_8 = 4.8 \cdot 10^{-14} (m) \quad \text{free running over 8 hours}$$

The stroke of the moving mirror is determined in chapter 3 and is 0.0345 (m). It is assumed that there needs to be some space between the moving mirror on the ODL and the sensor head of the fiber optic interferometer so the total OPD is estimated to be twice the stroke of the moving mirror, that is about 0.07 (m), plus a small margin of about 0.015 (m). This gives an OPD of 0.1 (m). Using the information from appendix D.3 the measured error due to the frequency stability of the laser is described below:

$$e_{\text{laser drift}} = -\frac{OPD \cdot \Delta\lambda_T}{2(\lambda_{\text{laser}} + \Delta\lambda_T)} \quad (4.25)$$

Where:

$e_{\text{laser drift}} (m)$ = Change of detected position due to laser drift

Filling in equation (4.25) for the calculated wavelength deviations gives the next two absolute results for the error of the detected position of the moving mirror due to laser drift.

$e_{\text{laser drift},1} = 1.0(nm)$ free running over 1 hour

$e_{\text{laser drift},8} = 1.5(nm)$ free running over 8 hours

4.9.3.2 Spectral linewidth

Ideally the used laser has a single frequency. Unfortunately in practice lasers have different frequency components within the laser beam. These frequency components also have different intensities. The spectral linewidth, or the Full Width at Half Maximum (FWHM), is a measure for the spectral width of the laser beam. This non-ideal behavior also causes an error in the measured position of the moving mirror. The FWHM for the grade 1 laser is obtained from appendix G.1.

$$FWHM = 15(kHz)$$

Similar to the frequency stability, applying equations (4.24) and (4.25) will give the error of the detected position of the moving mirror due to the spectral linewidth of the laser. Because the FWHM is defined as the spectral bandwidth between the frequencies where the laser has half its intensity, the calculation of the error will be made for half the FWHM ($= \Delta\nu$). See figure below.

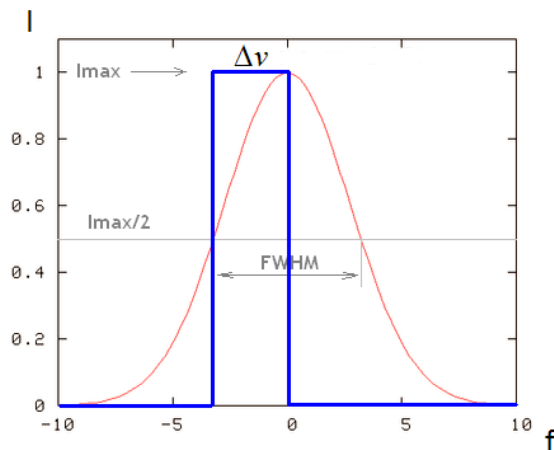


Figure 4-7 Modeled frequency deviation due to FWHM

The wavelength deviation is:

$$\Delta\lambda_{FWHM} = 6.0 \cdot 10^{-17} (m)$$

Where:

$$\Delta\lambda_{FWHM} (m) = \text{Wavelength deviation due to the FWHM}$$

Using equation (4.25) for the calculated wavelength deviation gives the absolute error in the detected position of the moving mirror due to the FWHM. The result is given below.

$$e_{FWHM} = 1.9 (pm)$$

Where:

$$e_{FWHM} (m) = \text{Change of detected position due to the FWHM}$$

4.9.4 Temperature

Introduction

Every measurement system is influenced by temperature more or less. This measurement system is no exception on this and is also influenced by temperature.

In this paragraph the influence of a small temperature fluctuation on the reference arm and the measurement arm will be analyzed. From a simple calculation it can be seen that the accuracy of the measurement system is highly influenced by small temperature disturbances on the reference, and the measurement arm. This calculation will be performed in this paragraph.

Assumptions

- The influence of the temperature on components other than the measurement and reference arm of the fiber optic interferometer can be neglected
- The temperature distribution over the reference arm is homogeneous
- The thermal coefficient of expansion of the entire fiber optic cable is equal to the thermal coefficient of Pyrex glass at room temperature
- The materials are homogeneous and isotropic

Modeling

Temperature fluctuations in the measurement arm and in the reference arm influence the accuracy of the measurement system. If the length of one of these arms changes, then the OPD will change as well. When the temperature of one of the fiber optic cables changes over time, the fiber optic cable of the measurement arm will stretch out or contract differently with respect to the cable of the reference arm. Consequently a change of the OPD will be measured over time. Now consider Figure 4-8. The OPD can be written as a function of OP_1 , OP_2 and OP_3 .

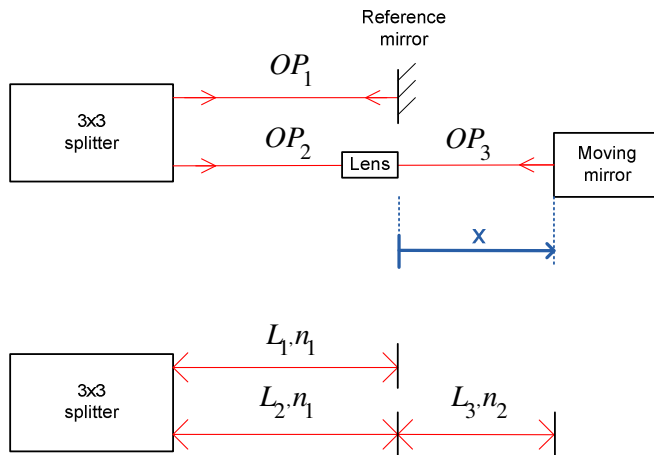


Figure 4-8 OPD of the fiber optic interferometer

The optical path difference of the two electromagnetic waves (EM) traveling through the waveguides with refractive indices n_1 and n_2 are defined in appendix D.3 as equation (D.26).

$$OPD = n_2 x_2 - n_1 x_1 \quad (4.26)$$

If the OPD of the fiber optic interferometer is determined for Figure 4-8, then in the upper drawing of this figure the optical paths of the reference arm and the measurement arm are shown. In the lower drawing the lengths of the fibers and the refractive index of the waveguides are given. Using equation (D.27) and considering that the refractive index now is not constant, will result in the following optical path difference.

$$OPD = 2(OP_1 - (OP_2 + OP_3)) \quad (4.27)$$

Rewriting this equation gives:

$$OPD = 2(n_1L_1 - (n_1L_2 + n_2L_3)) \quad (4.28)$$

Consider the case where the reference arm sustains a temperature change with respect to the measurement arm. The formula with which the error due to this temperature change can be calculated will now be determined. The mechanical strain is defined in equation (4.29).

$$\varepsilon = \frac{\Delta l}{l_0} \quad (4.29)$$

Where:

$\varepsilon (m/m)$ = Strain

$\Delta l (m)$ = Change of length

$l_0 (m)$ = Initial length

The strain can also be written as a function of the linear thermal expansion coefficient and the change of temperature.

$$\varepsilon = \alpha \Delta T \quad (4.30)$$

Where:

$\alpha (K^{-1})$ = Linear thermal expansion coefficient

$\Delta T (K)$ = Change of temperature

If equation (4.29) and (4.30) are combined then the next formula can be obtained:

$$\Delta l = l_0 \alpha \Delta T \quad (4.31)$$

With equation (4.31) the new OPD can be rewritten as a function of the temperature change of the reference arm.

$$OPD_{new} = 2(n_1L_1(1 + \alpha \Delta T) - (n_1L_2 + n_2L_3)) \quad (4.32)$$

Where:

$OPD_{new} (m)$ = New optical path difference

It was assumed that the temperature of the measurement arm remains constant. If the temperature in the reference arm changes over time the OPD described in equation (4.32) can be simplified to the next equation.

$$\frac{d(OPD)}{dt} = \frac{d}{dt} [2n_1L_1(1 + \alpha\Delta T)] \quad (4.33)$$

The refractive index is also dependent on the temperature. By applying the chain rule the next equation could be written for the change of the refractive index over time.

$$\frac{dn}{dt} = \frac{dn}{dT} \frac{dT}{dt} \quad (4.34)$$

By applying the product rule of differentiation and combining equations (4.36) and (4.37) the next equation can be obtained.

$$\frac{d(OPD)}{dt} = 2L_1 \frac{dn_1}{dt} \frac{dT}{dt} + 2L_1\alpha \frac{dn_1}{dt} \frac{dT}{dt} + 2L_1\alpha n_1 \frac{dT}{dt} \quad (4.35)$$

The change of the OPD over a certain time (dt_1), can be written in the next formula:

$$\frac{d(OPD)}{dt_1} = 2L_1\Delta T \frac{dn_1}{dt} + 2L_1\alpha\Delta T \frac{dn_1}{dt} + 2L_1\alpha n_1\Delta T \quad (4.36)$$

Where:

$dt_1 (s)$ = Time interval

Assume that the temperature of the reference arm is homogeneous, the material is homogeneous and isotropic and the thermal coefficient of expansion of the entire fiber optic cable is equal to the thermal coefficient of Pyrex glass at room temperature. With these assumptions the error caused by the temperature change of the reference arm is equal to the change of the OPD described by (D.27).

Result

The length of the reference arm is 1 (m), the temperature change is 1 (K), the refractive index of Pyrex glass is 1.55 and the thermal coefficient of expansion for Pyrex at room temperature is 8.5×10^{-6} (K^{-1}). The change of the refractive index over temperature of the waveguide material in the fiber optic cable is assumed to be equal to the value for fused quartz. On the temperature interval from 20 degrees Celsius to 30 degrees Celsius the average value of the refractive index change over temperature is -1.28×10^{-5} (K^{-1}). Because this is a negative value the refractive index decreases with increasing temperature. This means that this effect compensates for the elongation and contraction of the cable due to thermal strains. After the time interval dt_1 the error becomes:

$$e_T = 2L_1\Delta T \frac{dn_1}{dt} + 2L_1\alpha\Delta T \frac{dn_1}{dt} + 2L_1\alpha n_1\Delta T \quad \text{after a time } dt_1 \quad (4.37)$$

Where:

$e_r(m)$ = Error due to a temperature disturbance on the reference arm

Using the given values results in the total error:

$$e_{Temp} = 7.5 \cdot 10^2 \text{ (nm)} \quad \text{after a time } dt$$

This is a high error. Clearly this doesn't meet the requirement of 10 (nm). The influence of temperature has a very high impact on the error of position of the moving mirror.

Discussion

Different scenarios could be chosen to determine the influence of temperature on the fiber optic interferometer, but the following situation is chosen because it gives a good indication on the magnitude of the impact of a temperature change of either the reference arm or the measurement arm.

Reducing the temperature disturbances and shortening both the reference arm and the measurement arm will lead to higher accuracy of the fiber optic interferometer.

The waveguide material of a fiber optic cable is usually built up out of Silicium (Glass). Unfortunately, there are many different types of glass. For this calculation it was assumed that the change of refractive index over temperature has a negative value. But the exact type of material of the waveguide material is unknown and therefore it is not certain if this assumption is correct.

If this negative value of the change of refractive index over temperature compensates exactly for the thermal coefficient of expansion then the waveguide material is called "athermal". However the change of refractive index over temperature doesn't always have a negative value for all types of glass [42]. This means that the effect of the change of refractive index over temperature could also accumulate with the effect of thermal elongation or contraction and by this lead to a greater change of measured position over time.

4.9.5 Alignment

Introduction

Due to angular misalignment between the grin lens and the moving mirror, the light that's reflected from the moving mirror and couples back into the fiber optic interferometer is dependent on the position of the moving mirror relative to the position of the grin lens, and the magnitude of the angular misalignment. This angular misalignment could create an error in the measured position of the moving mirror.

Assumptions and modeling

The applied model and made assumptions are described in appendix D.4. The angular misalignment between the grin lens and the moving mirror is shown in Figure D-23 and is shown again below.

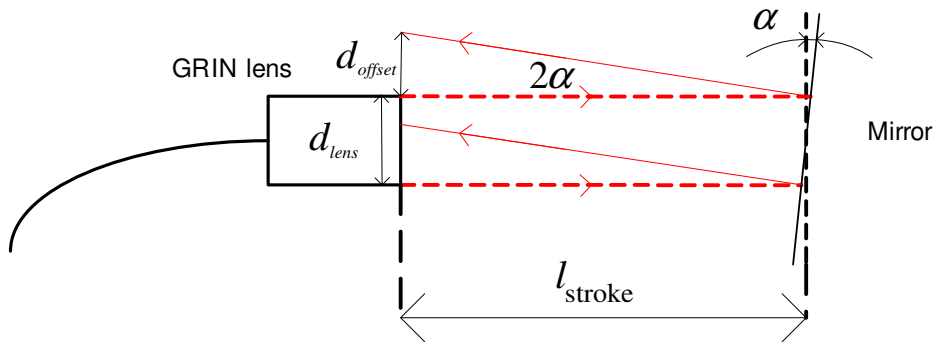


Figure 4-9 Geometric model of the angular misalignment between the mirror and the grIN lens

Result

The maximal error due to the angular misalignment between the grIN lens and the moving mirror can be seen below in Figure 4-9. Depending on the exact distance between the grIN lens and the moving mirror and the initial phase of the optic wave when exiting the splitter to the grIN lens, the maximal error can be determined when the moving mirror is exactly 0.05 (m) away from the grIN lens.

For the simulation of the error the same signal inputs are used that are determined in appendix C.3.

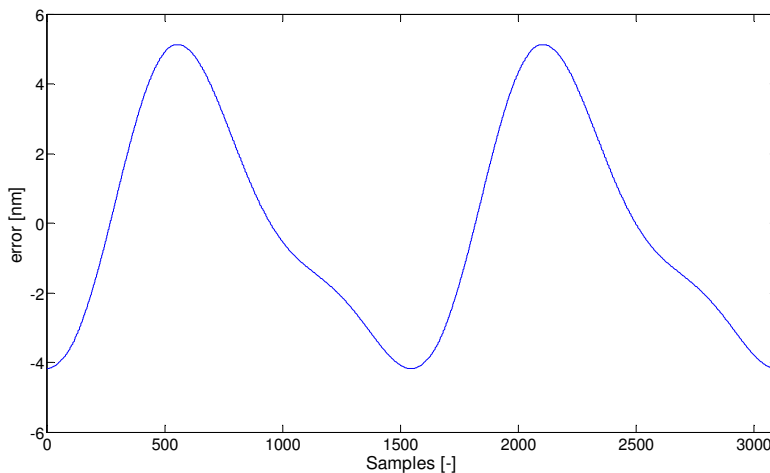


Figure 4-10 Simulated error of the measurement system for two fringe signals, due to angular misalignment between the lens and the moving mirror

The resulting error is a systematic error. The maximal error due to misalignment at the maximal distance away from the grIN lens is:

$$e_{\text{alignment}} = 5.1(\text{nm})$$

4.9.6 Photodiode

Introduction

The behavior of the photodiode could have an impact on the measured position of the moving mirror. Non-ideal behavior of the photodiode's responsivity could result in an error of the position of the moving mirror.

Assumptions

- The responsivity of the three photodiodes is the same

Modeling

The responsivity of the photodiode should be as high as possible. The higher the responsivity, the less signal is required for the same signal to noise ratio. The laser heat load and the amount of stray light within the cryogenic cooled zone of the FTS will also be lower for a smaller signal. Therefore the responsivity should be as high as possible.

When the photocurrent is measured over a single resistor, non-linear behavior of the photodiode could occur. When the photocurrent created within the photodiode is higher than the current corresponding to the breakdown voltage in the IV characteristic shown in Figure 4-11.

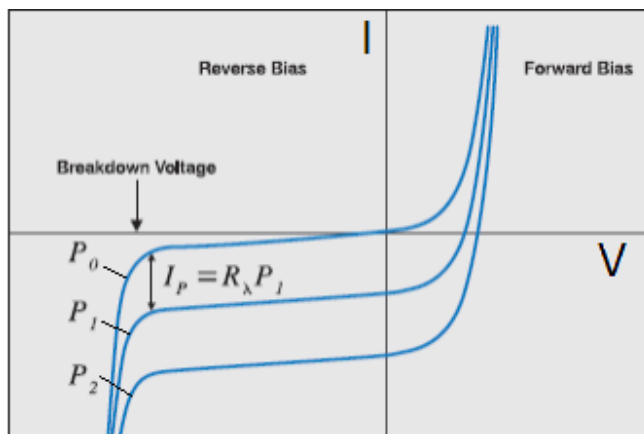


Figure 4-11 Typical IV characteristic of a photodiode [36]

There are two modes of operation of the photodiode, forward biased and reversed biased. For the measurement setup of the fiber optic interferometer the reverse biased mode or photoconductive mode of operation is used. In Figure 4-11 the reversed bias mode corresponds with the left quadrants in the IV diagram.

When there is no light incident on the photodiode, then the curve of P_0 applies. If some optical power P_1 incites on the photodiode, then the curve of the IV characteristic shifts downwards. If the optical power is increased again, then the curve shifts downwards again. An important aspect of the IV characteristic is the breakdown voltage of the photodiode. In reverse biased mode a positive voltage is applied on the cathode of the diode. The magnitude of the voltage determines the horizontal position on the IV curve of the photodiode. In Figure 4-11 the horizontal point of the breakdown voltage is indicated on the IV curve. If the reverse bias voltage is higher than the breakdown

voltage, in Figure 4-11 this is on the left side of the breakdown voltage, then the photodiode is used in its non-linear region. This means that the output current is not proportional to the incident optical power, but non-linearly dependent on the incident optical power.

In the reverse biased mode, linear operation is maintained as long as the photodiode is not saturated and the bias voltage is higher than the product of the load resistance and the photocurrent. Saturation is a condition in which there is no further increase in detector response as the input light is increased. The load resistance is the resistor over which the voltage is measured as the photocurrent passes through it.

Result

The maximum photocurrent created in the linear range @ 253 (K) is:

$$I_{nl} = \frac{U_{bias}}{R_{meas}} \quad (4.38)$$

For a 5 (V) reverse bias voltage and a 12K4 load resistance, the maximal photocurrent when the responsivity of the photodiode becomes non-linear is according to [39]:

$$I_{nl} = 0.4(mA)$$

The maximal photocurrent created in the photodiodes is calculated in appendix B.2.

$$I_{2max} = 0.09(mA)$$

The maximal photocurrents are smaller than the maximal photocurrent when the responsivity of the photodiode becomes non-linear. From this there can be concluded that the responsivity of the photodiodes will be linear and there won't be an effect on the accuracy or the precision of the measurement system.

Discussion

The minimal photocurrent created by the incident laser power on the photodiode should be higher than the dark current. Otherwise the signal can't be distinguished from the photocurrent.

The maximal incident laser power on the photodiode is not limited by the physical properties of the photodiode. The only problem is that the electronics behind the photodiode might not be able to handle too much current or that the characteristic behavior of the photocurrent as a function of the incident laser power becomes nonlinear [28].

An easier method to prevent nonlinear behavior of the responsivity of the photodiode is by using a reverse biased photodiode in combination with a transimpedance amplifier. In this configuration (which is used for the photodiode readout electronics built by SRON and is shown in appendix A.1) the reverse bias voltage over the photodiode doesn't change with a changing photocurrent, due to the virtual ground of the OPAMP.

4.9.7 ADC quantization error

The smallest detectable analogue voltage is defined by the Least Significant Bit (LSB) of the ADC. The maximal error due to the quantization of the ADC is equal to half the LSB and this is equal to half the resolution.

$$e_{adc} = \frac{1}{2} \cdot \text{res} = \frac{\lambda_{laser}}{2^{n_b+2}} \quad (4.39)$$

Where:

$n_b(-)$ = Number of bits in the ADC

$e_{adc}(nm)$ = Quantization error in the ADC

For the 12 bit ADC and the wavelength of the laser of 1550(nm) the quantization error is equal to:

$$e_{adc} = 0.095(nm)$$

4.9.8 Mechanical vibrations

The effect of mechanical vibrations on the measured position of the moving mirror should be as low as possible. The vibrations have the biggest impact on the accuracy and the precision of the measurements when the vibrations are transmitted into the reference arm and the measurement arm.

The experimental setup of the fiber optic interferometer should be built on an optic table to reduce the transmission of floor vibrations to the setup.

For the SAFARI application the situation is more complicated. A possible source of vibrations are the mechanical coolers that operate on 15 (Hz) and 45(Hz). These values have been given in section 3.3.

For the application of the fiber optic interferometer on SPICA it is unknown where exactly the sources of vibrations are, what the exact amplitudes of the vibrations are, what the compliance(s) and the mass(es) of the suspensions are and what the damping of the structures is. Because these specifications are necessary to make a vibration analysis, the analysis is not performed.

It is advised to mount the fiber optic interferometer with the highest possible stiffness. Possible vibration reduction methods are applying low stiffness suspensions between the fiber optic interferometer and the vibration source, building the setup of the fiber optic interferometer on a large mass or use a skyhook damper. Hypothetically speaking the use of a large mass would make the satellite too heavy and thereby too expensive. A suspension with a low stiffness and a low damping between the vibration source and the fiber optic interferometer might not be possible anywhere on the satellite, so a skyhook damper perhaps should be considered.

4.9.9 Error budgeting

The measurement system could have two types of errors. The first type of error is a systematic error. This type of error refers to the accuracy of the measurement system. The second type of error is a random error. This type of error refers to the precision of the measurement system.

Because the calculated precision errors are dependent on different parameters, the values are uncorrelated. Therefore the total precision error is the result of a linear uncorrelated combination of parameters. Then the total precision error of the measurement system can be written in the next equation [5].

$$e_{r,tot} = \sqrt{e_1^2 + e_2^2 + \dots + e_n^2} \quad (4.40)$$

Where:

$e_{r,tot} (nm_{rms})$ = Standard deviation of the total random error

If the parameters are correlated then the total error can be calculated with the next equation.

$$e_{r,tot} = e_1 + e_2 + \dots + e_n \quad (4.41)$$

Applying equation (4.40) to all the random errors in section 4.9 gives:

$$e_{r,tot} = 0.095 (nm_{rms})$$

In Table 4-5 an overview is given of the precision errors that have been determined in the content of this report.

Table 4-5 Overview of errors determined in this report that influence the precision

Precision	Error
Intensity noise	0.0016 (nm _{rms})
Laser line width	0.0019 (nm _{rms})
ADC quantization error	0.095 (nm _{rms})
Total precision	0.095 (nm _{rms})

The accuracy of the OPD metrology is defined by the systematic errors in the measurement system. The errors that have been determined in this report are assumed to be uncorrelated. Therefore the total accuracy can be calculated with equation (4.40).

An overview of these errors is shown in the table below.



Table 4-6 Overview of errors determined in this report that influence the accuracy

Accuracy	Error
Optical disturbance signals	4.9 (nm)
Laser stability	1.0 (nm) over 3600(s)
Temperature (for $\Delta T = 1$ (K))	750 (nm)
Alignment	5.1 (nm)
Photodiode	0 (nm)
Total accuracy	750 (nm)

From the results displayed in Table 4-5 and Table 4-6 it can be concluded that the precision of the measurement system is negligible compared to the accuracy of the measurement system, because there are 5 orders of magnitude difference in the errors.

4.10 Specifications overview

An overview of the initial system specifications of the OPD metrology is given below in Table 4-7.

Table 4-7 Specifications overview of the initial system configuration

Type of specification	Value	Meets requirements?
Accuracy	750 (nm)	No
Resolution	0.19 (nm)	Yes
Stroke	34.5 (mm)	Yes
Sample frequency	781 (Hz)	Yes
Heat load	1.3 (μ W)	Yes
Stray light power	42.3 (μ W)	No
Space qualified	No	No
Maximal required electrical power	6.67 (W)	No
Functionality at cryogenic temperature	No	No
Relative displacement measurement	Yes	Yes
Laser + electronics placed in room of 293 (K)	Yes	Yes
Sensor head placed near the ODL	Yes	Yes

Finally from these result the first main research question can be answered. This question states: "Is the current setup of UNASYS operational for the SAFARI instrument?" The answer to this question is: "**No.**"

5 Drift

From the previous chapter it is concluded that the current setup of LUNASYS is not yet operational for the SAFARI instrument. It is desired to know what should now be improved on the current setup of LUNASYS to make the system operational for the SAFARI application. The accuracy of the fiber optic interferometer that is specified in section 4.9 is far away from the required accuracy and this seemed to be the bottleneck of the design of LUNASYS for the SAFARI application. The main cause of this low accuracy is drift of the measured signal. Drift is a small continuous change in the measurement value of a measurement instrument over time, while the value that should be measured remains constant.

In this chapter research sub-question c) will be answered. It will be determined if temperature the dominant factor is causing the position drift of LUNASYS.

The cause of the drift is analyzed according to Figure 5-1.

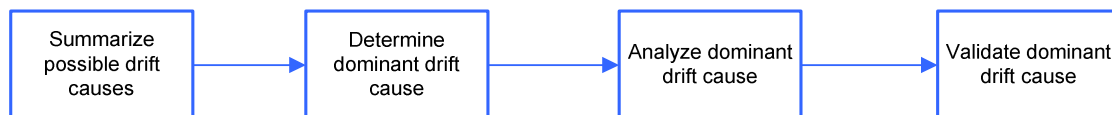


Figure 5-1 Block schedule representing the analysis of the cause of the drift

First the possible causes of the drift are summarized and each cause is analyzed. It seemed that temperature is a dominant factor causing the position drift. Hereafter, a model is made to determine where the impact of a temperature disturbance on the fiber optic interferometer will be the greatest. It seemed that the biggest impact of a temperature disturbance is on the reference arm and the measurement arm of the fiber optic interferometer. For this reason drift measurements are performed while the temperature in the measurement arm and the reference arm is measured, in order to see if the position drift and the temperature are related to each other.

5.1 Causes of drift

Introduction

There are many parameters that can cause drift in the measurement system. In this section different causes are summarized and the parameters that most likely cause the drift will be determined.

Assumptions

- Causes of drift other than the ones mentioned in this section have a negligible influence on the drift

Modeling

Consider the system model of the fiber optic interferometer that is described in paragraph 2.1 and is shown again below.

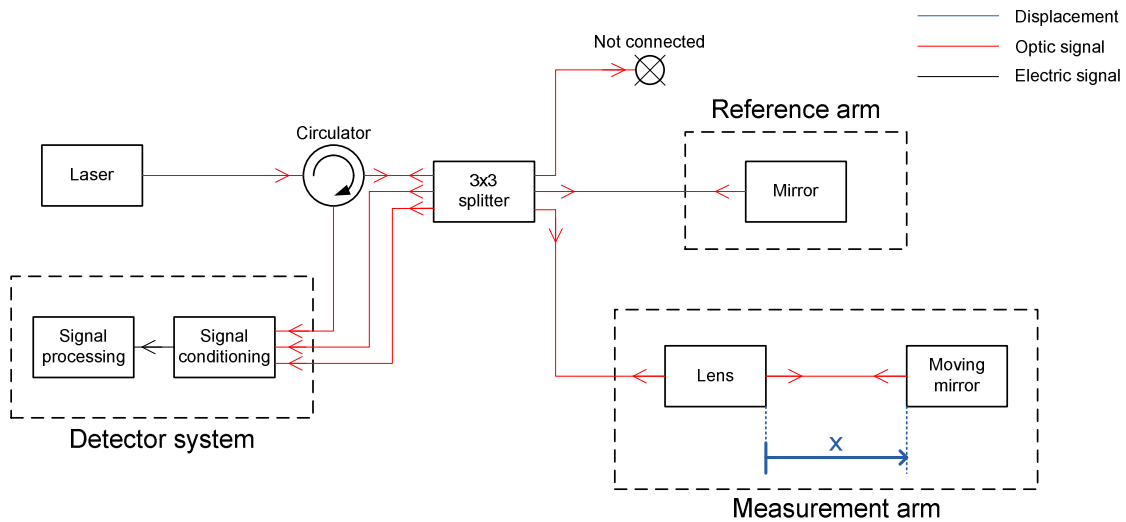


Figure 5-2 System model of the fiber optic interferometer

There are many things that could cause the drift of the measured signal. The most likely causes are given below.

The following parameters can cause drift in the system:

- Laser wavelength stability
- Mechanical vibrations
- Refractive index changes of the air
- Phase and gain changes of the 3x3 splitter over time
- Temperature disturbances on the measurement arm and reference arm

Result

The influence of the frequency stability of the laser on the drift is estimated in chapter 4. The impact on the accuracy was very low for the made calculation. It was assumed that the casing temperature of the laser should remain constant and may have a maximal fluctuation of 0.1 (K). In order to keep the casing temperature of the laser constant thermal insulation has been applied around the laser. Because the calculated drift didn't seem very high, the frequency stability of the laser hasn't been analyzed any further.

Another possible cause of the drift could be mechanical vibrations. Vibration measurements have been performed by TNO [29]. By attaching a voice coil on the fibers the error has been determined. The voice coil has been attached to all the fibers, except to the fibers in the measurement and the reference arm. Then a vibration of 2 and 10 (Hz) with amplitude of 3 (mm) was induced by the voice coil. The largest error caused by these vibrations on the displacement signal was 13 (nm). The fiber optic

interferometer is most sensitive for disturbances in the measurement arm and the reference arm. For this reason the entire setup of the fiber optic interferometer has been built up on a vibration isolation table at Technobis. During the measurements on a vibration isolation table the drift was still present in the signal to a large extent.

The measurement system has to be placed in vacuum, however all the measurements are performed in an environment without vacuum. Changes of the refractive index of air may create an OPD measured by the fiber optic interferometer and therefore influence the accuracy of the measurement system. A fluctuation of the refractive index of air over time could be a cause of the drift. In order to calculate this, Edlen's formula can be applied [37]. An online calculator has been used to calculate the effect of temperature, pressure and humidity on the refractive index of the fiber optic interferometer [38]. For an atmospheric pressure, that is 1013 (mbar) and a humidity of 50% the refractive index has been calculated for three different temperatures [38].

$$n_1 = 1.000268155 @ 20(^{\circ}\text{C})$$

$$n_2 = 1.000267213 @ 21(^{\circ}\text{C})$$

$$n_3 = 1.000266276 @ 22(^{\circ}\text{C})$$

This result has been filled into equation (C.7) in order to calculate the effect of the change of refractive index on the accuracy of the fiber optic interferometer.

By combining equation (D.25), (D.27), (D.28) and rewriting the equation, the next formula can be used to calculate the effect of the change of refractive index on the accuracy of the fiber optic interferometer.

$$e_n = OPD \left(\frac{1}{n_2} - \frac{1}{n_1} \right) \quad (5.1)$$

Where:

$$e_n (m) = \text{Error due to a change of refractive index}$$

It is assumed that only the air increases in temperature and the temperature of the other optical components remains constant. For an OPD of 0.1 (m) the error for a change of temperature from 20 degrees Celsius to 21 Celsius is calculated by using (5.1).

$$e_{n_2,air} = 94 (nm)$$

And for an OPD of 0.1 (m) and a change of temperature from 20 degrees Celsius to 22 Celsius, the error becomes:

$$e_{n_3,air} = 188 (nm)$$

The effect of the change of the refractive index could be an important influence on the drift.

Other parameters that can cause drift in the measurement system are phase and gain changes of the 3x3 splitter, but also longitudinal stretching of the fibers in the splitter due to temperature changes. These fibers within the splitter are part of the measurement and reference arm of the fiber optic interferometer.

There is little known about these effects. But it will be assumed that longitudinal stretching and contracting of the splitter due to temperature disturbances on the 3x3 splitter is small compared to temperature disturbances in the measurement and reference arm. Because the length of the splitter is 4.5 (cm) and is relatively small compared to the length of the measurement and reference arm. These lengths are respectively 22 (cm) and 46 (cm). Simply by discussion it is difficult to make a good estimate of the effect of the temperature on the phase and gain changes of the splitter, but for the moment it will also be assumed that these effects are negligible.

Temperature disturbances on the measurement and reference arm are considered. In chapter 4 the effect of these disturbances is estimated. Measured errors could become as high as 750 (nm). It was also seen that the change of the refractive index of the waveguide material over temperature could compensate or accumulate on the effect of the thermal strains caused by a change of temperature.

During the first integration test of the software and electronics of SRON with the optical hardware of Technobis, measurements already showed that the measurement system is highly sensitive to temperature disturbances on the reference and the measurement arm. During the integration test, a measurement was performed over a small time period. The result of the measurement is shown in Figure 5-3. In the first time interval of 0-9 (s) the sensors is left at rest. After this period a hand that functions as a heat source, is held close to the reference and measurement fiber. Now a lot of fringes were measured. Then after a few seconds the hand was pulled away from the measurement and reference arm and the amount of fringes decreases.

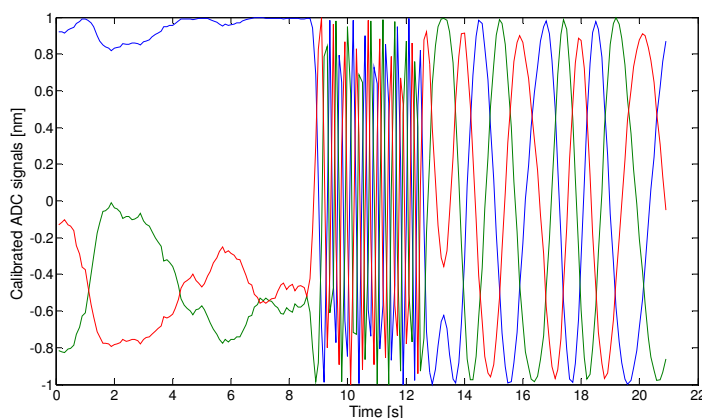


Figure 5-3 Fringe patterns measured during the integration test at SRON [9].

The measured displacement that corresponds to the three fringe patterns shown in Figure 5-3 is given in the figure below.

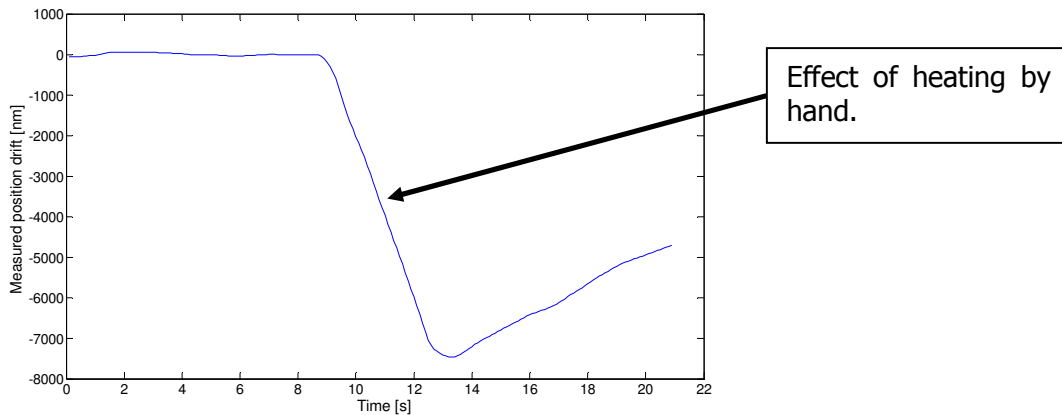


Figure 5-4 Measured displacement corresponding to the fringe patterns that has been measured during the integration test at SRON [9]

As can be seen on the fringe signal of Figure 5-3, the measurement and reference arm are highly sensitive to temperature disturbances.

It can be concluded that temperature disturbances on the measurement system are probably the main causes of the drift in the measurement system.

5.2 Experiments

Introduction

The results from the previous section indicate that temperature disturbances on the measurement system are probably the main cause of the drift of the measurement system. In this section different experiments will be performed in order to locate where the impact of temperature disturbances in the fiber optic interferometer is at its greatest. Finally research sub-question c) will be answered.

Assumptions

- The temperature distribution over a fiber segment is homogeneous
- Errors in the data from the temperature sensors are neglected
- The materials are homogeneous and isotropic
- Thermal coefficient of expansion is constant over temperature
- The fiber consists of two materials; the coating and a single waveguide material
- Young's modulus is constant over temperature
- No internal stresses are present within the fiber optic cable
- For the calculations of the thermal expansion the reference and the measurement arm only consist of fiber optic cables
- The effect of temperature disturbances on the 3x3 splitter has a negligible effect on the measured position drift

Modeling

Consider the system model of the fiber optic interferometer given in Figure 5-2. This model has been used to model possible external temperature disturbances on different locations of the fiber optic interferometer. A temperature disturbance is a temperature change over time with respect to the initial temperature. The model with these disturbances is given in Figure 5-5.

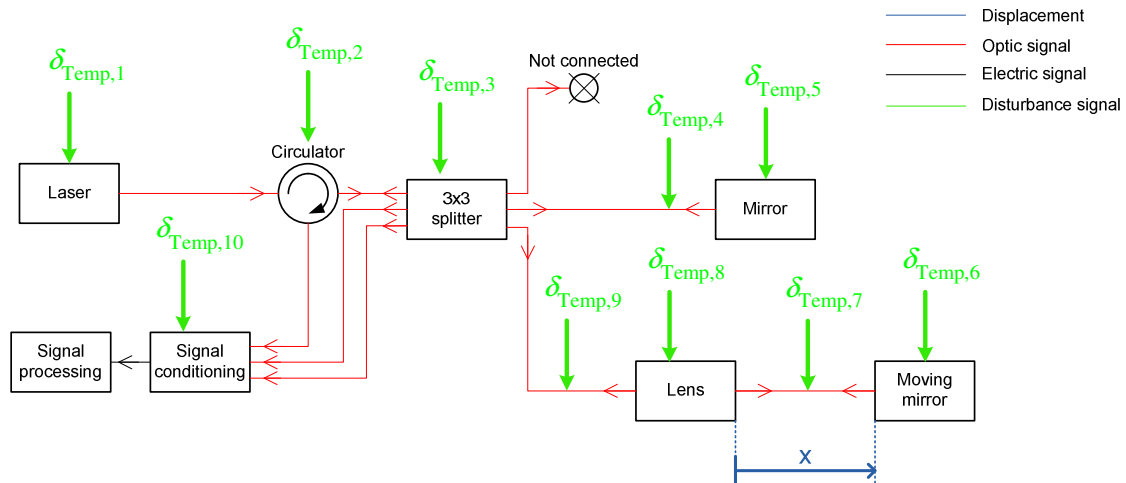


Figure 5-5 System model of the fiber optic interferometer with temperature disturbances acting on different components of the measurement system

Consider the situation where the fiber optic interferometer is in thermal equilibrium with its surroundings. Now the effect of the temperature disturbance acting on the fiber optic interferometer will be analyzed one by one.

The first temperature disturbance $\delta_{Temp,1}$ acts on the laser. It is known that the laser casing temperature should be maintained constant in order to maintain frequency stability of the laser. The effect of a temperature disturbance on the laser is examined by looking at the measured position signal while the laser is heated with a shrink heater. Before the heating occurred the signal was already drifting. During the heating, no significant changes occurred in the position signal with respect to the position signal before the heating. From this there can be concluded that a temperature disturbance on the laser is not the dominant factor causing the drift.

This same process has been repeated for disturbances $\delta_{Temp,2}$ and $\delta_{Temp,10}$. But again there was no visible effect of the temperature disturbance on the drift of the signal. Therefore it can be concluded that temperature disturbances on the detector electronics and on the circulator are not the dominant factor causing the drift either.

The temperature disturbance $\delta_{Temp,7}$ might have a considerable contribution on the measured drift. In section 5.1 an error of 94 (nm) could occur when the temperature of the air increased 1 degree Celsius. However for the SAFARI application the measurements will be performed in vacuum and in vacuum the refractive index remains constant with a change of temperature. Beside this, the order of magnitude of the impact on the drift for this temperature disturbance is smaller than the temperature disturbances acting on the measurement and the reference arm $\delta_{Temp,4}$, $\delta_{Temp,5}$, $\delta_{Temp,8}$ and $\delta_{Temp,9}$. To verify this, drift measurements were performed where the effect of the

temperature disturbance $\delta_{Temp,7}$ can be excluded. These drift measurements were performed with a grin lens without an AR coating and the moving mirror was removed from the experimental setup. This means that a Fresnel reflection on the outer surface of the lens that is in contact with the air reflects back into the fiber optic interferometer. A Fresnel reflection is a reflection that occurs when light passes through two waveguides of different refractive indices. A part of the light gets transmitted through the interfacing surface of these two refractive indices and a part of the light gets reflected on this interfacing surface. In these experiments this reflection is used to interfere with the signal reflected from the reference arm. As a consequence of this experimental setup, the effect of temperature disturbances on the moving mirror $\delta_{Temp,6}$ are excluded as well besides $\delta_{Temp,7}$. For now it is assumed that $\delta_{Temp,3}$, the effect of temperature disturbances on the 3x3 splitter have a negligible effect on the measured position drift of the fiber optic interferometer.

The thermal expansion and contraction of the fiber optic interferometer can be calculated by measuring the temperature on the reference and the measurement arm and using the known lengths and material types of the measurement and reference arm. By comparing the result of this calculation with the measured drift by the detector it can be determined if the effect of the disturbances $\delta_{Temp,4}$, $\delta_{Temp,5}$, $\delta_{Temp,8}$ and $\delta_{Temp,9}$ are the dominant factor causing the position drift of the fiber optic interferometer.

Consider Figure 5-6. The reference and the measurement arm are subdivided into different segments by the purple lines. In each segment a temperature sensor is placed. The 3x3 splitter is considered as a different segment.

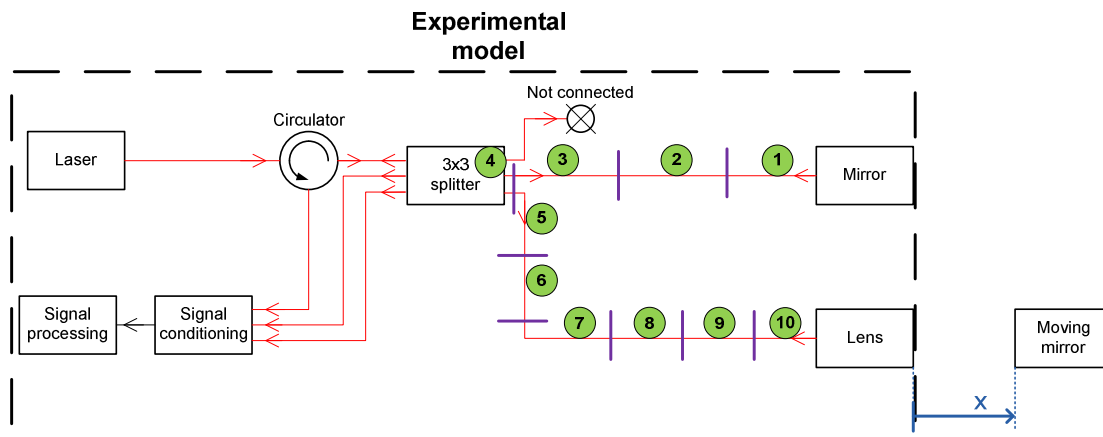


Figure 5-6 Experimental model of the fiber optic interferometer for the drift measurements, where the green dots indicate the position of the temperature sensors and the purple lines the boundaries of the different fiber segments

Pictures of the real implementation of the experimental setup are shown in the figures below.

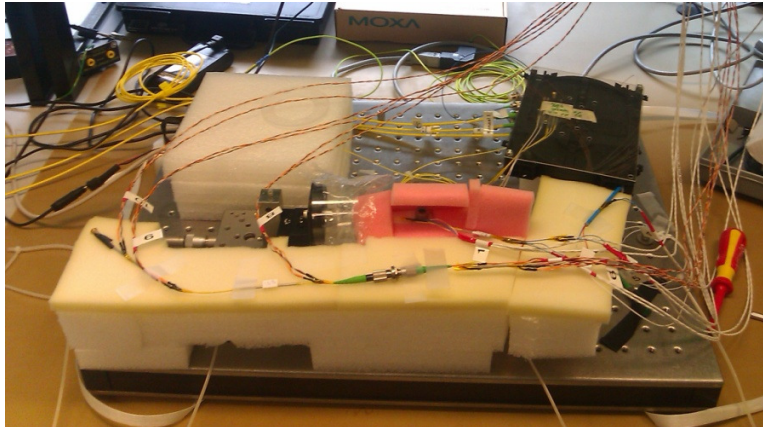


Figure 5-7 Picture of the experimental setup with the temperature sensors where the measurement and reference arm are not covered by thermal insulation, built up by Finn van Rij

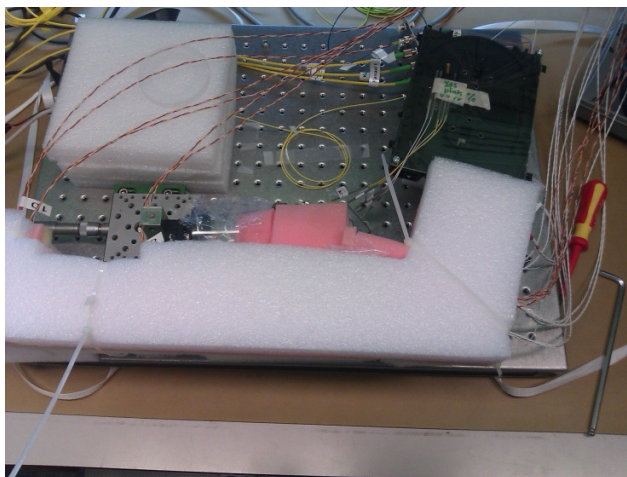


Figure 5-8 Picture of the experimental setup with the temperature sensors where the measurement and reference arm are covered by thermal insulation, built up by Finn van Rij

The reference arm is segmented in three elements and the measurement arm is segmented in six elements. The temperature sensor is placed in the middle of each element. In Table 5-1 the length of each element is given.

Table 5-1 Length of the fiber segments in the reference and the measurement arm

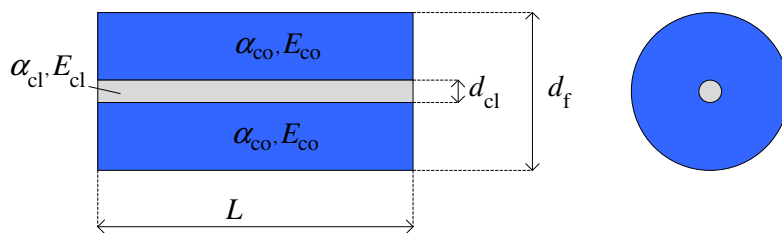
m (segment #)	1	2	3	4	5	6	7	8	9	10
Length (m)	0.09	0.06	0.07	0.045	0.07	0.06	0.13	0.06	0.08	0.06

The material properties of the materials of the fiber optic cable required to calculate the effective coefficient of thermal expansion are given in the table below.

Table 5-2 Material properties of the materials off which the fiber optic cable consists

Element	Material	E (Pa)	α (K ⁻¹)	A (m ²)	n (-)	dn/dt (K ⁻¹)
cladding	Pyrex	6,40E+10	8,50E-06	1,23E-08	1.55	-1,28E-05
coating	Acrylate	3,20E+09	7,50E-05	7,73E-07		

The given surfaces of the fiber are calculated in Appendix B.1 the other parameters are obtained from the Solidworks material library. One fiber segment will now be analyzed on its mechanical behavior due to thermal expansion. The cladding and the coating are fixed together, so the coating and the cladding cannot expand and contract freely from each other.

**Figure 5-9 Parameters of a fiber optic cable segment**

The left side of the fiber is fixed to the mechanical ground. The system is modeled by assuming that the cladding of the fiber and the coating of the fiber are able to expand and contract freely from each other. When the temperature in the fiber is raised homogeneously over the fiber, the two materials will have different elongations, δ_1 for the coating and δ_2 for the cladding, because $\alpha_{co} > \alpha_{cl}$. This is shown in Figure 5-10.

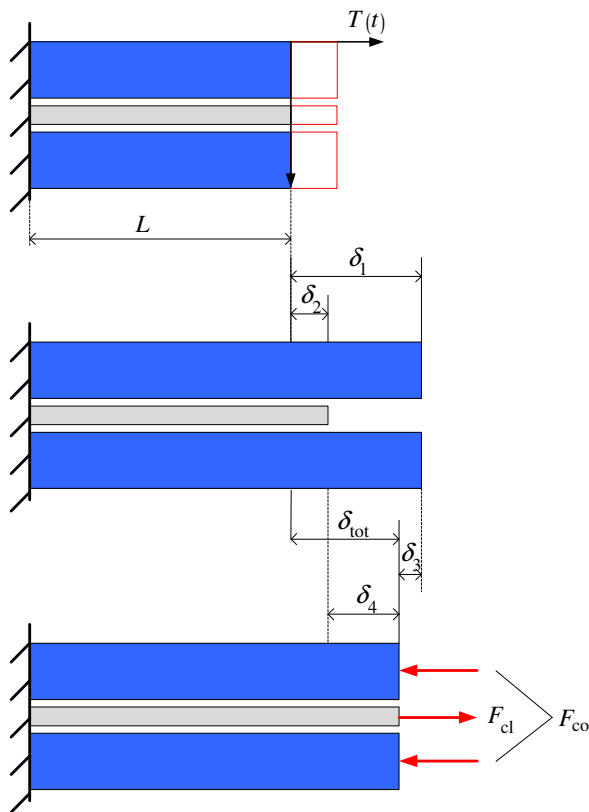


Figure 5-10 Elongation model of a fiber optic cable segment, used for the equations of compatibility

For the total elongation due to thermal expansion according to equation (4.31), there can be written:

$$\delta = l_0 \alpha \Delta T \quad (5.2)$$

Where:

$\delta(m)$ = Total elongation of the fiber optic cable segment

Because in reality the unfixed end is fixed to another segment of the fiber and the coating and the cladding are actually glued to each other, the expansion of the two materials must be the same. Now the axial forces in the coating and the sleeve must have magnitudes such that they shorten the coating and stretch the cladding until the final lengths of the coating and the cladding are the same. The force acting on the cladding and on the coating respectively is written in the next formula.

$$\delta = \frac{FL}{EA} \quad (5.3)$$

Where:

$F(N)$ = Force

$L(m)$ = Length

$E(N/m^2)$ = Young's modulus

$A(m^2)$ = Surface

Now the equation of compatibility can be written for the fact that the elongation of the coating and cladding shown in Figure 5-10 must be the same in the next formula [2].

$$\delta_{\text{tot}} = \delta_1 - \delta_3 = \delta_2 + \delta_4 \quad (5.4)$$

In Figure 5-10 only two forces are shown, one force acts on the cladding of the fiber F_{cl} and one force on the coating F_{co} . Note that the coating force is indicated as two arrows, but the resultant force on the coating is just F_{co} . The fiber doesn't move, therefore the resultant force acting on the fiber is equal to zero. Then from force equilibrium in the longitudinal direction of the fiber in Figure 5-10 there can be written:

$$F_{co} = F_{cl} \quad (5.5)$$

Where:

$F_{co}(N)$ = Resultant force acting on the fiber coating

$F_{cl}(N)$ = Resultant force acting on the fiber cladding

The total elongation of the fiber can be found by substituting F_{co} or F_{cl} and solving the equation of compatibility for the total elongation, by combining equations (5.2), (5.3) and (5.4).

$$\delta = \frac{(\alpha_1 E_1 A_1 + \alpha_2 E_2 A_2)(\Delta T)L}{E_1 A_1 + E_2 A_2} \quad (5.6)$$

An effective coefficient of thermal expansion for the entire fiber optic cable can now be determined.

$$\alpha_{\text{eff}} = \frac{(\alpha_1 E_1 A_1 + \alpha_2 E_2 A_2)}{E_1 A_1 + E_2 A_2} \quad (5.7)$$

Where:

$\alpha_{\text{eff}}(K^{-1})$ = Effective coefficient of thermal expansion

Using the material properties given in Table 5-2 and noting that in equation (5.7) subscript 1 corresponds to the coating of the fiber and subscript 2 corresponds to the fiber cladding, the effective coefficient of thermal expansion can be calculated.

$$\alpha_{eff} = 5.9 \cdot 10^{-5} (K^{-1})$$

The OPD for the system model given in Figure 5-5 can be determined according to equation (5.8).

$$OPD(t) = 2 \left[n_f L_{ref}(t) + n_a(t) x(t) - n_f L_{meas}(t) \right] \quad (5.8)$$

Where:

$n_f(-)$ = Refractive index of the fiber core

$n_a(-)$ = Refractive index of the air

$L_{ref}(m)$ = Length of the reference arm

$L_{meas}(m)$ = Length of the measurement arm until the lens

If the length of the reference and the measurement arm are constant, then a constant offset of the phase of the fringe signal would be measured. In this case the phase of the fringe signal is a measure for the displacement of the moving mirror and if the refractive index of the air would be constant over time and equal to one, then equation (4.14) applies:

$$x = \frac{\lambda \varphi}{4\pi n} \quad (5.9)$$

However, with the new experimental setup the refractive index of air and the displacement of the moving mirror don't affect the OPD anymore. In this case equation (5.8) changes to:

$$OPD(t) = 2n_f (L_{ref}(t) - L_{meas}(t)) \quad (5.10)$$

Now consider the model for the calculation of the position drift in Figure 5-11.

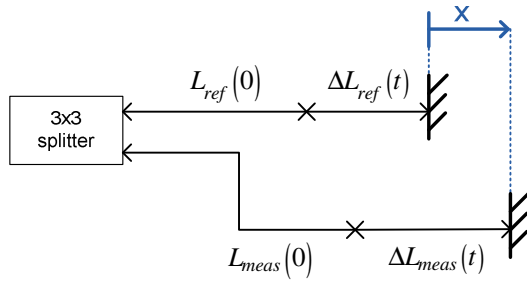


Figure 5-11 Model for the calculation of the position drift due to changes of length of the reference and the measurement arm

The drift can be calculated from the optical path difference of the light traveling in the measurement arm and the light traveling in the reference arm. The measured displacement by the measurement system would be x , and this value is equal to half the OPD described in equation (5.10). The measured position signal as a consequence of the temperature drift for the model given in Figure 5-11 is described in the formula below.

$$x_{drift}(t) = n_f (L_{meas}(t) - L_{ref}(t)) \quad (5.11)$$

In the algorithm equation (5.9) is used to calculate the displacement of the moving mirror. In this equation the value for the refractive index n is equal to one. This means that the drift signal that is calculated with the equation below should use the same value for the refractive index in order to correspond to the measured position drift.

$$x_{drift}(t) = L_{meas}(t) - L_{ref}(t) \quad (5.12)$$

Equation (5.12) will be used to calculate the drift due to the temperature disturbances. By rewriting equation (5.12) according to the parameters shown in Figure 5-11 the next formula is obtained as a function of the initial length at time $t=0$.

$$x_{drift}(t) = (L_{meas}(0) + \Delta L_{meas}(t)) - (L_{ref}(0) + \Delta L_{ref}(t)) \quad (5.13)$$

Now the drift can be calculated by writing equation (5.13) for all the segments m . For the measurement arm the next formula applies:

$$L_{meas}(t) = \sum_{m=1}^3 L_{0m} (1 + \alpha_{eff} (T_m(t) - T_m(0))) \quad (5.14)$$

Where:

$m(-)$ = Segment number

$L_{0m}(m)$ = Initial length of segment m

$T_m(K)$ = Temperature of segment m

And for the reference arm:

$$L_{ref}(t) = \sum_{m=5}^{10} L_{0m} (1 + \alpha_{eff} (T_m(t) - T_m(0))) \quad (5.15)$$

Now combining equations (5.12), (5.14) and (5.16) gives the final formula that is used for calculation of the drift due to the measured temperatures on the different segments of the reference arm and the measurement arm according to Figure 5-6.

$$x_{drift}(t) = \sum_{m=1}^3 L_{0m} (1 + \alpha_{eff} (T_m(t) - T_m(0))) - \sum_{m=5}^{10} L_{0m} (1 + \alpha_{eff} (T_m(t) - T_m(0))) \quad (5.16)$$

For the calculation of the thermal expansion of the reference and the measurement arm it is assumed that the reference and the measurement arm only consist of fiber optic cables.

The drift measurements from the OPD metrology are compared to the drift signal calculated with the measured temperatures and equation (5.16).

Results

It is expected that temperature disturbances have a low timeconstant in the order of several seconds or even minutes. The influence on the drift will therefore become more visible over a longer time period. Three drift measurements have been done. Two measurements have been performed that lasted for an hour and one measurement over a whole night. The night measurement is the most reliable, because at night the thermostat and the air circulation are minimal and therefore the environment is most stable. This will result in a more stable measurement.

In the next figure the temperature of segment 2, a segment in the measurement arm and the temperature of segment 6, a segment in the reference arm is plotted over time.

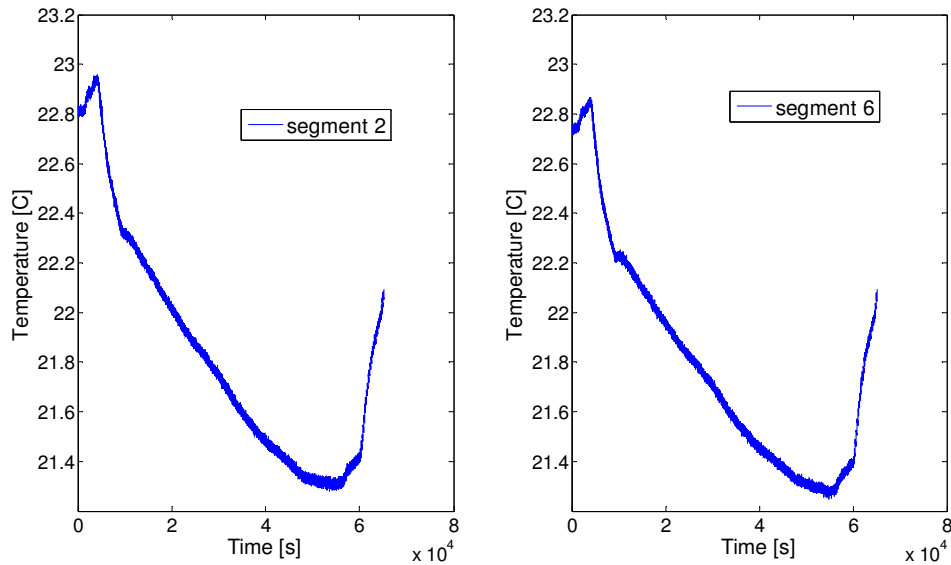


Figure 5-12 Measured temperatures of fiber segment 2 and fiber segment 6 over time. It can be seen that the temperature profiles of the two plots don't differ so much from each other

It can be seen from Figure 5-12 that both segments have similar temperature behavior. The temperatures measured over the other segments all look similar to these two plots, but differ slightly in temperature value. All the temperature plots for this measurement can be seen in appendix E.4.

In Figure 5-13 two measurements are shown. The left plot corresponds to the drift measured with the measurement system and the right plot corresponds to the calculated drift with the measured temperatures over all the segments.

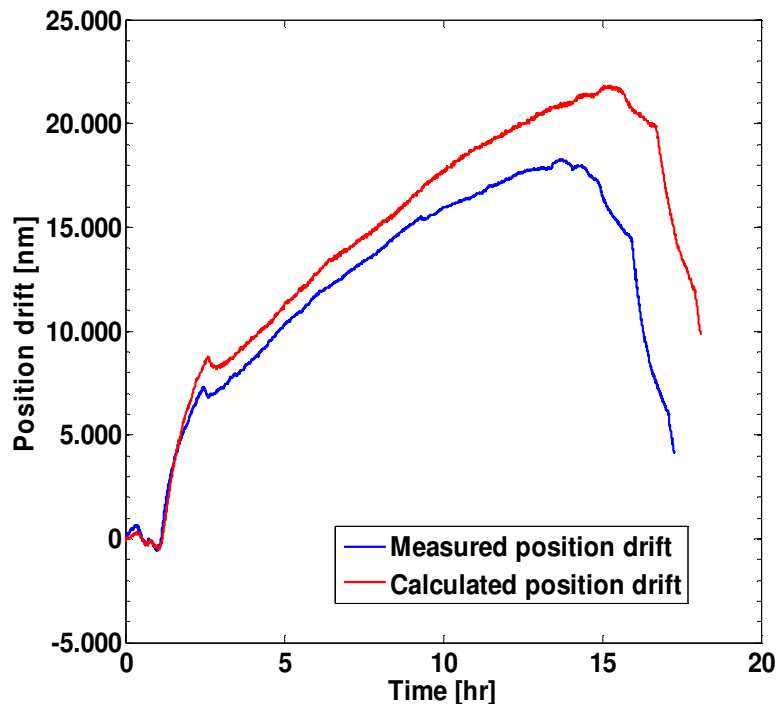


Figure 5-13 Measured position drift and calculated position drift, for drift measurement 3.

From Figure 5-13 it can be seen that the shape of the two plots are remarkably similar. This implies that the reference arm and the measurement arm are highly sensitive to temperature. Research sub question c) can now be answered. The question was: "Is temperature the dominant factor causing the position drift of LUNASYS?" From these experiments there can be concluded that the answer to this question is: "Yes". In fact the temperature disturbances on the reference arm and the measurement arm are the dominant factor causing the position drift of LUNASYS.

Validation

At Technobis there is nothing known about the effect of temperature on the phase and gain changes of the 3x3 splitter. In the model for the experiments, it has been assumed that the effect of temperature disturbances on the 3x3 splitter has a negligible effect on the measured position drift. This assumption can be validated by looking at the fringe signals measured on the ADC that are given in Appendix E. Now consider the calibrated fringe signal from drift measurement 3 given in Figure E-15. Two black horizontal lines are plotted in this fringe signal in Figure 5-14. The lines are plotted at the height of the initial maximal value of the fringe signal and the initial minimal value of the fringe signal.

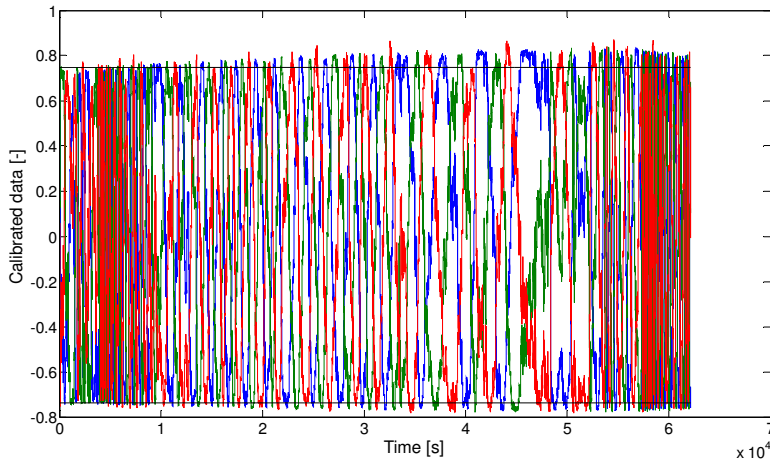


Figure 5-14 Calibrated fringe signal from drift measurement 3, showing how the initial peak to peak amplitude of the signal changes over time

From Figure 5-14 it can be seen that the amplitude of the raw data slightly changes over time. Also it can be seen in the plot below, that the temperature of the splitter decreases over time.

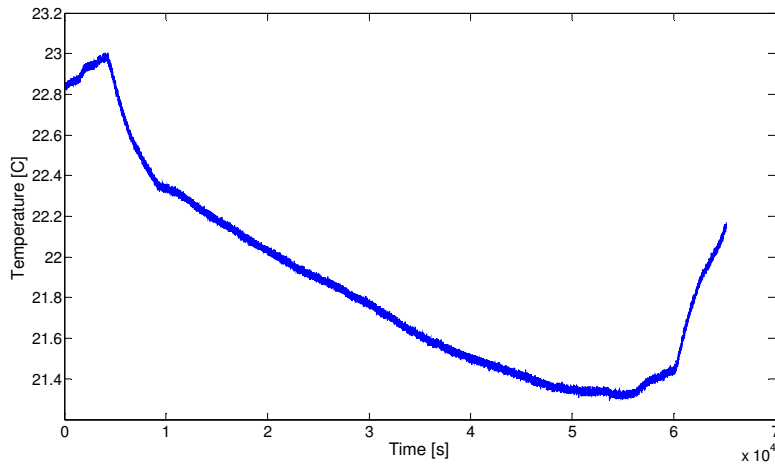


Figure 5-15 Measured temperature of the 3x3 splitter (fiber segment 4) for drift measurement 3

From these results there can be concluded that the gain of the splitter is related to the temperature. This could be explained by drawing the evanescent field of the light that passes through the core of a single mode fiber. For a normal single mode fiber a part of the light travels through the core and a part of the light travels through the cladding of the fiber. During the fabrication process of the fiber the fibers are twisted around each other and then they are heated and stretched out [26]. This means that inside the splitter a part of the evanescent field of the fiber goes beyond the cladding of the fiber that wouldn't have gone beyond the cladding of the fiber before the heating. On the

outside of the cladding of the fiber, where there is no overlap with the evanescent field of another fiber core, more light is lost.

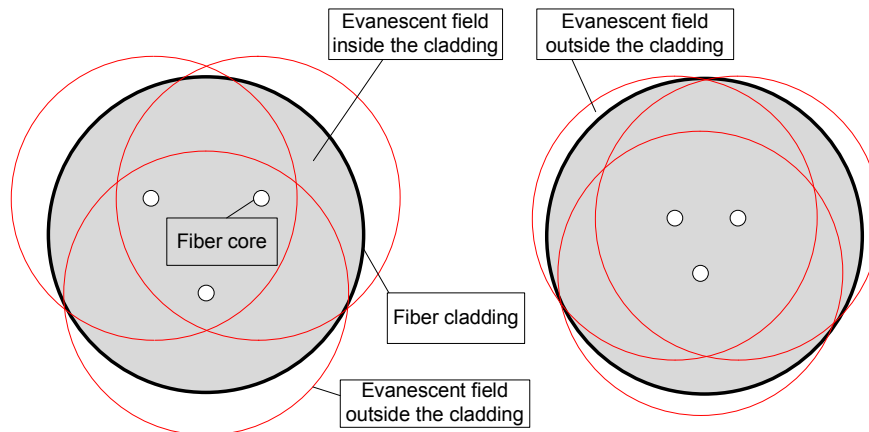


Figure 5-16 Cross section of the 3x3 splitter, with the evanescent field around the fiber cores

When the temperature of the splitter decreases, the fiber cores get closer to each other and the overlap of the evanescent field gets higher. Consequently less light is lost and the measured peak to peak amplitude of the three fringe signals becomes higher. However the amplitude of the fringe signal only changes slightly over time and the effect of an amplitude changes is not very high on the accuracy of a measurement, as can be seen from section D.4. In this section misalignment also creates a change of detected light over time. However, the longitudinal thermal expansion of the three fibers within the splitter is unknown and remains an uncertain factor.

It has also been assumed that the thermal coefficient of expansion and the modulus of elasticity are constant over the temperature. Because the temperature changes are of small orders, namely maximal two degrees Celsius, it is valid to assume that these properties remain constant.

Discussion

The gain used to calculate the drift is not completely correct. This can be seen clearly in Figure 5-13 where the drift measurement is plotted over a long time period. It will now be discussed what the main reasons for this difference could be.

For the experiments it is assumed that the errors in the data from the temperature sensors are neglected. The maximal error that can occur due to the tolerance band of the sensors can be determined by calculating the maximal position error due to a temperature change equal to the temperature tolerance band. The error band can be determined with the next formula:

$$e_{sensor} = \alpha_{eff} \Delta T_{tol} (L_{meas}(0) - L_{ref}(0)) \quad (5.17)$$

Where:

e_{sensor} (m) = Error due to the tolerance band of the temperature sensors

ΔT_{tol} (K) = Temperature tolerance band of the PT100's

$$\alpha_{eff} = 5.9 \cdot 10^{-6} (K^{-1}) \quad L_{meas}(0) = 0.46(m)$$

$$\Delta T_{tol} = 0.3(K) \quad L_{ref}(0) = 0.22(m)$$

Using these values the total error band as a consequence of the tolerance band of the sensor can be determined.

$$e_{sensor} = \pm 4.2(\mu m)$$

This is a high error and decreases the reliability of the measurements. This error looks like a modifying input on the sensor, however the fact that this error is not the same for all measurements implies that something else could be the cause of this.

But when looking at the measurements in Figure 5-13 it can be seen that the end point of the graphs differs more than this calculated tolerance. So the difference between the measured drift and the calculated drift would not be caused mainly by the tolerance band of the temperature sensor.

In order to increase the reliability of the measurements, the measurements could be repeated with high tolerance temperature sensors.

Another possible cause for the difference of the two plots shown in Figure 5-13 could be that the length is not measured accurate enough. Two other length configurations will be calculated below. Changing the length of element 3 and element 10:

$$L_{ref,2}(0) = L_{ref}(0) + 0.01(m)$$

$$L_{meas,2}(0) = L_{meas}(0) - 0.01(m)$$

For these new lengths the calculated drift becomes:

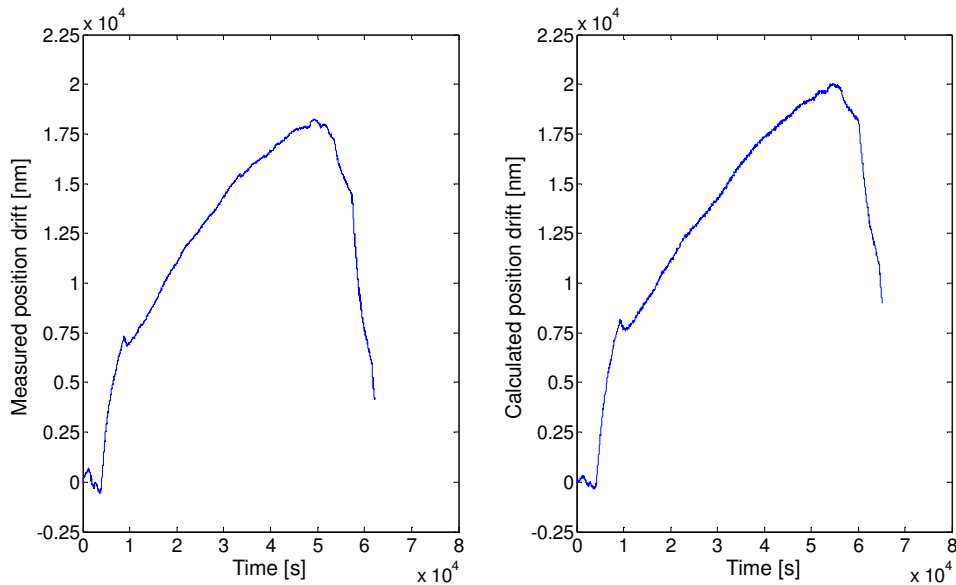


Figure 5-17 Measured position drift and calculated position drift for drift measurement 3, when the length of the reference arm is assumed to be longer and the length of the measurement arm is shorter

Increasing the reference arm with respect to the measurement arm gives a better approximation on the gain when the drift increases, but a worse approximation when the drift decreases.

Now the length is changed of element 3 and element 10 is changed again:

$$L_{ref,3}(0) = L_{ref}(0) - 0.01(m)$$

$$L_{meas,3}(0) = L_{meas}(0) + 0.01(m)$$

For these two new lengths the calculated drift becomes:

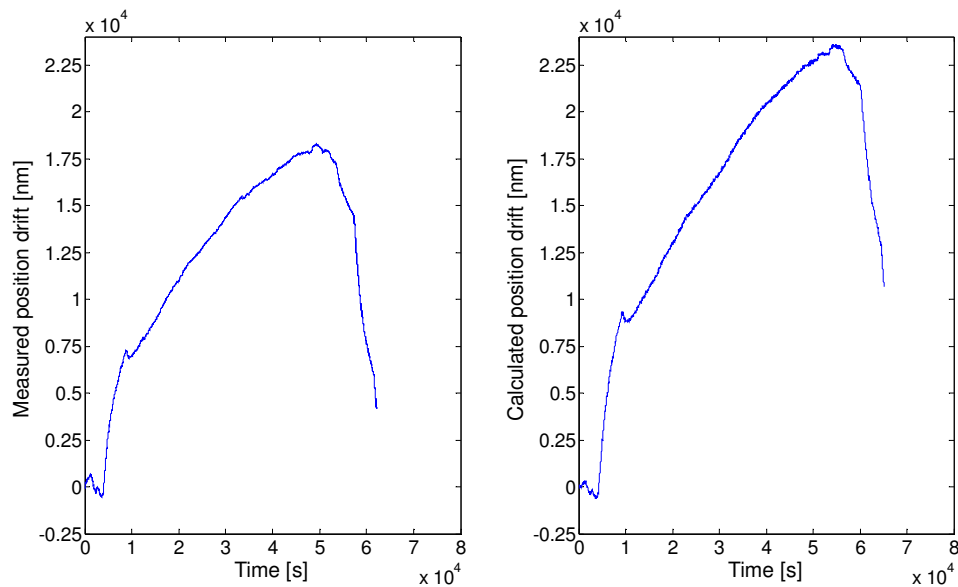


Figure 5-18 Measured position drift and calculated position drift for drift measurement 3, when the length of the reference arm is assumed to be shorter and the length of the measurement arm is longer

Increasing the measurement arm with respect to the reference arm gives a better approximation on the gain when the drift decreases, but a worse approximation when the drift increases. From the graphs in Figure 5-17 and Figure 5-18 it can be seen that the accuracy of the measured initial length isn't the main reason for the difference of the measured drift and the calculated drift.

When the temperature decreases, the calculated drift is higher than the measured drift and when the temperature increases, the calculated drift is lower than the measured drift. For the temperature measurements it has been assumed that the temperature distribution over an element is homogeneous. This assumption is probably incorrect. The average temperature is lower than the outside coating temperature because the core of the fiber is thermally insulated from the coating. This temperature difference will be greater if the thermal coefficient of conduction is lower. The thermal coefficient of the coating material is relatively low. About two orders of magnitude lower than copper for example. From the magnitude of the thermal coefficient of conduction there can be concluded that the temperature is not homogeneous in the radial direction of the fiber. The core temperature of the fiber couldn't be measured in this experiment. But when the temperature of the surroundings increases the core temperature will have a lower temperature than the surface temperature of the coating. Applying this temperature distribution to the equation of compatibility (5.4) will result in a lower effective coefficient of thermal expansion. For this reason the calculated drift will be higher than the measured drift when the temperature of the surrounding increases.

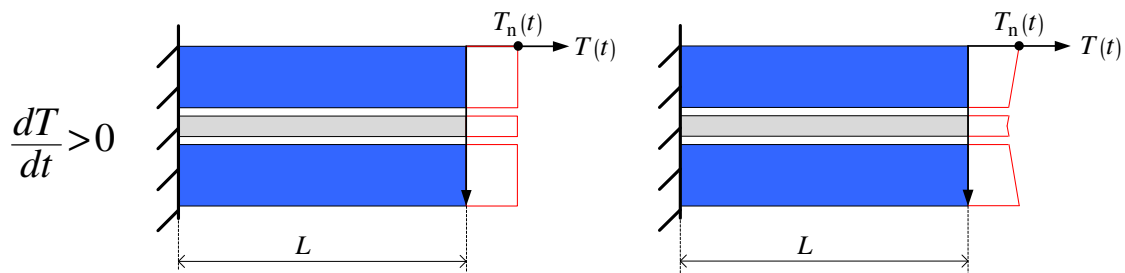


Figure 5-19 Temperature distribution over a fiber when the temperature of the surroundings increases and the core temperature is lower compared to the surroundings

If the temperature of the surroundings decreases the core temperature will have a higher temperature than the surface temperature of the coating. Applying this temperature distribution to the equation of compatibility will result in a higher effective coefficient of thermal expansion. For this reason the calculated drift will be higher than the measured drift when the temperature of the surrounding decreases.

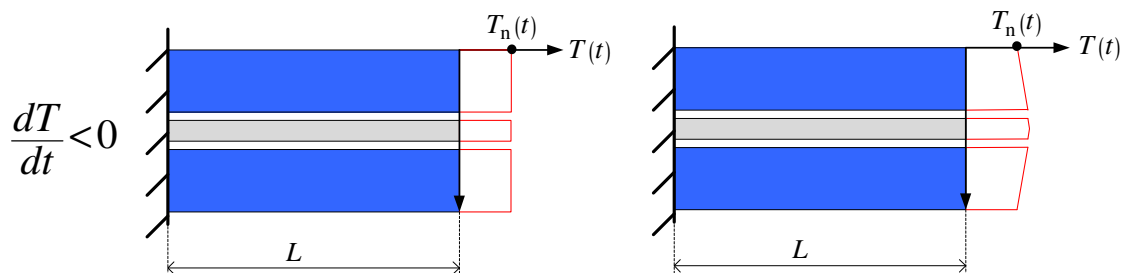


Figure 5-20 Temperature distribution over a fiber when the temperature of the surroundings decreases and the core temperature is higher compared to the surroundings

Furthermore, if the coating temperature increases more rapidly the temperature difference between the fiber coating and the fiber core will be greater. So the effective coefficient of thermal expansion is a function of the temperature rate of the fiber coating.

Though when looking at the drift measurements shown in appendix E.2 and E.3, this isn't the case. From this there can be concluded that there must be another explanation for this difference.

For the calculation of the thermal expansion of the reference and the measurement arm it is assumed that the reference and the measurement arm only consist of fiber optic cables. Actually they also consist of connectors, a lens and a mirror. The length of the lens and the mirror are respectively about 1 and 2 (cm). These lengths are relatively small compared to the total length of the fiber. The connectors are built up differently than the fiber optic cable, but also consist of a fiber cladding and some other material around it. For better measurements it can be recommended to remove these connectors from the setup and weld the fibers together.

Due to the low sample frequency and the cutoff frequency of the filter, higher frequency temperature fluctuations won't be detected. It would be better to perform the measurements with a data acquisition system that could sample with a higher frequency and use temperature sensors with less noise.

The longitudinal thermal expansion of the three fibers within the splitter is unknown and remains an uncertain factor, this is possibly the reason for the main difference between the two measured drift and the calculated drift shown in Figure 5-13.

So even though there are still some uncertainties in the measurements, the conclusion that can be drawn from the measurements remains the same. Namely that temperature is the dominant factor causing the position drift of LUNASYS, because the main shape of the two plots in Figure 5-13 are very similar.



6 System specifications after improvements

In chapter 4 the requirements for LUNASYS are stated. Since not all requirements are met, some improvements on the system need to be made. These improvements should eventually lead to a fiber optic interferometer that is operational for the SAFARI application.

In this chapter different improvements on the system will be made and new system specifications will be formulated with these improvements. The chapter is subdivided into different sections and in each section a different improvement will be treated. System specifications that are formed in this chapter will mostly be based on models and simulations that are made in chapter 4.

6.1 AR coating grin lens

Introduction

The largest optical disturbance signals in the fiber optic interferometer are caused by the grin lens. The maximal error caused by these optical disturbance signals was determined in section 4.9.2, and this error is 4.9 (nm). By using a grin lens with an AR coating the magnitude of the optical disturbance signals caused by the grin lens and therefore the maximal error in the measurement system could be reduced significantly.

Modeling

With a new grin lens that has an AR coating the return loss of the grin lens becomes 65 (dB) instead of 11.55 (dB) for the grin lens used in the initial system configuration. Just like the model used in section 4.9.2 the power of the optical disturbance signals is displayed as a ratio of the power of optical disturbance signals over the original signal in Table 6-1.

Table 6-1 Ratio of the power of each disturbance signal over the ideal calculated signal power that has been calculated in appendix C.3, given for all three photodiodes

Disturbance #	ratio photodiode 1	ratio photodiode 2	ratio photodiode 3
1	1.4E-04	0.0E+00	0.0E+00
2	2.6E-07	0.0E+00	0.0E+00
3	0.0E+00	2.0E-06	2.0E-06
4	4.4E-09	3.4E-09	3.5E-09
5	6.9E-07	7.0E-07	6.1E-07
6	6.9E-07	6.3E-07	5.5E-07
7	6.2E-07	6.1E-07	7.1E-07
8	1.6E-07	1.6E-07	1.9E-07
9	1.4E-07	1.3E-07	1.6E-07
Total disturbance	1.4E-04	4.2E-06	4.2E-06

In this scenario the largest optical disturbance signal comes from I_{u1} . In appendix D.2 it can be seen that this disturbance is caused by the circulator.

Result

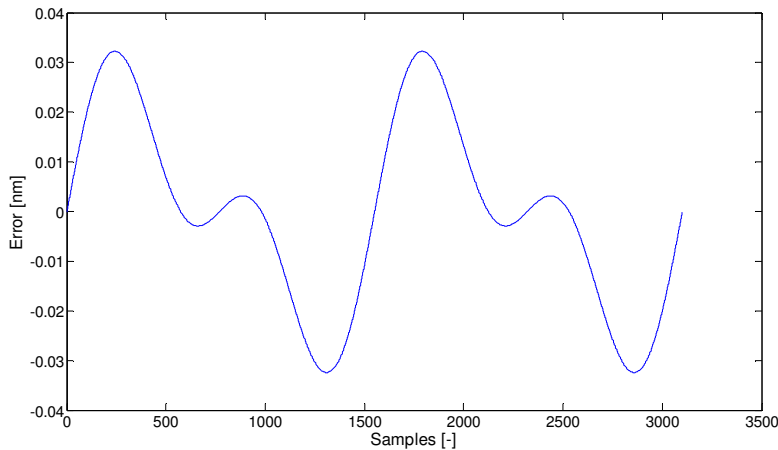


Figure 6-1 Simulated error of the measurement system for two fringe signals, due to angular misalignment between the lens and the moving mirror

The resulting error is a systematic error. The maximal error that can occur is equal to:

$$e_{\text{opt,dis}} = 0.03(\text{nm})$$

This error is much more acceptable compared to the error obtained with the grin lens without the AR coating. From this it can be concluded that it is preferred to use a grin lens with an AR coating.

6.2 Reduce the laser power

Introduction

In order to reduce the amount of stray light and the total heat load on the cryogenic cooled zone, the laser power could be downscaled. The effect of this would be a lower loss of optical power and therefore the amount of stray light and the total heat load on the cryogenic cooled zone are also reduced.

Before the drift experiments were performed it was considered if it would be possible to place the 3x3 splitter in the cryogenic cooled zone in order to reduce the total length of the reference and the measurement arm. Another benefit of this system configuration would be that the temperature in the cryogenic cooled zone is more stable and therefore the magnitude of the temperature disturbances would be lower. A drawback of this concept is that the 3x3 splitter would have to be able to function at 4.5 (K) but also that the heat load on the cryogenic cooled zone would become higher. The total heat load and the stray light power for this new situation will be determined in this section.

Assumptions

- All optical power lost in the 3x3 splitter is absorbed and transferred to heat.

Modeling

Instead of using a power output of the laser of 1 (mW), a 0.1 (mW) laser power output is used. Furthermore a new grin lens with an anti reflection coating is used. This new grin lens has an insertion loss of 1.0 (dB). The splitter is placed within the cryogenic cooled zone and it is assumed that all optical power lost by the 3x3 splitter is absorbed and transferred to heat.

For the laser power losses the same model is used as in section 4.5. A lot of optical power is lost in the end stop fiber of the 3x3 splitter. For this reason this fiber is lead out of the cryogenic cooled zone, because of this three fiber optic cables pass through the wall of the cryogenic cooled zone.

Result

In the figure below the result of the model for the previously described situation is represented.

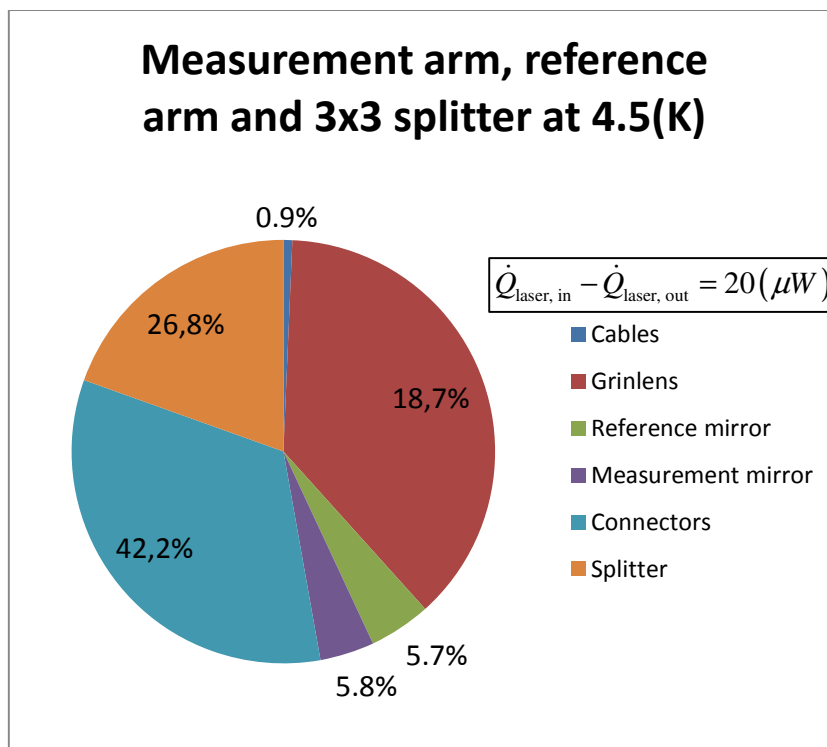


Figure 6-2 Distribution of the laser power loss of the components within the measurement arm, the reference arm and the 3x3 splitter placed within the cryogenic cooled zone of 4.5 (K).

The total power lost by the laser in the cryogenic cooled zone is two times less then for the situation described in section 4.5.

The new calculated amount of stray light:

$$P_{\text{stray light}} = P_{\text{grin lens}} + P_{\text{measurement mirror}} + P_{\text{reference mirror}} = 7.4(\mu W) + 0.8(\mu W) + 0.9(\mu W) = 9.1(\mu W)$$

The new total heat load on the cryogenic cooled zone can be calculated with this data. The standard heat load is slightly increased because now three cables pass through the wall of the cryogenic cooled zone.

$$\dot{Q}_{\text{standard load}} = 3\dot{Q}_{\text{fiber}} = 0.9(\mu W)$$

With these results the new total heat load can be calculated by applying equation (4.9).

$$\dot{Q}_{\text{total load}} = 0.9(\mu W) + 10.9(\mu W) = 11.8(\mu W)$$

Discussion

By reducing the laser power the magnitude of the signal also becomes lower. This means that the SNR is decreased when the laser power is decreased. From section 4.9.1 it could be seen that the impact of the intensity noise on the precision of the measurement system was very low, 1.6 (pm)

It can be expected that if the laser power is lowered one order of magnitude the influence of the intensity noise on the precision of the measurement system will remain low.

From Figure 6-2 it can be seen that the heat load by the laser can significantly be reduced by welding all the optical fibers together instead of using connectors.

As a result of this lower laser power the signals at the ADC will become lower and consequently the ADC won't clip anymore. The gain of the electronics needs to be reset in order to use the total range of the ADC, so that the resolution doesn't suffer from this smaller signal.

6.3 Stray light maze

Introduction

The initial calculated stray light power in section 4.5 of 42.3 (μW) and the newly calculated stray light power of 9.1 (μW) in section 6.2 both don't meet the required amount of stray light of 0.89 (μW). A measure needs to be taken in order to meet the requirement. A stray light maze has been designed in order to absorb most of the stray light power and transfer it to heat. In order to estimate the reduction of the stray light power due to the presence of this stray light maze the ray tracing method is used [1]. The maze is designed in such a way that the two moving parts of the maze don't contact each other. In this way no extra hysteresis, damping or wear is introduced on the ODL.

Assumptions

- The surfaces of the stray light maze are isothermal
- The surfaces of the stray light maze are opaque
- The emissivity of the black anodized Aluminium is 0.8 for all temperatures and for light with a wavelength of 1550 (nm)
- All stray light power is concentrated in one ray.
- Only specular reflections occur within the stray light maze

Modeling

For the model used to calculate the stray light power, that exits the stray light maze, the ray tracing method is used.

The concept of the designed stray light maze is shown in F.1. Black anodized Aluminium is used as absorption material of the stray light maze, because it absorbs infrared light and it is also very stiff. It is assumed that the emissivity of the black anodized Aluminium is 0.8 for all temperatures and for light with a wavelength of 1550 (nm). Also, it is assumed that all stray light power is concentrated within 1 ray that only reflects specular. The stray light power that exits the stray light maze can be calculated using equation (6.1) [1].

$$\dot{Q}_{\text{stray light}} = \dot{Q}_r (1 - \varepsilon)^{m_r} \quad (6.1)$$

Where:

$\dot{Q}_r (W)$ = Radiant energy leaving the fiber optic interferometer

$m_r (-)$ = Number of reflections

Result

A cross section of the stray light maze is shown in Figure 6-3. The stray light maze is drawn in the configuration when the moving mirror is as near as possible to the grin lens.

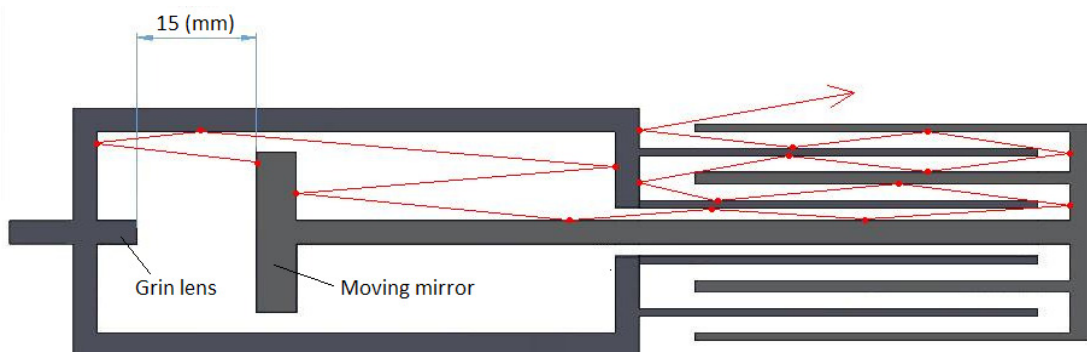


Figure 6-3 Stray light maze cross section with possible optical path of the stray light

18 Reflections are counted for the rays drawn in Figure 6-3. So by applying equation (6.1) the amount of stray light escaping from the fiber optic interferometer and entering

the cryogenic cooled zone can be calculated. The stray light power that has been calculated in section 6.2 has been used.

$$\dot{Q}_{\text{stray light}} = 2.4 \cdot 10^{-12} (\mu W)$$

This value is much lower than the required amount of stray light of 0.89 (μW), so the stray light requirement for LUNASYS is met.

The stray light power is absorbed and transferred to heat, the total heat load that was calculated in section 6.2 has to be recalculated now. This is done below.

$$\dot{Q}_{\text{total load}} = 0.9 (\mu W) + 20 (\mu W) = 20.9 (\mu W)$$

All materials in the stray light maze, including the mirror, are chosen as Aluminium. The total added mass on the moving actuator of the ODL is calculated by 3D design software Solidworks.

$$\rho_{\text{aluminium}} = 2730 (kg / m^3)$$

$$m_{\text{added, act}} = 29.5 (g)$$

In section 3.7 it was determined that the maximal extra mass on moving actuator should not be greater than 48 (g). This concept meets this requirement.

Validation

The required number of reflections can be calculated with equation (6.1). By using the initially calculated stray light power in section 4.5 of 42.3 (μW) the required amount of reflections is can be calculated.

$$m_r = 2.4$$

If the laser power is scaled down, the amount of stray light decreases and the needed amount of reflections also decreases. For the new calculated stray light power in section 6.2 of 0.89 (μW) the required amount of reflections is:

$$m_r = 1.4$$

The amount of reflections that occur in the stray light maze are higher than the minimal required amount of reflections for both situation, so the stray light power requirement is met for both situations mentioned above.

Discussion

For manufacturing reasons and weight saving reasons the shape of the stray light maze is chosen to be round.

Because the entire stray light maze is made out of 1 single material no thermal stresses occur that could cause undesired deflections of the mechanical structure resulting in contact between the two parts of the stray light maze.

The stray light analysis should be verified with stray light analysis software like ZEMAX and ASAP.

A more detailed design of the stray light maze should be made if more detailed requirements for the stray light maze are known.

A stray light shield, in the form of a tube, should be surrounding the reference and the measurement arm and the splitter, as it is assumed in section 4.5.

6.4 Thermal coefficient of expansion at 4.5 (K)

Introduction

The linear thermal coefficient of expansion of many materials decreases when extremely low temperatures are reached. If the thermal expansion of all the optical components of the measurement arm and the reference arm become zero, position drift due to thermal disturbances is completely eliminated.

In this section the thermal coefficient of different materials is considered and it will be verified if thermal disturbances play a role at a cryogenic temperature of 4.5 (K).

Modeling

In the next three figures the thermal coefficient of expansion for three different materials are shown. Two construction materials, Aluminium and Invar36 (which is famous for its low thermal coefficient of expansion), are shown below.

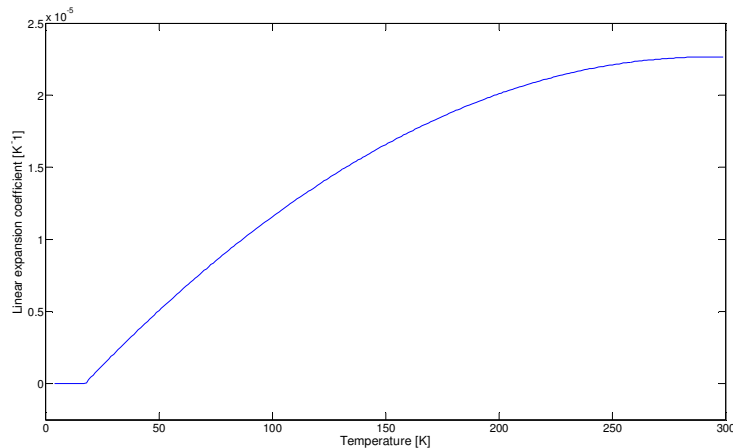


Figure 6-4 Linear thermal coefficient of expansion for Aluminium over the temperature [31]

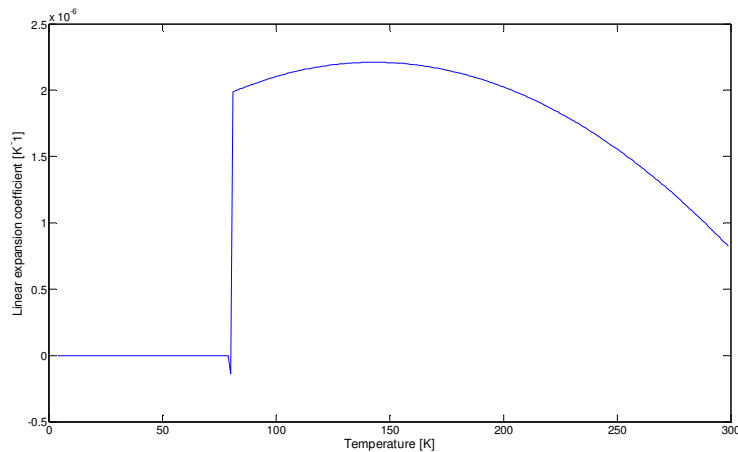


Figure 6-5 Linear thermal coefficient of expansion for Invar36 over the temperature [31]

The position drift due to temperature disturbances is mainly caused by expansion and contraction of the waveguide material Pyrex and the coating material Acrylate. The thermal coefficient of expansion of Pyrex is shown below in Figure 6-6.

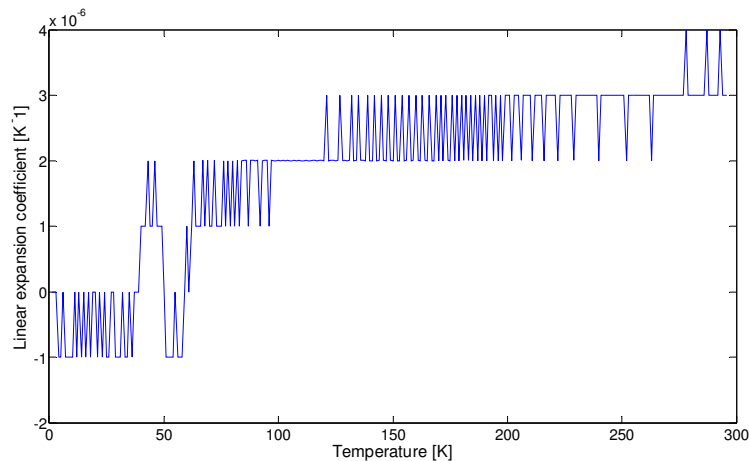


Figure 6-6 The thermal coefficient of expansion of Pyrex over temperature. PYREX is the waveguide material of the fiber optic cable. This data is obtained with the software Cryocomp from SRON.

Result

At 4.5 (K) Aluminium won't expand or contract anymore. Pyrex however, has a thermal coefficient of expansion equal to zero at 3 (K). By lowering the temperature from 4.5 (K) to 3 (K), position drift due to thermal disturbances could be eliminated.

Discussion

In order to reduce the temperature of the room with the FTS from 4.5 (K) to 3 (K), more electric power is required. The maximal available electrical power is limited and already at the boundaries of the specified available electrical power [23]. Therefore it is not possible to cool the room with the FTS to 3 (K).

The effect of refractive index changes over temperature at cryogenic temperature is unknown, because no data could be found about this property at these temperatures. Another uncertainty is the exact material type of the waveguide material of fiber optic cables. Of what material exactly is the waveguide material of the fiber optic cable made of? This is a question that is not answered with certainty in this report.

6.5 Drift improvements

Introduction

The main cause of the measured position drift, are the temperature disturbances acting on the measurement and the reference arm. The impact of these disturbances on the drift could be reduced by influencing some design parameters that determine the thermal expansion and contraction of a piece of material.

In this section the accuracy will be specified by the performed drift experiments. For these drift measurements the improvements are added to the system.

Modeling

In equation (4.37) it can be seen that by reducing the magnitude of the temperature disturbances and by shortening the lengths of the fibers of the measurement arm and then reference arm the measurement system becomes less sensitive to temperature disturbances. The initial length of the fibers in the reference arm was 1 (m) and the new lengths are given in section 5.2.

$$L_{meas}(0) = 0.46(m)$$

$$L_{ref}(0) = 0.22(m)$$

For the drift measurements shown in Appendix E these improvements were added to the system.

Besides that, the laser has been thermally insulated and the air in the measurement arm has been shielded with a tube around it to decrease the changes of the refractive index of the air.

Result

Over the measured time period the maximal temperature fluctuation on the measurement system was:

$$T_{max} - T_{min} = 0.14(K)$$

For this drift measurement (drift measurement 2), keeping the temperature disturbances to minimal has been successful. Drift measurement 1, described in appendix E.2, has a high temperature disturbance on the end of the measurement, which makes this measurement less reliable.

The magnitudes of the other errors in the measurement system are much smaller than the error due to the drift. Therefore, the estimate of the new accuracy has been based on the error measured in drift measurement 2.

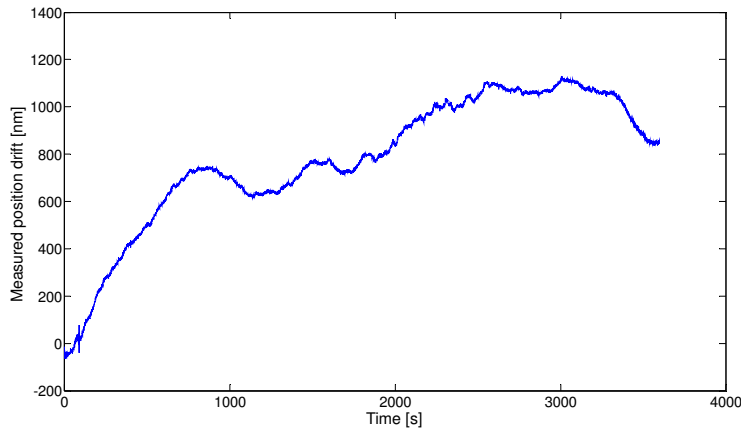


Figure 6-7 Measured drift signal for drift measurement 2

The error could be read from Figure 6-7.

1100(*nm*) over 3600 (s)

From this result it can be concluded that the accuracy of the measurement system still doesn't meet the required accuracy of the system, which is 10 (nm).

6.6 Lens and mirror choice

Introduction

Technobis has thought of some concepts for the grin lens and the moving mirror. In this section a choice will be made out of the concepts that meet the requirements for LUNASYS best.

Modeling

The concepts for the moving mirror and the lens are shown below in Figure 6-8.

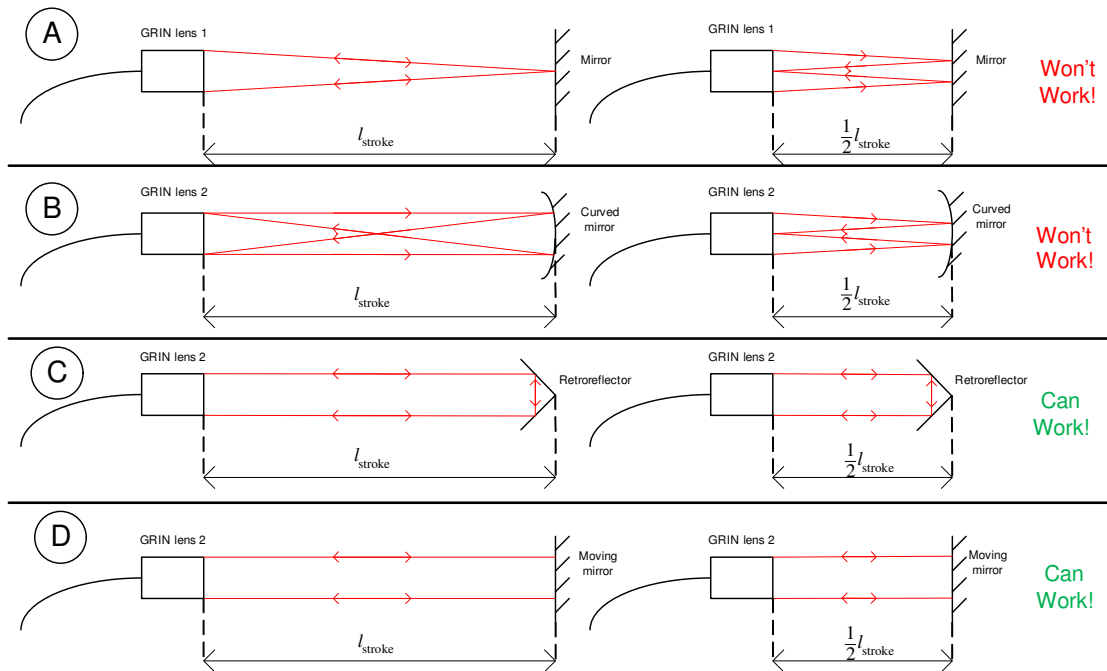


Figure 6-8 Concepts for the type of grIN lens and the moving mirror [22]

The main design goals are:

- Minimize the optical losses
- Obtain the highest possible accuracy

Consider Figure 2-7 that is shown below again.

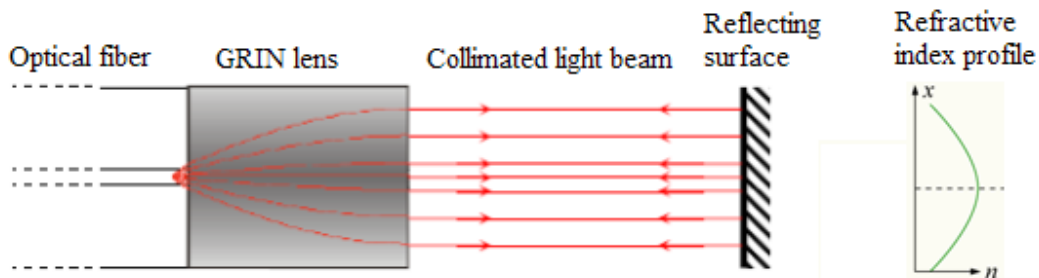


Figure 6-9 Schematic view of light beams collimated by a grIN lens reflecting on a mirror [20]

In this figure it can be seen that the light that is diffusely spread out of the fiber gets collimated. When the collimated beam reflects on a reflecting surface such as a mirror or a retro reflector and the light is returned normal to the surface of the lens, then the light gets coupled back into the fiber due to the working principle of the grIN lens.

Concepts A and B from Figure 6-8 both have light returning to the grIN lens that is not normal to the surface of the grIN lens. This means that most of the returning light doesn't couple back into the optical fiber core or that the amount of light that couples

back into the fiber core is independent on the position of the moving mirror. For this reason concepts A and B won't be used.

Concepts C and D remain, because there respectively a retro reflector and a mirror are used. These two concepts both have benefits and drawbacks. The main benefit of using a mirror is that it is insensitive to concentricity between the grin lens and the mirror. However, as can be seen from section 4.9.5 this concept is sensitive to angular misalignment between the moving mirror and the grin lens. For the retro reflector this is exactly the other way around. The retro reflector is insensitive to angular misalignment between the retro reflector and the grin lens, but it is sensitive to concentricity between the retro reflector and the grin lens.

A design choice has to be made based on the working conditions of the fiber optic interferometer.

Result

For the SAFARI application the next requirements for the FTS are given in section 3.4:

FTS mirror rotation tilt [6]	$<\pm 30$ (arcsec)
FTS mirror lateral displacement [6]	<100 (μm)

With an assumed distance between the grin lens and the moving mirror of 0.05 (m), based on Figure D-23 a mirror tilt of 30 (arcsec) corresponds to a lateral displacement at the coupled light back at the grin lens of:

$$d_{\text{offset}} = 420(\mu\text{m})$$

From this calculation it can be concluded that a larger offset of the light at the lens is obtained due to a rotation tilt of the FTS mirror than due to the FTS mirror lateral displacement. For this reason the best design choice would be to choose a concept that is less sensitive to angular misalignment than to concentricity.

Based on these considerations it can be concluded that concept C, using a retro reflector is the best design choice for the SAFARI application.

Discussion

By using a very thin retro reflector, the measurement system becomes less sensitive to temperature disturbances. It could also be chosen to use a retro reflector built on a piece of Aluminium, because this has a thermal coefficient of 0 at 4.5 (K).

6.7 New system specifications

With all the improvements added to the system the new system specifications are given

Table 6-2 Overview of the new system specifications of LUNASYS

Type of specification	Old specified value	New specified value	Meets requirements?
Accuracy	750 (nm) over 1 hour	1100 (nm) over 1 hour	No
Resolution	0.19 (nm)	0.19 (nm)	Yes
Stroke	34.5 (mm)	34.5 (mm)	Yes
Sample frequency	781 (Hz)	781 (Hz)	Yes
Heat load	1.3 (μ W)	20.9 (μ W)	Yes
Stray light power	42.3 (μ W)	2.4E-12 (μ W)	Yes
Space qualified	No	No	No
Maximal required electrical power	6.67(W)	6.67 (W)	No
Functionality at cryogenic temperature	No	No	No
Relative displacement measurement	Yes	Yes	Yes
Laser + electronics placed in room of 293 (K)	Yes	Yes	Yes
Sensor head placed near the ODL	Yes	Yes	Yes

From Table 6-2 there can be concluded that with all the improvements added to the system, the new system specifications still do not meet all the requirements.

7 New interferometer concepts

Introduction

In the previous chapters it became clear that there are still four requirements for LUNASYS that are not met. It also became evident that the accuracy due to drift is the bottleneck of the design. Temperature disturbances on the reference and measurement arm are the cause of this drift. So in order to make LUNASYS operational for the SAFARI application the design needs to be improved.

In this chapter new concepts for the interferometer will be suggested in order to solve the drift problem. First it will be shown that the improvements on the initial system configuration of the fiber optic interferometer won't be enough to reach the targeted requirements. Then some concepts for possible solutions will be presented. The working principle of the concepts will be shown and the main benefits and drawbacks of these concepts will be treated.

Modeling

The drift has an order of magnitude of 10^4 (nm). This has been calculated in chapter 4 and has been measured in chapter 5.

There are three main parameters that determine the magnitude of the drift for a temperature disturbance on the reference or measurement arm. These parameters are described in equation (4.37). The main parameters that influence the drift are the thermal coefficient of expansion, the length of the measurement or the reference arm, and the magnitude of the temperature change.

Not all materials could be used for fiber optic cable material. The waveguide material that is suitable for the laser light is limited. Pyrex glass, the material used for the fiber core and cladding is a suitable waveguide material. Pyrex has a thermal coefficient of expansion that is in the order of 10^{-6} (K^{-1}). From Figure 6-6 it can be seen that decreasing the temperature also decreased the thermal expansion of Pyrex, but at 4.5 (K) it still has the same order of magnitude. From this it can be concluded that the thermal coefficient of expansion of the waveguide material is not the parameter that has to be changed in order to effectively reduce the magnitude of the drift.

Reducing the magnitude of the temperature disturbances will also give smaller errors. Applying thermal insulation material around the fiber optic cables will reduce the magnitude of the temperature disturbance. This will reduce the temperature disturbances by about one order of magnitude; based on the initial disturbance of 1 (K) used in section 4.9.4 and the drift measurements of the thermally insulated fibers in appendix E.2 and E.3, this won't be enough to obtain the desired accuracy. It should also be considered that the lens can't be thermally insulated completely. Consequently, a part of the system will endure higher thermal disturbances.

The final parameter that remains to decrease the thermal expansion is the length of the measurement and the reference arm. The main reason why the initial system configuration was so highly sensitive to temperature disturbances is due to the long

lengths of the measurement and the reference arm. There are physical limitations of the optical components that prevent shortening the lengths of the measurement and the reference arm. E.g. the shortest length of the grin lens is still 1 (cm) and the splitter is 4.5 (cm). The grin lens and the splitter are standard components that should be custom made and therefore become expensive and the functionality can't be guaranteed. Also the amount of engineering that this would cost is very high. Possibly the entire system should be redesigned, e.g. by miniaturizing the reference arm and the measurement arm. The longitudinal thermal expansion of the fibers within the splitter could also become a problem. Therefore the splitter should also be miniaturized. This solution is used by TNO. However, the large investment required for this solution is not preferable.

Applying feedback is also a possibility, but in order to apply feedback a second sensor is required that could measure the disturbances with very high accuracy. If this feedback sensor is not able to measure with high accuracy, the total accuracy of the fiber optic interferometer won't be able to meet the targeted requirement. The problem with this solution is that finding a sensor that could measure all the disturbances is very difficult. Besides that, instead of solving the problems, it is preferred to prevent the problems from happening.

New interferometer concept 1

From the previous considerations, it can be concluded that by decreasing the length of the measurement and the reference arm the drift can be reduced effectively. With this in mind a new concept where those measures are applied has been developed. Consider Figure 7-1 where a new concept is shown for the fiber optic interferometer. In this concept instead of a moving mirror, a moving retro reflector is used.

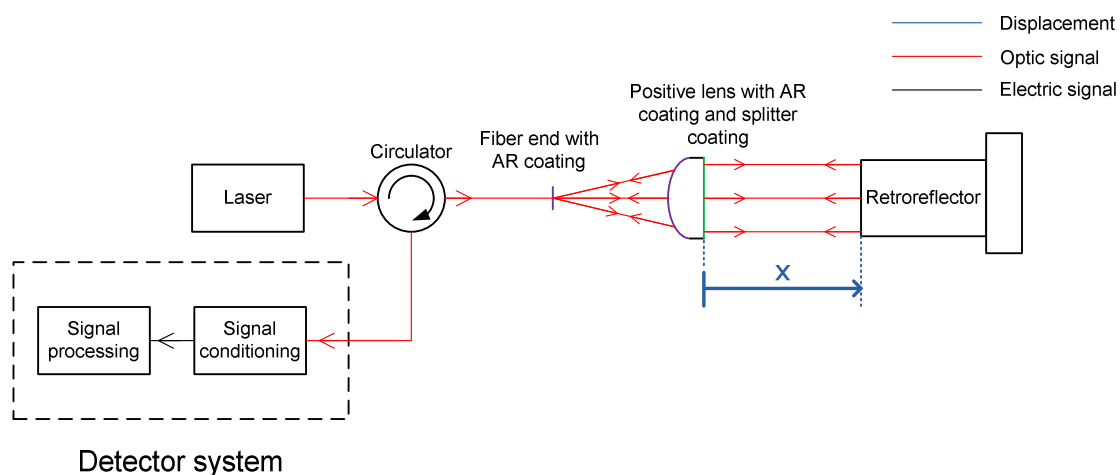


Figure 7-1 New interferometer concept 1

A monochromatic laser is used as a light source. First the light passes through a single mode fiber and then through a circulator. The circulator is used for the same reason as in the initial system configuration, to prevent damage to the laser caused by reflection in the system. After the circulator the light arrives at a fiber end that is cut off.

Due to the transition of the refractive index from the waveguide material of the fiber to the vacuum Fresnel reflections will occur. When the light is near normal incidence the reflection can be described in the next equation [3].

$$r = \left(\frac{n_1 - n_2}{n_1 + n_2} \right)^2 \quad (7.1)$$

Where:

$r(-)$ = Reflection

$n_1(-)$ = Refractive index of waveguide material 1

$n_2(-)$ = Refractive index of waveguide material 2

The refractive index in vacuum is 1, and the refractive index in the fiber core is about 1.6, with these values the reflection can be calculated.

$$r = 0,053$$

This means that about 5 percent of the laser power will be reflected back into the fiber. This reflected light is undesired and can be considered as an optical disturbance signal. This optical disturbance signal should be prevented. This can be done by using an 8 degrees facet fiber end or by depositing an AR coating on the fiber core. The AR coating is preferred, because in this way minimal light is lost and therefore less light is required. If less light is required, then the electrical power demands for the laser will be lower. The light that leaves the fiber end will diffusely spread into the surroundings. A positive lens is placed after the fiber end in order to collimate the light.

On normal beam splitters used in interferometry, coatings are used to set a certain transmission and reflection for the light incident on the beam splitter. These coatings are referred to as splitter coating in this report. The light beam that is collimated by the lens partially gets reflected on a splitter coating and partially gets transmitted. The transmitted beam reflects on the moving mirror (or on the moving retro reflector) and this light interferes with the light that is reflected on the splitter coating. The interference signal then goes through the circulator to the detector. Because there is only a single interference signal blind spots as described in A.4 will occur and there is no extra signal with a quadrature phase relation to this signal. In other words, a relative displacement can't be measured.

Alignment of the lens with the fiber end is very important. By using an Aluminium structure for the mounting of the lens and the fiber end, the alignment won't be affected by temperature disturbances, because the thermal coefficient of expansion of Aluminium is zero at 4.5 (K) as can be seen in Figure 6-4.

It is assumed that the thickness of the splitter coating could be about 1 (μm) thick. For a temperature disturbance of 1 (K), a thermal coefficient of expansion of about 10^{-5} (K^{-1}) and a refractive index of about 1.6 the error can be calculated. By applying equation (4.37) the following error in the measured position can be found:

$$e_{Temp} = 0.75 (pm)$$

Clearly the effect of temperature disturbances on the accuracy is much smaller compared to the initial system configuration of the fiber optic interferometer. In fact this is in improvement of 6 orders of magnitude!

By placing a highly accurate cryogenic temperature sensor (e.g. from the company Lakeshore) on the outer side of the splitter coating, it would even be possible to correct for this error.

New interferometer concept 2

The main problem with new concept 1 is that there is no quadrature phase related signal to the measurement signal. In order to obtain such a signal a second fiber end with a positive lens is added to the system. This second signal is derived by measuring the distance to another retro reflector attached to the same moving mirror. This is done in such a way that both retro reflectors make the same displacement x . By placing a 1x2 splitter just after the laser the same light source could be used for this second fiber. The two fibers leaving the 1x2 splitter then go to a circulator and go on in a similar way as the interferometer concept 1, as was shown in Figure 7-1. Unfortunately this causes a new problem, namely that the two interference signals that are detected at the detector system most likely won't have an exact quadrature phase relation. The phase relation depends on the optical paths travelled from the exits of the 1x2 splitter to the two splitter coating. From appendix C.4 it could be seen that the manipulator needs to be placed between the cavity of the retro reflector and the splitter coating.

This is why a manipulator behind the retro reflector of one of these two arms in order to manipulate the phase of the light that arrives at one of the splitter coatings. In this way a quadrature phase relation between the two signals is obtained. This concept is shown in Figure 7-2.

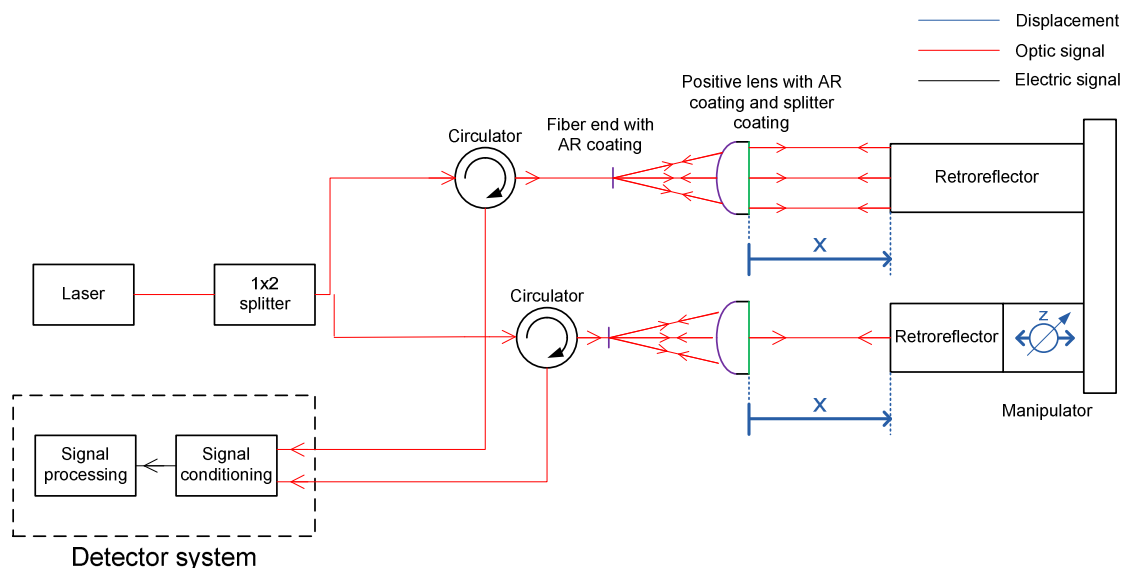


Figure 7-2 New interferometer concept 2

The optical paths travelled by the light can be used to determine the OPD for the two arms of this concept. A simplified representation for the OPD for both arms in concept 2 is shown in Figure 7-3. The lens is not considered in this model, only the splitter coating that is deposited on the lens.

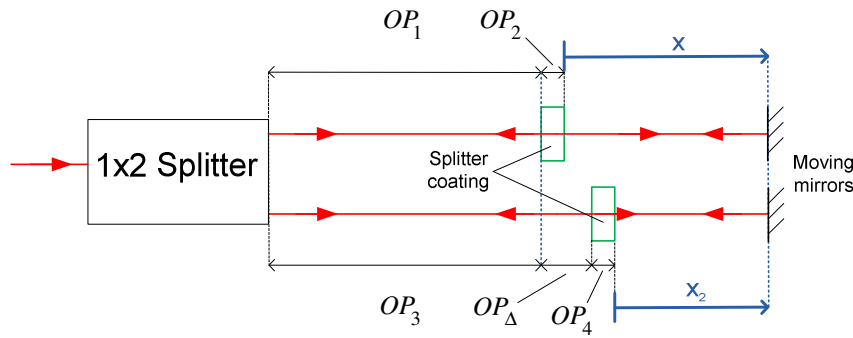


Figure 7-3 Optical paths in the arms of new interferometer concept 2

The 1x2 splitter splits the laser light in two arms. The OPD for the both arms of concept 2, is determined in the next two equations according to the parameters given in Figure 7-3.

$$OPD_1 = 2[(OP_1 + OP_2 + n \cdot x) - OP_1] = 2(n \cdot x + OP_2) \quad (7.2)$$

$$OPD_2 = 2[(OP_3 + OP_\Delta + OP_4 + n \cdot x_2) - (OP_3 + OP_\Delta)] = 2(n \cdot x_2 + OP_4) \quad (7.3)$$

Where:

$OP_\Delta (m)$ = Difference in OPD for the two arms

Now displacement x_2 needs to be expressed as a function of the displacement x .

$$n \cdot x_2 = n \cdot x + OP_2 - (OP_\Delta + OP_4) \quad (7.4)$$

By combining equation (7.3) and (7.4) the two final equations for the OPD could be obtained.

$$OPD_1 = 2(n \cdot x + OP_2) \quad (7.5)$$

$$OPD_2 = 2(n \cdot x + OP_2 - OP_\Delta) \quad (7.6)$$

Deleting the common initial phase results into the next two equations.

$$OPD_1 = 2(n \cdot x) \quad (7.7)$$

$$OPD_2 = 2(n \cdot x - OP_{\Delta}) \quad (7.8)$$

In order to obtain a quadrature phase relationship the difference in optical path must be equal to a quarter of a wavelength

$$OP_{\Delta} = \frac{\lambda}{4}$$

Because the light travels from the lens to the moving mirror and from the moving mirror back to the lens the manipulator needs to change the distance from the lens to the moving mirror with respect to the other arm with a displacement x_{Δ} that is half of OP_{Δ} .

$$x_{\Delta} = \pm \frac{\lambda}{8}$$

As calculated Temperature disturbances acting on OP_{Δ} over time will have a negligible effect on the accuracy. Because $e_{temp} = 0.75 (pm)$

If the interferometer would be used for commercial goals or in another surrounding where temperature disturbances or other disturbance would affect the quadrature phase relation between the two signals, equations (7.7) and (7.8) could be rewritten.

$$OPD_1(t) = 2(n \cdot x) \quad (7.9)$$

$$OPD_2(t) = 2(n \cdot x - OP_{\Delta}(t)) \quad (7.10)$$

In order to compensate for this change of the phase of the of the two signals with respect to each other, the two measured signals at the detector system could be used to apply feedback to an actuator placed on the position of the manipulator shown in Figure 7-2 or as shown in Figure 7-4. In Figure 7-4 contact with the moving mirror is avoided.

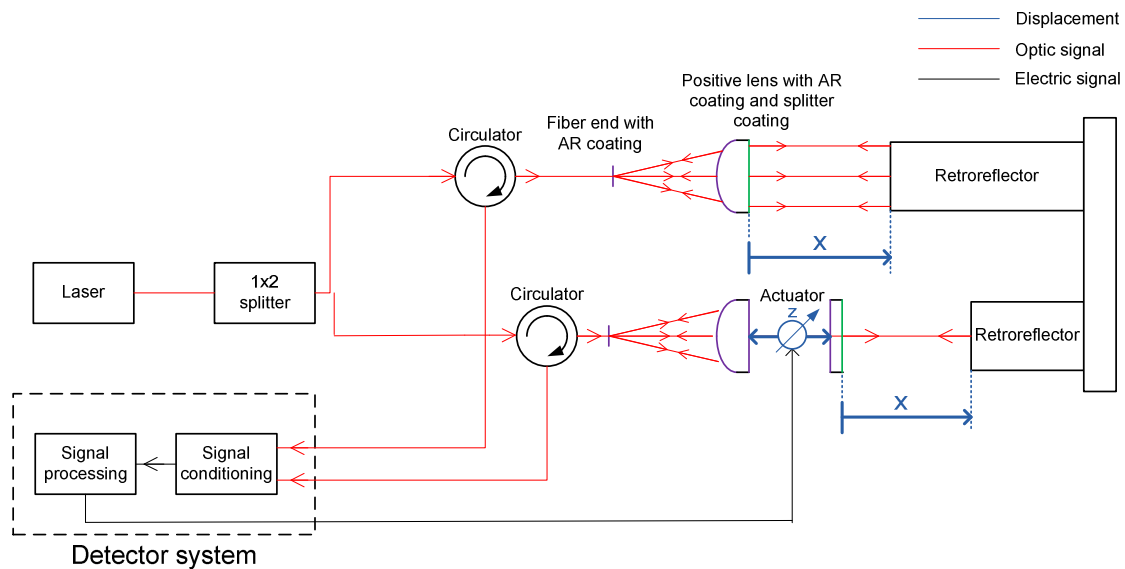


Figure 7-4 New interferometer concept 3

It is important that the alignment of the two lenses relative to the fiber ends should be positioned with high accuracy. This concept has several beneficial aspects. The main benefit is that the effect of temperature disturbances acting on the measurement and reference arm is greatly reduced (with a factor of 1,000,000).

The quadrature phase relation between the two signals should be corrected after the system is thermally stabilized. The direction of the compensation of the phase relationship relative to the non-compensated signal can be determined by trial and error. Another benefit is that the 1x2 splitter does not need to function at 4.5 (K), because it will be placed in an environment of 293 (K). Temperature disturbances are of low frequent nature. By using a high control bandwidth for the actuator the effect of temperature disturbances on the quadrature phase relation is minimized and the introduced time delay due to this feedback is minimal.

New interferometer concept 4

Another concept that could be used is modulation of the drive current of the laser. This concept is called new interferometer concept 4 and is shown in Figure 7-5.

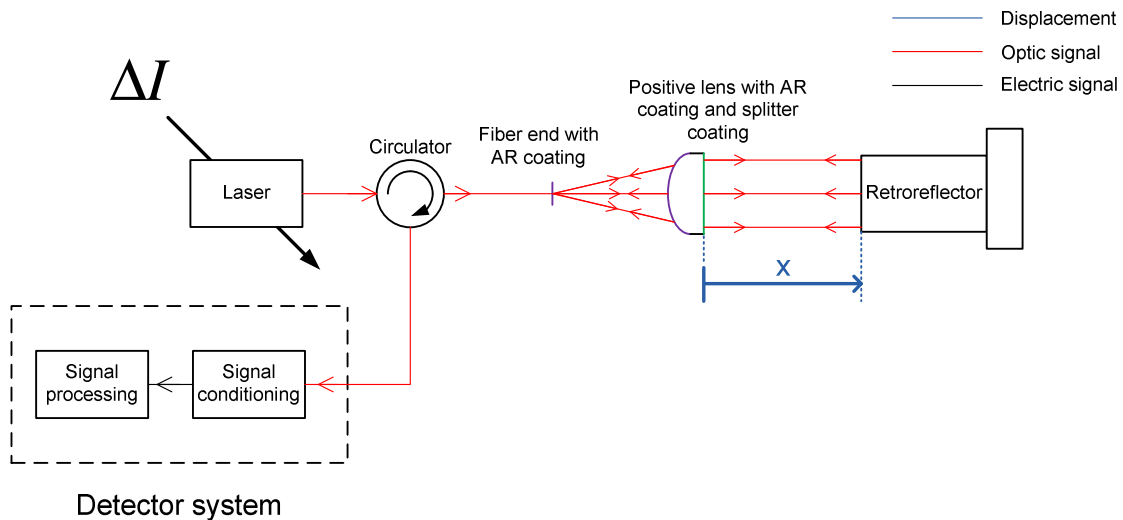


Figure 7-5 New interferometer concept 4

By changing the drive current of the laser the output wavelength of the laser can be tuned. If the drive current changes, then the wavelength changes. When the wavelength of the laser changes consequently the phase of the detected fringe signal will also change.

If the drive current now for instance changes as a sine function over time, then the output wavelength also changes as a sine function over time. If the frequency of this sine function is high enough, then with this concept a quadrature phase relation can be obtained. The main benefit of this concept is that only a single measurement arm is required.

New interferometer concept 5

Another concept that could be used is also based on the single arm interferometer concept, but now a multimode fiber core is used and a CCD camera to detect the fringe image. The light rays that leave the positive lens all travel a different path. Therefore the fringe pattern that is detected by the CCD camera will show different intensity profiles. From these different profiles a quadrature phase relation could also be obtained for instance by looking at the measured intensity in the points indicated by the two red dots. The upper red dot has a phase difference of approximately 90 degrees with respect to the phase of the lower red dot.

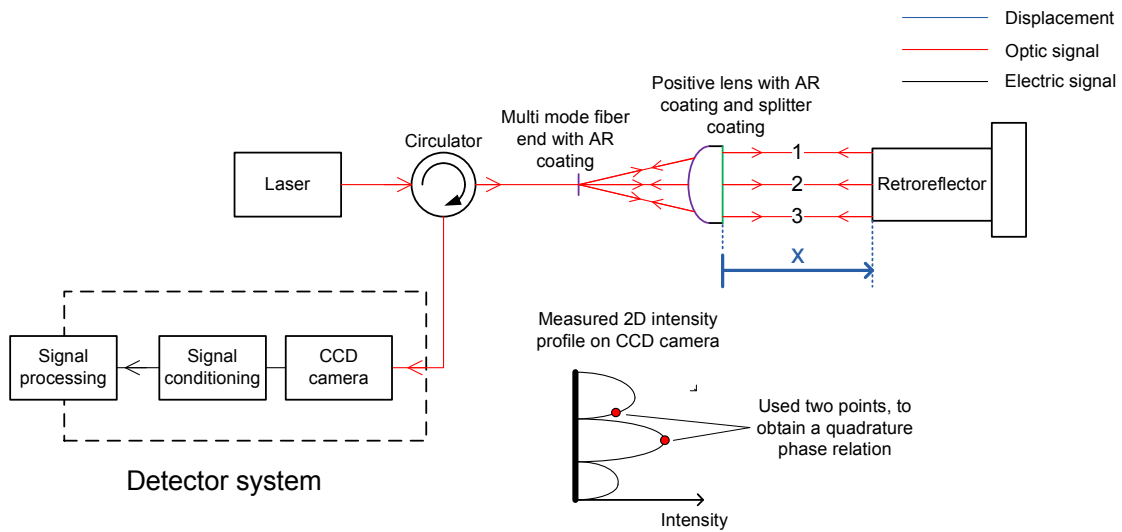


Figure 7-6 New interferometer concept 5

Result

From this section it can be concluded that in order to meet the requirements for the targeted accuracy and to make a relative displacement measurement, new interferometer concept 2 is the simplest concept and therefore should be used. The three concepts 3, 4 and 5 are more complex but could also function without the large sensitivity to temperature disturbances!

Discussion

Three configurations for the positive lens can be used. These configurations are shown in Figure 7-7.

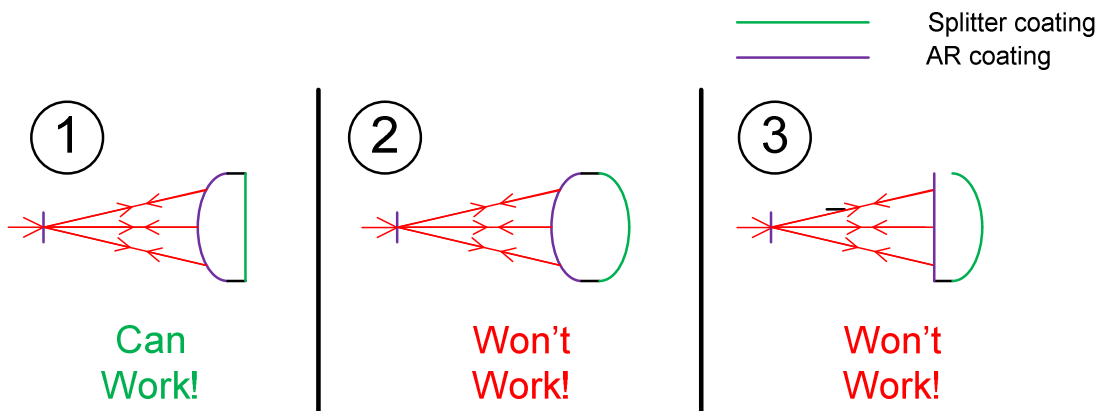


Figure 7-7 Three concepts for the positive lens used in the new interferometer concepts

There are a few things that need to be considered when one of the three concepts mentioned above is chosen.

- The amount of lost light should be minimized
- The light intensity coupled back into the fiber core should not be dependent on the position of the mirror
- The undesired reflections that couple back into the fiber should be minimal

The splitter coating should be placed on the right side of the lens in order to keep the size of the measurement and reference arm minimal and thereby keep the influence of the temperature disturbances to a minimum. The transmission of the left surface of the lens should be as high as possible in order to reduce the undesired reflections that couple back into the fiber core and reduce the amount of stray light. For this reason an AR coating is placed on the left side of the lens.

The only concept of the positive lens that will function is concept 1. This is because of the reflected light on the splitter coating. If a curved face on the right side of the lens is used, then the light that is reflected on the splitter coating will not travel the same path back into the fiber core. Most of the light won't couple back into the core at all!

A detailed analysis for the choice of the lens still needs to be made. The curvature, the size of the lens and the distance away from the lens still needs to be determined. This analysis for the detailed choice of the lens is beyond the scope of this document.



8 Conclusion and recommendations

8.1 Conclusions

In this thesis report it has been researched if LUNASYS is operational for the SAFARI instrument. The requirements for LUNASYS were not clear yet. These have been gathered, determined and checked.

After determining the requirements, the specifications of LUNASYS were checked. It became clear that the initial system configuration of LUNASYS does not meet the requirements. The most important design requirement that is not met, is the accuracy of the measurement system.

The accuracy is mainly dominated by thermal drift caused by temperature disturbances acting on the reference and the measurement arm. This cause has been analyzed in detail and experiments were performed to validate this. The calculated and measured value had some difference between them. This difference is most likely caused by longitudinal expansions and contractions of the fibers within the splitter that were not taken into account in the predictive model. Still the measurements were similar in a large measure, that it is valid to conclude that temperature disturbances on the reference and measurement are the dominant factor causing the measured position drift.

The setup of the fiber optic interferometer was improved in an attempt to meet the requirements. After applying the improvements, the new specifications of the system certainly improved, but still didn't meet all the requirements. The new system specifications after the improvements are given in the table below.

Table 8-1 New system specifications of LUNASYS after the improvements

Type of specification	Required value	Specified value	Meets requirements?
Accuracy	10 (nm) over 200(s)	1100 (nm) over 1 (hr)	No
Resolution	1 (nm)	0.19 (nm)	Yes
Stroke	34.5 (mm)	34.5 (mm)	Yes
Sample frequency	439 (Hz)	781 (Hz)	Yes
Heat load	100 (μW)	20.9 (μW)	Yes
Stray light power	0.89 (μW)	2.4E-12 (μW)	Yes
Space qualified	No	No	No
Maximal required electrical power	1.0 (W)	6.67 (W)	No
Functionality at cryogenic temperature	Yes	No	No
Relative displacement measurement	Yes	Yes	Yes
Laser + electronics placed in room of 293 (K)	Yes	Yes	Yes
Sensor head placed near the ODL	Yes	Yes	Yes

From this table it can clearly be seen what needs to be improved on the current setup of LUNASYS in order to reach the targeted requirements.

From this research it became clear that the maximal required power for the fiber optic interferometer doesn't meet the requirements, while it was assumed that this requirement was met.

In order to make the system space qualified, the exact requirements for space qualification need to be known.

A possible solution has been worked out to reduce the stray light power to acceptable levels. With this solution the stray light has been reduced with a factor 10^{12} .

After applying the improvements, the drift remained a problem. Further reduction of the drift or even compensation of the drift is possible; however, it would be wiser to prevent the drift from happening at all. For this it would be better to come up with a completely new concept which is based on minimizing the drift.

New concepts have been developed that need to be worked out in further detail. In these concepts the 3x3 splitter, which is an uncertainty factor for the accuracy and is limiting the functionality of the whole fiber optic interferometer at cryogenic temperature, is not used. The drift due to temperature disturbances acting on the measurement and the reference arm, that was limiting the accuracy will be reduced and only cause an error of $e_{\text{Temp}}=0.75$ (pm), this error is 10^6 times lower compared to the error in the initial system.



8.2 Recommendations

In order to comply with the requirements for the SAFARI instrument, the promising concept of the new interferometer concepts need to be worked out.

Perform the recommended analysis for the splitter coating and the positive lens that has to be used. Once that is done, measurements should be performed in order to verify the accuracy and the precision of the fiber optic interferometer.

The stray light analysis should be validated with stray light analysis software like ZEMAX and ASAP. Also, it was assumed that the stray light generated within the fiber optic cable could be neglected. This should be validated as well.

The most important requirements to make the system space qualified are: vacuum tolerance, the maximum radiation dose and the maximum radiation dose rate. Also very important is the reliability about the origin of the batch of the component and the test results of the batch. For space qualification there exist clear rules. It is best to use the expertise of SRON for space qualification of the fiber optic interferometer, because they are familiar with the applicable rules for this.

The heat load of LUNASYS on the cryogenic cooled zone is dominated by the laser power losses. The laser power losses are specified for room temperature. In order to verify that the requirements are still met at cryogenic temperature, measurements should be performed during cryogenic functionality tests. For this reason it would be convenient if the gain of the transimpedance amplifier could be set variable, f.e. by replacing the fixed resistor by a potentiometer.

Other benefits of using a potentiometer are that it will be easier to perform polarization measurements and clipping of the ADC can be prevented.

The lens needs to be custom made for the desired operating temperature.

The required electrical power needs to be reduced. Further reduction of the laser output power, improving the efficiency of the laser and reducing the required cooling power for the Peltier element inside the laser will help to reach this goal.

The laser casing temperature may deviate 0.1 (K) in order to follow the specs. If it deviates more, then the laser won't behave according to the specs. For this reason a temperature controlled box should be placed around the laser. It should be investigated if it is really necessary to use this, because then the fiber optic interferometer will consume even more electrical power.

Proper equipment for the alignment of the grin lens with the optic stage should be purchased. A linear stage with a higher resolution should be used to validate the accuracy of small displacements.

The decimation filter should be implemented correctly; else the contribution of noise will be much higher. A delta sigma ADC could be used. This ADC uses decimation and noise shaping and will result in much less noise power in the displacement signal.

The bandwidth of the decimation filter is below the required sample frequency of 439 (Hz). Averaging over less samples or increase the sample frequency of the ADC will increase the bandwidth of the digital filter.

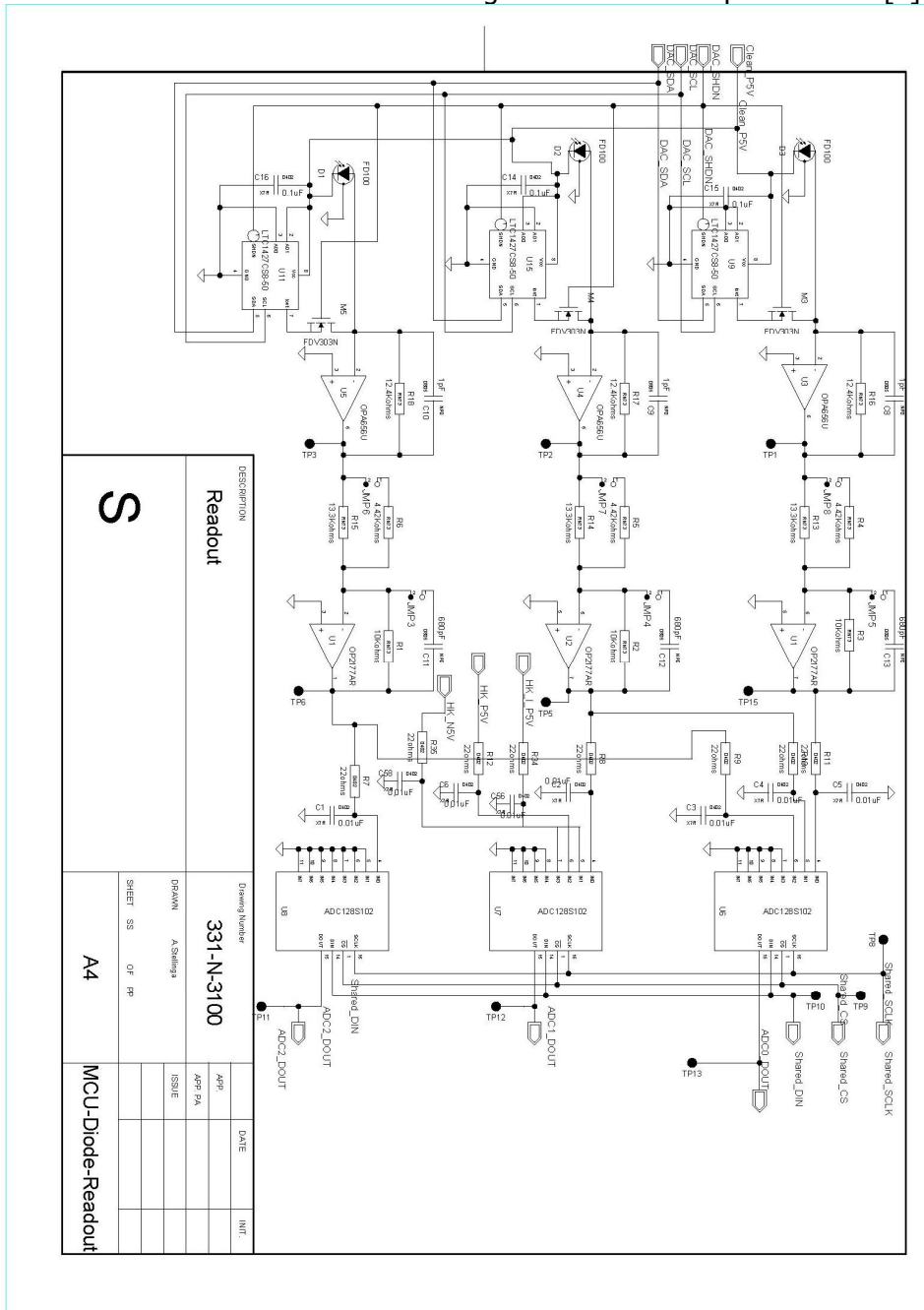
By following up all these recommendations the fiber optic interferometer can be improved such that it fulfills the requirements for within the SAFARI instrument that are stated this moment.



Appendix A Background information

A.1 MCU diode readout

This electronic circuit is used for the analogue readout of the photodiodes [8].





A.2 Baseline configuration of SPICA

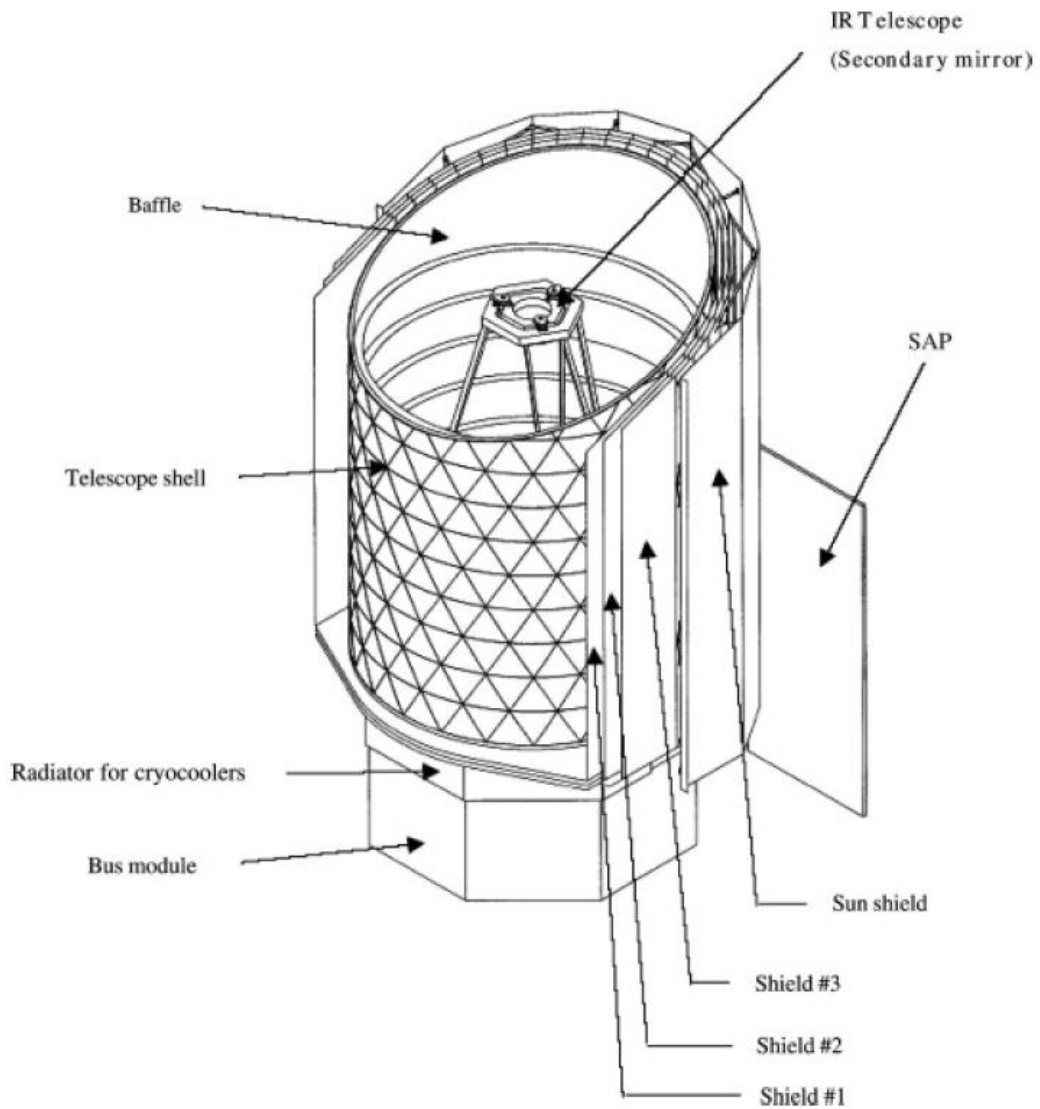


Figure A-1 Base line configuration of SPICA

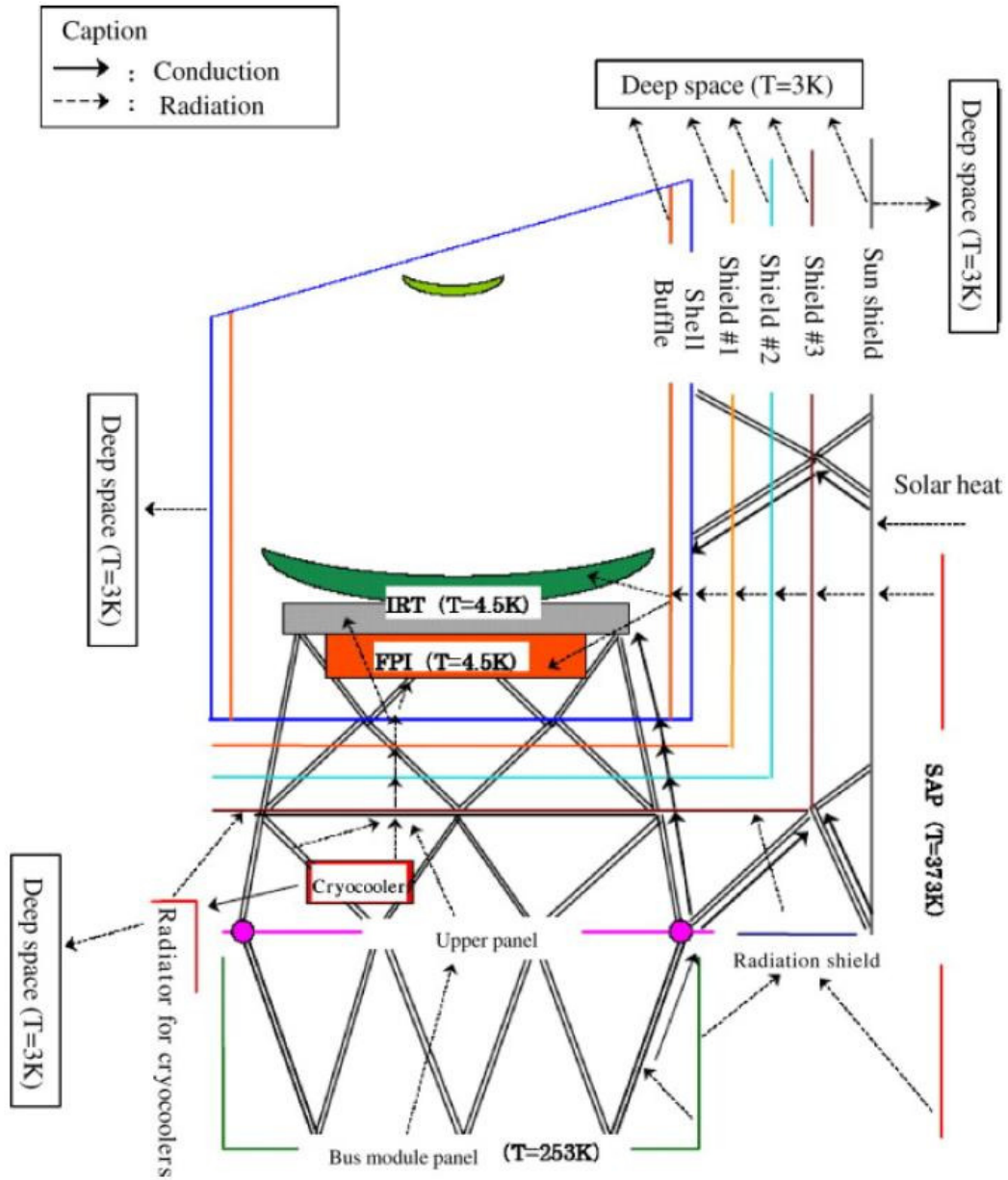
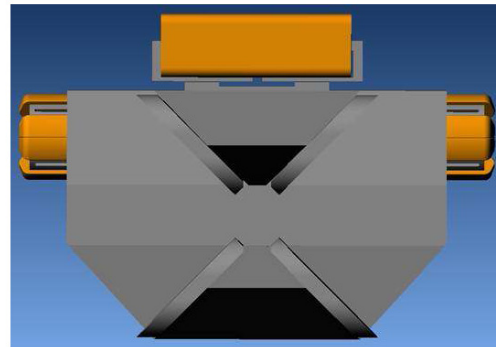
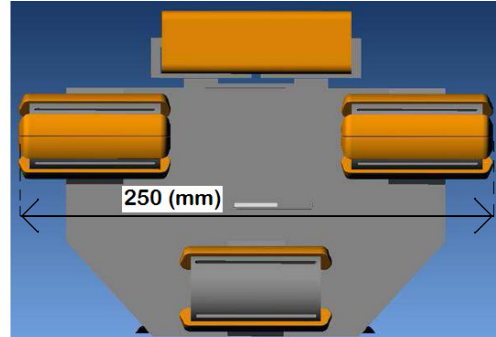
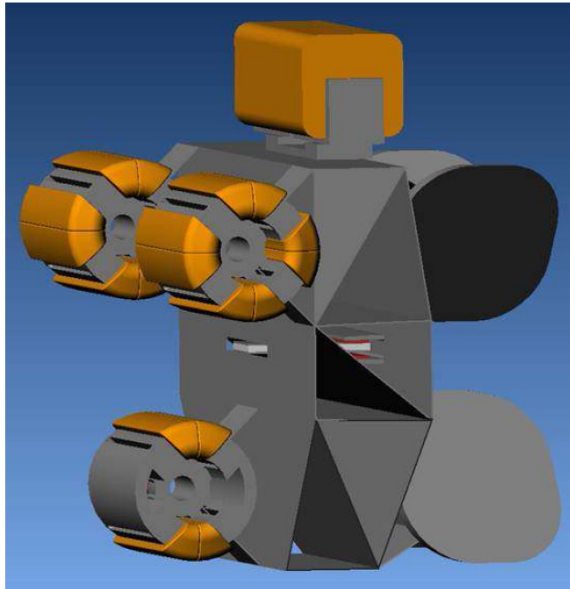


Figure A-2 Conceptual view of the SPICA cryogenic system which consists of an effective radiative cooling system and mechanical cryogenic coolers [16].

A.3 Drawing of the FTS mechanism

4th FTSM design



A.4 Quadrature

A benefit of using a 3x3 splitter instead of using a normal beam splitter (1x2 splitter) is that it enables the possibility for the fiber optic interferometer to measure the displacement direction. Consider a fiber optic interferometer with a normal 1x2 splitter and a wavelength used of $\lambda_{\text{laser}}=1550$ (nm).

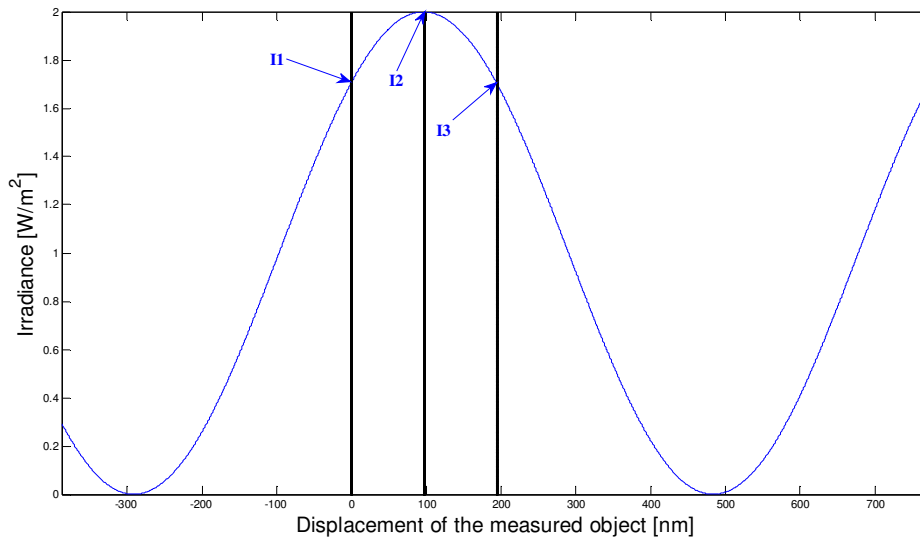


Figure A-3 Measured irradiances in a fiber optic interferometer based on a 1x2 splitter corresponding to three positions of the measured object

When the measured object has not displaced, a certain amount of irradiance on the photodiode is measured. Call this irradiance I1 as shown in Figure A-3. The exact value of the irradiance is not so important. So let's say that the value of this irradiance is for example $1.7 \text{ (W/m}^2\text{)}$. Now the measured object starts to move in an unknown direction, we assume this direction to be positive. The measured object moves $1/16$ of a wavelength ($=97\text{nm}$) and the signal reaches a peak value for the irradiance measured on the photodiode $I2 = 2.0 \text{ (W/m}^2\text{)}$. Finally the object moves again. As before the direction of the displacement is not known, but only the Irradiance is measured by the photodiode. A value of $1.7 \text{ (W/m}^2\text{)}$ is measured, this implies that a displacement of 97 (nm) is made but what is not known is if we measure I1 or I3. Both values correspond to a displacement of 97 (nm) . So what would be interesting to know is if the object made a positive displacement (away from the starting point) or a negative displacement (back to the starting point).

Now consider a fiber optic interferometer with a 3x3 splitter that has three interference signals with a phase difference of 120 degrees with respect to each other and the same laser wavelength as before. Now the same steps are repeated as for the 1x2 splitter.

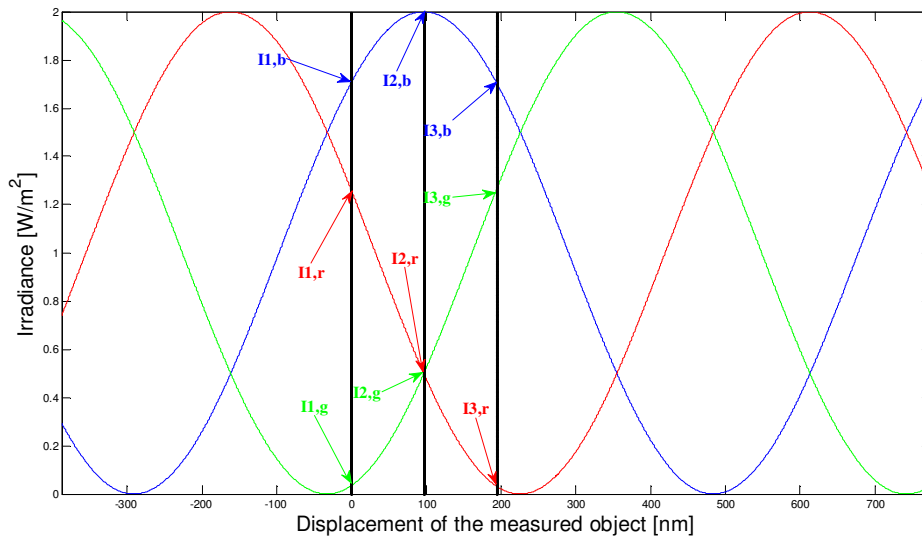


Figure A-4 Measured irradiances in a fiber optic interferometer based on a 3x3 splitter corresponding to three positions of the measured object

From Figure A-4 we see that in the initial position we measure the three signals $I_{1,b} = 1.7 \text{ (W/m}^2\text{)}$, $I_{1,r}$ and $I_{1,g}$. Then the measured object moves $1/16$ of a wavelength ($=97 \text{ (nm)}$) in the direction considered positive and the blue signal reaches a peak value for the irradiance measured on the photodiode, namely $I_{2,b} = 2.0 \text{ (W/m}^2\text{)}$. The green signal $I_{2,g}$ increases with respect to its previous measured irradiance $I_{1,g}$ and the red value $I_{2,r}$ decreases with respect to its previous measured irradiance $I_{1,r}$. If now the final displacement is made in an unknown direction and the blue photodiode measures an irradiance of $= 1.7 \text{ (W/m}^2\text{)}$. Then in this case the direction of the displacement can be determined by comparing the other two signals ($I_{3,g}$ and $I_{3,r}$) to its previous two values. For example if $I_{3,r}$ is smaller than $I_{2,r}$ or likewise if $I_{3,g}$ is larger than $I_{2,g}$ then the direction of the displacement must have been positive, as can be seen clearly from Figure A-4.

In general it could be stated that two signals waveforms that have a phase difference of a quarter of their output period are said to have a quadrature phase relationship. A quadrature phase relationship between two signals makes it possible to measure the direction of an absolute displacement.

Another additional benefit of using a quadrature phase relationship compared to a single interference signal is that the sensitivity is constant for a moving mirror. The sensitivity is defined as the sensor output (the power incident on the photodiode) divided by the sensor input.

$$S = \frac{\text{Output}}{\text{Input}} = \frac{I_{photo}}{x} \tag{A.1}$$

Where:

$S(W / m)$ = Sensitivity of the fiber optic interferometer

$P_{photo}(W)$ = Power incising on the photodiode

$x(m)$ = Displacement of the moving mirror

The sensitivity of the fiber optic interferometer is equal to the slope of the curve. Near the minimum and the maximum of Figure A-4 the slope is much less steep than near the inflection point. In Figure A-4 there is always a signal with a steep slope at any position. In this way so called blind spots are prevented. Blind spots are places where the slope of the signal is very low and almost zero. This occurs at the maxima and the minima of the signal.



Appendix B Power calculations

B.1 Standard heat load calculation

Introduction

The maximal heat load on the cryogenic cooled zone by LUNASYS is limited. The fiber optic cables that are used for LUNASYS have to travel from a relatively “warm” region of 253 (K) to a cooler region of 4.5 (K) as can be seen in Figure B-1. In this appendix the heat transferred by the fiber optic cables into the cryogenic cooled zone of 4.5 (K) called the standard heat load will be determined for a single cable.

In order to determine the standard heat load it needs to be known how the temperature is distributed over the fiber between the heat shield of 30 (K) and 4.5 (K). This will be obtained by numerically solving the differential heat equation that will be formulated for this problem. With this information it will be possible to calculate how much heat passes through the cryogenic cooled wall of 4.5 (K) by means of conduction as a consequence of putting the fibers through this wall. Two situations will be treated, a constant coefficient of conductivity and a variable coefficient of conductivity.

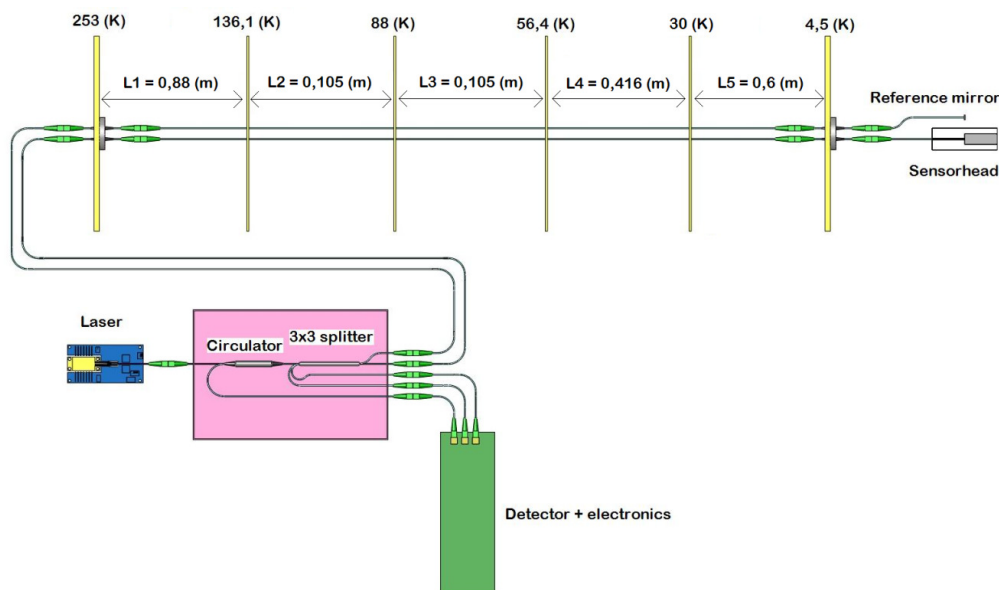


Figure B-1 Initial system configuration of the setup for LUNASYS

Assumptions

- LUNASYS is in steady state or in other words in thermal equilibrium with its surroundings
- Heat transfer by convection can be neglected

- There are no internal heat sources in the fiber
- All surfaces are opaque
- The view factor has been approximated
- All objects are considered to be gray objects
- The view factors are the same for all discretized elements
- Acrylate has the same thermal conductivity as Polyimide
- The temperature over the elements is homogeneous

Modeling

To model the temperature distribution over a fiber optic cable between the heat shields of 30 (K) and 4.5 (K) the general heat equation [11] is used.

$$\underbrace{\frac{\partial e}{\partial t}}_{\text{change of internal energy density}} + \underbrace{\frac{\partial q_i}{\partial x_i}}_{\text{change of heat flux through the system}} - \underbrace{\sigma_{ij} \frac{\partial \epsilon_{ij}}{\partial t}}_{\text{power of the stresses}} + \underbrace{\sum_{k=1}^n Q_k}_{\text{sum of all external heat sources}} - \underbrace{\sum_{v=1}^m Q_v}_{\text{sum of all internal heat sources}} = 0 \quad \text{in} \quad \underbrace{V(x_i)}_{\text{Volume of the solid}} \quad (\text{B.1})$$

Where:

$e(J)$ = Internal energy density

$q_i (W/m^2)$ = Component of the heat flux in direction $i = 1, 2, 3$

$\sigma_{ij} (N/m^2)$ = Mechanical stresses on surface $j = 1, 2, 3$ in direction $i = 1, 2, 3$

$\epsilon_{ij} (-)$ = State of strain on surface $j = 1, 2, 3$ in direction $i = 1, 2, 3$

The rate of change of the internal energy density is given in equation (B.2).

$$\frac{\partial e}{\partial t} = \rho c(T) \frac{\partial T}{\partial t} \quad (\text{B.2})$$

Where:

$\rho (kg/m^3)$ = Density of the material

$c (J/kgK)$ = Specific heat capacity of the material

The amount of heat flux entering and exiting the system by conduction is described in the equation below.

$$q_i = -k \frac{\partial T}{\partial x_i} \quad (\text{B.3})$$

And:

$$Q_i = -kA_s \frac{\partial T}{\partial x_i} \quad (\text{B.4})$$

Where:

$$A_s (m^2) = \text{Area}$$

The system is in vacuum so all heat transfer by convection can be neglected. By using equations (B.2) and (B.3) the general heat equation given in equation (B.1) can be rewritten.

$$\rho c(T) \frac{\partial T}{\partial t} - \frac{\partial}{\partial x_i} \left(k \frac{\partial T}{\partial x} \right)_i - \sigma_{ij} \frac{\partial \epsilon_{ij}}{\partial t} + \sum_{k=1}^n Q_{rad,k} = 0 \quad \text{in } V(x) \quad (\text{B.5})$$

Where:

$$Q_{rad,k} (W) = \text{Radiant heat component } k$$

If after some time thermal equilibrium is reached and the heat problem is considered one-dimensional, then the temperature rate is equal to zero and equation (B.5) becomes:

$$-\frac{\partial}{\partial x} \left(k \frac{\partial T}{\partial x} \right) + \sum_{k=1}^n Q_{rad,k} = 0 \quad \text{in } V(x) \quad (\text{B.6})$$

In the next figure, a fiber is displayed between the two final heat shields. The temperatures of the heat shields are considered to be homogeneous and the heat transfer from the hot shield to the cold shield is not relevant for this model.

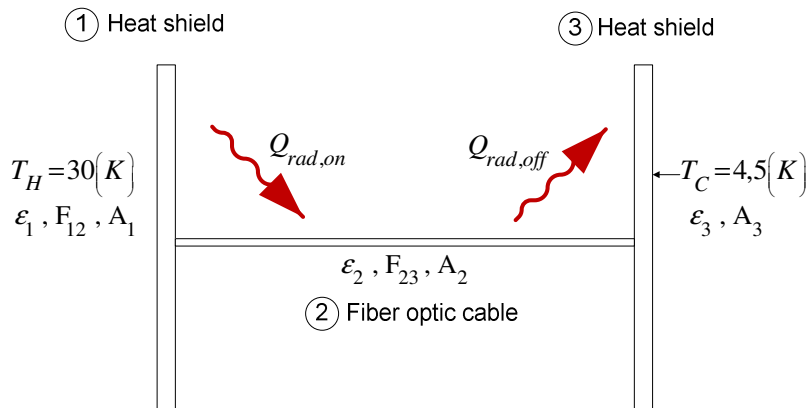


Figure B-2 Radiant heat exchange between a fiber and two heat shields

Now consider the fiber optic cable and the heat shields to be gray bodies. A certain amount of radiation is radiating from the hot wall of 30 (K) on the fiber $Q_{rad,on}$ and a

certain amount of radiation is radiating from the fiber on the cold wall of 4.5 (K) $Q_{rad,off}$. Then the heat equation described in equation (B.6) becomes:

$$-\frac{\partial}{\partial x} \left(k \frac{\partial T}{\partial x} \right) + (Q_{rad,on} - Q_{rad,off}) = 0 \quad \text{in } V(x) \quad (B.7)$$

The surfaces are all considered to be opaque, this means that no light is transmitted through the surfaces and that the amount of absorbed radiation is equal to the emissivity ε

The incoming radiating heat flux on the fiber can be determined with the following model.

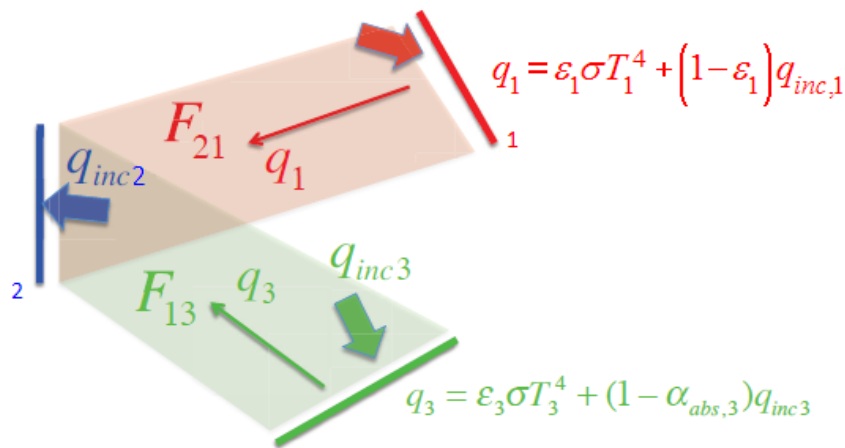


Figure B-3 Model for heat exchange between three surfaces [25].

The thermal network for the three surfaces shown in Figure B-3 can be written in the next three equations.

$$q_{inc,1} = F_{21} (\varepsilon_2 \sigma T_2^4 + (1 - \varepsilon_2) q_{inc,2}) + F_{31} (\varepsilon_3 \sigma T_3^4 + (1 - \varepsilon_3) q_{inc,3}) \quad (B.8)$$

$$q_{inc,2} = F_{12} (\varepsilon_1 \sigma T_1^4 + (1 - \varepsilon_1) q_{inc,1}) + F_{32} (\varepsilon_3 \sigma T_3^4 + (1 - \varepsilon_3) q_{inc,3}) \quad (B.9)$$

$$q_{inc,3} = F_{13} (\varepsilon_1 \sigma T_1^4 + (1 - \varepsilon_1) q_{inc,1}) + F_{23} (\varepsilon_2 \sigma T_2^4 + (1 - \varepsilon_2) q_{inc,2}) \quad (B.10)$$

Where:

q_{inc} (W / m^2) = Incident heat flux

$\varepsilon(-)$ = Emissivity

Since the exact path of the fiber through the heat shields is unknown, the view factors are approximated as followed:

$$F_{12} = \frac{A_2}{A_1}, \quad F_{13} = 1 - \frac{A_2}{A_1}$$

$$F_{21} = 0,5, \quad F_{23} = 0,5$$

$$F_{32} = \frac{A_2}{A_3}, \quad F_{31} = 1 - \frac{A_2}{A_3}$$

If the temperature of the fiber was constant over the length of the fiber, then the radiation on the fiber and from the fiber can be written in the next two equations [1].

$$Q_{rad,on} = \varepsilon_2 A_2 q_{inc,2} \quad (B.11)$$

$$Q_{rad,off} = \varepsilon_2 \sigma A_2 T_2^4 \quad (B.12)$$

Where:

$$\sigma (J / sm^2 K^4) = \text{Stefan - Boltzman constant}$$

Using these equations to fill into equation (B.7), leads to the following nonlinear differential equation:

$$-\frac{\partial}{\partial x} \left(k \frac{\partial T}{\partial x} \right) + \varepsilon_2 A_2 q_{inc,1} - \varepsilon_2 \sigma A_2 T_2^4 = 0 \quad \text{in } V(x) \quad (B.13)$$

For this equation the incident heat on the fiber optic cable needs to be solved by using equations (B.8), (B.9) and (B.10).

The non linear differential equation will be solved numerically in Matlab. For this reason the fiber optic cable needs to be discretized over its length. This means that it has to be divided into many small pieces. For equation (B.13) it was assumed that the temperature of the fiber is constant over the length of the fiber, but this is not true. After discretization, it is assumed that the view factors F_{12} , F_{21} , F_{23} and F_{32} are the same for all the elements. The radiation on the elements described in equations (B.11) and (B.12) can be rewritten into equations per element:

$$Q_{rad,on,i} = \varepsilon_2 A_i q_{inc,2i} \quad (B.14)$$

$$Q_{rad,off,i} = \varepsilon_2 \sigma A_i T_i^4 \quad (B.15)$$

Where:

- $A_i (m^2)$ = Outer surface of element i
 $T_i (K)$ = Temperature of element i
 $q_{inc,2i} (W / m^2)$ = Incident heat flux on element i
 $Q_{rad,on,i} (W)$ = Radiating heat entering element i
 $Q_{rad,off,i} (W)$ = Radiating heat leaving element i

The sum of all the incident heat on all the elements is equal to the total incident heat on the fiber optic cable.

$$q_{inc,2} = n_e \cdot q_{inc,2i} \quad (B.16)$$

Where:

$n_e (-)$ = Number of discretized elements

In Figure B-4 two elements are displayed with the heat flows acting on the elements. Note that the radiation is divided by two. Half of the radiation component acts on the left side of each element and the other half of the radiation component acts on the right side of each element. This accounts for the total radiation on and from the elements. Q_c is the conducted heat. It is assumed that the temperature over the elements is homogeneous.

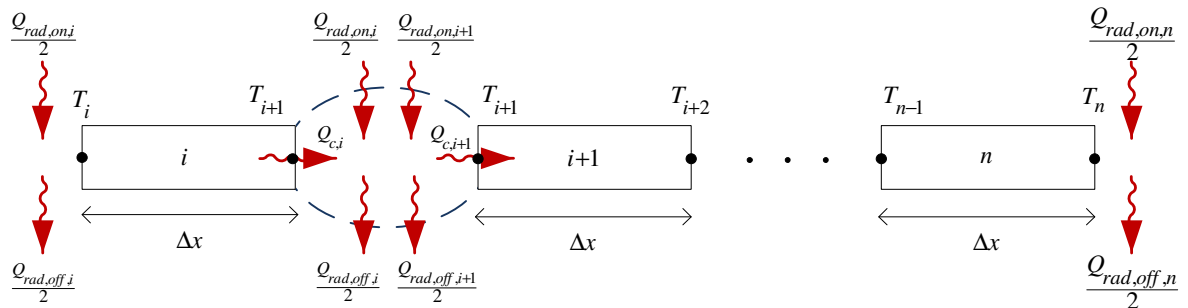


Figure B-4 Heat balance model for the discretized elements of the fiber optic cable

The heat equation can now be solved by making a heat balance on the nodes between the elements. In the next equation a heat balance is made on node T_{i+1} . At cryogenic temperatures, the coefficient of thermal conductivity is strongly dependent on temperature. Therefore, in this equation the coefficient of thermal conductivity is element dependent.

$$Q_{c,i} - Q_{c,i+1} + \left(\left(\frac{Q_{rad,on,i}}{2} + \frac{Q_{rad,on,i+1}}{2} \right) - \left(\frac{Q_{rad,off,i}}{2} + \frac{Q_{rad,off,i+1}}{2} \right) \right) = 0 \quad (B.17)$$

By using a discretized version of equation (B.3), the previous formula results in the next equation.

$$-k_i A_c \left(\frac{T_{i+1} - T_i}{\Delta x} \right) - \left(-k_{i+1} A_c \frac{T_{i+2} - T_{i+1}}{\Delta x} \right) + \left(\left(\frac{Q_{rad,on,i}}{2} + \frac{Q_{rad,on,i+1}}{2} \right) - \left(\frac{Q_{rad,off,i}}{2} + \frac{Q_{rad,off,i+1}}{2} \right) \right) = 0 \quad (B.18)$$

Where:

k_i (W / mK) = Thermal coefficient of conduction of element i

A_c (m²) = Cross section of the fiber optic cable

Δx (m) = Element length

The radiation acting on an element is determined by using the average temperature of an element.

$$Q_{rad,on,i} = \varepsilon_2 O \Delta x q_{inc,1i} \quad (B.19)$$

$$Q_{rad,off,i} = \varepsilon_2 \sigma O \Delta x (0,5(T_i + T_{i+1}))^4 \quad (B.20)$$

Where:

O (m) = Circumference of the fiber optic cable

The incident radiation per element can be rewritten by using equations (B.8), (B.9) and (B.10).

$$q_{inc,1i} = F_{21} \left(\varepsilon_2 \sigma (0,5(T_i + T_{i+1}))^4 + (1 - \varepsilon_2) q_{inc,2i} \right) + F_{31} \left(\frac{\varepsilon_3 \sigma T_3^4}{n_e} + (1 - \varepsilon_3) q_{inc,3i} \right) \quad (B.21)$$

$$q_{inc,2i} = F_{12} \left(\frac{\varepsilon_1 \sigma T_1^4}{n_e} + (1 - \varepsilon_1) q_{inc,1i} \right) + F_{32} \left(\frac{\varepsilon_3 \sigma T_3^4}{n_e} + (1 - \varepsilon_3) q_{inc,3i} \right) \quad (B.22)$$

$$q_{inc,3i} = F_{13} \left(\frac{\varepsilon_1 \sigma T_1^4}{n_e} + (1 - \varepsilon_1) q_{inc,1i} \right) + F_{23} \left(\varepsilon_2 \sigma (0,5(T_i + T_{i+1}))^4 + (1 - \varepsilon_2) q_{inc,2i} \right) \quad (B.23)$$

Rewriting these equations gives:

$$\begin{aligned}
 q_{inc,1i} - F_{21}(1-\varepsilon_2)q_{inc,2i} - F_{31}(1-\varepsilon_3)q_{inc,3i} - \left(F_{21}\varepsilon_2\sigma(0,5(T_i+T_{i+1}))^4 + F_{31}\frac{\varepsilon_3\sigma T_3^4}{n} \right) &= 0 \\
 -F_{12}(1-\varepsilon_1)q_{inc,1i} + q_{inc,2i} - F_{32}(1-\varepsilon_3)q_{inc,3i} - \left(F_{12}\frac{\varepsilon_1\sigma T_1^4}{n} + F_{32}\frac{\varepsilon_3\sigma T_3^4}{n} \right) &= 0 \\
 -F_{13}(1-\varepsilon_1)q_{inc,1i} - F_{23}(1-\varepsilon_2)q_{inc,2i} + q_{inc,3i} - \left(F_{13}\frac{\varepsilon_1\sigma T_1^4}{n} + F_{23}\varepsilon_2\sigma(0,5(T_i+T_{i+1}))^4 \right) &= 0
 \end{aligned}$$

By writing these equations into a matrix form, the following matrix is obtained:

$$\begin{bmatrix}
 1 & -F_{21}(1-\varepsilon_2) & -F_{31}(1-\varepsilon_3) & -\left(F_{21}\varepsilon_2\sigma(0,5(T_i+T_{i+1}))^4 + F_{31}\frac{\varepsilon_3\sigma T_3^4}{n} \right) \\
 -F_{12}(1-\varepsilon_1) & 1 & -F_{32}(1-\varepsilon_3) & -\left(F_{12}\frac{\varepsilon_1\sigma T_1^4}{n} + F_{32}\frac{\varepsilon_3\sigma T_3^4}{n} \right) \\
 -F_{13}(1-\varepsilon_1) & -F_{23}(1-\varepsilon_2) & 1 & -\left(F_{13}\frac{\varepsilon_1\sigma T_1^4}{n} + F_{23}\varepsilon_2\sigma(0,5(T_i+T_{i+1}))^4 \right)
 \end{bmatrix} \quad (B.24)$$

Combining equations (B.18), (B.19) and (B.20) into one single equation gives the final function f that needs to be solved numerically.

$$\begin{aligned}
 f = & -k_i A_c \left(\frac{T_{i+1} - T_i}{\Delta x} \right) - \left(-k_{i+1} A_c \frac{T_{i+2} - T_{i+1}}{\Delta x} \right) + \\
 & \left((0,5\varepsilon_2 O \Delta x q_{inc,2i} + 0,5\varepsilon_2 O \Delta x q_{inc,2i+1}) - (0,5\varepsilon_2 \sigma O \Delta x (0,5(T_i+T_{i+1}))^4 + 0,5\varepsilon_2 \sigma O \Delta x (0,5(T_{i+1}+T_{i+2}))^4) \right) = 0 \quad (B.25)
 \end{aligned}$$

Performing row operations until row reduced echelon form is obtained gives the incident heat by radiation on the three surfaces described by the model shown in Figure B-2. By applying the solutions for the incident radiation on all the fiber elements in equation (B.25), the final equations for all the elements described in function f needs to be solved numerically. With the assumption that the thermal conductivity is constant the heat equation f can be rewritten into the next form:

$$f = f(T_1, T_2, \dots, T_n) \quad (B.26)$$

If the thermal conductivity is not constant but a function of the temperature and the elements consist of two different materials, then the discretized model must be changed.

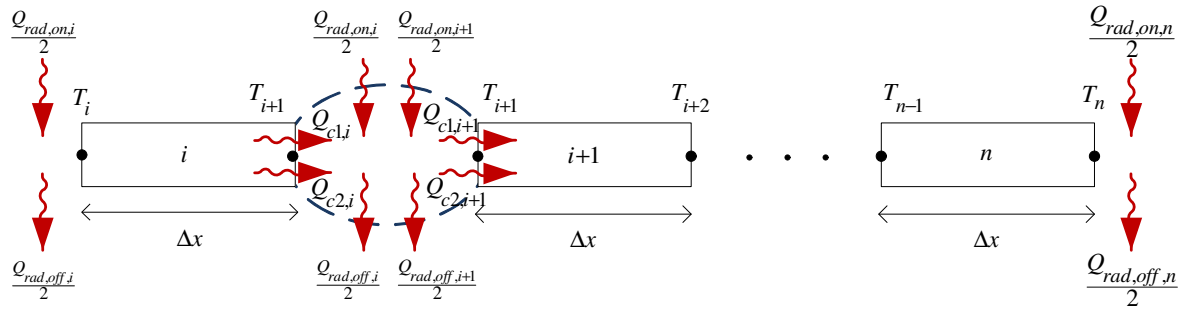


Figure B-5 Heat balance model for the discretized elements of the fiber optic cable, where the elements consist of two types of materials

The thermal conductivity of materials at cryogenic temperatures is dependent of the temperature. This can be written as:

$$k_{1i} = k_1(T_i) \quad \text{and} \quad k_{2i} = k_2(T_i) \tag{B.27}$$

The thermal conductivity of Polyimide $k_1(T_i)$ as a function of the temperature is shown in Figure B-6. It is assumed that Polyimide has the same thermal conductivity as Acrylate. Acrylate is the material that the fiber coating is made of.

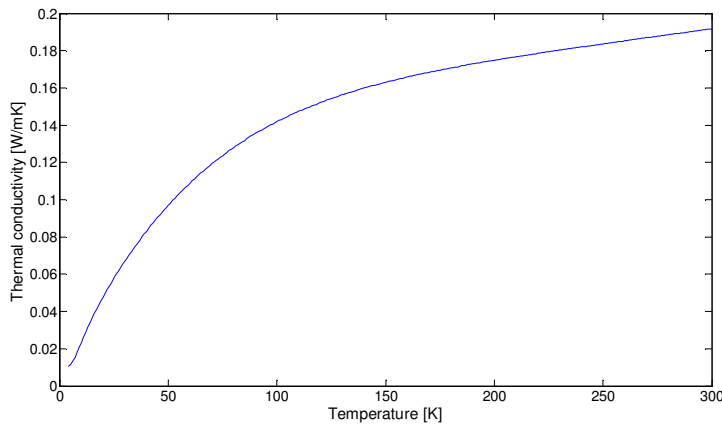


Figure B-6 Temperature dependent thermal conductivity of Polyimide [31]

The thermal conductivity of Pyrex $k_2(T_i)$ as a function of the temperature is shown in Figure B-7.

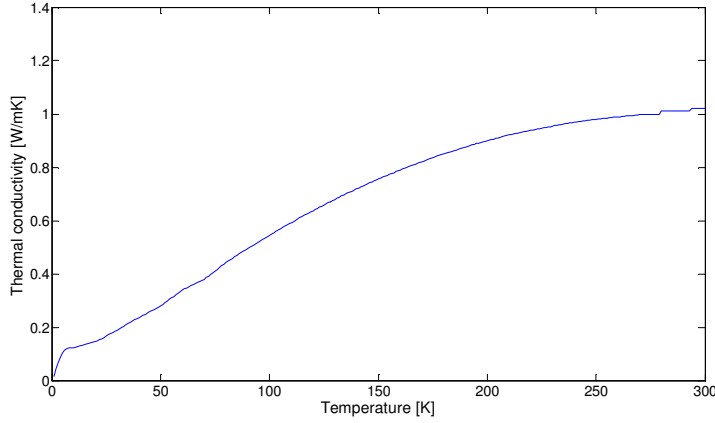


Figure B-7 Temperature dependent thermal conductivity of Pyrex [31]

From the previous graphs it can be concluded that it is not valid to choose a constant thermal conductivity determined at room temperature. An average thermal conductivity has been chosen for the two materials between a temperature of 4.5 (K) and 30 (K).

$$k_{ave} = \frac{A_{coating} \cdot k_1(17(K)) + A_{cladding} \cdot k_2(17(K))}{A_{coating} + A_{cladding}} \quad (B.28)$$

For a constant thermal conductivity the final equation for f becomes:

$$f = -k_{ave} A_c \left(\frac{T_{i+1} - T_i}{\Delta x} \right) - \left(-k_{ave} A_c \frac{T_{i+2} - T_{i+1}}{\Delta x} \right) + \left((0,5\varepsilon_2 O \Delta x q_{inc,2i} + 0,5\varepsilon_2 O \Delta x q_{inc,2i+1}) - (0,5\varepsilon_2 \sigma O \Delta x (0,5(T_i + T_{i+1}))^4 + 0,5\varepsilon_2 \sigma O \Delta x (0,5(T_{i+1} + T_{i+2}))^4) \right) = 0 \quad (B.29)$$

The heat transfer by conduction described in equation (B.17) becomes:

$$Q_{c1,i} = -0,5(k_{1i} + k_{1i+1}) A_{c1} \left(\frac{T_{i+1} - T_i}{\Delta x} \right) \quad (B.30)$$

$$Q_{c2,i} = -0,5(k_{2i} + k_{2i+1}) A_{c2} \left(\frac{T_{i+1} - T_i}{\Delta x} \right) \quad (B.31)$$

The thermal conductivity of the cladding of the fiber is assumed to be constant. The value $k_2(17(K))$ for the thermal conductivity has been used. Therefore equation (B.31) can be simplified to the next equation.

$$Q_{c2,i} = -k_2(17(K)) A_{c2} \left(\frac{T_{i+1} - T_i}{\Delta x} \right) \quad (B.32)$$

Rewriting equation (B.25) gives the equation for a thermal conductivity dependent on the temperature.

$$f = -0,5(k_{i+1} + k_{i+1})A_c \left(\frac{T_{i+1} - T_i}{\Delta x} \right) - \left(-k_2(17(K))A_c \frac{T_{i+2} - T_{i+1}}{\Delta x} \right) + \left((0,5\varepsilon_2 O \Delta x q_{inc,2i} + 0,5\varepsilon_2 O \Delta x q_{inc,2i+1}) - (0,5\varepsilon_2 \sigma O \Delta x (0,5(T_i + T_{i+1}))^4 + 0,5\varepsilon_2 \sigma O \Delta x (0,5(T_{i+1} + T_{i+2}))^4) \right) = 0 \quad (B.33)$$

The nonlinear equations for all the elements described in equation (B.29) for a constant average thermal conductivity and the non linear equations for a variable thermal conductivity described in equation (B.33) will be solved by using a Newton–Raphson iteration [10].

Consider a system of n equations:

$$\begin{aligned} f_1(x_1, x_2, \dots, x_n) &= 0 \\ f_2(x_1, x_2, \dots, x_n) &= 0 \\ &\vdots \\ f_n(x_1, x_2, \dots, x_n) &= 0 \end{aligned}$$

By taking the Taylor series expansion p to the first order over some estimate point $(x_{1k}, x_{2k}, \dots, x_{nk})$ rearrange it in a matrix-vector form, and then solve for (x_1, x_2, \dots, x_n) gives:

$$\begin{bmatrix} x_{1,k+1} \\ x_{2,k+1} \\ \vdots \\ x_{n,k+1} \end{bmatrix} = \begin{bmatrix} x_{1k} \\ x_{2k} \\ \vdots \\ x_{nk} \end{bmatrix} - \begin{bmatrix} \frac{\partial f_1}{\partial x_1} & \frac{\partial f_1}{\partial x_2} & \cdots & \frac{\partial f_1}{\partial x_n} \\ \frac{\partial f_2}{\partial x_1} & \frac{\partial f_2}{\partial x_2} & \cdots & \frac{\partial f_2}{\partial x_n} \\ \vdots & \vdots & \ddots & \vdots \\ \frac{\partial f_n}{\partial x_1} & \frac{\partial f_n}{\partial x_2} & \cdots & \frac{\partial f_n}{\partial x_n} \end{bmatrix}_{(x_{1k}, x_{2k}, \dots, x_{nk})}^{-1} \begin{bmatrix} f_1(x_{1k}, x_{2k}, \dots, x_{nk}) \\ f_2(x_{1k}, x_{2k}, \dots, x_{nk}) \\ \vdots \\ f_n(x_{1k}, x_{2k}, \dots, x_{nk}) \end{bmatrix} \quad (B.34)$$

And this could be rewritten to [10]:

$$\mathbf{x}_{k+1} = \mathbf{x}_k - \mathbf{J}_k^{-1} \mathbf{f}(\mathbf{x}_k) \quad \text{with} \quad \mathbf{J}_k(m, n) = \left[\frac{\partial f_m}{\partial x_n} \right]_{x_k} \quad (B.35)$$

Equation (B.35) will be used to solve the non linear equations.

Explanation Matlab code

Consider the case when the number of elements $n_e=5$. By using equation (B.36) the next vectors could be written.

$$\mathbf{x}_1 = \begin{bmatrix} x(1) \\ x(2) \\ x(3) \\ x(4) \\ x(5) \end{bmatrix} \quad \mathbf{f}(\mathbf{x}_1) = D = \begin{bmatrix} \text{formule}(T_{start}, x(1), x(2)) \\ \text{formule}(x(1), x(2), x(3)) \\ \text{formule}(x(2), x(3), x(4)) \\ \text{formule}(x(3), x(4), x(5)) \\ \text{formule}(x(4), x(5), T_{end}) \end{bmatrix}$$

Where "formule" a function is written in Matlab that uses equation (B.29) or equation (B.33). Now the Jacobian matrix is filled into the next matrix.

$$\mathbf{J}_k(\mathbf{x}_1) = C = \begin{bmatrix} \text{diff}2(T_{start}, x(1), x(2)) & \text{diff}3(T_{start}, x(1), x(2)) & 0 & 0 & 0 \\ \text{diff}1(x(1), x(2), x(3)) & \text{diff}2(x(1), x(2), x(3)) & \text{diff}3(x(1), x(2), x(3)) & 0 & 0 \\ 0 & \text{diff}1(x(2), x(3), x(4)) & \text{diff}2(x(2), x(3), x(4)) & \text{diff}3(x(2), x(3), x(4)) & 0 \\ 0 & 0 & \text{diff}1(x(3), x(4), x(5)) & \text{diff}2(x(3), x(4), x(5)) & \text{diff}3(x(3), x(4), x(5)) \\ 0 & 0 & 0 & \text{diff}1(x(4), x(5), T_{end}) & \text{diff}2(x(4), x(5), T_{end}) \end{bmatrix}$$

With "diff1", "diff2" and "diff3" as functions written in Matlab. In the m-file xx is used instead of x. Iterating for the next temperature according to the following relation:

$$\mathbf{x}_2 = \mathbf{x}_1 - \mathbf{J}_1^{-1} \mathbf{f}(\mathbf{x}_1)$$

Iterating until the vector \mathbf{x}_k converges gives the final vector \mathbf{x} that contains the temperature over the length of the fiber optic cable.

Results

The used parameters for the simulation can be found in the m-file "inputparameters.m". Combined with the functions written in Matlab: "formule.m", "diff1.m", "diff2.m", "diff3.m" and "tempiteratie.m" the temperature distribution over the fiber is numerically solved.

The temperature distribution over the fiber optic cable is shown in Figure B-8 for the two described situations.

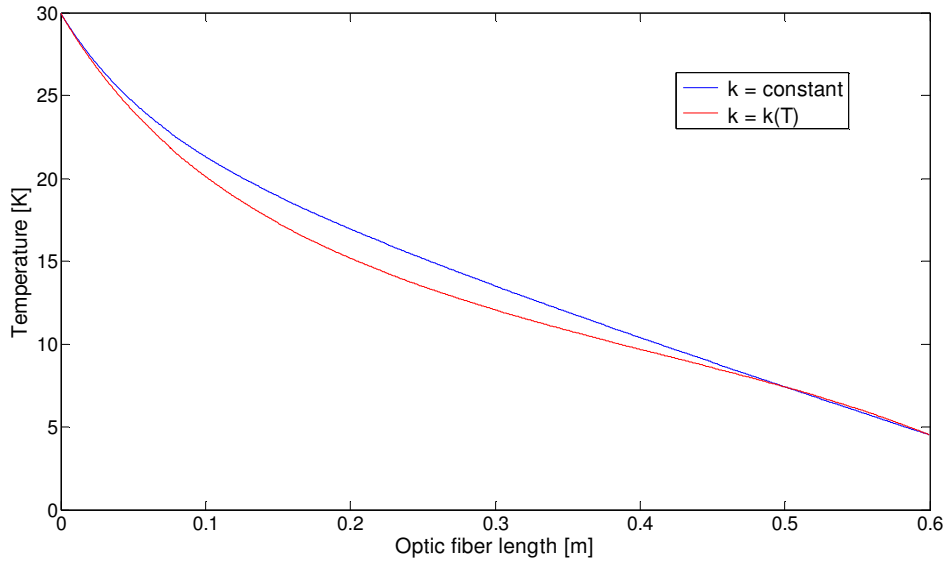


Figure B-8 Simulated temperature distributions for the scenario when the thermal conductivity is constant and for the scenario when the thermal conductivity is a function of the temperature

For both cases of the thermal conductivity the temperature distribution on the end of the fiber is almost the same. By applying (B.4) for the last elements next to the cryogenic cooled wall of 4.5 (K), the results for both temperature distributions are obtained. The thermal conductivities that has been used for the calculation of the heat transferred by the fiber respectively are calculated according to equation (B.28) and by using $k_1(4.5 \text{ (K)})$. The results of these calculations are given below.

$$\begin{aligned} \dot{Q}_{\text{fiber}} &= 1.7 (\mu\text{W}) & \text{for } k &= 0,069 (\text{W/mK}) \\ \dot{Q}_{\text{fiber}} &= 0.3 (\mu\text{W}) & \text{for } k &= k_1 (4.5 \text{ (K)}) = 0,01104 (\text{W/mK}) \end{aligned}$$

Validation

It has been assumed that an average constant thermal coefficient of conductivity could be used for Pyrex. The cross section of the coating is much larger than the cross section of the cladding of the fiber optic cable, but the thermal coefficient of conductivity of the cladding is higher than the conductivity of the coating.

$$\begin{aligned} A_{\text{coating}} &= 7.73 \cdot 10^{-7} (\text{m}^2) & \text{and } k_1 (4.5 \text{ (K)}) &= 0.011 (\text{W / mK}) \\ A_{\text{cladding}} &= 1.23 \cdot 10^{-8} (\text{m}^2) & \text{and } k_2 (4.5 \text{ (K)}) &= 0.089 (\text{W / mK}) \end{aligned}$$

According to equation (B.4) the conducted heat is proportional to the parameter Ak . And the product of these two parameters gives the following result.

$$A_{\text{coating}} k_1 = 8.3 \cdot 10^{-9} \text{ (Wm / K)}$$

$$A_{\text{cladding}} k_1 = 1.1 \cdot 10^{-9} \text{ (Wm / K)}$$

From this result it can be concluded that most of the conducted heat will go through the coating and not through the cladding. Therefore it is a valid assumption to assume that an average constant thermal coefficient of conductivity for Pyrex could be used.

B.2 Laser power loss

Introduction

In order to determine the value of the signals at the photodiodes and to determine how much power will be lost in certain optical components, the laser power needs to be determined on different components within the system.

A model will be made for the laser power losses within the system. For each part the parameters that determine the optical losses will be looked up in the datasheets and will then be used to determine the power losses within the fiber optic interferometer.

Assumptions

- The insertion loss is defined by the maximal loss of each component
- Between the connector and the photodiode there are no losses
- All losses are valid for a temperature of 20 degrees Celsius
- Cross talk in the system is neglected

Modeling

Consider the system model of sensing in Figure B-9. The model consists of several blocks. These blocks represent different subsystems within the interferometer. When laser light travels through a certain subsystem a part of the light gets transmitted through the subsystem and a part of the light is lost within the subsystem. The power attenuation within a subsystem is described by equation (B.36).

$$P_{out} = P_{in} A_{IL} \quad \text{or} \quad P_{out} = 10^{A_{dB}/10} P_{in} \quad (\text{B.36})$$

Where:

$P_{in} (W)$ = Optical power on the input of the subsystem

$P_{out} (W)$ = Optical power on the output of the subsystem

$A_{IL} (-)$ = Attenuation of the subsystem due to insertion loss

$A_{IL} (dB)$ = Attenuation of the subsystem due to insertion loss in dB

The power loss in a subsystem can be determined with the formula for the attenuation given in (B.36). By using this equation the following relation can be obtained.

$$P_{loss} = P_{in} - P_{out} \quad (\text{B.37})$$

Where:

$P_{loss} (W)$ = Optical power lost in a subsystem

For the attenuation of the splitter, equation (2.1) can be applied. The power transformation matrix for the splitter used in the old system configuration is determined with the data from appendix G.6. Using equation (2.1) results in the next formula for the attenuation of the splitter to the outputs:



$$P_{sp.out} = \begin{bmatrix} P_{bl} \\ P_{or} \\ P_{wh} \end{bmatrix} = \begin{bmatrix} T_{11} & T_{12} & T_{13} \\ T_{21} & T_{22} & T_{23} \\ T_{31} & T_{32} & T_{33} \end{bmatrix} \begin{bmatrix} P_{bl} \\ P_{or} \\ P_{wh} \end{bmatrix} = \begin{bmatrix} 0.318 & 0.357 & 0.259 \\ 0.301 & 0.305 & 0.318 \\ 0.352 & 0.305 & 0.280 \end{bmatrix} \begin{bmatrix} P_{bl} \\ P_{or} \\ P_{wh} \end{bmatrix}$$

Where:

$P_{bl}(W)$ = Optical power in the blue cable

$P_{or}(W)$ = Optical power in the orange cable

$P_{wh}(W)$ = Optical power in the white cable

Result

The attenuations that are used for the model given in Figure B-9 are summarized in Table B-1. The values in Table B-1 are obtained from the datasheets of all the optical components. The datasheets can be found in Appendix G. Note that for the photodiode the responsivity (A/W) is used instead of the insertion loss.

Table B-1 Insertion losses of all optical components used in the initial system configuration of the fiber optic interferometer

Information source	Component	Name	Insertion loss (dB)
Datasheet connector	Connector	A2,A6,A11,A15,A20,A24,A28	0.40
Test datasheet circulator	Circulator 1-2	A4	1.10
Test datasheet circulator	Circulator 2-3	A4	1.10
Datasheet fiber optic cable	End stop	A9	82.20
Meas. from Baas BV	Ref. mirror	A13	0.22
Meas. from Technobis	Grin lens	A17	0.36
Datasheet photodiode	Photodiode	A22,A26,A30	0.22
Approximation	Meas. mirror	A18	0.22
Datasheet fiber optic cable	Cable	A1,A3,A5,A7,A8,A10,A12,A14,A16,A19,A21,A23,A25,A27,A29	0.0042
Test datasheet 3x3 splitter	3x3 Splitter	white => white	5.53
		white => orange	4.97
		white => blue	5.87
		orange => white	5.16
		orange => orange	5.16
		orange => blue	4.47
		blue => white	4.53
		blue => orange	5.21
		blue => blue	4.97

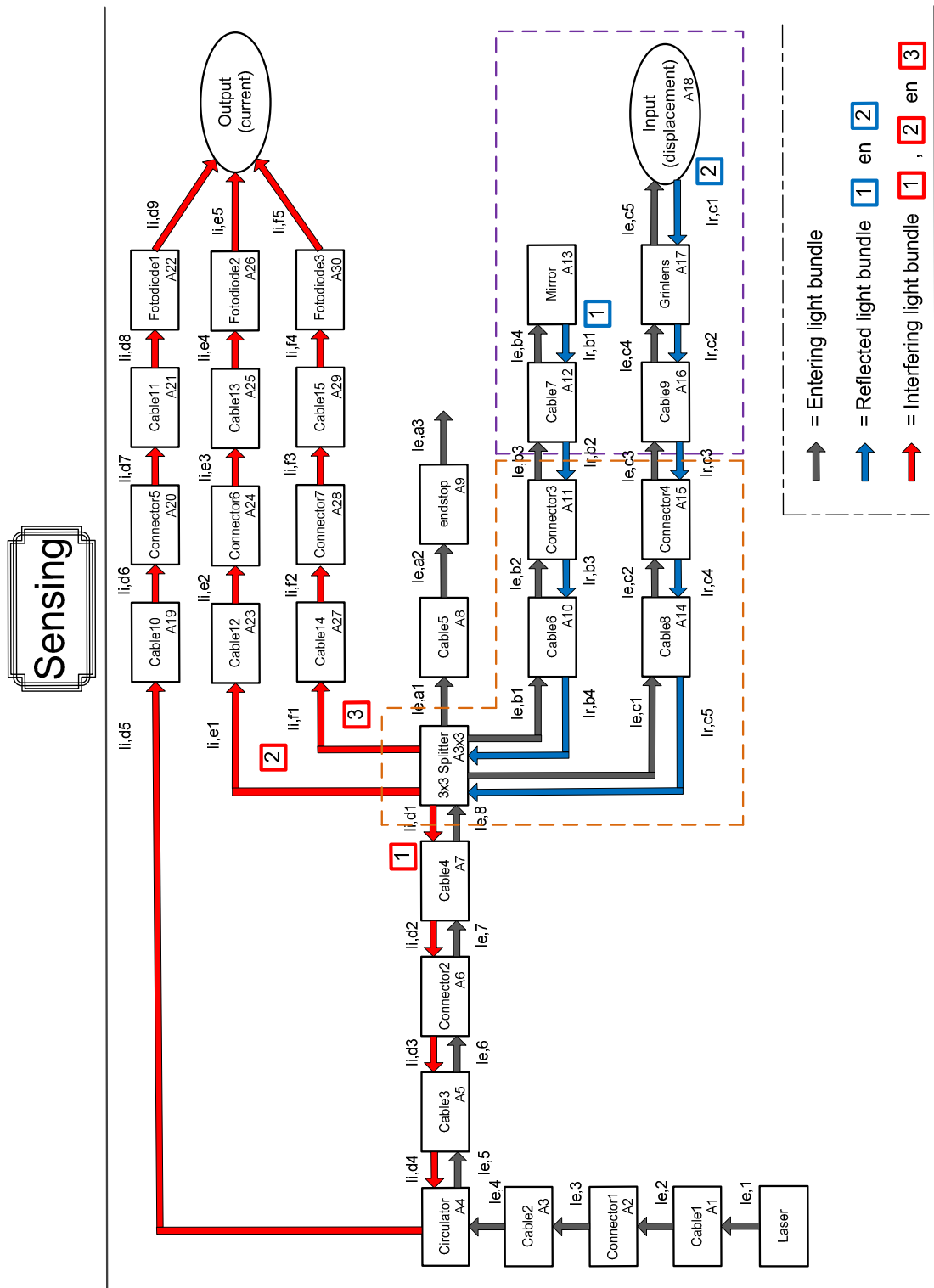


Figure B-9 Sensing model of the fiber optic interferometer, containing the attenuation, the power inputs and power outputs of all optical components in variable form.

Table B-2 Calculated optical power at different locations pointed out in Figure B-9. Entering light

	$P_{\text{laser}}(\mu\text{W})$	$P_{\text{loss}}(\mu\text{W})$		$P_{\text{laser}}(\mu\text{W})$	$P_{\text{loss}}(\mu\text{W})$		$P_{\text{laser}}(\mu\text{W})$	$P_{\text{loss}}(\mu\text{W})$
$I_{e,1}$	1000.0	0.0						
$I_{e,2}$	999.0	1.0						
$I_{e,3}$	911.1	87.9						
$I_{e,4}$	910.2	0.9						
$I_{e,5}$	706.6	203.7						
$I_{e,6}$	705.9	0.7						
$I_{e,7}$	643.8	62.1						
$I_{e,8}$	643.2	0.6						
or. ⁽¹⁾	$P_{\text{laser}}(\mu\text{W})$	$P_{\text{loss}}(\mu\text{W})$	bl. ⁽¹⁾	$P_{\text{laser}}(\mu\text{W})$	$P_{\text{loss}}(\mu\text{W})$	wh. ⁽¹⁾	$P_{\text{laser}}(\mu\text{W})$	$P_{\text{loss}}(\mu\text{W})$
$I_{e,a1}$ ⁽²⁾	193.8	17.9	$I_{e,b1}$ ⁽²⁾	204.8	17.9	$I_{e,c1}$ ⁽²⁾	226,6	17.9
$I_{e,a2}$	193.6	0.2	$I_{e,b2}$	204.6	0.2	$I_{e,c2}$	226,4	0.2
$I_{e,a3}$	0.0	193.6	$I_{e,b3}$	186.6	18.0	$I_{e,c3}$	206,5	19.9
			$I_{e,b4}$	186.4	0.2	$I_{e,c4}$	206,3	0.2
						$I_{e,c5}$	194,1	12.2

Reflected light

bl. ⁽¹⁾	$P_{\text{laser}}(\mu\text{W})$	$P_{\text{loss}}(\mu\text{W})$	wh. ⁽¹⁾	$P_{\text{laser}}(\mu\text{W})$	$P_{\text{loss}}(\mu\text{W})$
$I_{r,b1}$	177.1	9.3	$I_{r,c1}$	184.4	9.7
$I_{r,b2}$	176.9	0.2	$I_{r,c2}$	173.3	11.1
$I_{r,b3}$	161.4	15.6	$I_{r,c3}$	173.2	0.2
$I_{r,b4}$	161.2	0.2	$I_{r,c4}$	157.9	15.2
			$I_{r,c5}$	157.8	0.2

Interfering light

bl. ⁽¹⁾	$P_{\text{laser}}(\mu\text{W})$	$P_{\text{loss}}(\mu\text{W})$	wh. ⁽¹⁾	$P_{\text{laser}}(\mu\text{W})$	$P_{\text{loss}}(\mu\text{W})$	or. ⁽¹⁾	$P_{\text{laser}}(\mu\text{W})$	$P_{\text{loss}}(\mu\text{W})$
$I_{i,d1}$ ⁽²⁾	92.2	27.0	$I_{i,e1}$ ⁽²⁾	101.0	27.0	$I_{i,f1}$ ⁽²⁾	98.8	27.0
$I_{i,d2}$	92.1	0.1	$I_{i,e2}$	100.9	0.1	$I_{i,f2}$	98.7	0.1
$I_{i,d3}$	84.0	8.1	$I_{i,e3}$	92.0	8.9	$I_{i,f3}$	90.0	8.7
$I_{i,d4}$	83.9	0.1	$I_{i,e4}$	91.9	0.1	$I_{i,f4}$	89.9	0.1
$I_{i,d5}$	65.1	18.8						
$I_{i,d6}$	65.1	0.1						
$I_{i,d7}$	59.3	5.7						
$I_{i,d8}$	59.3	0.1						

Output current

bl. ⁽¹⁾	$I(\mu\text{A})$	wh. ⁽¹⁾	$I(\mu\text{A})$	or. ⁽¹⁾	$I(\mu\text{A})$
$I_{i,d9}$	56.3	$I_{i,e5}$	87.3	$I_{i,f5}$	85.4

Power loss in 4,5K zone (μW)	
Meas. arm + ref. arm	Meas. arm + ref. arm + 3x3 splitter
43.0	157.4

¹⁾ The splitter loss after entering and exiting is the accumulated loss for all three cables.

²⁾ The splitter has different losses depending on the color of the cable. These are blue, white and orange.

The power loss inside the 4.5 (K) zone is calculated for two configurations of the fiber optic interferometer:

Configuration 1:

The measurement arm and the reference arm inside the 4.5 (K) zone.

Configuration 2:

The measurement arm, the reference arm and the 3x3 splitter inside the 4.5 (K) zone.

For configuration 1, the optical power loss within the cryogenic cooled zone is given in Figure B-10 below.

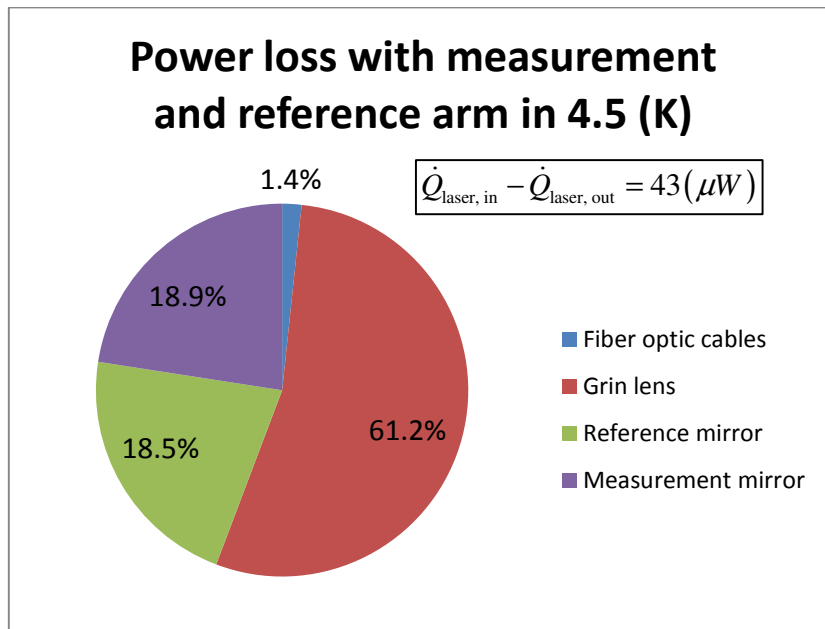


Figure B-10 Distribution of the optical power loss of all the parts within the measurement arm and the reference arm in the cryogenic cooled zone of 4.5 (K)

For configuration 1, where not only the measurement arm and the reference arm are placed within the cryogenically cooled zone of 4.5 (K), the optical power loss of the laser is determined again. Note that in the end stop a lot of power is lost. In order to prevent this power from being unleashed in the cryogenically cooled zone of 4.5 (K), the end stop should be placed outside of the 4.5 (K) zone.

If a laser input power of 0.1 (mW) is used instead of 1 (mW). The result of the optical power loss is represented in Figure B-11.

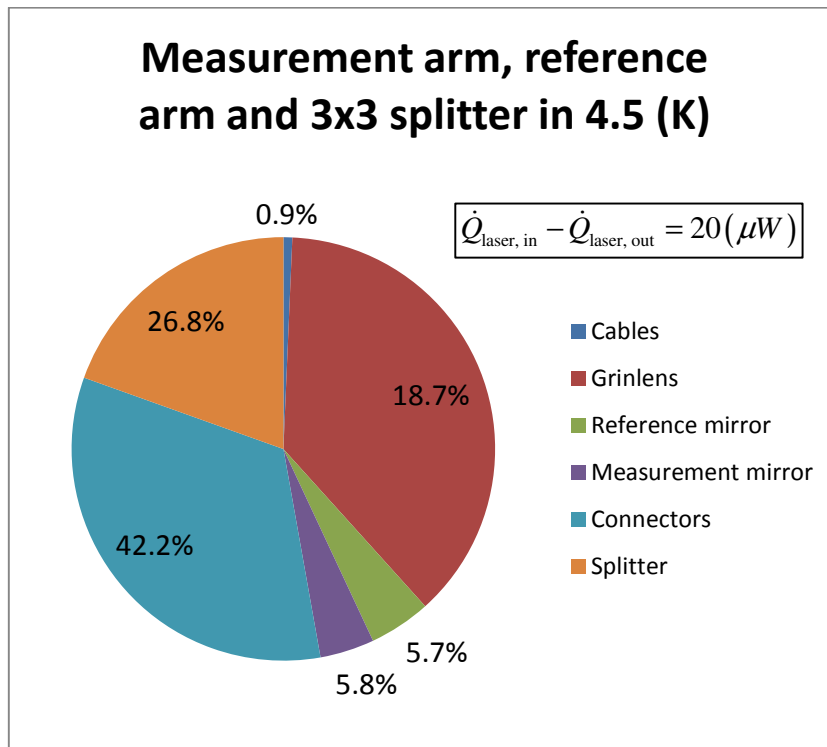


Figure B-11 Distribution of the laser power loss of all the parts within the measurement arm, the reference arm and the 3x3 splitter in the cryogenically cooled zone of 4.5 (K)

Discussion

For the calculations with the reflection of the measurement and reference mirror a reflection coefficient of 95 percent was used. These values seemed realistic values for standard optic components, but unfortunately the components used in the initial system configuration had a lower reflection coefficient.

Appendix C Algorithm

C.1 Wave superposition

The superposition of waves of the same frequency is described in [3]. A solution of the differential wave equation can be written in the form:

$$E(x, t) = E_0 \sin[\omega t - (kx_{OPD} + \varepsilon_i)] \quad (C.1)$$

Where:

$E_0 (N/C)$ = Amplitude of the harmonic disturbance

$\omega (rad/s)$ = Wave frequency

$t (s)$ = Time

$k (-)$ = Wave number

$x_{OPD} (m)$ = Distance from the source of the wave to the point of observation

$\varepsilon_i (rad)$ = Initial phase at the emitter

For the wave number there can be written:

$$k = \frac{2\pi}{\lambda} \quad (C.2)$$

To separate the time and space parts of the phase there can be written

$$\alpha(x, t) = -(kx_{OPD} + \varepsilon_i) \quad (C.3)$$

Consider two different waves that propagate away from the point of observation, located in the origin.

$$\varphi = (kx_1 + \varepsilon_1) - (kx_2 + \varepsilon_2)$$

$$\varphi = k(x_1 - x_2) + (\varepsilon_{i1} - \varepsilon_{i2})$$

With:

$$\varphi = \frac{2\pi}{\lambda}(x_1 - x_2) + (\varepsilon_{i1} - \varepsilon_{i2}) \quad (C.4)$$

Where:

$\lambda(m)$ = Wavelength

$\varphi(rad)$ = Phase

If the waves are initially in phase at their respective emitters: $\varepsilon_{i1} = \varepsilon_{i2}$

$$\varphi = \frac{2\pi}{\lambda}(x_1 - x_2) \quad (C.5)$$

In practice when the fiber optic interferometer is started up the initial phase is set to zero, so that the same result is obtained as in equation (C.5). The optical path difference OPD between the two travelling waves in the interferometer could be written in the next form if there is taken into account that the light travels twice the difference of the displacements of the two waves:

$$x_{OPD} = 2(x_1 - x_2) \quad (C.6)$$

Then the final result for the displacement as a function of the phase of the interference pattern could be written as:

$$x_{OPD} = \frac{\lambda\varphi}{4\pi n} \quad (C.7)$$

Where:

$n(-)$ = Refractive index of the waveguide

The refractive index in vacuum is equal to one. In air however it is almost equal to one. For some calculations in this report it is approximated that the refractive index in air is equal to one ($n_{air} \approx 1$). In this case the next formula applies.

$$x_{OPD} = \frac{\lambda\varphi}{4\pi} \quad (C.8)$$

C.2 Clarke transform

The magnitude of the currents produced by the photodiodes each have an absolute phase difference of 120° with respect to each other. This is due to the main working principle of the 3x3 splitter. The currents are given in the next formulas:

$$I_1(OPD) = A_1 \left(1 + V_1 \cos \left(\frac{2\pi}{\lambda} OPD \right) \right) \quad (C.9)$$

$$I_2(OPD) = A_2 \left(1 + V_2 \cos \left(\frac{2\pi}{\lambda} OPD + \frac{2\pi}{3} \right) \right) \quad (C.10)$$

$$I_3(OPD) = A_3 \left(1 + V_3 \cos \left(\frac{2\pi}{\lambda} OPD + \frac{4\pi}{3} \right) \right) \quad (C.11)$$

Where:

$I(A)$ = Current signal

$A(A)$ = Current offset

$V(-)$ = Visibility or contrast

In order to reduce the error caused by the different offsets and amplitudes of the signals, the signals need to be calibrated [7]. Therefore the offsets of the signals needs to be deleted and the amplitudes need to be normalized to a value of one. Of course the calibration should be performed while losing as little information of the signal as possible. After calibration the signal I_1 becomes I_s , I_2 becomes I_+ and I_3 becomes I_- . The result for the calibrated three currents is written in the next three formulas:

$$I_s(OPD) = A_0 \left(1 + V_0 \cos \left(\frac{2\pi}{\lambda} OPD \right) \right) \quad (C.12)$$

$$I_+(OPD) = A_0 \left(1 + V_0 \cos \left(\frac{2\pi}{\lambda} OPD + \frac{2\pi}{3} \right) \right) \quad (C.13)$$

$$I_-(OPD) = A_0 \left(1 + V_0 \cos \left(\frac{2\pi}{\lambda} OPD + \frac{4\pi}{3} \right) \right) \quad (C.14)$$

Where:

$A_0(A)$ = Calibrated current offset

$V_0(-)$ = Calibrated visibility or the calibrated contrast

By projecting these formulas to a complex reference frame the three signals all consist of a real part and an imaginary part. Transformation to a complex reference frame can be written in a matrix transformation. In electrical engineering this transformation is known as the Clarke transform or a $\alpha\beta\gamma$ -transformation. This transformation is also known as sin-cos processing, this is because the projection basically consists of taking the sine of the phase of the three signals, which gives the horizontal component of the projection and the cosine of the phase of the three signals, which gives the vertical component of the projection. In this way a so called quadrature relationship of the signals is obtained. Applying this transformation to the equations (C.12), (C.13) and (C.14) is performed below.

$$\begin{bmatrix} I_{Re} \\ I_{Im} \end{bmatrix} = A_0 \begin{bmatrix} \cos(0) & \cos\left(\frac{2\pi}{3}\right) & \cos\left(\frac{4\pi}{3}\right) \\ \sin(0) & \sin\left(\frac{2\pi}{3}\right) & \sin\left(\frac{4\pi}{3}\right) \end{bmatrix} \cdot \begin{bmatrix} I_s \\ I_+ \\ I_- \end{bmatrix}$$

$$\begin{bmatrix} I_{Re} \\ I_{Im} \end{bmatrix} = A_0 \begin{bmatrix} 1 & -\frac{1}{2} & -\frac{1}{2} \\ 0 & \frac{1}{2}\sqrt{3} & -\frac{1}{2}\sqrt{3} \end{bmatrix} \cdot \begin{bmatrix} I_s \\ I_+ \\ I_- \end{bmatrix} = \frac{1}{2} A_0 \begin{bmatrix} 2 & -1 & -1 \\ 0 & \sqrt{3} & -\sqrt{3} \end{bmatrix} \cdot \begin{bmatrix} I_s \\ I_+ \\ I_- \end{bmatrix}$$

The final projection becomes:

$$\begin{bmatrix} I_{Re} \\ I_{Im} \end{bmatrix} = \frac{1}{2} A_0 \begin{bmatrix} 2 & -1 & -1 \\ 0 & \sqrt{3} & -\sqrt{3} \end{bmatrix} \cdot \begin{bmatrix} I_s \\ I_+ \\ I_- \end{bmatrix} \quad (C.15)$$

Where:

$I_{Re}(A)$ = Real component of the projection

$I_{Im}(A)$ = Complex component of the projection

The three projections of the signals on the complex plane are displayed in Figure C-1.

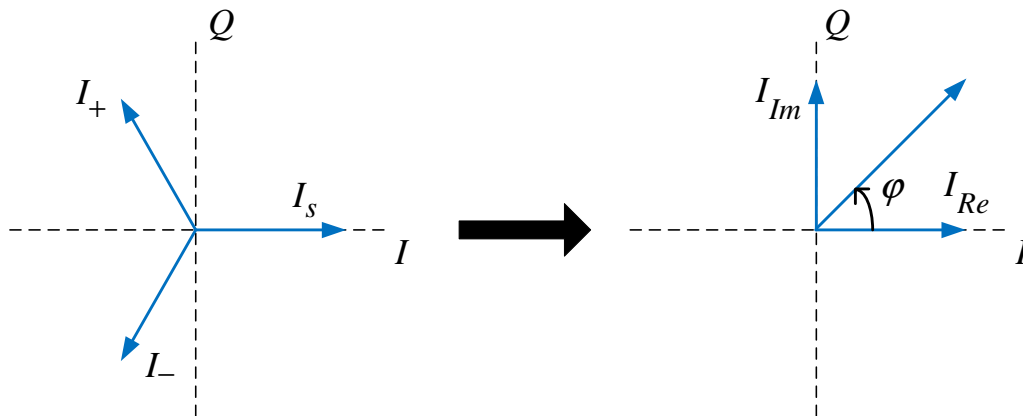


Figure C-1 Phase diagram of the three photodiode signals with 120 degrees phase difference with respect to each other, displayed in a Q-S plane. These signals are projected on the same plane after a Clarke transformation or sin-cos processing

The argument of the complex vector corresponds to the phase of the projection of the intensities in the complex plane and can be determined geometrically.

$$\varphi = \left| \arctan \left(\frac{I_{Im}}{I_{Re}} \right) \right| \quad (C.16)$$

Plugging in the relation obtained in (C.16) into (C.8) gives:

$$\varphi = \left| \arctan \left(\sqrt{3} \frac{I_+ - I_-}{2I_s - (I_+ + I_-)} \right) \right| \quad (C.17)$$

With equation (C.17) the phase can be determined that is a measure for the displacement of the moving mirror. This formula is applied in the algorithm of the electronics and software made by SRON.



C.3 Detector signal

Introduction

With the results obtained in appendix B.2 the current signals produced by the three photodiodes will be determined in this appendix. The calibrated signals of these three currents will also be determined. These signals are required for further calculation of the errors of the measured mirror position.

Assumptions

- The laser power and the visibility of the three ideal signals at the photodiodes are determined for the situation where no other disturbances influence the signal.
- The photodiode readout can be simplified to a single transimpedance amplifier and a first order active low pass filter.
- ADC doesn't clip.

Modeling

For certain calculations on the accuracy of the measurement system it is required to predict what the laser power and the visibility of the three ideal signals will be at the photodiodes if no other disturbances influence the signal. The three signals all consist of the interference pattern between the reflected light of the measurement mirror and the reference mirror. In the splitter and after the splitter the phase of the three signals has been changed with respect to each other. The offset and the amplitude of the three signals are different from each other as a consequence of the difference in attenuation or each signal exiting the splitter. Between the splitter and the detector the signals also have a different attenuation. Photocurrents are the currents created by the photodiodes. The ratio of the measurement signal over the reference signal after the splitter will be the same as on the photodiode. This relation is used in combination with the calculated photocurrents to determine the signals at the detector.

Next example one of the three cables after the splitter leading the detector is considered to be P_1 . For the attenuation of the splitter, (2.1) can be applied.

$$P_{sp,out} = \begin{bmatrix} P_1 \\ P_2 \\ P_3 \end{bmatrix} = \begin{bmatrix} T_{11} & T_{12} & T_{13} \\ T_{21} & T_{22} & T_{23} \\ T_{31} & T_{32} & T_{33} \end{bmatrix} \begin{bmatrix} P_{meas} \\ P_{ref} \\ 0 \end{bmatrix} = \begin{bmatrix} 0.318 & 0.357 & 0.259 \\ 0.301 & 0.305 & 0.318 \\ 0.352 & 0.305 & 0.280 \end{bmatrix} \begin{bmatrix} P_{meas} \\ P_{ref} \\ 0 \end{bmatrix}$$

Where:

$P_{\text{meas}}(W)$ = Power of the laser returned from the measurement arm

$P_{\text{ref}}(W)$ = Power of the laser returned from the reference arm

$P_1(W)$ = Power of the laser in detector arm 1

$P_2(W)$ = Power of the laser in detector arm 2

$P_3(W)$ = Power of the laser in detector arm 3

The signal within P_1 consists of an interference pattern of two signals.

$$P_1 = P_{1,\text{meas}} + P_{1,\text{ref}} \quad (\text{C.18})$$

Where:

$P_{1,\text{meas}}(W)$ = Laser power returned from the measurement arm in detector arm 1

$P_{1,\text{ref}}(W)$ = Power of the laser returned from the reference arm in detector arm 1

If these two signals are calculated separately before they interfere, then the equations (C.19) and (C.20) could be written for the visibility and the laser power of the signal at photodiode 1 described in equation (4.16). If the maximal value of this signal results from constructive interference the next equation can be written:

$$P_{1,\text{ref}} + P_{1,\text{meas}} = A_1 + A_1V_1 \quad (\text{C.19})$$

Similar if the minimal value of this signal results from destructive interference in the case that the signal from the reference arm is bigger than the signal from the measurement arm the next equation can be written:

$$P_{1,\text{ref}} - P_{1,\text{meas}} = A_1 - A_1V_1 \quad (\text{C.20})$$

Solving equations (C.19) and (C.20) for the visibility and the laser power results in the next equations:

$$A_1 = P_{1,\text{ref}} \quad (\text{C.21})$$

And:

$$V_1 = \frac{P_{1,\text{meas}}}{P_{1,\text{ref}}} \quad (\text{C.22})$$

For the current at the photodiodes the following relation can be written.

$$A_1 V_1 + A_1 = I_{\text{photo},1} \quad (\text{C.23})$$

As mentioned before, the ratio of the laser power and visibility does not change by the attenuation of the light in the detector arm. With this ratio the visibility and the laser power can be calculated at all the photodiodes using the following formula.

$$\frac{A_1}{V_1} = r_1 \quad (\text{C.24})$$

From the results displayed in Table B-2 the exact values of the currents on the three photodiodes and the power of the two interfering signals after the splitter can be obtained. Combining equations (C.23) and (C.24) for the given returned laser power in the reference arm and the measurement arm results in the next values.

$$P_{\text{ref}} = 161.2 (\mu\text{W})$$

$$P_{\text{meas}} = 157.8 (\mu\text{W})$$

Table C-1 Parameters for the calculated current signals defined by equations (C.9),(C.10) and (C.11).

Photocurrent	Current offset	Visibility of the contrast
$I_{\text{photo},1} = 56.3 (\mu\text{A})$	$A_1 = 32.4 (\mu\text{A})$	$V_1 = 0.74$
$I_{\text{photo},2} = 87.3 (\mu\text{A})$	$A_1 = 44.5 (\mu\text{A})$	$V_1 = 0.96$
$I_{\text{photo},3} = 85.4 (\mu\text{A})$	$A_1 = 48.3 (\mu\text{A})$	$V_1 = 0.77$

For noise calculations it is desired to express the signals generated in the photodiodes in rms currents. The rms values of the signals at the photodiodes can be determined with equation (C.25). This equation could also be used for signal 2 and 3.

$$I_{\text{rms},1} = \frac{\text{Amp}}{\sqrt{2}} = \frac{A_1 V_1}{\sqrt{2}} \quad (\text{C.25})$$

Where:

$\text{Amp}(A)$ = Amplitude of the signal

$I_{\text{rms},1}(A_{\text{rms}})$ = Rms current amplitude of the signal

This gives:

$$I_{1,\text{rms}} = \frac{A_1 V_1}{\sqrt{2}} = 16.9(\mu\text{A})$$

$$I_{2,\text{rms}} = \frac{A_2 V_2}{\sqrt{2}} = 30.3(\mu\text{A})$$

$$I_{3,\text{rms}} = \frac{A_3 V_3}{\sqrt{2}} = 26.2(\mu\text{A})$$

The maximal voltages at the ADC can be determined taking the gains of the transimpedance amplifier and the gain of the low pass filter into account.

$$V_{\text{max}} = I_{\text{photo}} G_{\text{trans}} G_{\text{filter}} \quad (\text{C.26})$$

Where:

V_{max} (V) = Maximal voltage at the ADC

I_{photo} (A) = Current created in the photodiode

G_{trans} (V/A) = Gain of the transimpedance amplifier

G_{filter} (V/V) = Gain of the low pass filter

The gains for equation (C.26) are determined with the electrical scheme displayed in Figure C-2 and the component values given in Table C-2.

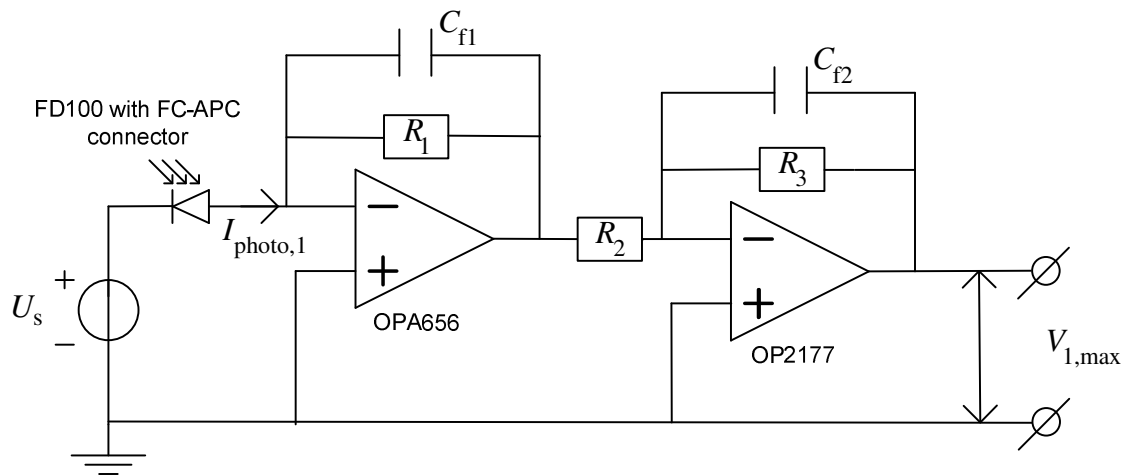


Figure C-2 Simplified electrical scheme used for the photodiode readout in the detector system.

The resistor and capacitor values used in Figure C-2 are given in the table below.

Table C-2 Values of the electrical components used in Figure C-2

Component	R_1	R_2	R_3	C_{f1}	C_{f2}
Value	12.4 (k Ω)	3.33 (k Ω)	10 (k Ω)	1 (pF)	680 (pF)

The gains described in equation (C.26) are:

$$G_{\text{trans}} = R_1 = 12.4 \cdot 10^3 (V / A)$$

$$G_{\text{filter}} = \frac{R_3}{R_2} = 3 (V / V)$$

Applying equation (C.26) results in the following maximal voltages at the ADC.

$$V_{1,\text{max}} = 2.38 (V)$$

$$V_{2,\text{max}} = 3.68 (V)$$

$$V_{3,\text{max}} = 3.64 (V)$$

The range of the ADC is 0-3 Volts so a few signals at the ADC will clip. For now it is assumed that the ADC won't clip.

A plot of the three voltage signals resulting from equations (4.16), (4.17) and (4.18) for a mirror moving at constant velocity is shown in Figure C-3.

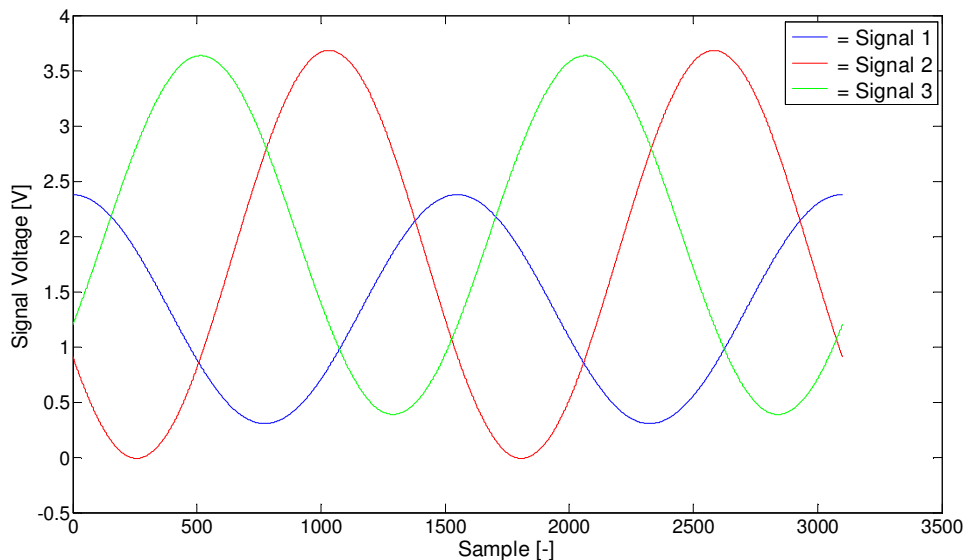


Figure C-3 Non-calibrated simulated signals in the ADC for a mirror moving with constant velocity

Similar to the current signals described in equations (C.27), (C.28) and (C.29) now at the ADC three voltage signals are obtained.

$$U_1(OPD) = A_{v1} \left(1 + V_{v1} \cos \left(\frac{2\pi}{\lambda} OPD \right) \right) \quad (C.27)$$

$$U_2(OPD) = A_{v2} \left(1 + V_{v2} \cos \left(\frac{2\pi}{\lambda} OPD + \frac{2\pi}{3} \right) \right) \quad (C.28)$$

$$U_3(OPD) = A_{v3} \left(1 + V_{v3} \cos \left(\frac{2\pi}{\lambda} OPD + \frac{4\pi}{3} \right) \right) \quad (C.29)$$

For calibration of the voltage signals described in equations (C.27), (C.28) and (C.29) the next equation is applied:

$$U_c(OPD) = \frac{(U(OPD) - A_v)}{A_v V_v} \quad (C.30)$$

Where:

$U_c(V)$ = Calibrated voltage signal

$U(V)$ = Voltage signal at the ADC

$A_v(V)$ = Voltage offset of the voltage signal at the ADC

$V_v(-)$ = Visibility of the voltage signal at the ADC

Rewriting this equation in Matlab results in the next algorithm:

$$U_c(OPD) = \frac{U(OPD) - \frac{1}{2} [\max(U(OPD)) + \min(U(OPD))]}{\frac{1}{2} [\max(U(OPD)) - \min(U(OPD))]} \quad (C.31)$$

Performing the calibration on the three voltage signals at the ADC, results in the three signals below. After calibration the signal U_1 becomes U_s , U_2 becomes U_+ and U_3 becomes U_- .

$$U_s(OPD) = A_0 \left(1 + V_0 \cos \left(\frac{2\pi}{\lambda} OPD \right) \right) \quad (C.32)$$

$$U_+(OPD) = A_0 \left(1 + V_0 \cos \left(\frac{2\pi}{\lambda} OPD + \frac{2\pi}{3} \right) \right) \quad (C.33)$$

$$U_-(OPD) = A_0 \left(1 + V_0 \cos \left(\frac{2\pi}{\lambda} OPD + \frac{4\pi}{3} \right) \right) \quad (C.34)$$

A plot of these three signals is shown in Figure C-4 below:

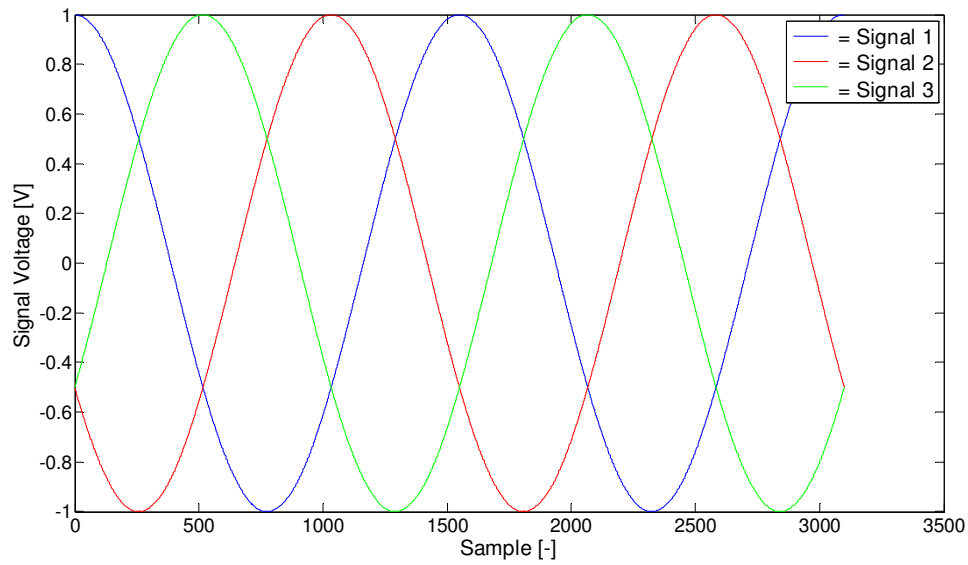


Figure C-4 Calibrated simulated signals in the ADC for a mirror moving with constant velocity

C.4 Interference signal

The Poynting vector is described by:

$$\vec{S} = c^2 \epsilon_0 \vec{E} \times \vec{B} \quad (\text{C.35})$$

The magnitude of \vec{S} is the power per unit area crossing a surface whose normal is parallel to \vec{S} .

Now consider a linear polarized harmonic plane wave of an electric field and a magnetic field traveling through free space in the direction of \vec{k} :

$$\vec{E} = \vec{E}_0 \cos(\vec{k} \cdot \vec{r} - \omega t) \quad (\text{C.36})$$

$$\vec{B} = \vec{B}_0 \cos(\vec{k} \cdot \vec{r} - \omega t) \quad (\text{C.37})$$

Now filling in the equations (C.36) and (C.37) into (C.35) results into the next equation, that describes the instantaneous flow of energy per unit area per unit time.

$$\vec{S} = c^2 \epsilon_0 \vec{E}_0 \times \vec{B}_0 \cos^2(\vec{k} \cdot \vec{r} - \omega t) \quad (\text{C.38})$$

The irradiance is defined as the average energy per unit area per unit time. The time averaged value of the magnitude of the Poynting vector, symbolized by $\langle S \rangle_T$, is a measure of the irradiance. Over a time interval T that is much larger than the period τ of the electromagnetic wave ($T \gg \tau$) there could be written:

$$I \equiv \langle S \rangle_T = \frac{c^2 \epsilon_0}{2} |\vec{E}_0 \times \vec{B}_0| \quad (\text{C.39})$$

The previous equation could be written, because the next two relations are valid.

$$\frac{1}{T} \int_{t-T/2}^{t+T/2} \cos^2(\vec{k} \cdot \vec{r} - \omega t) dt = \frac{1}{2} \quad \text{for } (T \gg \tau)$$

$$|\mathbf{E}| = c|\mathbf{B}|$$

The irradiance is proportional to the square of the electric field. An alternative way of describing equation (C.39) as a function of the electric field is given below.

$$I = c \epsilon_0 \langle E^2 \rangle_T \quad (\text{C.40})$$

Consider now the superposition of two electromagnetic waves that are out of phase by $k\Delta x$ radians. The parameter Δx could be considered as the OPD of the two waves. Figure C-5 that is shown below, shows two these waves.

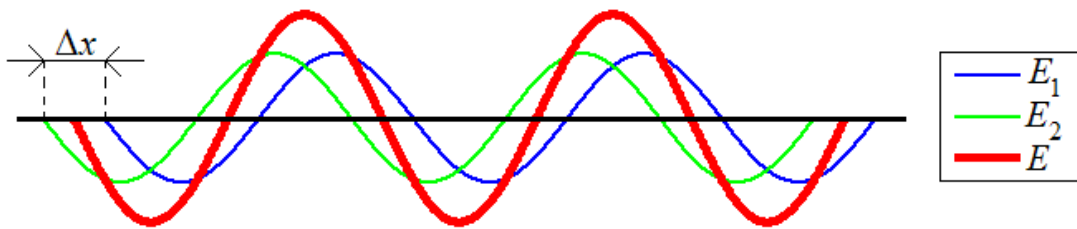


Figure C-5 Interference of two electromagnetic waves

The two waves are described by the next two equations.

$$E_1(x, t) = E_{01} \sin(\omega t - k(x + \Delta x)) \quad (C.41)$$

$$E_2(x, t) = E_{01} \sin(\omega t - kx) \quad (C.42)$$

Where:

$\Delta x(m)$ = Optical path difference

It now the amplitudes of the waves have the same magnitude and the difference between the space parts of the phase of the waves is defined by $k\Delta x$ as shown below:

$$E_{01} = E_{02} \quad \text{and} \quad \alpha_2 - \alpha_1 = k\Delta x$$

Then by combining equations (C.43), (C.44), (D.34) and (D.35) and taking the assumptions mentioned above into account it can be proven that the resultant wave is described in equation (C.43) For this the next trigonometric relation is used:

$$\sin \beta - \sin \gamma = 2 \cos \frac{1}{2}(\beta - \gamma) \sin \frac{1}{2}(\beta + \gamma)$$

The resultant wave is described below.

$$E = 2E_{01} \cos\left(\frac{k\Delta x}{2}\right) \sin\left[\omega t - k\left(x + \frac{\Delta x}{2}\right)\right] \quad (C.43)$$

The irradiance of the resultant wave described in equation (C.40) can be determined by combining equation (C.40) and (C.43). This leads to the next result.

$$\begin{aligned}
I_i &= c\epsilon_0 \langle E^2 \rangle_T \\
I_i &= c\epsilon_0 \left\langle \left(2E_{01} \cos\left(\frac{k\Delta x}{2}\right) \sin\left[\omega t - k\left(x + \frac{\Delta x}{2}\right)\right] \right)^2 \right\rangle_T \\
I_i &= c\epsilon_0 \left(2E_{01} \cos\left(\frac{k\Delta x}{2}\right) \right)^2 \left\langle \left(\sin\left[\omega t - k\left(x + \frac{\Delta x}{2}\right)\right] \right)^2 \right\rangle_T \\
I_i &= \frac{1}{2} c\epsilon_0 \left(4E_{01}^2 \cos^2\left(\frac{k\Delta x}{2}\right) \right)
\end{aligned}$$

Rewriting the result obtained above gives:

$$I_i = 2c\epsilon_0 E_{01}^2 \cos^2\left(\frac{k\Delta x}{2}\right) \quad (\text{C.44})$$

In general there is defined

$$k = \frac{2\pi}{\lambda} \quad \text{and} \quad \Delta x = OPD$$

Filling this in into equation (C.44) gives:

$$I_i = 2c\epsilon_0 E_{01}^2 \left[\cos^2\left(\frac{2\pi}{\lambda} \frac{OPD}{2}\right) \right] \quad (\text{C.45})$$

By using the next trigonometric relation the irradiance could be rewritten:

$$\begin{aligned}
\cos^2 A &= \frac{1}{2} + \frac{1}{2} \cos 2A \\
I_i &= 2c\epsilon_0 E_{01}^2 \left[\cos^2\left(\frac{2\pi}{\lambda} \frac{OPD}{2}\right) \right] \\
I_i &= 2c\epsilon_0 E_{01}^2 \left[\frac{1}{2} + \frac{1}{2} \cos\left(\frac{2\pi}{\lambda} OPD\right) \right] \\
I_i &= c\epsilon_0 E_{01}^2 \left[1 + \cos\left(\frac{2\pi}{\lambda} OPD\right) \right] \quad (\text{C.46})
\end{aligned}$$

The equation below is the relation for the signal at the three photodiodes obtained from SRON; it seemed that this relation is not implemented correctly in the software by SRON.

$$I_s(x) = A_0 \left(1 + V_0 \cos\left(\frac{2\pi}{\lambda} x\right) \right)$$

The parameter x should be replaced by OPD.

Appendix D Errors

D.1 Intensity noise

Introduction

Due to the presence of noise, the signals that are used for the algorithm to determine the displacement deviate from the mean measured value and this causes an uncertainty in the measurement. This uncertainty can be expressed as a factor that influences the precision of the mirror position.

In the content of this report by intensity noise there is meant; the noise on the detected signal that seems to be a fluctuation of the intensity of the signal. This includes all different noise sources that have an effect on the value of the processed signal into the algorithm, except for phase noise of the laser.

In this paragraph the effect of intensity noise on three simulated signals from appendix C.3 will be modeled. By comparing these noise signals to ideal signals the effect of the intensity noise on the precision of the measured mirror position is estimated.

Assumptions

- The noise sources are assumed to be white; this means that they have a constant voltage spectral density (VSD) over the entire frequency spectrum
- The influence of the diode capacitance and resistance is neglected
- Active electronic components of analogue electronics besides the active first order low pass filter don't affect the VSD of the noise
- The influence of noise and/or jitter on the digital electronics is negligible
- Other noise sources besides intensity noise are neglected
- It is assumed that the filter transfer functions are the same for all three signals
- The dark current of the photodiode is neglected
- The temperature of the electronics is assumed to be at room temperature. That is 293 (K).
- The maximal signal voltage at the ADC is equal to the peak to peak voltage
- Phase of the three signals is not affected by the filters

Modeling

Noise must be treated as power, so the sum of two uncorrelated noise sources is a superposition of the powers. The resulting value for the power dissipated in a resistor is P_{tot} . The voltages over an impedance or voltage sources in series are called v_{tot} and currents through an impedance or parallel current sources are called i_{tot} .

$$P_{tot} = P_1 + P_2 \tag{D.1}$$

For the total noise voltage there can be written:

$$v_{tot} = \sqrt{v_1^2 + v_2^2 + \dots + v_n^2} \quad (D.2)$$

And for the total noise current:

$$i_{tot} = \sqrt{i_1^2 + i_2^2 + \dots + i_n^2} \quad (D.3)$$

Where

$v_n (V_{rms})$ = Rms noise voltage

$i_n (A_{rms})$ = Rms noise current

The relation between Power spectral density and the voltage spectral density is given in equation (D.4).

$$PSD = VSD^2 \quad (D.4)$$

Where:

$PSD (V^2 / Hz)$ = Power spectral density

$VSD (V / \sqrt{Hz})$ = Voltage spectral density

The relation between the noise power and the noise power spectral density is described in relation (D.5) from [4].

$$CPS = \int_{0}^{f_B} PSD \cdot df \quad (D.5)$$

Where:

$CPS (W)$ = Cumulative power spectrum

$f_B (Hz)$ = Spectral bandwidth

In Figure D-1 a simplified model is made for the intensity noise generated within the analogue electronics for the detector system of the fiber optic interferometer based on [14] and [15]. Referring to Appendix C.3, the electronic schematic for the readout of signal 1 is modeled. It is assumed that all filter transfer functions are the same for each signal.

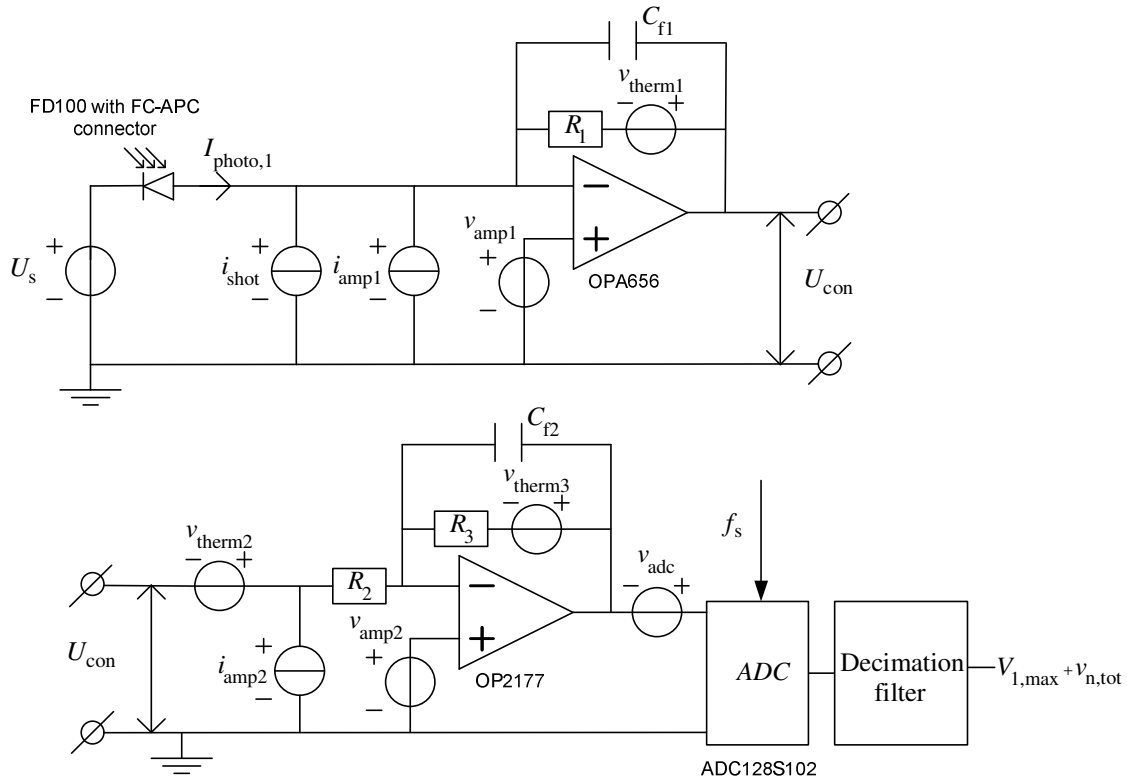


Figure D-1 Simplified intensity noise model of the analogue electronics based on the electronic circuit shown in Appendix A.1

The working principle of a decimation filter basically works as follows. A signal is oversampled and a low-pass anti-aliasing filter is applied. Then the bit stream exiting the ADC is averaged and down sampled. The filter takes n_s samples, adds the values together, and then divides them by n_s again. The difference equation is described in equation (D.6).

$$y[n] = \frac{1}{M} \sum_{k=0}^{M-1} x[n-k] \quad (\text{D.6})$$

Where:

$M(-)$ = Number of samples that are averaged

$n_s(-)$ = Sample number

Now a Discrete Time Fourier Transform (DTFT) is performed on equation (D.6). For a DTFT the next formula is used.

$$X(\Omega) = \sum_{n=-\infty}^{\infty} x[n] e^{-j\Omega n} \quad (\text{D.7})$$

Where:

Ω (rad / s) = Frequency in the digital domain

The DTFT of equation (D.6) results in:

$$Y(\Omega) = X(\Omega) \frac{1}{M} \sum_{k=0}^{M-1} e^{-j\Omega k} \quad (D.8)$$

Using this formula the following frequency response in the digital domain of the decimation filter can be obtained.

$$H_D(\Omega) = \frac{Y(\Omega)}{X(\Omega)} = \frac{1}{M} \sum_{k=0}^{M-1} e^{-j\Omega k} \quad (D.9)$$

Note that by applying a z-transform to the difference equation (D.6) and using relation (D.10) the same result should be obtained.

$$z^{-1} = e^{-j\Omega n} \quad (D.10)$$

The magnitude of the decimation filter $|H_D(\Omega)|$ described in (D.9) is shown in the figure below for a sample frequency of the ADC of 100 (kHz).

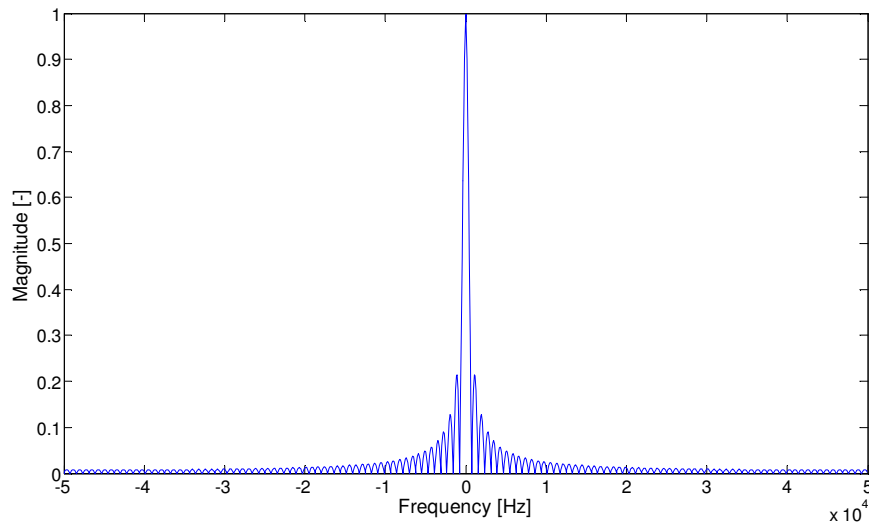


Figure D-2 Frequency response of the digital decimation filter

Off coarse only the positive frequencies of the decimation filter are considered. These are shown in a logarithmic plot below. Also indicated is the required sample frequency of 439 (Hz) in order to prevent aliasing.

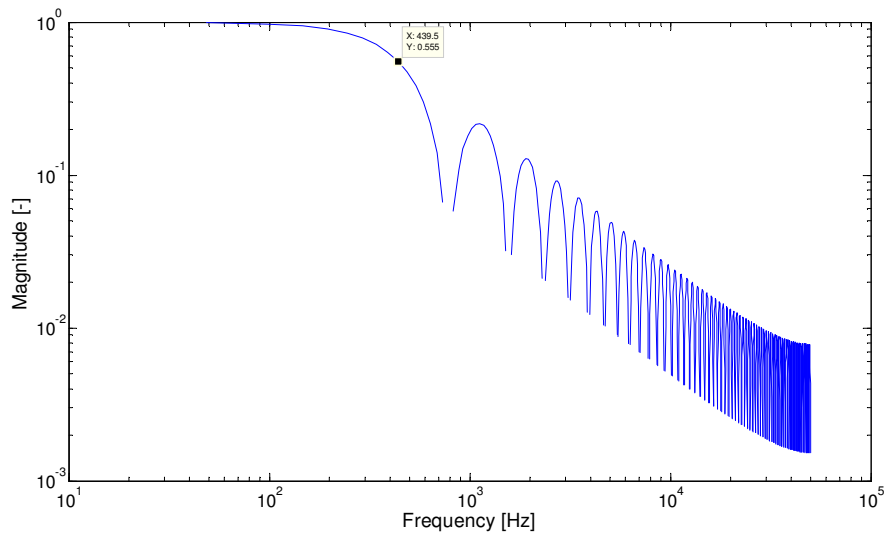


Figure D-3 Frequency response of the digital decimation filter plotted on a logarithmic scale

So basically a decimation filter effectively reduces the amount of noise by averaging. This effect could easily be illustrated by showing two PSD plots for a white noise source. When a PSD is plotted against the spectral bandwidth and the signal is sampled with sample frequency f_{s1} , then the area under the curve corresponds to the cumulative power spectrum of the noise. If now the signal is oversampled with a sample frequency f_{s2} , then the power spectral density of the noise is lower but the power of the noise is the same. It's just "spread out" over a larger bandwidth. If now an ideal digital low pass filter is applied at frequency $f_{s1} = f_F$, clearly the surface under the PSD curve is much less, depending on how much the signal is oversampled.

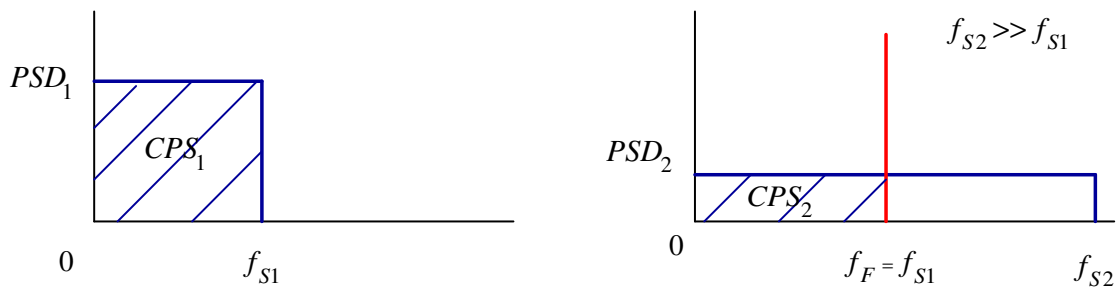


Figure D-4 Effect of oversampling and applying a digital low pass filter, on the power spectral density of a white noise source

The other filter used in Figure D-1 is an analogue first order active low pass filter. The transfer function for this filter is given below.

$$H_A(\omega) = \frac{R_3}{R_2} \frac{1}{(1 + R_3 C_{f2} \omega)} \quad (D.11)$$

The magnitude of this low pass filter $|H_A(\omega)|$ is shown in Figure D-5.

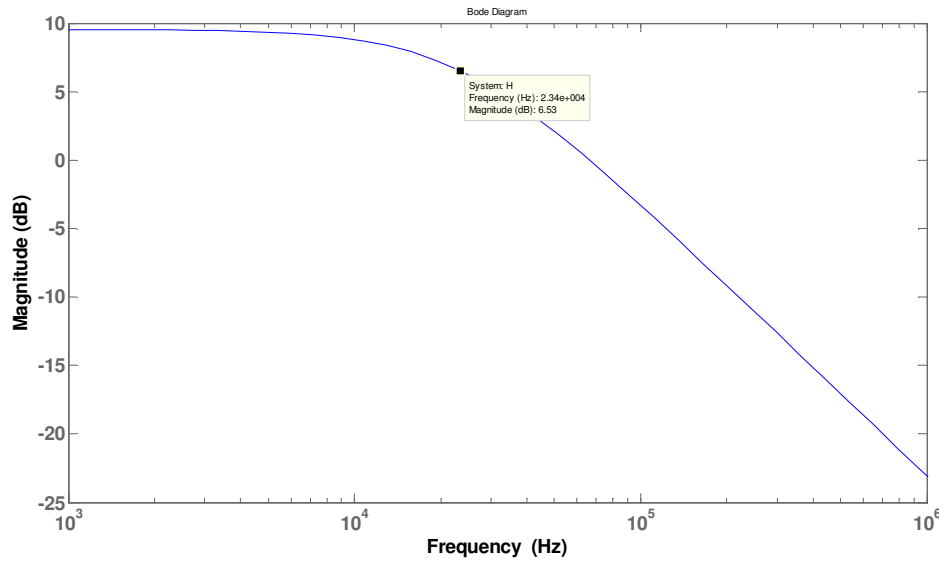


Figure D-5 Frequency response of the active first order analogue low pass filter

By combining equations (D.4) and (D.5) the cumulative power spectrum can be expressed as a function of the voltage- or current spectral densities of the different noise sources given in Figure D-1. This results in the next equation.

$$CPS = \int_0^{f_B} VSD^2 df \quad (D.12)$$

Because it is desired to know what the voltage root mean square value of the intensity noise is after the decimation filter, the cumulative amplitude spectrum at f_B can be used. This is at the fully cumulated end value [4]. The same conclusion could be taken when looking at the equivalent noise bandwidth [13].

$$CAS(f_B) = \sqrt{CPS(f_B)} \quad (D.13)$$

Where:

$CAS(V_{rms})$ = Cumulative amplitude spectrum

With this newly obtained relation, equation (D.12) can be rewritten into:

$$CAS(f_B) = \sqrt{\int_0^{f_B} VSD_{out}^2 df} \quad (D.14)$$

Where:

$VSD_{out} (V/\sqrt{Hz}) =$ Voltage spectral density on the output of the decimation filter

Now it needs to be determined what the spectral bandwidth of the noise is. The ADC samples the signal at 100 (kHz), but the digital filter only works until 50 (kHz). This is because of the next reason: "When sampling, the signal frequency is not allowed to contain frequencies above the Nyquist frequency" [4]. So as a consequence of this, the spectral bandwidth for the intensity noise is defined as:

$$f_B = \frac{f_{sample,ADC}}{2} = 50(kHz)$$

The different noise sources shown in Figure D-1 are all placed in the noise model at different points. For the effect of the filters on the voltage spectral density, two situations are described in Figure D-6. A VSD of a noise source entering before the analogue low pass filter and a VSD of a noise source entering after the analogue low pass filter.

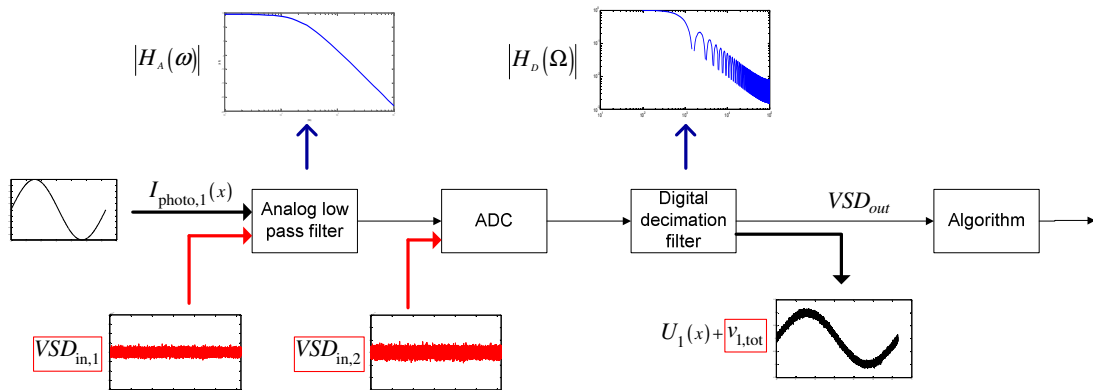


Figure D-6 Two given possible configurations for the noise VSD generated within the analogue electronics that affect the measured signal before it enters the algorithm. The plots in this figure are made for the signal from photocurrent 1.

The contribution of all the noise based sources on the total noise $v_{1,tot}$ on the voltage signal before the algorithm can be determined by calculating the effect of each noise source on the output separately.

$$v_{n,tot} = \sqrt{v_{n1}^2 + v_{n2}^2 + v_{n3}^2 + v_{n4}^2 + v_{n5}^2 + v_{n6}^2 + v_{n7}^2 + v_{n8}^2 + v_{n9}^2} \quad (D.15)$$

Where:

$v_{n,tot} (V_{rms})$ = Total noise contribution on the processed data signal on photodiode n

When reading out the photodiode different types of noise are generated within the readout. Some noise sources are specified in datasheets of the components and some noise sources need to be calculated. First the types of noise that need to be calculated are given. The first is thermal noise. Thermal noise arises from the thermally induced random motion of charge carriers like electrons. For the amount of thermal noise within a resistor equation (D.16) is given [12].

$$v_{therm} = \sqrt{4k_B T_R R} \quad (D.16)$$

Where:

$v_{therm} (V/\sqrt{Hz})$ = Thermal noise voltage spectral density

$k_B (J / K)$ = Boltzmann's constant = $1.380 \cdot 10^{-23} (J / K)$

$T_R (K)$ = Resistor temperature

$R (\Omega)$ = Electrical resistance

The shot noise results from the random passage of individual charge carriers across a potential barrier. The amount of shot noise generated within a photodiode is described in the next formula [12].

$$i_{shot} = \sqrt{2qI_{DC}} \quad (D.17)$$

Where:

$i_{shot} (A/\sqrt{Hz})$ = Shot noise current spectral density

$q (C)$ = Charge of the electron = $1,602 \cdot 10^{-19} (C)$

$I_{DC} (A)$ = Average DC diode current

Finally the quantization noise of an ADC is described by (D.18) according to [12] and [23].

$$v_{adc} = \frac{U_{signal}}{2^{n_{bits}} \sqrt{n_{bits} f_{s,adc}}} \quad (D.18)$$

Where:

$v_{adc} \left(\text{V}/\sqrt{\text{Hz}} \right)$ = Quantization noise voltage spectral density

$f_{s,adc} \left(\text{Hz} \right)$ = Sample frequency of the ADC

$n_{\text{bits}} (-)$ = Number of bits in the ADC

$U_{\text{signal}} \left(\text{V} \right)$ = Total peak to peak voltage range of the signal at the ADC

According to [14] and [15] the static amplification of noise $v_{\text{amp}2}$ through the analogue low pass filter can be written as:

$$v_{n6} = v_{\text{amp}2} \frac{R_2 + R_3}{R_2} \quad (\text{D.19})$$

Where:

$v_{\text{amp}2} \left(\text{V}/\sqrt{\text{Hz}} \right)$ = Amplifier 2 noise voltage spectral density

For this noise source the frequency dependent amplification by the analogue low pass filter can be rewritten.

$$v_{n6} = v_{\text{amp}2} \left(1 + |H_A(\omega)| \right) \quad (\text{D.20})$$

From the datasheet of the OPA656, the opamp used for the transimpedance amplifier, the VSD is shown in the next plot.

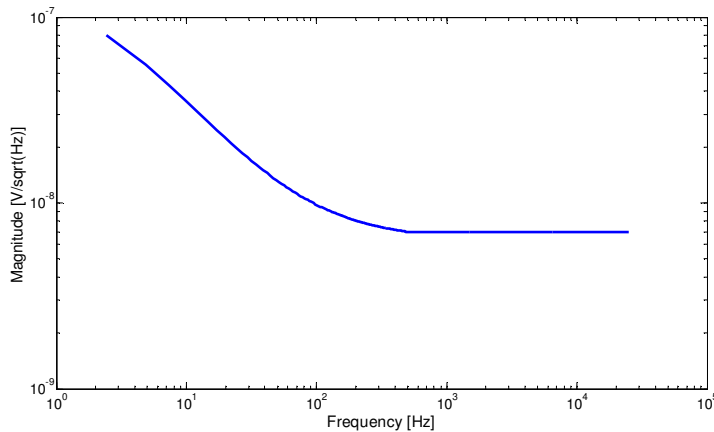


Figure D-7 Voltage spectral density of the voltage noise generated in the OPA656

The noise calculations for $v_{\text{amp}1}$ will be performed for the voltage spectral density shown in Figure D-7.

With all these given equations, the effect of each noise source displayed in Figure D-1 on the output of the decimation filter before the algorithm $v_{1,tot}$ can be modeled. This is done in Table D-1 below. The surroundings of the electronics will be at a temperature of 253 (K). For the calculation it is assumed that the temperature of the electronics is very high, 293(K), due to heating of the electronics. Furthermore it is assumed that the maximal signal voltage at the ADC is equal to the peak to peak voltage. Also the phase of the three signals is not affected by the filters, because the frequency of the fringe signals is the same, the phase shift due to filtering is also the same.

Table D-1 an overview of the contribution of all different intensity noise sources on the output voltage signal before the algorithm. These formulas are made for the readout of photodiode 1 and could also be applied to the readout of photodiodes 2 and 3

Noise source	Formula	Output noise
$i_{shot} = 5.3(pA/\sqrt{Hz})$	$v_{n1} = \sqrt{\int_{f_B} (\sqrt{2qI_{photo,1}R_1} H_A(\omega) H_D(\Omega))^2 df}$	$v_{n1} = 3.1(\mu V_{rms})$
$i_{amp1} = 1.3(fA/\sqrt{Hz})$	$v_{n2} = \sqrt{\int_{f_B} (i_{amp1}R_1 H_A(\omega) H_D(\Omega))^2 df}$	$v_{n2} = 0.001(\mu V_{rms})$
$v_{amp1} = 7.0(nV/\sqrt{Hz})$	$v_{n3} = \sqrt{\int_{f_B} (v_{amp1} H_A(\omega) H_D(\Omega))^2 df}$	$v_{n3} = 1.41(\mu V_{rms})$
$v_{therm1} = 14.2(nV/\sqrt{Hz})$	$v_{n4} = \sqrt{\int_{f_B} (\sqrt{4kTR_1} H_A(\omega) H_D(\Omega))^2 df}$	$v_{n4} = 0.84(\mu V_{rms})$
$i_{amp2} = 0.2(pA/\sqrt{Hz})$	$v_{n5} = \sqrt{\int_{f_B} (i_{amp2}R_2 H_A(\omega) H_D(\Omega))^2 df}$	$v_{n5} = 0.04(\mu V_{rms})$
$v_{amp2} = 7.9(nV/\sqrt{Hz})$	$v_{n6} = \sqrt{\int_{f_B} (v_{amp2} (1 + H_A(\omega)) H_D(\Omega))^2 df}$	$v_{n6} = 4.0(\mu V_{rms})$
$v_{therm2} = 7.3(nV/\sqrt{Hz})$	$v_{n7} = \sqrt{\int_{f_B} (\sqrt{4kTR_2} H_A(\omega) H_D(\Omega))^2 df}$	$v_{n7} = 0,43(\mu V_{rms})$
$v_{therm3} = 12.7(nV/\sqrt{Hz})$	$v_{n8} = \sqrt{\int_{f_B} (\sqrt{4kTR_3} H_D(\Omega))^2 df}$	$v_{n8} = 0.25(\mu V_{rms})$
$v_{adc} = 725(nV/\sqrt{Hz})$	$v_{n9} = \sqrt{\int_{f_B} \left(\frac{U_{range,ADC}}{2^{n_{bits}} \sqrt{n_{bits} f_{s,adc}}} H_D(\Omega) \right)^2 df}$	$v_{n9} = 9.2(\mu V_{rms})$

The result for the noise rms voltages on the output of the decimation filter before the algorithm is determined with numerical integration in Matlab. The total noise follows by applying equation (D.15) to the result shown in Table D-1.

As discussed in appendix C.3 the irradiance of the light on the three photodiodes differs from each other. Therefore the photocurrents created in the photodiodes also have different values. As a consequence of this the shot noise in the three photodiodes is different and the voltage signal on the three ADC's that is proportional to the photocurrent will also be different from each other. This can be seen in Table D-2, where the noise contributions of all the intensity noise sources on the output after the decimation filter are given for the three photodiode readouts.

Table D-2 Noise VSD on the output signal before the algorithm

VSD Number	V_{n1}	V_{n2}	V_{n3}	V_{n4}	V_{n5}	V_{n6}	V_{n7}	V_{n8}	V_{n9}
VSD photodiode 1 ($\mu\text{V}/\sqrt{\text{Hz}}$)	3.1	0.0	1.4	0.8	0.0	4.0	0.4	0.3	9.3
VSD photodiode 2 ($\mu\text{V}/\sqrt{\text{Hz}}$)	3.9	0.0	1.4	0.8	0.0	16.1	0.4	0.3	14.4
VSD photodiode 3 ($\mu\text{V}/\sqrt{\text{Hz}}$)	3.8	0.0	1.4	0.8	0.0	16.1	0.4	0.3	14.0

The total noise contribution of the three signals after filtering on the main signal is given below in Table D-3 by similar calculations performed for photodiode 1.

Table D-3 CAS voltages on the output signal before the algorithm

Total noise voltage	$V_{n,tot}$
CAS photodiode 1 (μV)	11.0
CAS photodiode 2 (μV)	24.3
CAS photodiode 3 (μV)	24.1

Now it will be explained how this noise is coupled on the precision of the signal. Consider again the three non-calibrated signals shown in Figure C-3. For each signal the noise is calculated separately and a different noise source is added to each signal. If the total calculated intensity noise is added to the signal before the algorithm, the result is shown in Figure D-8. Note that the noise is so small that it is not visible in the signal on this scale.

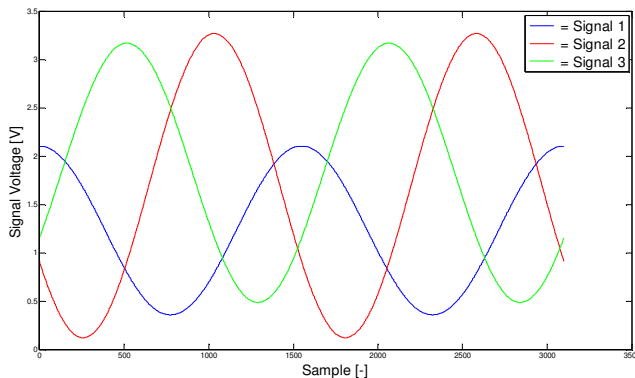


Figure D-8 Non-calibrated simulated signals in the ADC with added noise for a mirror moving with constant velocity.

If this signal with the noise on it is calibrated, and on the calibrated signal the Clarke transformation is applied and the displacement of the mirror is calculated, then this will give the displacement x_{noise} . If for an ideal signal without noise the displacement x_{sim} is calculated, then the error resulting from the difference between these two displacements can be described according to equation (D.12)

$$e_{\text{int,n}} = x_{\text{ideal}} - x_{\text{noise}} \quad (\text{D.21})$$

Where:

$e_{\text{int,n}}$ (nm) = Displacement error due to the intensity noise

x_{ideal} (nm) = Simulated ideal displacement

x_{noise} (nm) = Simulated displacement with intensity noise within the signal

Result

Simulating the noise and the three signals on the photodiode for a mirror moving with constant velocity and applying equation (D.21) gives the simulated error shown in Figure D-9.

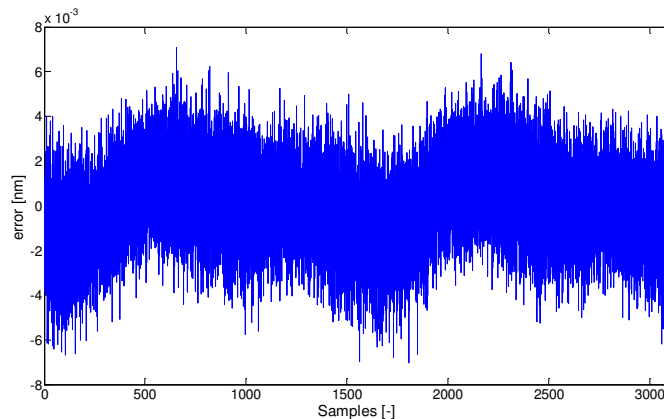


Figure D-9 Simulated error signal due to the presence of intensity noise on the three signals that are used to calculate the displacement

The standard deviation of this noise signal is equal to the error caused by the analogue electronics:

$$e_{\text{int},n} = 1.7 (\text{pm})$$

Validation

The dark current of the photodiode is maximal 3 (nA), compared to the smallest noise current from the photodiodes of 56.3 (μA) this is negligible.

All diodes have a certain parasitic capacitance called the junction capacitance [36]. The junction capacitance of the photodiode is 1.5 (pF), if the frequency behavior of this parasitic capacitance is modeled then the effect of this capacitance on the voltage spectral density of the opamp noise can be modeled. For stability of the opamp a feedback capacitance C_{f1} is placed in the feedback path of the transimpedance amplifier. This can be seen in Figure D-10.

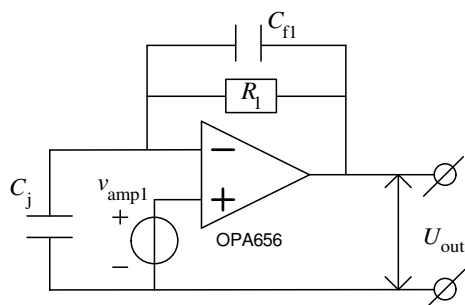


Figure D-10 Voltage noise model of the transimpedance amplifier

The transfer function for the voltage noise to the output is determined below.

$$\frac{U_{out}}{v_{amp1}} = \frac{C_j + R_1 // C_{f1}}{C_j} = \frac{\frac{1}{C_j s} + \frac{R_1 \frac{1}{C_{f1} s}}{R_1 + \frac{1}{C_{f1} s}}}{\frac{1}{C_j s}} = \frac{\frac{1}{C_j s} + \frac{R_1 C_{f1} s}{1 + R_1 C_{f1} s}}{\frac{1}{C_j s}} = 1 + \frac{R_1 C_j C_{f1} s^2}{1 + R_1 C_f s}$$

$$H_{amp}(s) = \frac{U_{out}}{v_{amp1}} = \frac{1 + R_1 C_f s + R_1 C_j C_{f1} s^2}{1 + R_1 C_f s}$$

An asymptotic approximation of the magnitude bode plot of H_{amp} is shown below in Figure D-11.

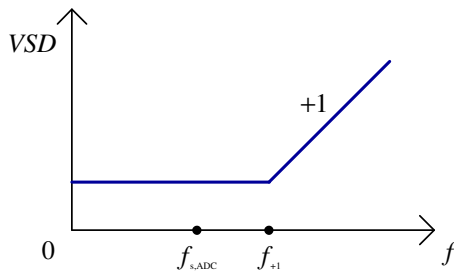


Figure D-11 Asymptotic approximation for the frequency behavior of the opamp noise caused by the junction capacitance of the photodiode

The frequency of f_{+1} could be algebraically determined by stating:

$$|H_{amp}(s)| = \sqrt{2}$$

But with Matlab it is calculated that f_{+1} is in the order of (Ghz). Clearly the effect of the junction capacitance is negligible. A similar result could be obtained for the noise current of the opamp and the shot noise of the photodiode. If the impedance of the two capacitances has about the same order of magnitude as the resistor, then the effect of the parasitic capacitance of the diode would become visible. Then the photocurrent would be split up in a current component that goes directly to the ground and another part that is amplified by the transimpedance amplifier. Roughly speaking this happens when the impedance of the junction capacitance 1 (pF) of the diode is about the same order as the impedance of the resistor 10 (kΩ).

$$\left. \begin{array}{l} Z_R = Z_C \\ 10^4 = \frac{1}{\omega 10^{-12}} \end{array} \right\} \omega = 10^8 \text{ (rad/s)} \approx f = 10^7 \text{ (Hz)}$$

Because this frequency is also much higher than the sample frequency of the ADC, the effect of the diode capacitance is also negligible.

The anti aliasing filter (passive low pass filter) before the ADC, is not included into the noise model, because the cutoff frequency of this filter is much higher than the sample

frequency of the ADC. This will not affect the noise VSD. The anti aliasing filter is shown in appendix A.1. $R = 22 \text{ } (\Omega)$ and $C = 0.01 \text{ } (\mu\text{F})$. This gives:

$$f_{\text{aliasing,filter}} = \frac{1}{2\pi RC} = 7.2 \cdot 10^5 \text{ (Hz)}$$

The effect of the anti aliasing filter is shown in the asymptotic approach of the magnitude plot. Figure D-12 shows that the cutoff frequency of this filter is higher than the sample frequency of then ADC, so the effect of the anti aliasing filter should not be taken into account.

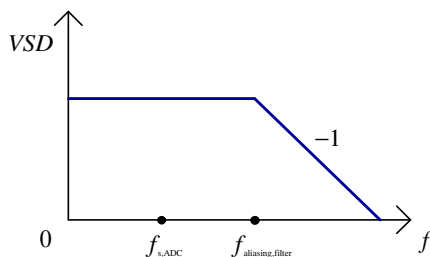


Figure D-12 Asymptotic approach of the magnitude plot for the anti aliasing filter

From the performed drift measurements that are shown in appendix E.4 the peak to peak precision error could be seen. In the figure below the black circle shows the region of the graph where there is zoomed in on the graph.

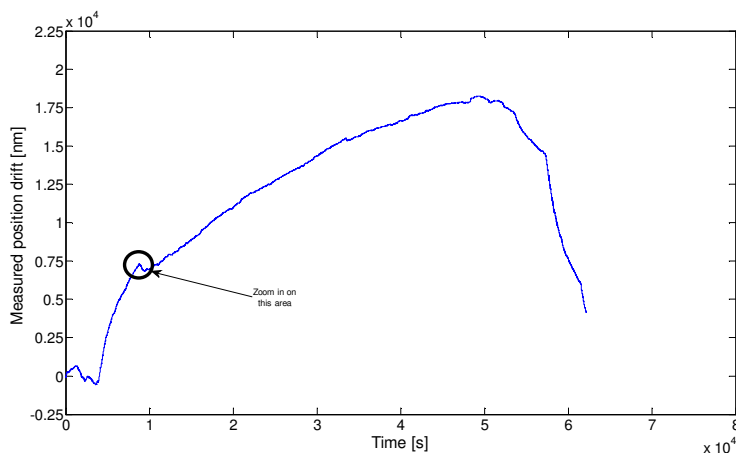


Figure D-13 Drift measurement 3 with the black circle indicating the area of the graph where there is zoomed into

The region that is zoomed into in Figure D-13 is shown in the next figure.

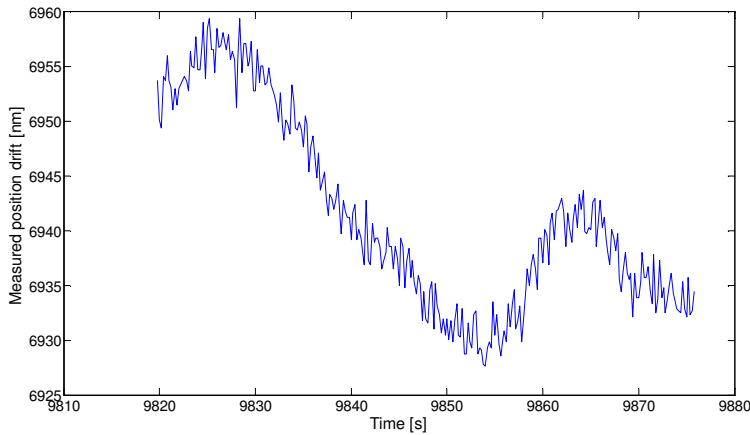


Figure D-14 Zoomed in on an area of drift measurement 3

In this figure mainly two effects can be seen: Thermal effects that are low frequent of nature and electric effects that are high frequent of nature. These electric effects are a good indication of the precision of the measurement system. It is presumed that the precision is mainly caused by electric noise.

From this figure it seems that the measured peak to peak noise amplitude is about 5 (nm). Expressed in nm_{rms} , this is about:

$$e_{int,n} = \frac{5}{2\sqrt{2}} (nm_{rms}) = 1.8 (nm_{rms})$$

This value is 3 orders of magnitude higher than the calculated noise in this appendix.

During an experiment a 50 (mA) input for the laser is used, one voltage signal over time is considered on one of the ADC's (ADC3). This signal is shown in the figure below.

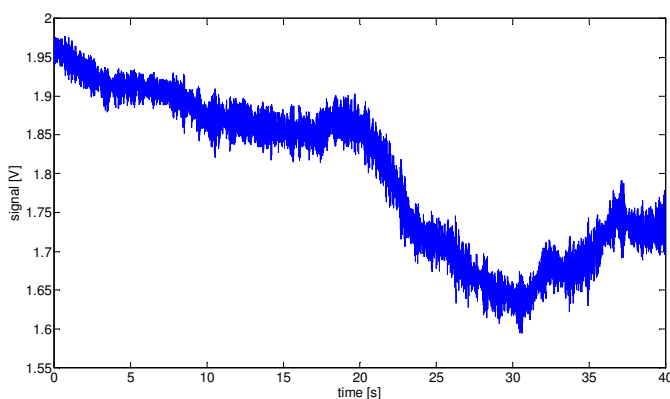


Figure D-15 Voltage signal on an ADC measured over time, during a noise experiment

This noise signal is analyzed in Matlab by making a FFT of this signal. The result is plotted on a linear scale below

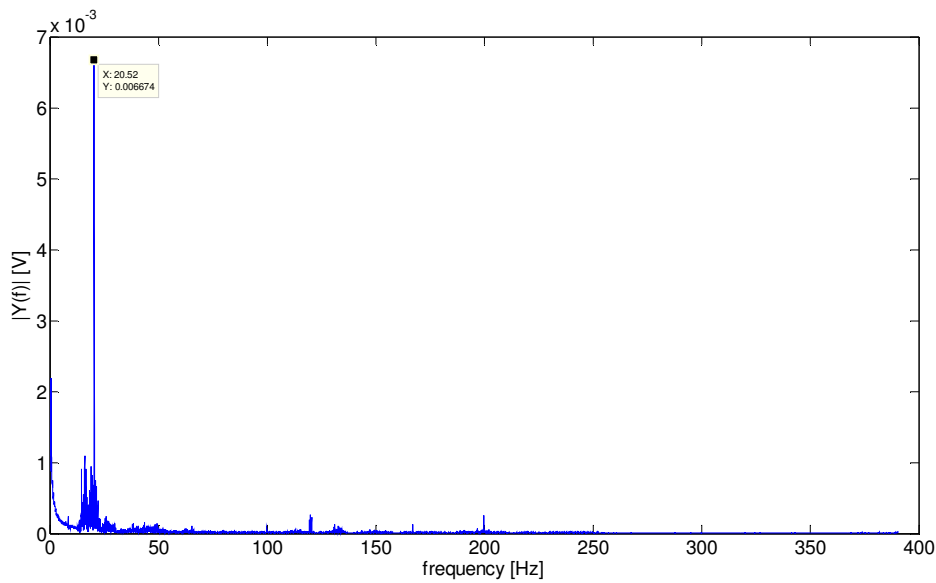


Figure D-16 FFT of the voltage signal on the ADC, during a noise experiment

In this figure it can clearly be seen that there are low frequency components present in the signal, but the signal is dominated by frequency component between 15 (Hz) and 22 (Hz).

The same figure is plotted on a logarithmic scale in the figure below. The red dashed line indicates an ideal $1/f$ line.

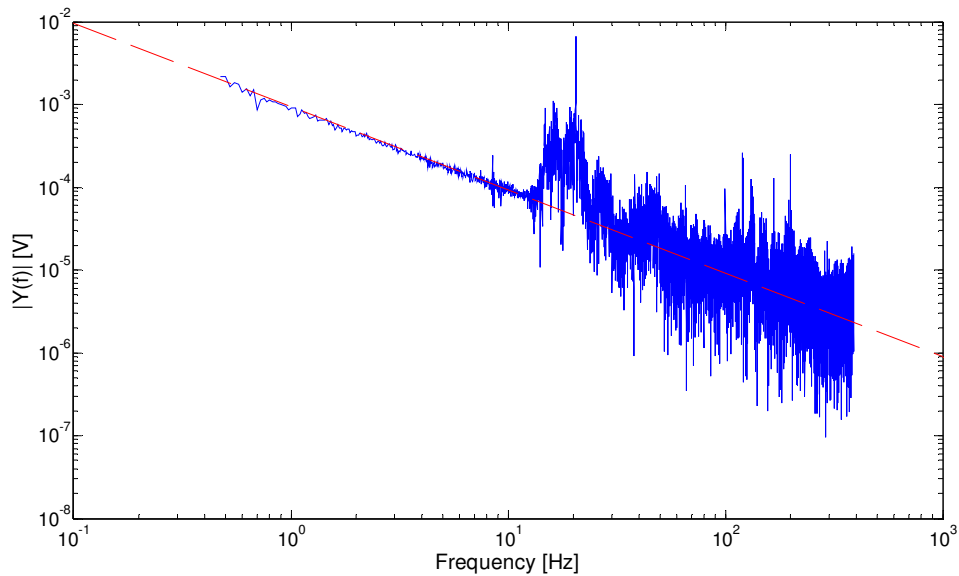


Figure D-17 of the voltage signal on the ADC plotted on a logarithmic scale, during a noise experiment

In this plot it can be seen clearly that signal is not only dominated by frequency components between 15 (Hz) and 22 (Hz), but it also shows strong 1/f characteristics.

This result indicates that it was not valid to model most of the noise sources as white noise sources or another 1/f noise source was not modeled.

Probably the photon noise is the cause of this 1/f characteristic. Photon noise results from the inherent statistical variation in the arrival rate of photons incident on the photodiode.

Discussion

By using a Delta Sigma ADC in combination with a digital filter even lower noise levels can be reached [4].

The noise in the opamps has a 1/f noise component in the noise spectrum; this can be seen in the datasheets of the opamps. Therefore it is not correct to assume that the opamp VSD is completely white. An asymptotic approach of the effect on a logarithmic scale is shown in Figure D-18. This spectral noise distribution is applicable for the noise voltage spectral density in the opamp.

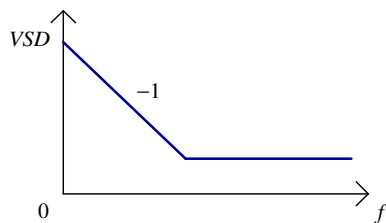


Figure D-18 Asymptotic approach of the VSD of the opamp noise

The 1/f noise for the OPA656 has been modeled, but the 1/f behavior of the OP2177 is specified in the datasheet as 0.1 (Hz) to 10 (Hz) as 0.4 (μV) p-p. If this value was amplified by the analogue low pass filter by three, the noise voltage from this OPAMP at the ADC would be 5.4 (μV) instead of 4.0 (μV). The effect of this on the total noise would still be very small.

Also it should be noted that the analogue low pass filter should be filtering but in fact it is only amplifying the noise. This effect is most clearly seen for the input voltage noise in this amplifier. From Table D-1 it can be seen:

$$v_{amp2} = 7.9(nV / \sqrt{Hz}) \quad \text{gives:} \quad v_{n6} = 4.0(\mu V_{rms})$$

While the ADC noise is a lot bigger but in the final noise signal after filtering the amplification is less compared to the input voltage noise of the amplifier.

$$v_{adc} = 725(nV / \sqrt{Hz}) \quad \text{gives:} \quad v_{n9} = 9.2(\mu V_{rms})$$

Utilizing a higher order low pass filter would result in a lower noise on the output. Then the ADC noise would become dominant. The ADC noise could be reduced by increasing the number of bits of the ADC.

On 29-11-2011 it became known to me that the decimation filter is not implemented in the system as mentioned in this report. The decimation filter treated in this report averages the last M samples and the latest sample is equal to the average of the

previous 127 (which have been averaged already). Continuing like this would give 128 averaged samples. In this report it is assumed that the 127 are not used and the one sample left is used. In the implemented filter 128 samples saved in a buffer, these samples are averaged and the averaged value is used. Then the buffer is cleared and the process is repeated. This means that the transfer function for the decimation filter is not correct and therefore the estimation of the noise is not correct for the initial configuration of the fiber optic interferometer. In fact the noise in the current setup will be higher than the estimated noise in this thesis report.



D.2 Optical disturbance signals

Introduction

Undesired reflections and cross talk can create undesired optical signals within the measurement system that interact with the optical signal that's containing the information about the measured position of the moving mirror. The position error caused by these optical disturbances is modeled and determined in this appendix.

Assumptions

- Losses in the fiber optic cables are neglected
- The reflections on the grin lens are also modeled on the way back from the moving mirror. Other reflections on the way back from the moving mirror are neglected
- All optical disturbance signals interfere constructively with the ideal signal
- The phase between the disturbance signal and the ideal signal doesn't change in time

Modeling

The error caused by optical disturbance signals is modeled as followed. The influence of an optical disturbance signal on the accuracy is determined when the ideal signal interferes constructively or destructively with the optical disturbance signal. The attenuation of all these optical signals can be calculated in the same way as in equation (B.36) in appendix B.2. In Figure D-19 the location of the place where the optical disturbance signals arise are shown. In Table D-4 the magnitude with respect to the main optical signal, source, the type and the source of the optical disturbance signals are given. Also the name of the optical disturbance signal in Figure D-19 is given.

Table D-4 Information about the optical disturbance signals

Part	Information source	Description	Name	Magnitude(dB)
Circulator	test datasheet circulator	directivity	$I_{u,1}$	50.00
Connector 2	datasheet connector	return loss	$I_{u,2}$	75.00
3x3 splitter	test datasheet 3x3 splitter and datasheet 3x3 splitter	directivity	$I_{u,3}$	65.00
Con. + end stop	Datasheet fiber optic cable	End stop return	$I_{u,4}$	82.20
Connector 3	datasheet connector	return loss	$I_{u,5}$	60.00
Connector 4	measurements from Technobis	without AR coating	$I_{u,6}$	60.00
		without AR coating way back	$I_{u,7}$	11.55
Grin lens	measurements from Technobis	without AR coating way back	$I_{u,8}$	11.55

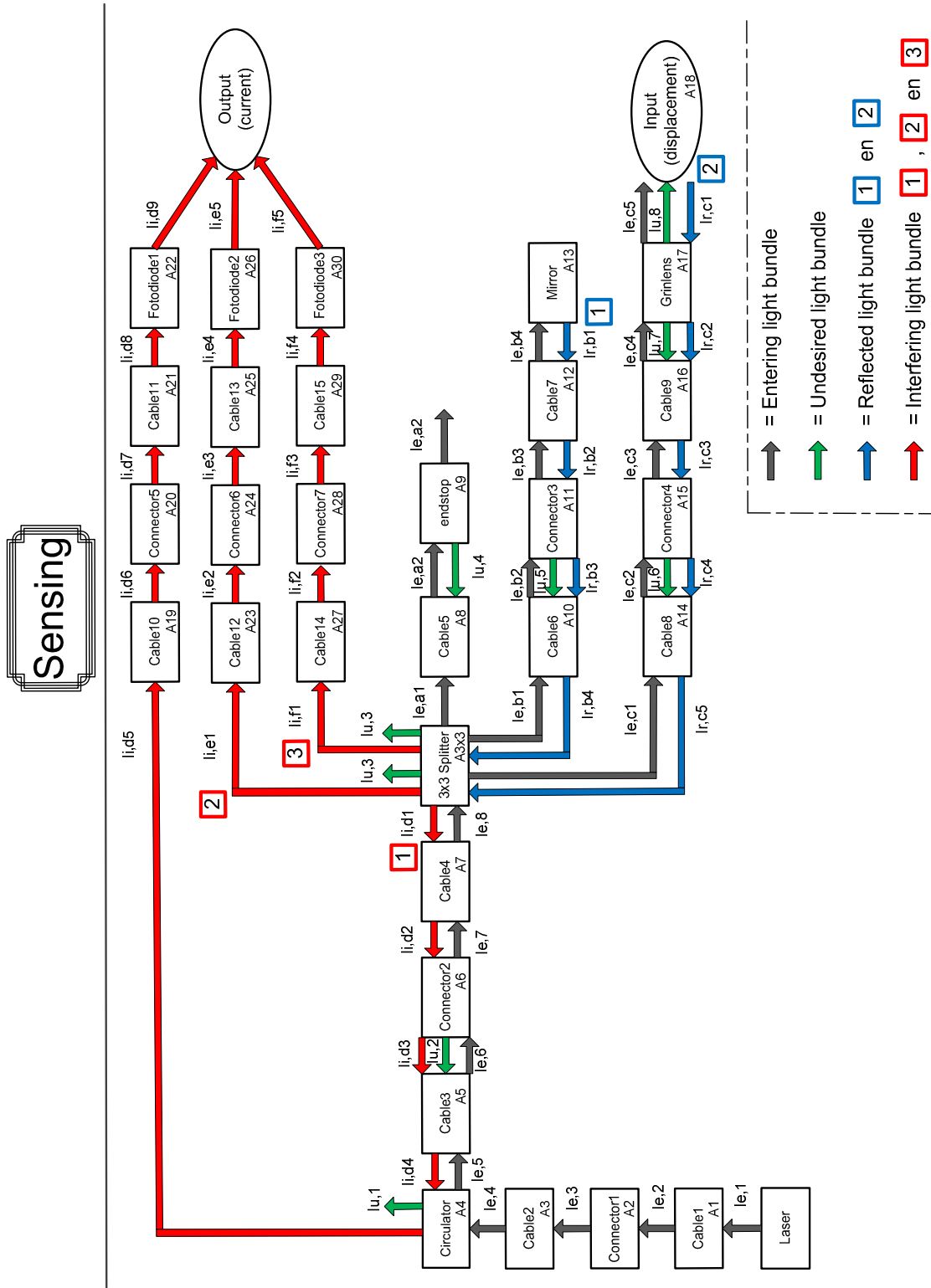


Figure D-19 Location of the optical disturbance signals that arise within the fiber optic interferometer

By applying equation (B.36) on the disturbance signals like in appendix B.2, the power of each disturbance signal can be calculated for each photodiode. The result of this calculation is displayed as a ratio of the power of the original signal in Table D-5. Also the ratio of the ideal signal over the sum of all optical disturbance signals (the total disturbance) is shown in this table for all three photodiodes.

Table D-5 Ratio of each disturbance signal over the ideal calculated signal that has been calculated in appendix C.3. This ratio is given for all three photodiodes

Disturbance #	Ratio photodiode 1	Ratio photodiode 2	Ratio photodiode 3
$I_{u,1}$	1.4E-04	0.0E+00	0.0E+00
$I_{u,2}$	2.6E-07	0.0E+00	0.0E+00
$I_{u,3}$	0.0E+00	2.0E-06	2.0E-06
$I_{u,4}$	4.4E-09	3.4E-09	3.5E-09
$I_{u,5}$	6.9E-07	7.0E-07	6.1E-07
$I_{u,6}$	6.2E-07	6.1E-07	7.1E-07
$I_{u,7}$	3.6E-02	3.6E-02	4.2E-02
$I_{u,8}$	3.0E-02	3.0E-02	3.5E-02
Total disturbance	6.7E-02	6.6E-02	7.6E-02

Now these disturbances need to be coupled to the error that they cause in the measurement system. The ideal current signals defined by equations (C.9), (C.10) and (C.11) with the parameters given in Table C-1 are used as the ideal signal and then the signal is calibrated. Now with this ideal signal the displacement x_{ideal} is simulated with the algorithm for a mirror moving over a distance of 1550 (nm) with constant velocity. A new simulation is performed for the situation where the disturbance signals are added to the ideal signal as it is assumed that they constructively interfere with each other. Then the system is calibrated for this ideal signal with the disturbances and the displacement $x_{opt,dis}$ is calculated for this signal. Again the signal is simulated with the algorithm for a mirror moving over a distance of 1550 (nm) with constant velocity. The simulated error signal can be determined by subtracting these two signals from each other like in (D.21).

$$e_{opt,dis} = x_{ideal} - x_{opt,dis} \quad (D.22)$$

Where:

$e_{opt,dis}$ (nm) = Displacement error due to optical disturbances

$x_{opt,dis}$ (nm) = Simulated displacement with optical disturbances within the signal

Result

The error due to the optical disturbance signals for a mirror moving over a distance of 1550 (nm) with constant velocity is shown below in Figure D-20.

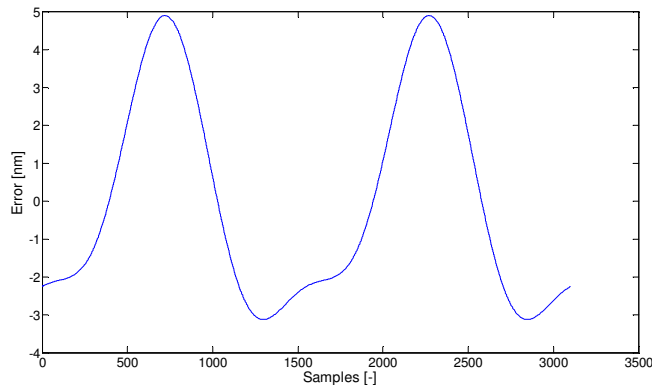


Figure D-20 Simulated error of the measurement system due to the influence of optical disturbance signals

The resulting error is a systematic error. The maximal error that can occur is equal to:

$$e_{\text{opt,dis}} = 4.9 \text{ (nm)}$$

Validation

The losses in the fiber optic cables are neglected for this model. In appendix B.2 the power losses within the fiber optic cables seemed to be very small compared to the other optical losses. From the modeled results in Table B-2 the exact loss is calculated:

$$\frac{P_{\text{loss, fibers}}}{P_{\text{loss, total}}} = \frac{5.8 \text{ (}\mu\text{W)}}{758.9 \text{ (}\mu\text{W)}} \cdot 100\% = 0.8\%$$

As expected this is very low compared to the other losses, so the assumption to neglect the losses for this model is valid.

In this appendix it is assumed that the reflections on the way back from the moving mirror besides the reflections from the grin lens can be neglected. From Table D-5 it can be seen that the only significant reflection occurs from the grin lens. Other reflections are at least two orders of magnitude smaller than the grin lens reflection.

It is assumed that the phase between the disturbance signal and the ideal signal doesn't change in time. This assumption is not very realistic because this would mean that in time all the waveguide material where the laser light passes through should have a constant length. In reality temperature rates will occur and the influence of the optical disturbance signals on the measurement signal will therefore also change in time. However for a constant length of the light waveguide material this is a good approximation for the error caused by optical disturbances in the system.



D.3 Laser frequency deviations

In order to determine the effect of frequency deviations on the error of the measured position by the interferometer, these deviations need to be coupled to equation (C.7). This equation couples the detected fringe pattern to the measured displacement. Now first there need to be started from the basic light equations. The frequency of an electromagnetic wave is described as:

$$v = \frac{c}{\lambda} \tag{D.23}$$

Where:

$c(m/s)$ = Speed of light in vacuum = $3.0 \cdot 10^8 (m/s)$

$v(Hz)$ = Frequency

Another basic equation in optics is given below.

$$\lambda = \frac{\lambda_0}{n} \tag{D.24}$$

Where:

$\lambda_0 (m)$ = Wavelength in vacuum

Now defining the number m as the normalized phase for one wavelength:

$$\varphi = 2\pi m \tag{D.25}$$

Where:

$m(-)$ = Parameter as a measure for the wavelengths fraction

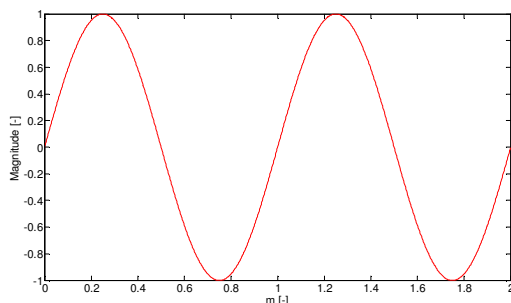


Figure D-21 plot of 2 sine periods as a function of parameter m

In general the optical path difference for two electromagnetic waves (EM) traveling through two different waveguide materials is defined as:

$$OPD = n_2 x_2 - n_1 x_1 \quad (D.26)$$

Where:

$OPD(m)$ = Optical path difference

$n_1(-)$ = Refractive index of waveguide material 1

$n_2(-)$ = Refractive index of waveguide material 2

$x_1(m)$ = Distance travelled by EM wave 1

$x_2(m)$ = Distance travelled by EM wave 2

The optical path difference for two electromagnetic waves (EM) traveling through the same waveguide with the refractive index n is defined as:

$$OPD = n(x_2 - x_1) \quad (D.27)$$

The dimensionless parameter m is related to the OPD as follows:

$$m = \frac{OPD}{\lambda} \quad (D.28)$$

Now the model of the fiber optic interferometer given in Figure 2-3 is considered. The relation between the displacement of the moving mirror of the fiber optic interferometer and the measured phase of the fringe signal is described by equation (C.7) given below.

$$x = \frac{\lambda \phi}{4\pi n} \quad (D.29)$$

The wavelength deviation needs to be expressed in terms of the frequency deviations of the laser. The next two formulas are obtained by using equation (D.23).

$$\Delta v = \frac{c}{\Delta \lambda} \quad \text{and} \quad v_{\text{laser}} = \frac{c}{\lambda_{\text{laser}}}$$

Where:

$\Delta v(Hz)$ = Frequency deviation from the center frequency of the laser

$v_{\text{laser}}(Hz)$ = Frequency of the laser

Combining the two previous equations and rewriting:

$$c = \frac{v_{\text{laser}}}{\lambda_{\text{laser}}} = \frac{\Delta v}{\Delta \lambda}$$

$$\Delta \lambda = \frac{\Delta v}{v_{\text{laser}}} \lambda_{\text{laser}}$$

And now rewriting this result and rewriting the frequency deviation by using equation (D.23), gives equation (D.30)

$$\Delta \lambda = \frac{\Delta v}{v_{\text{laser}}} \lambda_{\text{laser}} = \frac{\Delta v \lambda_{\text{laser}}^2}{c} \quad (\text{D.30})$$

Now the wavelength of the laser is changing because the frequency of the laser changes. As a result of this difference in frequency an error in the measured position is caused. The effect of this error is modeled by assuming that the laser wavelength is constant, but the measured phase of two situations changes due to the laser stability. The first scenario is the ideal case when the measured phase as it should be. The second case is a change of phase due to the fact that the frequency of the laser changes. The difference in phase measured by these signals called φ_{drift} is a measure for the effect of the deviation of the frequency of the laser on the measured position of the moving mirror. This process is described in the equation below. The deviation of the frequency of the laser over time is called laser drift.

$$x_{\text{laser drift}} = \frac{\lambda_{\text{laser}}}{4\pi} (\varphi_{\text{normal}} - \varphi_{\text{drift}}) \quad (\text{D.31})$$

Where:

$e_{\text{laser drift}} (m)$ = Change of detected position due to laser drift

$\varphi_{\text{normal}} (rad)$ = Ideal phase

$\varphi_{\text{drift}} (rad)$ = Drifted phase

Rewriting equation (D.31) gives:

$$e_{\text{laser drift}} = \frac{\lambda_{\text{laser}}}{2} \left(\frac{\varphi_{\text{normal}}}{2\pi} - \frac{\varphi_{\text{drift}}}{2\pi} \right)$$

Using equation (D.25) results in:

$$e_{\text{laser drift}} = \frac{\lambda_{\text{laser}}}{2} (m_{\text{normal}} - m_{\text{drift}})$$

Now applying (D.28) and taking into account that the wavelength of the drifted signal is equal to the laser wavelength plus a change in wavelength caused by the laser frequency deviation. The optical path difference in both cases remains the same.

$$e_{\text{laser drift}} = \frac{\lambda_{\text{laser}}}{2} \left(\frac{OPD}{\lambda_{\text{laser}}} - \frac{OPD}{\lambda_{\text{laser}} + \Delta\lambda} \right)$$

Where:

$\Delta\lambda (m)$ = Wavelength deviation from the center wavelength of the laser

Now applying simple algebra gives:

$$e_{\text{laser drift}} = \frac{OPD}{2} \left(1 - \frac{\lambda_{\text{laser}}}{\lambda_{\text{laser}} + \Delta\lambda} \right)$$

$$e_{\text{laser drift}} = \frac{OPD}{2} \left(\frac{\lambda_{\text{laser}} + \Delta\lambda}{\lambda_{\text{laser}} + \Delta\lambda} - \frac{\lambda_{\text{laser}}}{\lambda_{\text{laser}} + \Delta\lambda} \right)$$

And the final result is the relation between

$$e_{\text{laser drift}} = -\frac{OPD \cdot \Delta\lambda}{2(\lambda_{\text{laser}} + \Delta\lambda)} \quad (D.32)$$

D.4 Mirror and lens alignment

Introduction

Due to angular misalignment between the grIN lens and the moving mirror the light that's reflected from the moving mirror and coupled back into the fiber optic interferometer, is dependent on the position of the moving mirror relative to the position of the grIN lens and the magnitude of the angular misalignment.

In this section, first it will be shown why the angular misalignment affects the accuracy of the measurement system. Then a 2 dimensional geometric model of an angular misalignment will be given and for this model it will be shown how the effect on the accuracy is determined. Finally the error due to misalignment will be given.

Assumptions

- All optic parts are assumed to be ideal, in surface roughness, surface flatness, aberrations etc. do not influence the accuracy
- The entire surface of the lens is used (the actual value is 90%)
- The distribution of the power density over the optic fiber core diameter is homogeneous over the diameter of the fiber core. All power is in the core
- The grIN lens cross section has a square shape
- The minimal misalignment of the grIN lens and the measurement mirror is 0.5 degrees with the current alignment facilities for these parts
- The OPD is equal to 0.1 (m)
- The misalignment of the linear optical stage can be neglected

Modeling

The following configuration is used for the moving mirror and the measurement mirror in this appendix.

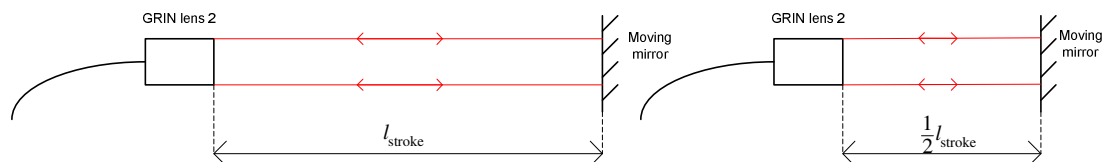


Figure D-22 Configuration of the moving mirror and the grIN lens.

The moving mirror is shown placed in two positions away from the grIN lens, which is in a fixed position.

Now consider an angular misalignment between the fixed grIN lens and the moving mirror in the 2 dimensional representation shown in Figure D-23.

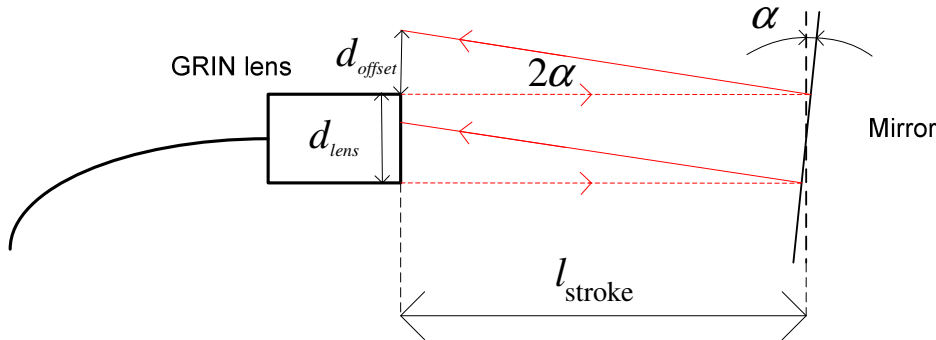


Figure D-23 Geometric model of the angular misalignment of the mirror with the grin lens

The amount of light coupled back into the grin lens is dependent on the position of the moving mirror. When the mirror moves away from the grin lens, the amount of light that is coupled back into the grin lens is reduced. From the next equations it will be shown that the phase of the fringe signal, which is a measure for the displacement of the moving mirror, is influenced by the intensity of the two interfering waves.

The linear superposition of two waves can be written as [3]:

$$E_0 \sin(\omega t + \alpha) = E_{01} \sin(\omega t + \alpha_1) + E_{02} \sin(\omega t + \alpha_2) \quad (D.33)$$

Where:

α (rad) = Wave phase

$E(-)$ = Amplitude

The amplitude of the resultant wave can be written as [3]:

$$E_0^2 = E_{01}^2 + E_{02}^2 + 2E_{01}E_{02} \cos(\alpha_2 - \alpha_1) \quad (D.34)$$

And the phase of the resultant wave can be written as [3]:

$$\tan \alpha = \frac{E_{01} \sin \alpha_1 + E_{02} \sin \alpha_2}{E_{01} \cos \alpha_1 + E_{02} \cos \alpha_2} \quad (D.35)$$

From equation (D.35) it can be seen that the amplitude of the both waves influences the phase of the resultant wave. So if there is an angular misalignment between the surface of the grin lens and the mirror, the amount of light coupled back into the grin lens will be dependent on the position of the measurement mirror and therefore the error will be a function of the position of the measurement mirror. The error will be greatest when the displacement is maximal.

It is assumed that the entire surface of the grin lens is used to couple light back into the lens and that the OPD is 0.1 (m).

By using standard geometry the angular misalignment of the lens and the moving mirror can be calculated when no light couples back into the lens. The lens diameter can be obtained from the datasheet of the grin lens from appendix G.7 and the length of the stroke is equal to half the OPD.

$$d_{\text{offset}} = 1(\text{mm})$$

$$l_{\text{stroke}} = 50(\text{mm})$$

With these values the angular misalignment when no light couples back into the grin lens can be calculated.

$$\alpha_{\text{offset}} = 0.55^\circ$$

Between the situations of a perfectly aligned mirror and a misaligned mirror, where all light is lost into the surrounding, a part of the light is coupled back into the lens, depending on the position of the mirror. In order to calculate how much light couples back into the lens for a given angular misalignment, a few assumptions have to be made. The first assumption is that the lens has a square cross section. The second assumption is that the distribution of the power density over the lens is homogeneous over the square surface of the lens. This means that the light intensity is not Gaussian distributed over the lens surface.

With these assumptions it will be shown how misalignment between the grin lens and the moving mirror will affect the accuracy.

The lost power of the light due to misalignment is expressed as a percentage of the light that is coupled back into the lens, when there would be no misalignment. This can be written as followed:

$$p_{\text{loss,lens}} = \frac{P_{\text{loss,lens}}}{P_{\text{no loss,lens}}} \cdot 100\% \quad (\text{D.36})$$

Where:

$$p_{\text{loss,lens}} (\%) = \text{Percentage of lost light}$$

$$P_{\text{loss,lens}} (W) = \text{Power of lost light}$$

$$P_{\text{no loss,lens}} (W) = \text{Power coupled back into the lens}$$

The light just before the splitter interferes with the light from the reference arm. There is a constant attenuation on the light entering back into the grin lens towards the splitter (equation (B.36) applies). This means that the percentage of the lost light at the grin lens is the same percentage of the lost light before the splitter.

The measurement system is calibrated for the case where no light is lost. Similar to section D.1 two signals are simulated and the error is determined by calculating the difference between the two signals. The first signal is the ideal signal when no light is lost due to misalignment and the second signal is the signal where a certain percentage

of the light is lost due to misalignment. The simulated error signal can be determined by subtracting these two signals from each other like in (D.21).

$$e_{\text{align}} = x_{\text{ideal}} - x_{\text{loss,lens}} \quad (\text{D.37})$$

Where:

$e_{\text{align}}(m)$ = Displacement error due to angular misalignment

$x_{\text{loss,lens}}(m)$ = Simulated displacement with optical losses due to misalignment

The error is determined when the lost optical power is maximal; this is when the moving mirror is in the most distant position away from the grin lens.

Result

The grin lens and the moving mirror are manually aligned with each other, without the use of any optical alignment equipment. It is assumed that the moving mirror and the grin lens have a maximal angular misalignment of 0.25 degrees.

The offset of the light bundle on the grin lens caused by this angle can be calculated by applying basic geometry. This situation is graphically illustrated in Figure D-23.

$$d_{\text{offset}} = 0.44(\text{mm})$$

The offset of the light bundle on the grin lens is proportional to the optical loss of the light. The result for an alignment error of 0.25 degrees between the lens surface and the measurement mirror, corresponds to the loss percentage that can be calculated using the following equation.

$$p_{\text{loss,lens}} = \frac{d_{\text{offset}}}{d_{\text{lens}}} \cdot 100\% \quad (\text{D.38})$$

Where:

$d_{\text{offset}}(m)$ = Offset of the light bundle on the grin lens

$d_{\text{lens}}(m)$ = Diameter of the grin lens

Applying equation (D.38) with the previous results gives:

$$p_{\text{loss,lens}} = 44\%$$

The maximal error due to the angular misalignment between the grin lens and the moving mirror can be seen below in Figure D-24. The main causes for this error depend on the exact distance between the grin lens and the moving mirror and the initial phase of the optic wave when it exits the splitter towards the grin lens.

The maximal error is determined when the moving mirror is exactly 0.05 (m) away from the grin lens. On this distance a plot of the maximal error is made for different initial phases of the optic wave.

For the simulation of the error the same signal inputs as determined in appendix C.3 are used.

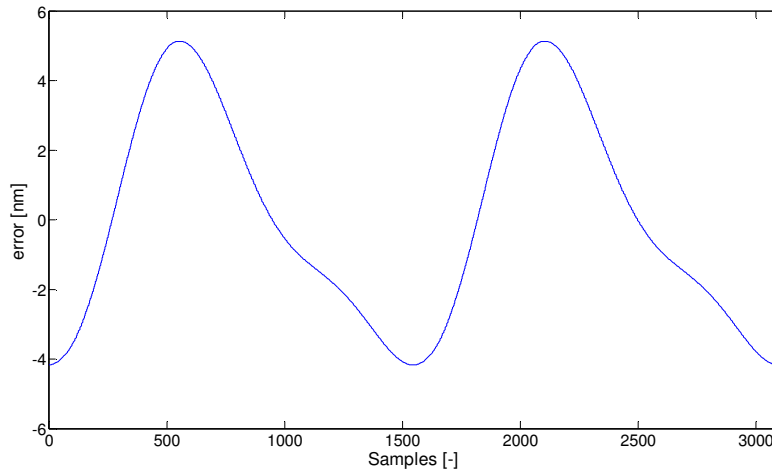


Figure D-24 Error due to angular misalignment of the grin lens and the moving mirror

The maximal error due to misalignment is:

$$e_{\text{align}} = 5.1 \text{ (nm)}$$

Validation

The misalignment of the linear optical stage is 100 – 200 (μrad). This corresponds to 0.0055 – 0.011 (degrees). Compared to the angular misalignment of the moving mirror and the grin lens, this is negligible.

Appendix E Experimental data

E.1 Specifications of the experimental setup

In order to read out the temperature sensors, the Fluke Data acquisition system 2640A is used. The temperature is measured with a PT100 DM-301 class B temperature sensor from company Labfacility. Four wire resistance measurements with sensor wires are performed on the PT100 to read out the temperature. The DAQ system has 20 analogue inputs, so this means that maximal 10 temperature sensors could be used. Furthermore the PT100 sensors are set by using a calibration table [40].

A Class B PT100 has a tolerance band of ± 0.3 degrees Celsius at 0 degrees Celsius and a temperature error of 0.8 degrees Celsius at 200 degrees Celsius. It is assumed that the temperature error is about 0.3 degrees Celsius over the used temperature range. The temperature could be calculated from the measured resistance with equation (E.1).

$$T_m = aR_m + b \quad (\text{E.1})$$

Where:

T_m ($^{\circ}\text{C}$) = Measured temperature

R_m (Ω) = Measured resistance

a (K / Ω) = Sensitivity of the PT100

b (K) = Conversion factor

From [40]:

$$T_m(100(\Omega)) = 0^{\circ}\text{C} = 273.15(\text{K})$$

And the sensitivity is:

$$a = \frac{1}{0.385055(\Omega / \text{K})} = 2.597(\text{K} / \Omega)$$

The conversion factor becomes:

$$b(^{\circ}\text{C}) = -2.597(^{\circ}\text{C} / \Omega) \cdot 100(\Omega) = -259.7032^{\circ}\text{C}$$

By using these calculated values, equation (E.1) becomes:



$$T_m (\text{°C}) = \frac{1}{0.385055 (\Omega/\text{°C})} R_m - 259.7032 (\text{°C}) \quad (\text{E.2})$$

The measurement system of the inteferometer measured 5 minutes longer than the DAQ for the temperature sensors. So when the data has been processed in Matlab the last 5 minutes of measurements are not used.

The temperature signal is sampled at 2 (Hz) and the signal of the fiber optic interferometer is plotted at 5 (Hz).

Because the signal of the temperature sensors suffers a lot from noise the calculated drift signal has to be filtered with a low pass filter. A digital tenth order butterworth low pass filter is used. The cutoff frequency of this filter is 0.025 (Hz), the same filter is applied for all three measurements.

E.2 Drift measurement 1

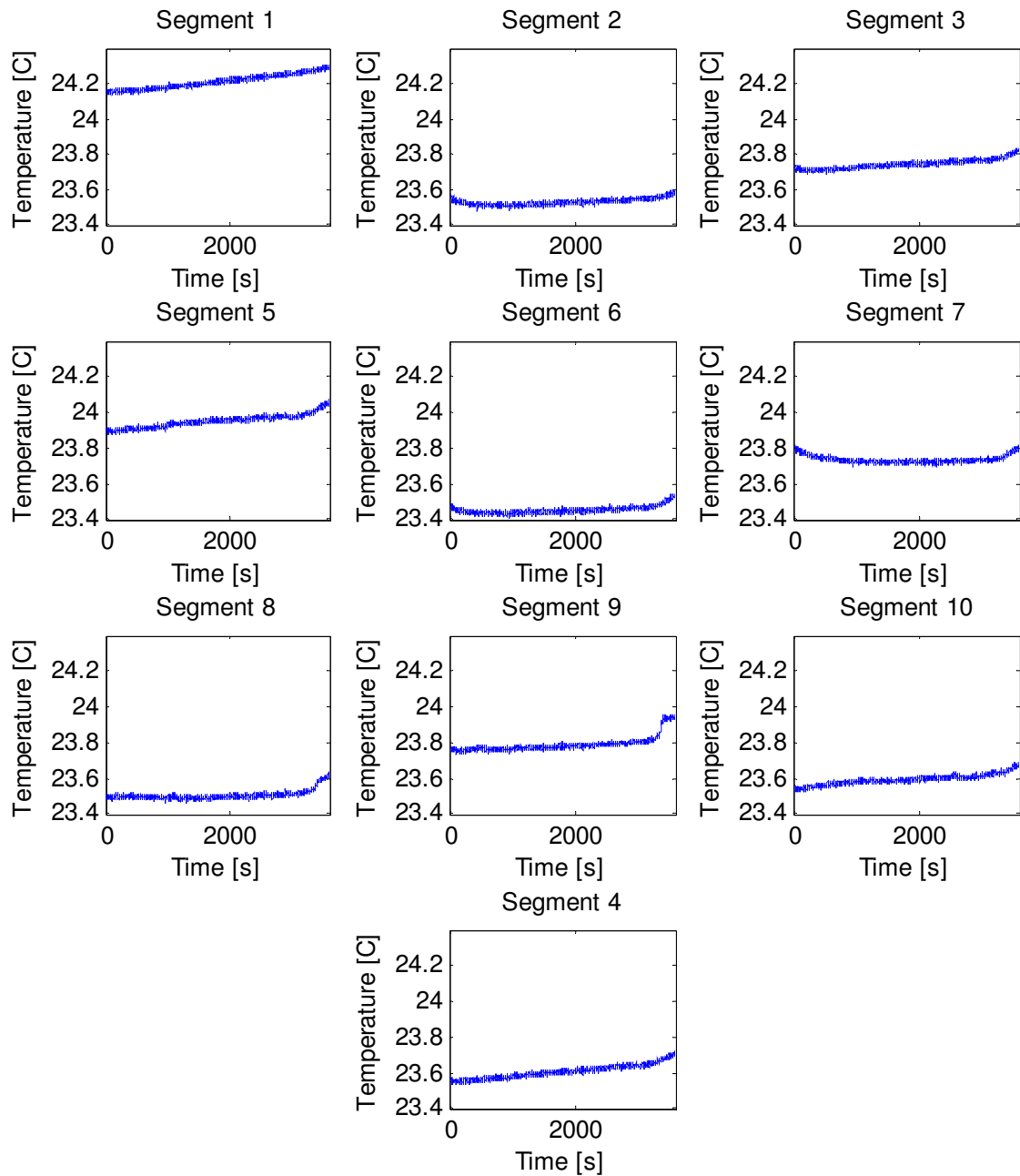


Figure E-1 Measured temperatures on the different fiber segments for drift measurement 1

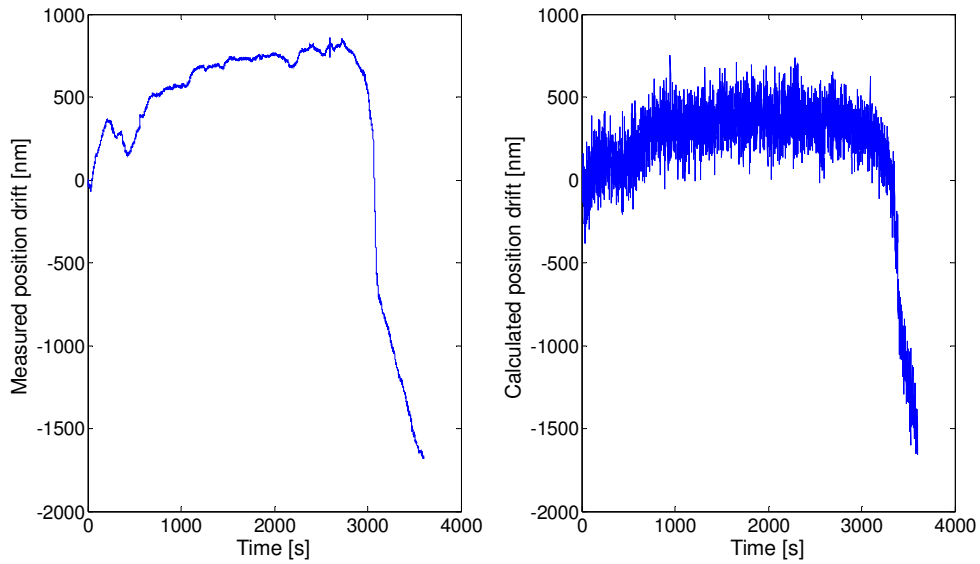


Figure E-2 Measured position drift and calculated unfiltered position drift for drift measurement 1

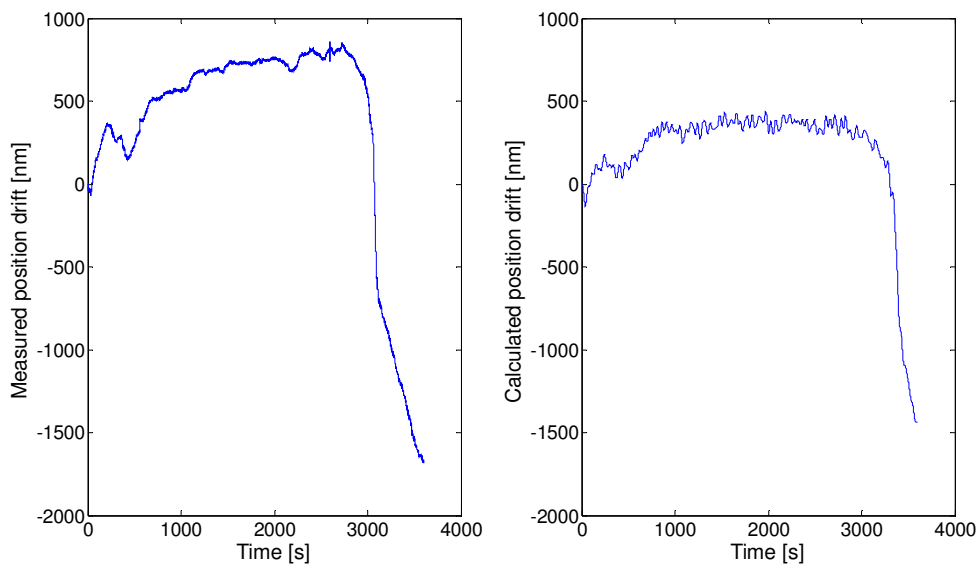


Figure E-3 Measured position drift and calculated filtered position drift for drift measurement 1

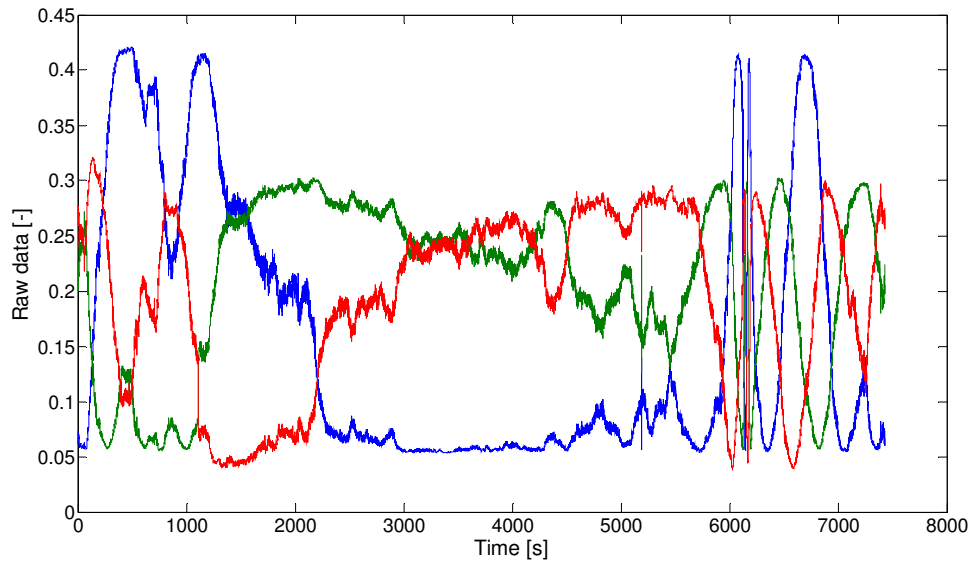


Figure E-4 Raw data from the three ADC's for drift measurement 1

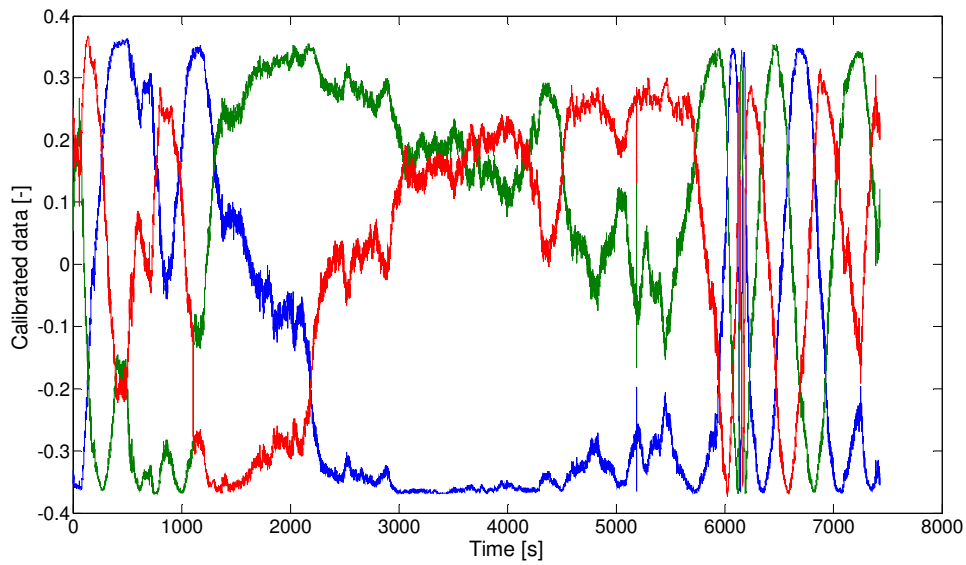


Figure E-5 Calibrated data from the three ADC's for drift measurement 1



E.3 Drift measurement 2

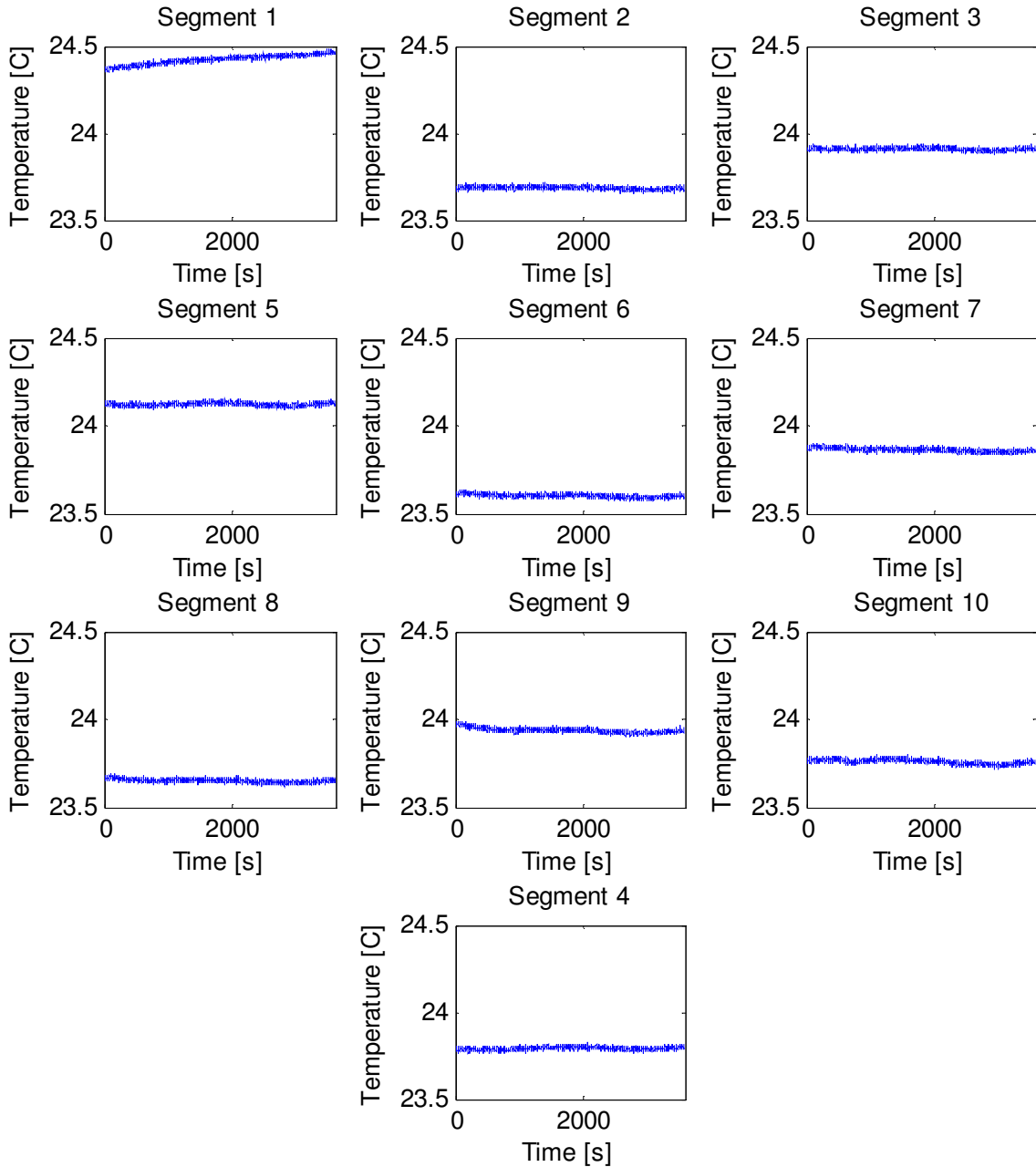


Figure E-6 Measured temperatures on the different fiber segments for drift measurement 2

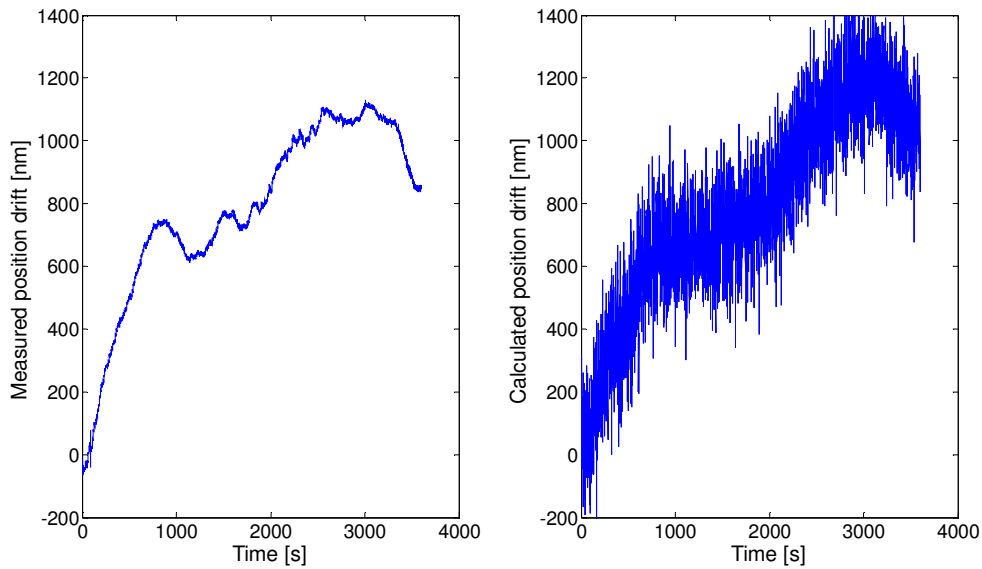


Figure E-7 Measured position drift and calculated unfiltered position drift for drift measurement 2

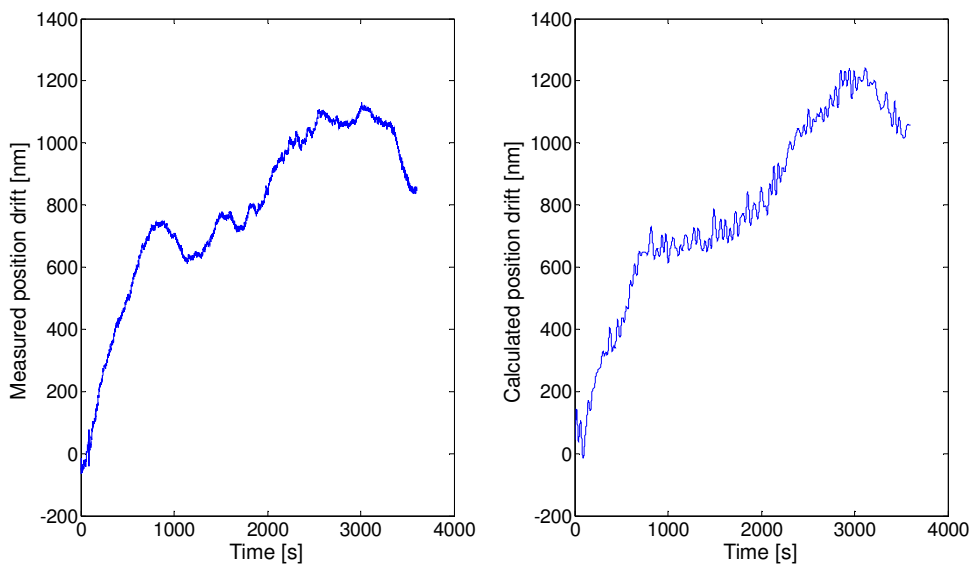


Figure E-8 Measured position drift and calculated filtered position drift for drift measurement 2

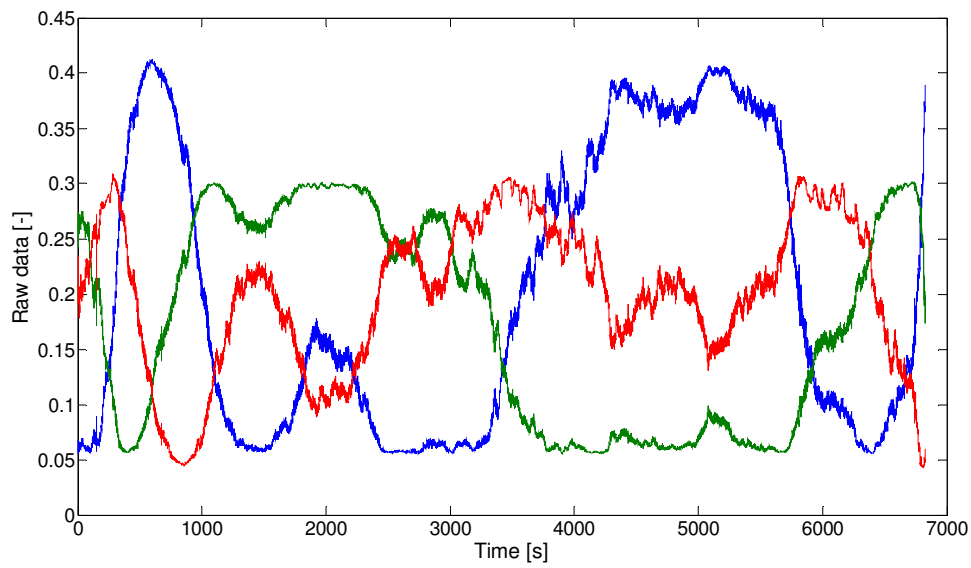


Figure E-9 Raw data from the three ADC's for drift measurement 2

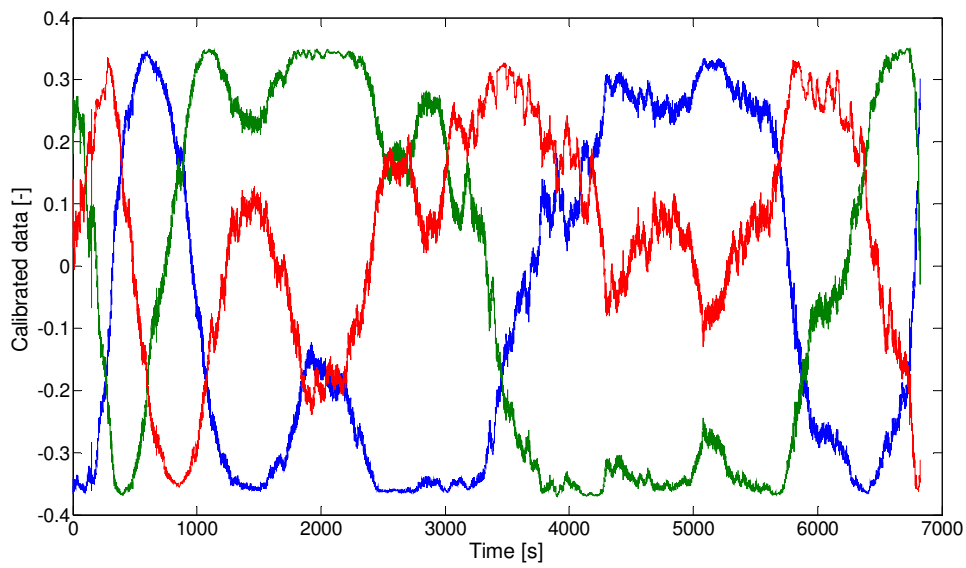


Figure E-10 Calibrated data from the three ADC's for drift measurement 2

E.4 Drift measurement 3

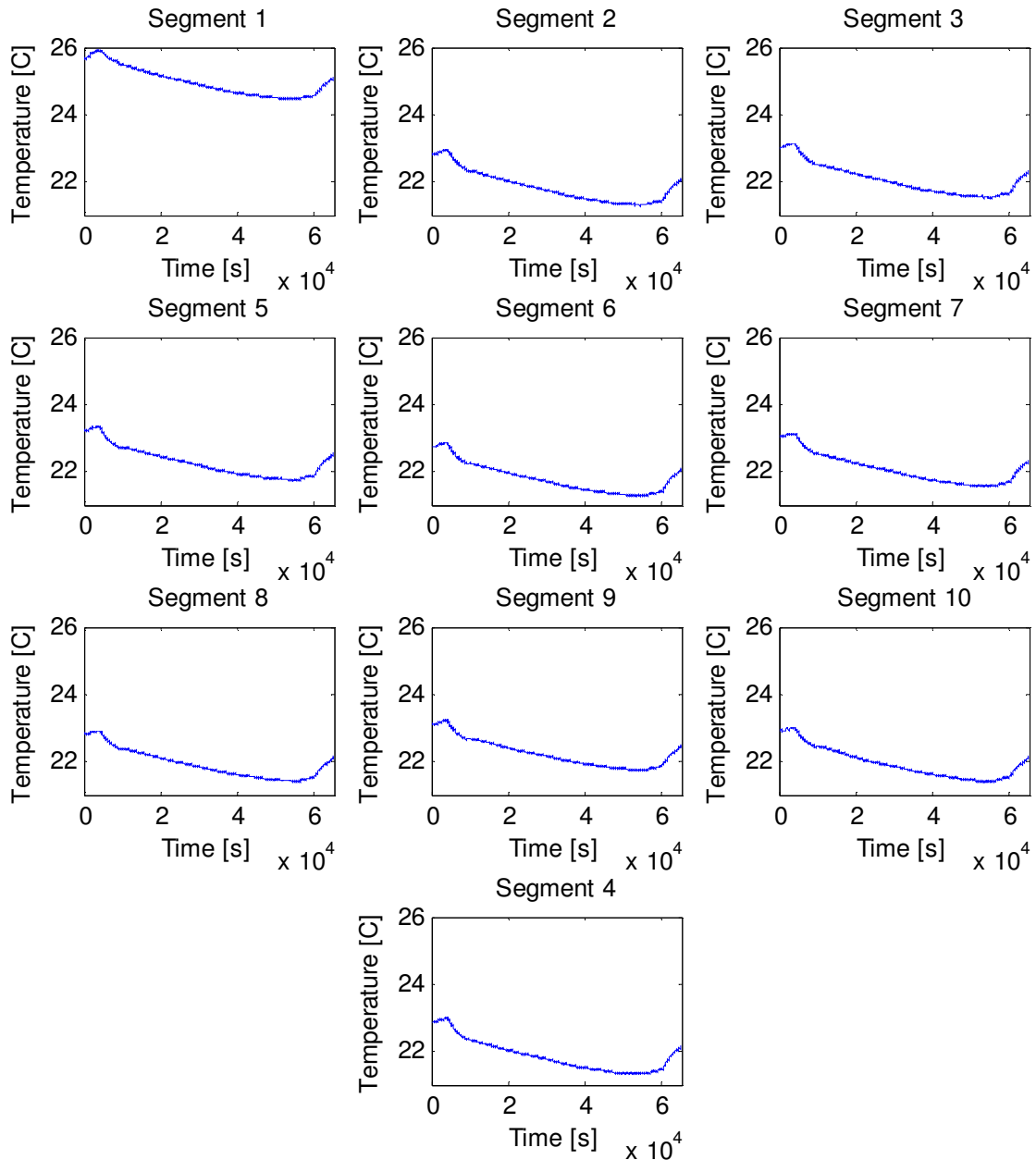


Figure E-11 Measured temperatures on the different fiber segments for drift measurement 3

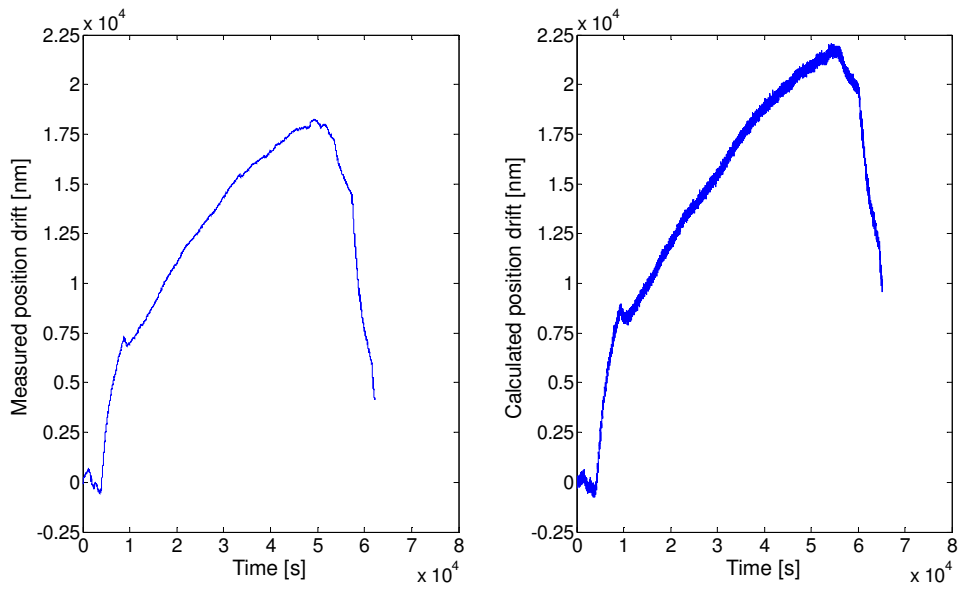


Figure E-12 Measured position drift and calculated unfiltered position drift for drift measurement 3

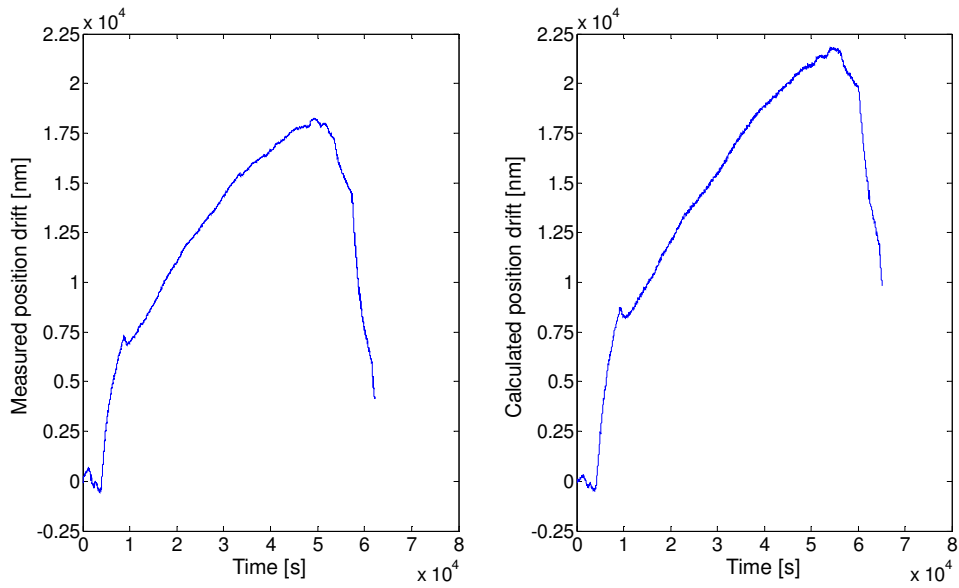


Figure E-13 Measured position drift and calculated filtered position drift for drift measurement 3

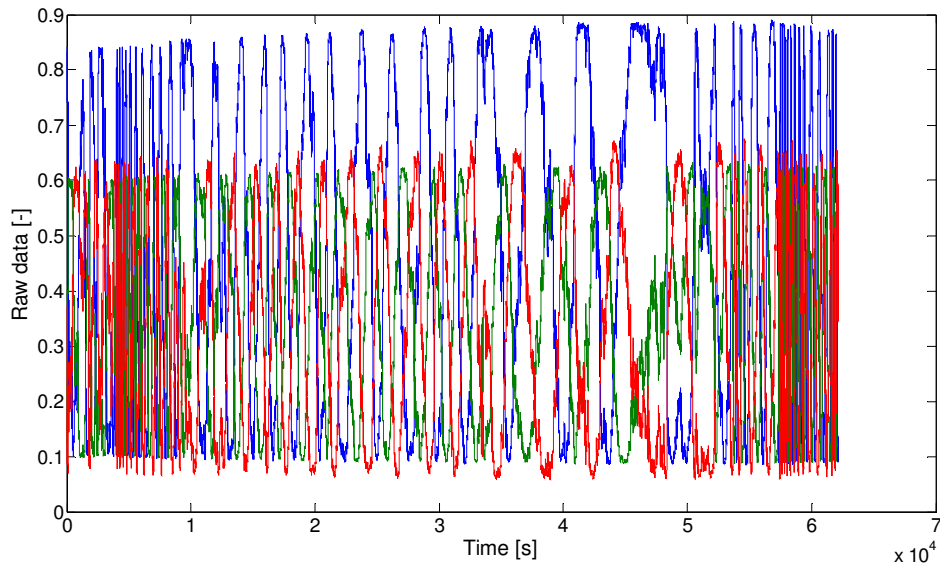


Figure E-14 Raw data from the three ADC's for drift measurement 3

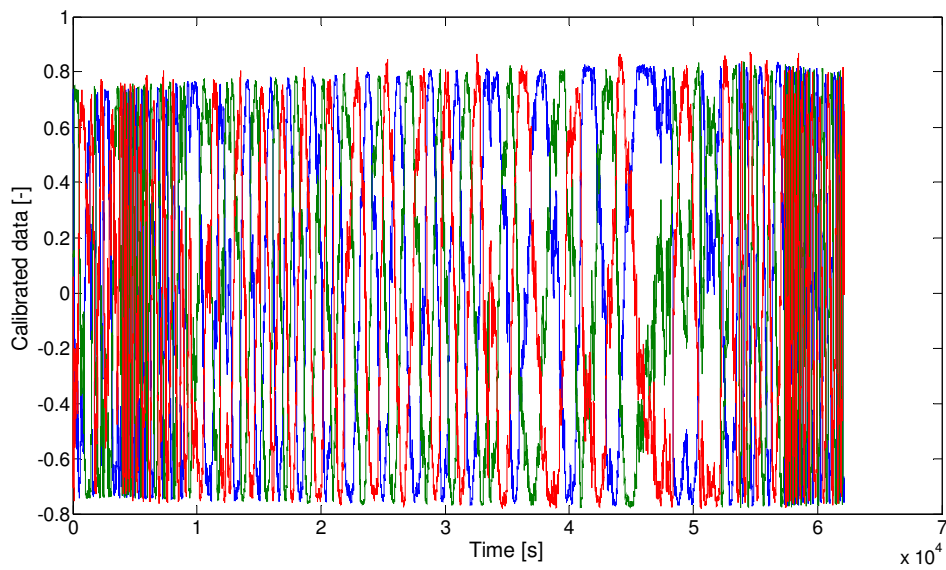


Figure E-15 Calibrated data from the three ADC's for drift measurement 3



Appendix F System improvements

F.1 Stray light maze

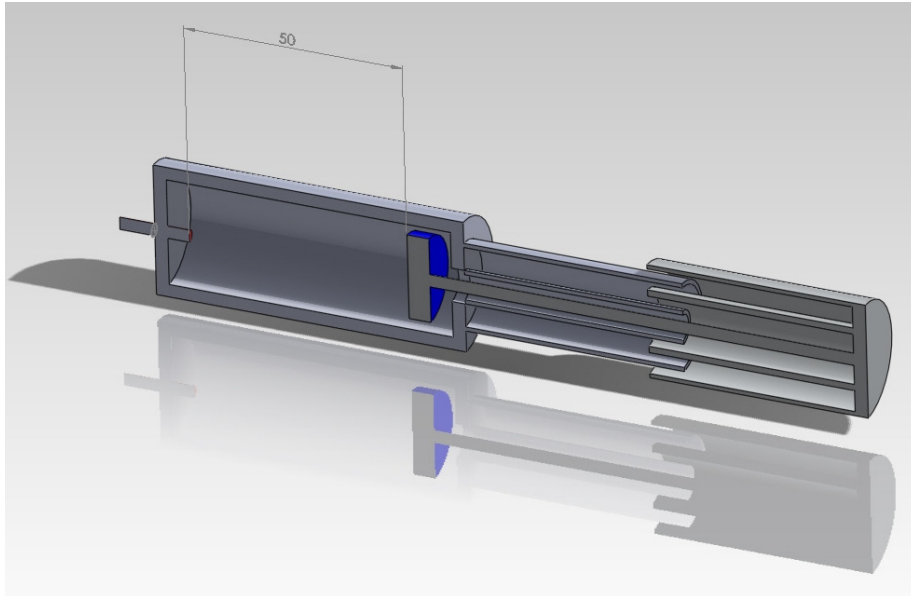


Figure F-1 Stray light maze in folded out configuration

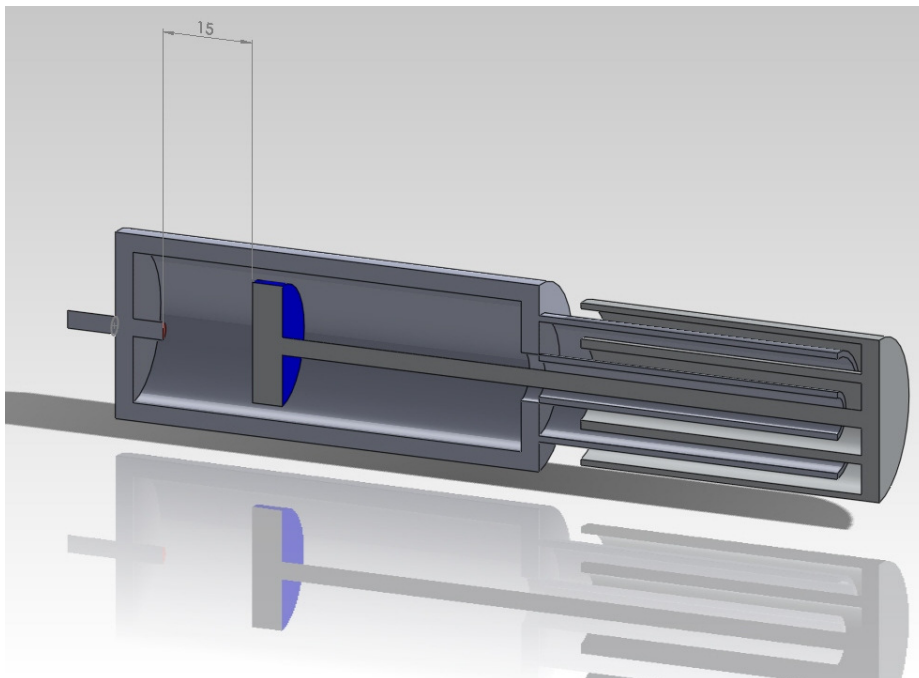


Figure F-2 Stray light maze in folded in configuration



F.2 Stray light maze dimensions

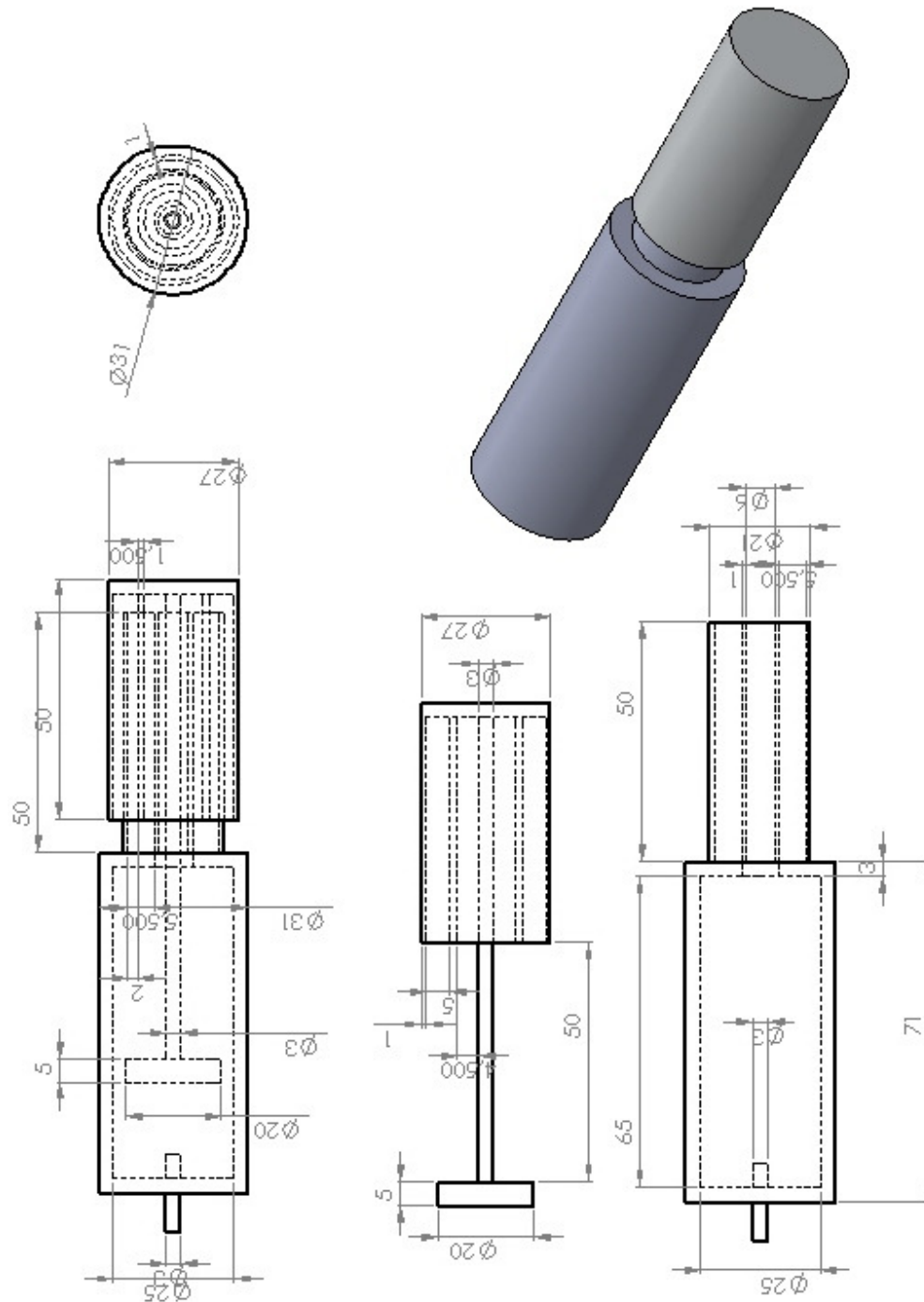


Figure F-3 Dimensions of the stray light maze

Appendix G Datasheets

G.1 Laser datasheets



RIO ORION™ Series 1550nm Low Phase Noise Narrow Linewidth Laser Module

Key features

- Single longitudinal mode
- Center wavelength: 1530nm-1565nm, ITU-T DWDM 100 GHz C-band or custom
- Low phase noise
- Very narrow linewidth, long coherence length
- Ultra low RIN
- Excellent SMSR
- Unmatched wavelength stability over life and temperature
- Wavelength tunability
- Direct power modulation
- Extremely low sensitivity to vibration and acoustic noise
- SMF and PM fiber pigtail options
- Compact size, low power dissipation
- Easy to set-up and use
- Digital controller and firmware with multiple (SPI, RS-232, RS-485) interface options
- Telcordia GR-468 qualified
- RoHS compliant

Applications

- Interferometric fiber optic sensing
- Brillouin Distributed Temperature and Strain Sensors (DTSS)
- LIDAR
- Test & Measurement

Data Sheet
May 2011



Description

The ORION™ devices are compact laser modules employing the RIO high-performance External Cavity Laser (ECL). This laser design is based on RIO's proprietary planar technology (PLANEX™) and consists of a gain chip and a planar lightwave circuit including waveguide with Bragg grating, forming a laser cavity with significant advantages, such as:

- Low phase and frequency noise, narrow linewidth
- Low relative intensity noise (RIN)
- High stability, compact planar mechanical design
- Small form factor, low power dissipation package
- Fast wavelength tuning and power modulation

These features enable the ORION™ module to provide a stable, self-contained, easy-to-use alternative to complicated, sensitive to the ambient environment and expensive fiber laser sources.

The ORION™ module uses reliable, Telcordia qualified and industry proven components, and employs low noise, digital laser bias current and temperature control circuitry to set and monitor laser performance. External monitoring and control can be employed via a standard interfaces, using RIO-supplied software. The ORION™ module is an ideal source for commercial and military fiber optic sensing applications, such as interferometric and Brillouin DTSS systems for oil & gas, security and smart infrastructure.

Rev.0.1.1

Proprietary Information
© Redfern Integrated Optics (RIO), Inc.
3350 Scott Blvd, Bldg 62
Santa Clara, CA 95054 USA

Tel (408) 970 3500
Fax (408) 970 3200
sales@rio-inc.com

All preliminary information contained herein is believed to be accurate and is subject to change without notice. No responsibility is assumed for its use. Redfern Integrated Optics, Inc., its subsidiaries and affiliates, or manufacturer, reserve the right to make changes, without notice, to product design, product components, and product manufacturing methods. Some specific combinations of options may not be available. Please contact Redfern Integrated Optics for more information. ©Redfern Integrated Optics, Inc. All rights reserved.



Absolute Maximum Ratings

Operation of the device beyond these maximum conditions may degrade device performance, lead to device failure, shorter lifetime, and will invalidate the device warranty.

Parameter	Min	Max	Unit
Storage temperature	- 40	+ 85	°C
Module supply voltage		5.5	V
ESD-susceptibility		500	V
Fiber bend radius	35		mm
Tensile strength, fiber to the package		5	N

Optical and Electrical Specifications

At recommended TEC set temperature T_s and bias current I_b

Parameter	Symbol	Condition	Min	Typ	Max	Unit
Output Optical Power	P_{out}	CW	See ordering information			mW
Power Stability over case temperature range ¹	dP_{out}	0 to +70 °C		±10		%
		+10 to +55 °C		±5		
		≤ ±1 °C			±0.2	
Center Wavelength (ITU grid)	λ	± 40 pm standard ²	1530		1565	nm
Wavelength tuning range ³	λ_T	via TEC temperature change	30			pm
Wavelength stability over case temperature range ¹	$d\lambda$	0 to +70 °C		±10		pm
		+10 to +55 °C		±5		
		≤ ±1 °C			±0.5	
Relative Intensity Noise	RIN	≥ 1kHz			-140	dB/Hz
		≥ 500 kHz	Shot noise limited			
Side Mode Suppression Ratio	SMSR	CW, at specified P_{out}	40			dB
Optical S/N Ratio	S/N	≥ 500 pm from λ	60			dB
Polarization Extinction Ratio ⁴	PER	E-field along slow axis	20			dB
Optical Isolation	ISO		40			dB
Voltage Supply	V_{cc}		4.75	5	5.25	V

1. Customized power and wavelength stability requirements are available upon request.
2. Customized center wavelength and set resolution, including ITU-T C-band is available. See ordering information page
3. Phase continuous wavelength tuning by changing TEC temperature settings. Some performance parameters will change over tuning range.
4. With PM-fiber PANDA option. See ordering information page.

Frequency Stability and Modulation Specifications

Parameter	Symbol	Condition	Min	Typ	Max	Unit
Frequency stability ¹	ν_{rt}	Free running, over 1 hour		± 2	± 4	MHz
	ν_{rb}	Free running, over 8 hours		± 3	± 6	
Fast frequency modulation bandwidth	f_m	Sinusoidal modulation	DC		100 ³	kHz
Frequency fast tuning range ^{2,3}	$\Delta\nu$	Sinusoidal modulation at 10 kHz; input voltage 4V p-p	100	200		MHz p-p
Frequency fast tuning efficiency ³	η_m	Sinusoidal modulation at 10 kHz	25	50		MHz/V
Tuning voltage magnitude	V_{tune}		-4		+4	V
Output power modulation index ²	M	Sinusoidal modulation at 10 kHz; wavelength tuning 100 MHz p-p		5	10	%

1. After 1 hour stabilization, tested with heterodyning of two lasers at constant case temperature.
2. Frequency will lead to modulation of output power.
3. Tuning efficiency will vary over modulation bandwidth. Contact RIO for more information.

Rev. 0.1.1

Proprietary Information
© Redfern Integrated Optics (RIO), Inc.
3350 Scott Blvd, Bldg 62
Santa Clara, CA 95054 USA

Tel (408) 970 3500
Fax (408) 970 3200
sales@rio-inc.com

All preliminary information contained herein is believed to be accurate and is subject to change without notice. No responsibility is assumed for its use. Redfern Integrated Optics, Inc., its subsidiaries and affiliates, or manufacturer, reserve the right to make changes, without notice, to product design, product components, and product manufacturing methods. Some specific combinations of options may not be available. Please contact Redfern Integrated Optics for more information. ©Redfern Integrated Optics, Inc.. All rights reserved.



Linewidth and Phase Noise Specifications

For Product Performance Grades see ordering information. At recommended TEC set temperature T_s and bias current I_b ,

Parameter	Symbol	Conditions	Grade 1	Grade 3	Grade4	Unit
Spectral Linewidth, FWHM ¹	$\Delta\lambda_L$	Measured @ -20	15	5	3	kHz
Phase Noise Typical Values ²	PhN	@ 10 Hz	123	41	20	$\mu\text{rad}/\text{rt-Hz}$
		@ 200 Hz	22	8	4	1 m OPD

1. As measured with RIO's self-heterodyne test setup, value for Lorentzian model.

2. As measured with RIO's interferometric phase noise test setup, OPD in the SM fiber length.

Thermal Specifications

Parameter	Symbol	Condition	Min	Typ	Max	Unit
Operating temperature range (case)	T_c		0		+ 70	$^{\circ}\text{C}$
Power Dissipation	P_{th}	At 50 $^{\circ}\text{C}$ case temperature		4		W
Power Dissipation	P_d	Over case temperature range			6	W
Total current	I_{max}	Over case temperature range			1.5	A

Connectors

#	Description
A	FC/APC connector on pigtailed fiber.
B	Interface D-9 Female connector for power supply, external monitoring and control. Control Interface

Interface connector B

Pin #	Function SPI	Function RS-232	Function RS-485	Note
1	Vcc +5V	Vcc +5V	Vcc +5V	4.75 V Min, 5.25V Max, Regulated, Low noise (<100mVp-p)
2	MISO (output)	Tx	Data +; 1 k Ω diff impedance	
3	MOSI (input)	Rx	Data -; 1 k Ω diff impedance	
4	Modulation (input)	Modulation (input)	Modulation (input)	1 k Ω impedance
5	GND	GND	GND	
6	/Ready-Warning (output)	/Ready-Warning (output)	/Ready-Warning (output)	Active low, needs external pull up
7	/SPI SS (input)	Not used	Not used	3.3 to 5V TTL compatible
8	SPI CLK (input)	Not used	Not used	3.3 to 5V TTL compatible
9	/Enable (input)	/Enable (input)	/Enable (input)	12K internal pull up to Vcc (active low)
Configuration	4-wire SPI slave. Bit order: MSB first. Bit rate: \leq 2 MHz. MISO and MOSI: 3.3V drive, TTL level compatible, data centered on rising clk. /SS: Slave Select (active low). CLK: Idle state is low, data clocked on rising edge.	9600 Baud. 8 Data Bits. No Parity Bit. 1 Stop Bit. No Flow Control. TTL asynchronous serial option available at request	9600 Baud. 8 Data Bits. No Parity Bit. 1 Stop Bit. No Flow Control.	

Rev.0.1.1

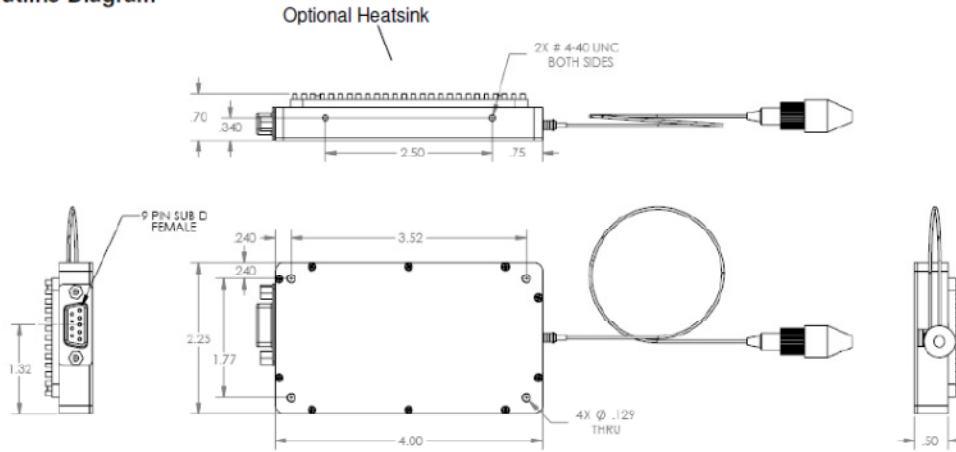
Proprietary Information
© Redfern Integrated Optics (RIO), Inc.
3350 Scott Blvd, Bldg 62
Santa Clara, CA 95054 USA

Tel (408) 970 3500
Fax (408) 970 3200
sales@rio-inc.com

All preliminary information contained herein is believed to be accurate and is subject to change without notice. No responsibility is assumed for its use. Redfern Integrated Optics, Inc., its subsidiaries and affiliates, or manufacturer, reserve the right to make changes, without notice, to product design, product components, and product manufacturing methods. Some specific combinations of options may not be available. Please contact Redfern Integrated Optics for more information. ©Redfern Integrated Optics, Inc. All rights reserved.



Outline Diagram

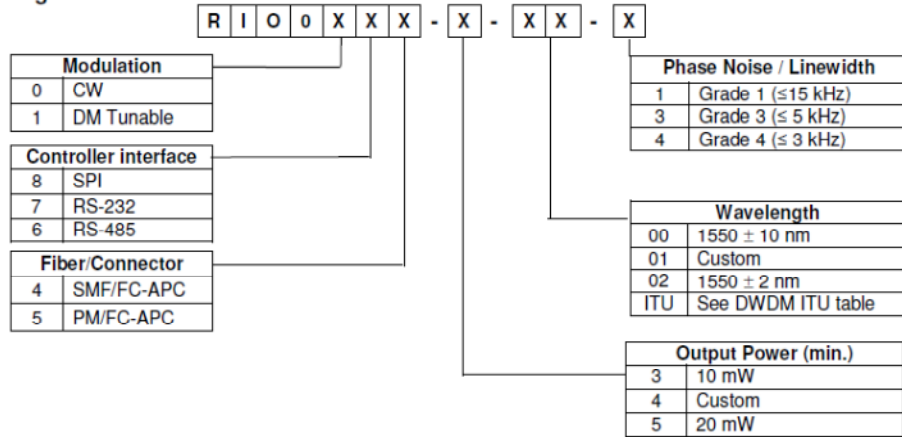


- ORION Housing Material Options:**
- Aluminum (standard)
 - Nickel-plated Copper (optional)

Reliability and Certifications

- Qualified according to Telcordia GR-468-CORE
- CE certified

Ordering Information



Rev.0.1.1
Proprietary Information
 © Redfern Integrated Optics (RIO), Inc.
 3350 Scott Blvd, Bldg 62
 Santa Clara, CA 95054 USA

Tel (408) 970 3500
 Fax (408) 970 3200
 sales@rio-inc.com

All preliminary information contained herein is believed to be accurate and is subject to change without notice. No responsibility is assumed for its use. Redfern Integrated Optics, Inc., its subsidiaries and affiliates, or manufacturer, reserve the right to make changes, without notice, to product design, product components, and product manufacturing methods. Some specific combinations of options may not be available. Please contact Redfern Integrated Optics for more information. ©Redfern Integrated Optics, Inc. All rights reserved.



Accessories

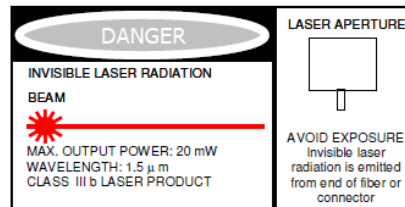
Accessory PN	Description
RIO008X-KIT	5V DC power supply, CD w/ GUI & USB/SPI Aardvark adaptor with cable
RIO018X-KIT	5V DC power supply, CD w/ GUI & USB/SPI Aardvark adaptor with cable (DM Tunable)
RIO007X-KIT	5V DC power supply, CD w/ GUI & RS232 interface cable
RIO017X-KIT	5V DC power supply, CD w/ GUI & RS232 interface cable (DM Tunable)
RIO006X-KIT	5V DC power supply, CD w/ GUI & RS485 interface cable
RIO016X-KIT	5V DC power supply, CD w/ GUI & RS485 interface cable (DM Tunable)
RIO0HS	External heatsink w/ hardware

DWDM ITU Wavelength

ITU channel number	ITU Frequency THz	Wavelength nm	ITU channel number	ITU Frequency THz	Wavelength nm	ITU channel number	ITU Frequency THz	Wavelength nm
15	191.50	1565.50	30	193.00	1553.33	45	194.50	1541.35
16	191.60	1564.68	31	193.10	1552.52	46	194.60	1540.56
17	191.70	1563.86	32	193.20	1551.72	47	194.70	1539.77
18	191.80	1563.05	33	193.30	1550.92	48	194.80	1538.98
19	191.90	1562.23	34	193.40	1550.12	49	194.90	1538.19
20	192.00	1561.42	35	193.50	1549.32	50	195.00	1537.40
21	192.10	1560.61	36	193.60	1548.51	51	195.10	1536.61
22	192.20	1559.79	37	193.70	1547.72	52	195.20	1535.82
23	192.30	1558.98	38	193.80	1546.92	53	195.30	1535.04
24	192.40	1558.17	39	193.90	1546.12	54	195.40	1534.25
25	192.50	1557.36	40	194.00	1545.32	55	195.50	1533.47
26	192.60	1556.55	41	194.10	1544.53	56	195.60	1532.68
27	192.70	1555.75	42	194.20	1543.73	57	195.70	1531.90
28	192.80	1554.94	43	194.30	1542.94	58	195.80	1531.12
29	192.90	1554.13	44	194.40	1542.14	59	195.90	1530.33

Laser Safety Information

Laser Modules are classified as FDA/CDRH Class IIIb laser products per CDRH, 21 CFR 1040 laser safety requirements.



Rev.0.1.1

Proprietary Information
© Redfern Integrated Optics (RIO), Inc.
3350 Scott Blvd, Bldg 62
Santa Clara, CA 95054 USA

Tel (408) 970 3500
Fax (408) 970 3200
sales@rio-inc.com

All preliminary information contained herein is believed to be accurate and is subject to change without notice. No responsibility is assumed for its use. Redfern Integrated Optics, Inc., its subsidiaries and affiliates, or manufacturer, reserve the right to make changes, without notice, to product design, product components, and product manufacturing methods. Some specific combinations of options may not be available. Please contact Redfern Integrated Optics for more information. ©Redfern Integrated Optics, Inc.. All rights reserved.



G.2 Laser test report



Test Report RIO ORION™ Laser Module

Serial Number	800473
Part Number	RIO0174-3-00-1
Test Date	11/23/2010
Operator	PB
QA	GM

Parameter	Value	Units
Firmware Version	0.9.3	-
Operating thermistor resistance (Rset)*	6.05	kΩ
Operating bias current (Ibias)	110	mA
Maximum bias current (Imax)	130	mA
Output Power at Rset and Ibias	11.1	mW
Center wavelength at Rset and Ibias	1550.148	nm
Linewidth (FWHM from Lorentzian -20dB)	13.9	kHz
Side Mode Suppression Ratio at Rset and Ibias	56	dB

*Corresponding to operating temperature of: 37 °C

Rev.0.1.0

Proprietary Information

© Redfern Integrated Optics, Inc. (RIO)
3350 Scott Blvd, Bldg 62
Santa Clara, CA 95054 USA

Tel (408) 970 3500
Fax (408) 970 3200
sales@rio1.com

800473



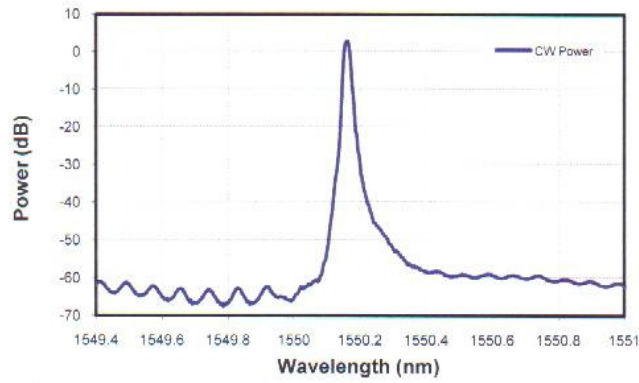


Fig. 1: Spectrum (CW, Rset, Ibias)

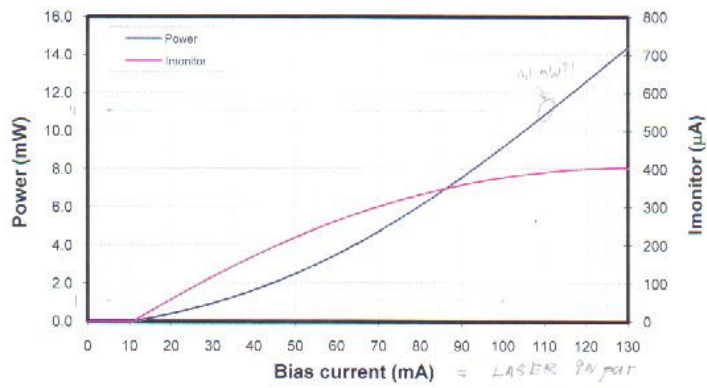


Fig.2: Laser Output Power and Imonitor vs. Bias Current at Rset

Rev.0.1.0
Proprietary Information
 © Redfern Integrated Optics, Inc. (RIO)
 3350 Scott Blvd. Bldg 62
 Santa Clara, CA 95054 USA

Tel (408) 970 3500
 Fax (408) 970 3200
 sales@rio1.com

800473



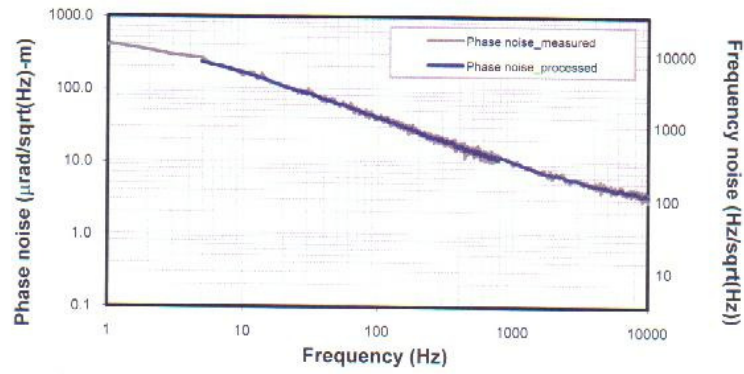


Fig. 3: Phase Noise at Rset, Ibias, normalized to 1m path difference

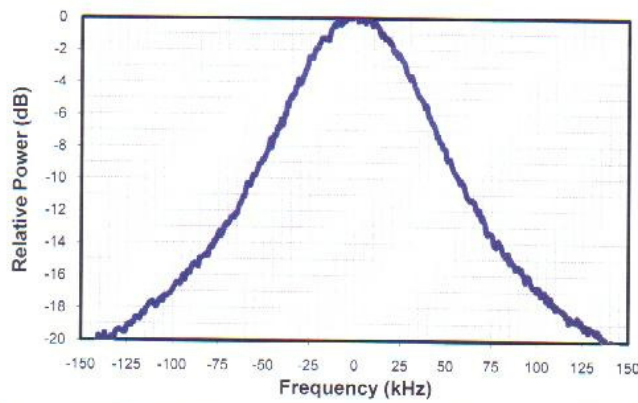


Fig. 4: Linewidth (CW, Rset, Ibias) measured using self-heterodyne, 100 MHz IF frequency.

G.3 Datasheet circulator



**Opto-Link
Corporation Ltd**

Polarization Independent Optical Circulators

Fiber Optic Circulator is a non-reciprocal device that redirects light from port to port in one direction. The device is designed for use in WDM systems, optical amplifiers and sensor applications. The component features high power, high isolation, high return loss, and excellent environmental stability.

Types


- 3 & 4 Ports
- High Power (300/1000mW)
- 1310nm/1550nm Window

Applications

- WDM Systems
- Dispersion Compensation
- Sensor Applications
- Optical Amplifiers
- OTDR Applications

Features

- Excellent Stability and Reliability
- High Isolation
- High Return Loss
- Low Insertion Loss
- Low Polarization Dependent Loss
- Low Polarization Mode Dispersion



COPYRIGHT © 2002-2007 Opto-Link Corporation Ltd.
Tel: +852 2480-6106 Fax: +852 2480-1621 Email: contact@optolinkcorp.com Website: www.optolinkcorp.com



SPECIFICATIONS

Polarization Independent Optical Circulators (1310nm, 1550nm)

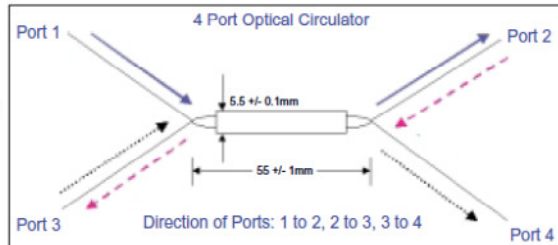
Parameter	3 ports	4 ports	Units
Wavelength Range	1310, 1550	1310, 1550	nm
Transmitting Direction	1->2, 2->3	1->2, 2->3, 3->4	--
Insertion Loss	< 0.8	< 0.8	dB
Channel Isolation	> 50	> 45	dB
PDL	< 0.1	< 0.15	dB
PMD	< 0.05	<0.05	ps
TDL	0.15	0.15	dB
WDL	0.15	0.15	dB
Return Loss	> 50	> 50	dB
Cross Talk	> 50 (up to 60)	> 50 (up to 60)	dB
Handling Power	300, 1000	300, 1000	mW
Operating Temperature	0 to +70	0 to +70	°C
Storage Temperature	-40 to +85	-40 to +85	°C

*Above specifications are for device without connectors.

Polarization Independent Optical Circulators (C+L Band)

Parameter	3 ports	4 ports	Units
Wavelength Range	1525 - 1610	1525 - 1610	nm
Transmitting Direction	1->2, 2->3	1->2, 2->3, 3->4	--
Insertion Loss	< 0.9	< 1.2	dB
Channel Isolation	> 40	> 30	dB
PDL	< 0.15	< 0.2	dB
PMD	< 0.05	< 0.05	ps
TDL	0.2	0.2	dB
WDL	0.4	0.4	dB
Return Loss	> 50	> 50	dB
Cross Talk	> 50	> 50	dB
Handling Power	500	500	mW
Operating Temperature	0 to +70	0 to +70	°C
Storage Temperature	-40 to +85	-40 to +85	°C

*Above specifications are for device without connectors.



ORDERING CODES

OLCIR - I - [] - [] - [] - []

Port	Code
3 ports	3
4 ports	4

Handling Power	Code
300mW	300
1000mW	1000

Wavelength	Code
1310 nm	131
1550 nm	155
1525 - 1610nm	CL

Cable Diameter	Code
250 um	25
900 um	90

Connector Type	Code
No Connector	NC
FC/PC	FP
SC/PC	SP
FC/APC	FA
SC/APC	SA
LC/PC	LP
MU/PC	MP
Others	XX

■ Opto-Link Corporation Ltd. reserves the right to make changes to the products described herein without notice.

COPYRIGHT © 2002-2007 Opto-Link Corporation Ltd.
 Tel: +852 2480-6106 Fax: +852 2480-1621 Email: contact@optolinkcorp.com Website: www.optolinkcorp.com

G.4 Test datasheet circulator

CIRCULATOR TEST DATA SHEET

$T_{trans} = 10^{\left(-\frac{dB}{10}\right)}$

Description: 3-port 1550nm circulator, P grade, SMF-28e with 900um loose tube, 1m, FC/APC connector, 300mw

Part Number: OLCIR-1-3-155-300-90-FA
S/N: 10000185

Parameters	Unit	Specification	Test Data
Operating Wavelength	(nm)	1550 ± 30	1550 ± 30
Max. Insertion Loss(Port1 to Port2) 1→2	(dB)	≤ 1.1	0.99 ✓
Max. Insertion Loss(Port2 to Port3) 2→3	(dB)	≤ 1.1	0.98 ✓
PDL(Port1 to Port2) Polarization dependent loss	(dB)	≤ 0.10	0.03
PDI(Port2 to Port3)	(dB)	≤ 0.10	0.05
Minimum Isolation 2→1 ?	(dB)	≥ 40	53
DIR directivity (1→3) = cross talk	(dB)	≥ 50	60
Return Loss bv. 1→1 ?	(dB)	≥ 60	60
PMD Polarization mode dispersion	(ps)	< 0.1	0.03
Power Handling	(mW)	300	
Operating Temperature	(°C)	-40-70	
Storage Temperature	(°C)	-40-85	
Dimension	mm	∅ 5.5×50	

Port1 (red) SN: XXXXXX Port2 (blue)

Port3 (white)

Tested By: Xie Xialing Date: 2010-10-06 Reviewed by: Gong Jia Date: 2010-10-06

G.5 Datasheet 3x3 splitter

Specifications for 1xN, MxN Truly Fused Tree & Star Couplers				
Port Configuration	1x3	3x3	1x4	2x4 or 4x4
Insertion Loss	≤ 5.8dB	≤ 6.2 dB	≤ 7.0 dB	≤ 8.0 dB
Uniformity	≤ 1.0 dB	≤ 2.0dB	≤ 1.0 dB	≤ 2.0dB
Wavelength	1310 or 1550nm			
Typical Directivity	≥ 65dB for NxN ≥ 40dB for 1xN			
Typical Thermal Stability	≤ ±0.1dB			

Specifications for 1X3 couplers and 1x4 couplers		
Desired Split Ratio	Insertion Loss(dB)	Product Number
10/45/45	11.5/4.5/4.5	23-403XX-13-11201
20/40/40	8.0/5.0/5.0	23-403XX-13-21201
30/35/35	6.2/5.6/5.6	23-403XX-13-31201
33/33/33	5.8/5.8/5.8	23-403XX-13-01201
40/30/30	5.0/6.2/6.2	23-403XX-13-41201
50/25/25	4.0/7.0/7.0	23-403XX-13-51201
60/20/20	3.2/8.2/8.2	23-403XX-13-61201
70/15/15	2.5/9.6/9.6	23-403XX-13-71201
80/10/10	2.0/11.5/11.5	23-403XX-13-81201
25/25/25/25	7.3/7.3/7.3/7.3	23-403XX-14-01201
40/20/20/20	4.9/8.3/8.3/8.3	23-403XX-14-41201
40/20/20/20	5.5/9.3/9.3/9.3	23-403XX-24-41201
40/20/20/20	5.5/9.3/9.3/9.3	23-403XX-34-41201
40/20/20/20	5.5/9.3/9.3/9.3	23-403XX-34-41201

XX=31 for 1310
XX=55 for 1550

Ordering Information

Product Number: (For Corning SMF-28 Fiber)

23 - 4 _____ - _____ - _____ 1 2 _____ 1

03 = 100 kpsi	Wavelength	Port configuration	Split ratio	Package Style	Connector Style
32 = 200 kpsi	31 = 1310nm 55 = 1550nm	13 = 1X3 33 = 3X3 14 = 1X4 44 = 4X4		12, or Modular Boxes	0 = None See connectors link below

Specifications	
Central Wavelengths	1270-1350 OR 1510-1590nm
Insertion Loss	See chart below
Uniformity	≅ 1.5 dB for 33/33/33 split
Typical Directivity	≅ 50dB
Typical Thermal Stability	≅ ±0.1dB over -40°C to 85°C
Packaging	Comes in package 12 and can be repackaged into modular boxes. See package link below.

Specifications for 1X3 couplers and 1x4 coupler		
Desired Split Ratio	Insertion Loss (dB)	Product Number
20/40/40	8.2/5.2/5.2	46-403XX-13-21201
30/35/35	6.2/5.6/5.6	46-403XX-13-31201
33/33/33	6.0/6.0/6.0	46-403XX-13-01201
40/30/30	4.7/6.4/6.4	46-403XX-13-41201
50/25/25	3.6/7.3/7.3	46-403XX-13-51201
60/20/20	2.7/8.4/8.4	46-403XX-13-61201
70/15/15	1.9/9.6/9.6	46-403XX-13-71201
80/10/10	1.3/11.7/11.7	46-403XX-13-81201
25/25/25/25	7.5/7.5/7.5/7.5	46-403XX-14-01201
		XX=31 for 1310±40 XX=55 for 1550±40

Ordering Information

Product Number: (For Corning SMF-28 Fiber)

46 - 4 _____ - _____ - 0 _____ 1

Fiber code	Wavelength	Port configuration	Package style	Connector Style
03 = 100 kpsi	31 = 1310nm	13 = 1X3	Use modular box enclosures only. See link	0 = None
32 = 200 kpsi	55 = 1550nm	14 = 1X4		See link below



G.6 Test datasheet 3x3 splitter

For information or questions:
 Gould Fiber Optics
 1121 Benfield Boulevard
 Millersville, MD 21108 U.S.A.
 Telephone: 410-987-5600
 FAX: 410-987-1201



DEFINITION OF COUPLER TERMS

I. COUPLERS/SPLITTERS



- A. EXCESS LOSS (dB): $-10 \text{ Log} \left(\frac{O1+O2}{I1} \right)$
- B. COUPLING RATIO (%) $\left(\frac{O2}{O1+O2} \right)$
- C. COUPLING LOSS (dB): O1 Port = $-10 \text{ Log} \left(\frac{O1}{O1+O2} \right)$, O2 Port = $-10 \text{ Log} \left(\frac{O2}{O1+O2} \right)$
- D. INSERTION LOSS (dB): Excess Loss + Coupling Loss + Polarization Effects (singlemode only)
- E. UNIFORMITY (dB): Maximum Insertion Loss - Minimum Insertion Loss
- F. DIRECTIVITY (dB): $-10 \text{ Log} \left(\frac{I2}{I1} \right)$ (with all outputs terminated for zero reflection)
- G. POLARIZATION (singlemode only) AND THERMAL STABILITY: Maximum change in coupling ratio through all polarization orientations and/or specified temperature ranges.
- H. Gould multimode and large core couplers are manufactured and tested under fully filled launch conditions.

II. SINGLEMODE WAVELENGTH DIVISION MULTIPLEXERS/DEMULTIPLEXERS



- A. INSERTION LOSS (dB): Excess Loss + Coupling Loss at λ_1 and λ_2 .
- B. ISOLATION (dB): The optical power separation in channels O1 and O2 between the specified wavelengths. Assumes input levels are the same for each wavelength.

Gould products may be manufactured under one or more of the following U.S. patents: Re.33,298 (4,632,513), 4,798,438, 4,834,481, 4,772,065, 5,355,426, 5,644,666, 5,500,917, 5,682,453, 5,809,198. Product may be manufactured under license from British Telecommunications, plc. U.S. patent 4,798,436 and corresponding foreign patents may apply. 44-0149 Rev. B

TEST RESULTS

Serial Number..... 4158333
 Fiber Type.....Corning SMF-28, 100kpsi
 Test Date.....17-Nov-10

Test Wavelength..... 1550 nm
 CLEAR -----> CLEAR.. 5.83 dB
 CLEAR -----> ORANGE.. 4.97 dB
 CLEAR -----> BLUE... 5.87 dB

ORANGE -----> CLEAR.. 5.16 dB
 ORANGE -----> ORANGE 5.16 dB
 ORANGE -----> BLUE.. 4.47 dB

BLUE -----> CLEAR... 4.53 dB
 BLUE -----> ORANGE.. 5.21 dB
 BLUE -----> BLUE.... 4.97 dB

If this product is supplied with bare fiber leads, it is the responsibility of the end-user to handle the product with the appropriate care. Especially when installing connectors or routing the fibers in trays and racks. Gould will not honor any warranty claims for damage to any device caused by mishandling of bare fiber leads.

Serial Number Suffixes: Some Gould products may contain serial numbers that contain an 'R' or 'B' suffix. 'R' indicates that the coupler contains red identification markings on the input and output leads. 'B' indicates that the coupler contains blue identification markings on the input and output leads.

DATASHT\TEMPLATE\3X3.XLS
 Issue 970721

Gould Technology LLC
 1121 Benfield Blvd
 Millersville, MD 21108
 USA

00-0948 G.xls

Tel: 410-987-5600
 Fax: 410-987-1201
 Email: info@gouldfo.com
 Web: www.gouldfo.com

G.7 Datasheet Grin lens



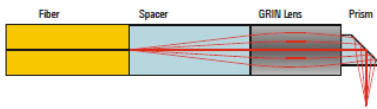
Customized GRIN Lens Assemblies

GRIN Fiber Pigtails

Applications: fiber optical sensors, biophotonic probes, optical switches, fiber coupling

- Fiber Pigtails using Gradient Index Rod Lenses
- Focussing, collimating and imaging GRIN lenses
- Use of special fibers on request
- AR and beam splitting coatings on request
- 8° angled facet of fiber and optics possible

Please ask for customized solutions



Examples:

Fiber optic sensor



- mounted in stainless steel tube
- GRIN lens diameter: 0.5 / 1.0 / 1.8 mm
- Tube diameter: 0.7 / 1.2 / 2.0 mm
- Side opening for prism exit possible



- SMF Pigtail using glass ferrule and capillary
- GRIN lens diameter: 1.8 mm
- Capillary diameter: 2.8 mm



- SMF Pigtail using glass ferrule, mounted in stainless steel tube
- GRIN lens diameter: 0.5 / 1.0 / 1.8 mm
- Tube diameter: 0.7 / 1.2 / 2.0 mm



- Multimode Fiber Pigtail using customized SMA 905 connector and integrated GRIN lens

Variations due to modifications of the production process are possible.
It is the user's responsibility to determine suitability for the user's purpose.

GRIN Arrays

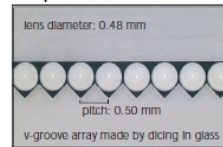
Linear Lens Arrays for collimation / imaging of fiber bundles

Application: telecom components, optical switches, sensor arrays

- 1x8, 1x12, 1x16 GRIN Rod Lens Arrays
- Pitches 250 (± 1) μm / 500 (± 1) μm
- Lens diameter: 240 (± 1) μm / 480 (± 1) μm
- Lens NA: 0.35 / 0.5 / 0.2

Please ask for customized solutions

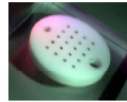
Example:



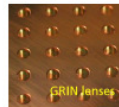
2-D Lens Arrays

Application: multi-imaging sensors, read-out of biochips

Examples:



- 4x5 GRIN Rod Lens
- Array Pitch: 1.60 (± 0.01) mm
- Lens diameter: 1.0 mm
- Lens NA: 0.6
- Mount: machinable ceramic



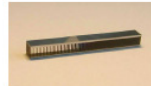
- Pitch: 4.50 (± 0.02) mm
- Lens diameter: 1.8 mm
- Lens NA: 0.6
- Mount: brass

Cylindrical Lens Arrays

Application: line pattern generation, 1:1 imaging, slow axis divergence reduction of HPDL-bars (SAC arrays)



- Pitch: 0.5 / 1.0 / 1.3 mm
- NA of single lens: 0.2 / 0.5
- Suppression of crosstalk by absorber layers possible
- Beam homogenization



Revision 03/2009

GRINTECH GmbH

Schillerstraße 1
07745 Jena, Germany

Phone: +49 (0) 3641 / 2276-0
Fax: +49 (0) 3641 / 2276-11

www.grintech.de
info@grintech.de

G.8 Datasheet connector

DIAMOND

Fiber Optic Components

CABLE ASSEMBLIES AND ADAPTERS

The Mini-AVM connector has been developed after market request of a smaller and lighter version of our acclaimed AVM connector for harsh environment, especially space applications. The Mini-AVM combines two leading edge technologies: the AVM MIL-style fiber system and the base construction of Diamond Micro Interface (DMI) connector. Commercial Off-The-Shelf (COTS) availability and economy backed by component availability from stock and quick turnaround of terminations and assemblies. The Mini-AVM is aligned precisely in rotation and therefore it can be used for both standard SM and MM fibers, as well as for PM technologies and multi-fiber bundles. Our Power Solution (PS) technology can also be applied to this connector. Harsh environment applications will range from Space to underwater, applying to mobile, aviation, shipboard, oil coverhole, etc.

FEATURES

- Compact, small and lightweight
- Low loss thanks to Diamond Active Core Alignment (ACA)
- High return loss thanks to Diamond polishing technique and A.C.A.
- Miniatured MIL-style retainer system with high vibration shock resistant
- AlTiN/AlN - ZrO2 material for ultra low CTE mismatch

STANDARDS

- ESCC 226910 Follows ESA standard for space
- The Mini-AVM is now following an ESTEC Qualification program, due to be completed by the end of 2011

AVAILABLE AS

- Termination connector (commercial, enhanced or space grade)
- Connector set to be terminated with Diamond special equipment
- Multi-fiber custom connector set as assembled terminations
- Mating adapters (commercial, enhanced, space grade)

Mini-AVM

SINGLE MODE FC/APC
MULTIMODE FC/APC
PM FC/APC
FS APC*

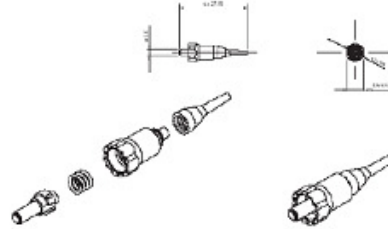


MINI-AVM CONNECTOR DIMENSIONS

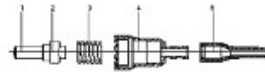
Connectors for 900um buffer coatings for loose tube up to 12mm cable

Available types: Mini-SM FC, APC, PM, FS

Material: According to part list



BILL OF MATERIAL - BOM



POS.	DESCRIPTION	NAME	MATERIAL	AVIM	WEIGHT (g.)
1	Pinset	Coaxial Titanium	ZrO ₂ UNIS P2000		0.27
2	DM-4mg	Titanium	UNIS R6600		0.00
3	DM-FRP	Substrate Glass	S439F		0.12
4	Outer shell	Titanium	UNIS R6600		0.69
5	MINI-AVM EXACT BOLT	Thermally Stable Titanium (C417)	UNIS 0007		0.00
				Total	1.12

*APC/APC/PM & FS connector only

NOTE: Diamond standard color codes are as follows: Black for MM and SM FC, and green for SM APC.

ORDER INFORMATION

When ordering mating adapters, please refer to the part numbers provided in the enclosed PM list. When ordering pigtail or cable assemblies, please refer to the connector type description in the Available types section, and fill in the Simulux, Duplex, Multiple Fiber Assemblies order form according to those descriptions.



DIAMOND SA - Via del Poggio 7 - 00196 Lariano - Tel: 0761 24211
SA - Via del Poggio 45-47 - FS - 01191 766 65 00 - 0761 242111 (fax)
www.diamond-fp.com

CONNECTOR SUBJECT TO CHANGE WITHOUT NOTICE

4/5

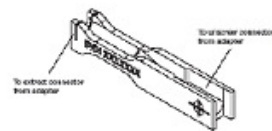
SPECIFICATIONS

Mechanical Performance	MINI-AVM - TECHNICAL CHARACTERISTICS		Standards	MINI-AVM ADAPTER DIMENSIONS		Standards
	CONNECTIONS (DIN)	CONNECTIONS (DIN)		CONNECTIONS (DIN)	CONNECTIONS (DIN)	
Working capacity	2M mating cycles	5.010E	IEC 61089-2-1	2M mating cycles	ESCC 226910	
Shock, impact	6 Gmp, 10ms, 10ms	5.010E	IEC 61089-2-1 method B	10000 shock pgs per min	ESCC 226910	
Vibration	Sine, 10g, 10ms	5.010E	IEC 61089-2-1	104g random 10ms per axis	ESCC 226910	
Environment Characteristics						
Operating temperature	-40°C to +85°C, 1h	5.010E	IEC 61089-2-1	-55°C to +125°C, 2000h	ESCC 226910	
Min. operating temperature	-40°C to +125°C	5.010E	IEC 61089-2-1	Min. 50 years	ESCC 226910	
Temperature shock	NA	NA	NA	NA	ESCC 226910	
Case	100% 40%	5.010E	IEC 61089-2-1	100% 40%	ESCC 226910	
HTH test	100% 40%	5.010E	IEC 61089-2-1	100% 40%	ESCC 226910	
Emp test	100% 40%	5.010E	IEC 61089-2-1	100% 40%	ESCC 226910	
Flammability	NA	NA	NA	100% 40%	ESCC 226910	
Optical Characteristics	For ISO 6382 fiber			For ISO 6382 fiber		
Insertion Loss, IL	0.14dB typical (max) 0.20dB	5.010E	IEC 61089-2-1 method B	0.20dB typical, max 0.26dB	ESCC 226910	
Return Loss, RL	FC: >40dB, APC: >50dB	5.010E	IEC 61089-2-1 method B	FC: >40dB, APC: >50dB	ESCC 226910	
Extinction Ratio, ER	FC: >20dB, APC: >30dB	5.010E	IEC 61089-2-1	FC: >20dB, APC: >30dB	ESCC 226910	
Characteristics Characteristics	Characteristics Characteristics					
Termination	2M, 10 cycles 100%	5.010E	IEC 61089-2-1	NA		
Mini-terminated	4.7M, 10% 100%	5.010E	IEC 61089-2-1			
Mini-terminated	NA, 100%	5.010E	IEC 61089-2-1			
Embedding element	100% 4-5mm	5.010E	IEC 61089-2-1			

* Mini-Centering PM/Diamond fiber

ESCC (ESA) Space Component Code/notes

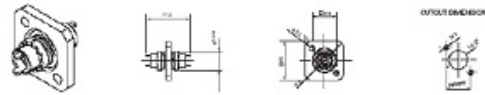
MINI-AVM MOUNTING TOOL



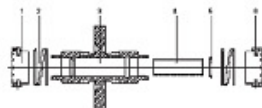
MINI-AVM ADAPTER AND DIMENSIONS

Available type: Square flange adapter for wall mount

Material: According to part list



BILL OF MATERIAL - BOM



POS.	DESCRIPTION	NAME	MATERIAL	PC BOM	WEIGHT (g.)
1	Anti-reflection ring (AR)	Titanium	UNIS R6600		0.29
2	Anti-reflection ring (AR)	Steel case steel	L43 10		0.07
3	Wedge body	Titanium	UNIS R6600		0.11
4	Splice sleeve	Zirconium	DMC		0.19
5	Clip for splice sleeve	Steel case steel	L43 10		0.01
6	Pin for Anti-reflection ring (AR)	Steel case steel	L4305		0.01
				Total	0.67

G.9 Datasheet optical fiber

Corning® SMF-28e+® Photonic Optical Fiber

CORNING



*A full spectrum fiber
for components and
assemblies with
tighter geometry for
more consistent
splicing*

*Corning's SMF28e+®
photonic fiber provides
further evidence of
Corning's long history of
service to original
equipment
manufacturers (OEMs).
This fiber's attributes are
specifically customized for
optical connectorization
and component
applications, allowing
OEMs to reduce
manufacturing costs,
standardize processes, and
improve performance.*

Applications:

- Connectors
- EDFA
- Couplers
- Pigtails
- DWDM components
- Other components

Features:

- Industry-leading optical and geometry specifications
- Exceptional performance and splice-ability
- Suitable for all transmission systems and fully compatible with SMF-28e+® optical fiber, the world's most widely demanded full-spectrum fiber
- In compliance with, or exceeds the industry's most stringent requirements including:
 - ITU-T Recommendations G.652 (Tables A, B, C & D)
 - IEC Specifications 60793-2-50 Type B1.3
 - TIA/EIA 492-CAAB
 - Telcordia Generic Requirements GR-20-Core
 - ISO 11801 OS2
- Improved macro-bend specification from less than 0.05 dB to less than 0.03 dB, allowing better handling and ease of installation
- Tighter zero dispersion wavelength specification
- New coating for improved micro-bending
- Smaller coating outside diameter (242 µm nominal) for improved usage in ribbon applications

SMF-28e+^{*} Photonic

Optical Specifications

Fiber Cutoff Wavelength (λ_{ct})	≤ 1280 nm	
	Wavelength (nm)	Maximum Value* (dB/km)
	1310	≤ 0.35
Maximum Attenuation	1383 \pm 3**	≤ 0.35
	1490	≤ 0.24
	1550	≤ 0.20
	1625	≤ 0.23
* Maximum specified attenuation value available within the stated ranges		
** Attenuation post-hydrogen aging according to IEC 60793-2-50 Section C.5 for B.1.3 fibers.		
Mode-field Diameter	Wavelength (nm)	MFD (μ m)
	1310	9.2 \pm 0.4
	1550	10.4 \pm 0.5
Dispersion	Wavelength (nm)	Dispersion Value [ps/(nm \cdot km)]
	1550	≤ 18.0
	1625	≤ 22.0
Zero Dispersion Wavelength (λ_0): 1304 nm \leq λ_0 1324 nm		
Zero Dispersion Slope (S_0): ≤ 0.088 ps/(nm 2 \cdot km)		
Polarization Mode Dispersion (PMD)	Value (ps/ \sqrt km)	
PMD Link Design Value	$\leq 0.06^*$	
Maximum Individual Fiber	≤ 0.1	
* Complies with IEC 60794-3: 2001, Section 5.5, Method 1, September 2001		
The PMD link design is a term used to describe the PMD of concatenated lengths of fiber (also known as PMD ₀). This value represents a statistical upper limit for total PMD. Individual PMD values may change when fiber is cabled. Corning's fiber specification supports network design requirements for 0.5 ps/ \sqrt km maximum PMD.		
Point Discontinuity	Wavelength (nm)	Point Discontinuity (dB)
	1310	≤ 0.05
	1550	≤ 0.05

SMF-28e+* Photonic

Key Geometric, Mechanical and Environmental Specifications

Cladding Diameter (µm)	125.0 ± 0.3
Core-Clad Concentricity (µm)	≤ 0.3
Cladding Non-Circularity (%)	≤ 0.7
Core Diameter (µm)	8.2
Coating Diameter (µm)	242 ± 5
Coating-Cladding Concentricity (µm)	< 12
Coloring Diameter* (µm)	250 +15/-9
Fiber Curl (m)	≥ 5.0 radius of curvature

* If applicable

Environmental Test	Test Condition	Induced Attenuation 1310 nm, 1550 nm & 1625 (dB/km)
Temperature Dependence (°C)	-60 to 85 *	≤ 0.05
Temperature-Humidity Cycling (°C)	-10 to 85 * up to 98% RH	≤ 0.05
Water Immersion (°C)	23 * ± 2	≤ 0.05
Dry Heat Soak (°C)	85 * ± 2	≤ 0.05
Damp Heat (°C)	85 * at 85% RH	≤ 0.05
Operating Temperature Range (°C)	-60 to 85	
Proof Test (kpsi)	≥ 200	
Lengths	Available up to 50.4 km per spool	

* Reference temperature: 23°C

Performance Characterizations*

Numerical Aperture	0.12		
Refractive Index Difference (%)	0.36		
Effective Group Index of Refraction (N_{eff})	1.4670 @ 1310 nm 1.4677 @ 1550 nm		
Fatigue Resistance Parameter (N_f)	20		
Coating Strip Force	Dry: 0.6 lb. (3N) Wet 14 day room temperature: 0.6 lb. (3N)		
Rayleigh Backscatter Coefficient	-77 dB @ 1310 nm -82 dB @ 1550 nm		
Macrobend Loss			
Mandrel Diameter (mm)	Number of Turns	Wavelength	Induced Attenuation** (dB)
32	1	1550	≤ 0.03
50	100	1310	≤ 0.03
50	100	1550	≤ 0.03
60	100	1625	≤ 0.03

* Values in this table are nominal or calculated values

** The induced attenuation due to fiber wrapped around a mandrel of a specified diameter.

The Single-Mode Fiber for Connectors and Components

Corning uses its legendary geometry control and quality leadership to manufacture SMF-28e+[®] photonic fiber. We focus on tailoring product attributes that allow OEMs to minimize scrap and overall insertion loss while improving active and splice performance. Through precise manufacturing techniques, we assure geometric performance along the entire length of fiber while maintaining nominal mode-field performance.

We proof stress the entire length of SMF-28e+[®] photonic fiber to ≥ 200 kpsi, which provides OEMs with increased reliability and reduced handling concerns. In addition, we specify a fiber cutoff wavelength of 1280 nm, enabling operability at both 1310 nm and 1550 nm in bare fiber applications.

Designed for Versatility and Performance

For better understanding of the applicable value to customers, Corning has completed studies using active and passive alignment techniques as well as modeled results. This research shows that significant splice performance improvement can result from focusing on nominal geometry performance and reducing deviation of a fiber's core-clad concentricity, cladding diameter, cladding non-circularity and fiber curl. This improvement minimizes high-loss outliers and reduces the average splice loss, contributing to maximized OEM process efficiencies.

Corning manufactures the family of SMF-28e+[®] fibers using an Outside Vapor Deposition (OVD) process, which produces a totally synthetic, ultra-pure fiber. As a result, Corning fibers have consistent geometric properties, high strength, and low attenuation. OEMs can count on Corning SMF-28e+[®] photonic fiber to deliver excellent performance and reliability, reel after reel. Measurement methods comply with ITU recommendations G650, IEC 60793-1, and Telcordia GR20-CORE.

Formulas

Dispersion:

$$D(\lambda) \approx \frac{S_0}{4} \left[\lambda - \frac{\lambda_0^4}{\lambda^3} \right] \text{ ps/(nm}\cdot\text{km)}$$

For $1200 \text{ nm} \leq \lambda \leq 1625 \text{ nm}$

Cladding Non Circularity:

$$\frac{\text{Cladding}}{\text{Non - Cladding}} = \left[1 - \frac{\text{MinCladdingDiameter}}{\text{MaxCladdingDiameter}} \right] \times 100$$

For more information about Corning's leadership in Specialty Fiber technology visit our website at www.corning.com/specialtyfiber

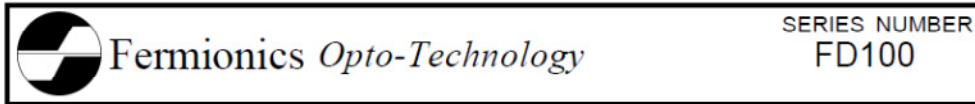
To obtain additional technical information, an engineering sample or to place an order for this product, please contact us at:

Corning Incorporated Tel: +1-607-974-9974
 Fax: +1-607-974-4122
 E-mail: specialtyfiber@corning.com

© 2010 Corning Incorporated



G.10 Datasheet photodiode



High Speed InGaAs PIN Photodiodes
diameter of active area=100 μm

DESCRIPTION

High-speed, low dark current, low capacitance photodiode for high speed communication systems, LANs, and FDDI applications. The photosensitive area is 100 microns in diameter. Planar-passivated device structure.

ABSOLUTE MAXIMUM RATINGS (T=25°C)

PARAMETER	RATING	UNITS
Storage Temperature	-40 to +100	°C
Operating Temperature	-40 to +85	°C
Forward Current	5	mA
Reverse Current	0.5	mA
Reverse Voltage	30	V

OPTICAL AND ELECTRICAL CHARACTERISTICS (T=25°C)

PARAMETER	SYMBOL	TEST CONDITIONS	MIN	TYP	MAX	UNITS
Responsivity	R	$\lambda = 1300 \text{ nm}$	0.80	0.90	-	AW
		$\lambda = 1550 \text{ nm}$	0.85	0.95	-	
Dark Current	I_d	$V_R=5\text{V}$	-	0.5	3	nA
Rise/Fall Time	t_R/t_F	$V_R=5\text{V}$	-	0.3	0.7 [ⓐ]	ns
Capacitance	C	$V_R=5\text{V}$	-	1.1	1.5 [ⓑ]	pF

[ⓐ] $t_R/t_F < 0.4 \text{ ns}$ for diodes mounted on ceramic submounts

[ⓑ]C < 1.2 pF for diodes mounted on ceramic submounts

PACKAGE OPTIONS

PART NUMBER	PACKAGE DESCRIPTION
FD100W	TO-18 with AR-coated flat window cap
FD100L	TO-18 with lens cap
FD100S2	type S2 alumina ceramic submount
FD100S3	type S3 alumina ceramic submount
FD100FC	TO-style diode installed in FC-connector receptacle
FD100SC	TO-style diode installed in SC-connector receptacle
FD100ST	TO-style diode installed in ST-connector receptacle
FD100F(core/cladding)	TO-style diode with integral fiber pigtail (specify fiber core/cladding)

Fermionics Opto-Technology
☎ 805-582-0155

4555 Runway Street
fax 805-582-1623

Simi Valley, CA 93063
www.fermionics.com

 Fermionics <i>Opto-Technology</i>	SERIES NUMBER FD100
---	-------------------------------

High Speed InGaAs PIN Photodiodes

TYPICAL CHARACTERISTICS

Fig. 1 Spectral Response (R vs λ)

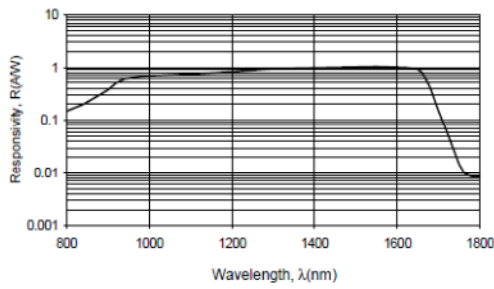


Fig. 2 Dark Current vs Reverse Voltage

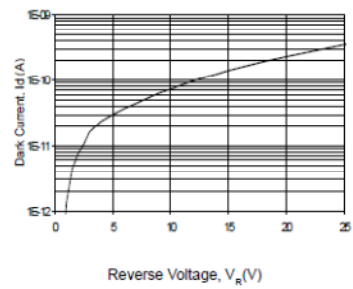


Fig. 3 Capacitance vs Reverse Voltage

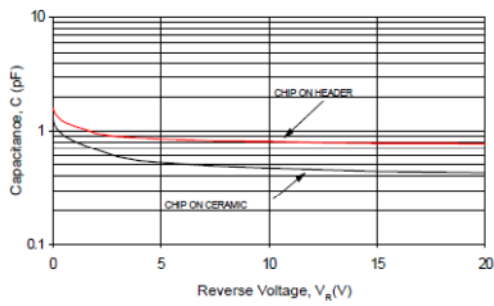
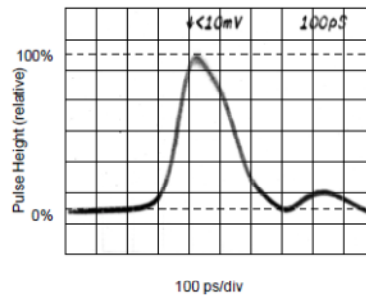


Fig. 4 Response to Optical Impulse



Fermionics *Opto-Technology*
 ☎ 805-582-0155

4555 Runway Street
 fax 805-582-1623

Simi Valley, CA 93063
www.fermionics.com



Bibliography

- [1] *Basic heat and mass transfer*. **A.F. Mills**, University of California, Prentice Hall, second edition
- [2] *Mechanics of materials*. **J.M. Gere and S.P. Timoshenko**, Stanford university, Stanley Thornes, 1999, fourth SI edition, pp 96-99.
- [3] *Optics*. **E. Hecht** Adelphi university, Addison Wesley, fourth edition, pp 282 - 285
- [4] *The design of high performance mechatronics*, **R. Munnig Schmidt, G. Schitter, J. van Eijk**, Delft University, IOS press, 2011.
- [5] *Principles of measurement systems*, **J.P. Bentley**, university of Teeside, Prentice Hall, 2005 fourth edition.
- [6] *SPICA SAFARI FTSM SPIE/PEP presentation 29/29 June 2010*, **T. van den Dool, R. Hamelinck, B. Kruizinga, H. Visser, W. Gielesen**, NSO ref. nr. :PEP 10008
- [7] *SAFARI MCU: Fiber interferometer prototyping*, **D. van Loon**, doc. no: SRON-MCU-TN-001, 14 December 2010
- [8] *SAFARI MCU: Design prototype 3-fiber interferometer readout*, **A. Stellinga**, doc. nr.: SRON-MCU-TN-002 ,10 November 2010
- [9] *SAFARI MCU: fiber interferometer integration test*, **D. van Loon**, doc. nr.: SRON-MCU-TN-xxx, 26 July 2011
- [10] *Applied numerical methods using Matlab*, **W. Yang, W. Cao, TS. Chang, J. Morris**, John Wiley & sons, 2005, Chapter 4
- [11] *Mechanical analysis for engineering*, **D.J. Rixen**, Delft university of technology, Version5.0, June 2011
- [12] *Noise model of the He-4 setup*, **A. Nieuwenhuizen**, SRON, April 1996 , version 1.3
- [13] *Equivalent noise bandwidth*, **T.J. Sobering**, Technote 1, SDE consulting, May 1991 revised 25 June 2008
- [14] *Opamp noise analysis*, **T.J. Sobering**, Technote 1, SDE consulting, May 1999 revised 19 November 2002
- [15] *Opamps for everyone*, **B. Carter**, Literature number SLOD006, Texas instruments, 2008 Chapter 10
- [16] *SPICA and its instrumentation*, **T. Nakagawa**, JAXA, 19th international symposium on space terahertz technology, Groningen, 28-30 April 2008

- [17] *SPICA/SAFARI cryogenic magnetic bearing Fourier transform spectrometer mechanism*, **T. van den Dool, R. Hamelinck, B. Kruizinga, B. Braam, W Gielesen, N.Loix, D. van Loon**, international conference on space optics, 4-8 October 2010
- [18] *Alternative fringe sensor for DARWIN mission*, **L.K. Cheng, R. Koops, A. Wielders, W. Ubachs**, TNO science and industry
- [19] *Polytechnisch zakboek*, **P.H.H. Leijendeckers, J.B. Fortuin, F. van Herwijnen, G.A. Schwippert**, Reed business information, 2003 50^e druk.
- [20] *Utilizing three-way fiber coupler within fiber optic interferometry*, **M. Haverdings**, Technobis, 1 June 2011
- [21] *Specifications*, **A.J. de Koning, V.J. Docter**, Technobis, 16 November 2010
- [22] *Specifications 2*, **A.J. de Koning, V.J. Docter**, Technobis, 29 March 2010
- [23] *Correspondence with D. van Loon from SRON*
- [24] *Correspondence with T. van den Dool from TNO*
- [25] Correspondence with **D. Rixen from TUDelft**
- [26] *Correspondence with M. van der Hoek from vanderHoek Photonics*
- [27] *Correspondence with S. Lee from RIO Laser*
- [28] *Correspondence with Fermionics (manufacturer of the FD100)*
- [29] *Fiber interferometer, waar we nu staan*. **M. Sandtke, N. Dijkhuizen, P. Toet, L. Cheng, T. van den Dool, D. Lo Cascio**. TNO Delft, 9 July 2008
- [30] *Physics for mechanical engineers*. **R. Munnig Schmidt**, Tudelft, Physics for mechanical engineers ME1611, 2009
- [31] <http://cryogenics.nist.gov/MPropsMAY/material%20properties.htm>
- [32] http://www.ips-innovations.com/low_emissive_wall_coatings_ref.htm
- [33] *Fundamentals of engineering thermodynamics*. **M.J. Moran**, Chichester England, Wiley, 2002
- [34] *The art of Electronics*, **P. Horowitz, W. Hill**, Cambridge university press, second edition, 2004
- [35] *Fundamentals of signals and systems*, **E.W. Kamen, B.S Heck**, Pearson Apprentice Hall, third edition, 2007
- [36] http://www.optics.arizona.edu/palmer/OPTI400/SuppDocs/pd_char.pdf
Photodiode characteristics, UDT sensors

- [37] *MSD Class_short*, **J. Ellis**, TUDelft, June 2010
- [38] <http://emtoolbox.nist.gov/Wavelength/Edlen.asp> , *Edlen's formula*
- [39] http://www.optics.arizona.edu/palmer/OPTI400/SuppDocs/pd_char.pdf,
Photodiode characteristics
- [40] http://www.esrf.eu/exp_facilities/ID18/pages/exp/data/sensors/pt100.html,
calibration table PT100
- [41] http://en.wikipedia.org/wiki/Fused_quartz
- [42] http://www.lightmachinery.com/Materials/schott_tie19_temperature_coefficient_of_refractive_index.pdf



Nomenclature and abbreviations

Nomenclature

Symbol	Meaning	SI Units
$P_{sp,out}$	Power of the splitter on the output	W
$P_{sp,in}$	Power of the splitter on the input	W
T_p	Splitter power transformation matrix	-
f_{in}	Optic wave function entering the splitter	-
f_{out}	Optic wave function exiting the splitter	-
S	Sensitivity of the fiber optic interferometer	W/m
P_{photo}	Power incident on the photodiode	W
x	Displacement of the moving mirror	m
I	Emissive power	W
λ	Wavelength of the electromagnetic wave	m
T	Temperature of the blackbody	K
h	Planck's constant	m^2kg/s
k_B	Boltzmann's constant	m^2kg/s^2K
NEP_{det}	Allowable noise equivalent power at the focal plane array	W/sqrt(Hz)
T_{FTS}	Desired reference temperature in the MZFTS	K
$T_{max,FTS}$	Maximum allowable temperature in the MZFTS	K
t_{scan}	Scan time of the FTS mechanism	s
$P_{max,FTS}$	Maximal available power for the FTS	W
f_{fpa}	Sample frequency	Hz
f_{signal}	Signal frequency	Hz
$Att_{ODL-foc}$	1550(nm) light attenuation, from the ODL to the focal plane array	-
NEP_{ODL}	Allowable noise equivalent power at the ODL	W/sqrt(Hz)
N_{ODL}	Noise level or stray light power at the ODL	W/sqrt(Hz)
f_{fringe}	Fringe signal frequency at the photodiode	Hz
v_{max}	Maximal velocity of the moving mirror	m/s
$f_{sample,ADC}$	Sample frequency of the ADC	Hz
res	Resolution of the measurement system	m
n_{bits}	Number of bits in the ADC	-
U_{range}	Total voltage range of the ADC	V
U_{signal}	Total peak to peak voltage range of the signal	V

E	Measure to what displacement U_{signal} corresponds	m
OPD	Optical Path Difference	m
λ_{laser}	Laser wavelength	m
f_{eff}	Effective sample frequency	Hz
dU	Change of internal energy	J
dQ	Heat added to the system	J
dW	Work done by the system	J
\dot{Q}_{in}	Power entering the cryogenic cooled zone	W
\dot{Q}_{out}	Power exiting the cryogenic cooled zone	W
$\dot{Q}_{\text{total load}}$	Total heat load on the cryogenic cooled zone	W
$\dot{Q}_{\text{laser load}}$	Heat load on the cryogenic cooled zone caused by the laser	W
$\dot{Q}_{\text{standard load}}$	Standard heat load on the system	W
$\dot{Q}_{\text{laser in}}$	Laser power entering the cryogenic cooled zone	W
$\dot{Q}_{\text{laser out}}$	Laser power exiting the cryogenic cooled zone	W
\dot{Q}_{fiber}	Heat reaching the cryogenic cooled wall by conduction of the fiber	W
$P_{\text{stray light}}$	Stray light power within the cryogenic cooled zone	W
I	Current signal	A
A	Current offset	A
V	Visibility or contrast	-
ϵ	Strain	-
Δl	Change of length	m
l_0	Initial length	m
α	Linear thermal expansion coefficient	K^{-1}
ΔT	Change of temperature	K
OPD_{new}	New Optical Path Difference	m
dt_1	Time interval	s
e_T	Error due to a temperature disturbance on the reference arm	m
n_b	Number of bits in the ADC	-
e_{ADC}	Quantization error in the ADC	m
$e_{r,\text{tot}}$	Standard deviation of the total random error	m_{rms}
e_n	Error due to a change of refractive index	m_{rms}
δ	Total elongation of the fiber segment	m
F	Force	N
L	Length	m
E	Young's modulus	N/m^2
A	Surface	m^2
F_{co}	Resultant force acting on the fiber coating	N

F_{cl}	Resultant force acting on the fiber cladding	N
α_{eff}	Effective coefficient of thermal expansion	K^{-1}
n_f	Refractive index of the fiber core	-
n_a	Refractive index of the air	-
L_{ref}	Length of the measurement arm	m
L_{meas}	Length of the reference arm	m
m	segment number	-
L_{0m}	Initial length of segment number m	m
T_m	Temperature of segment m	K
e_{sensor}	Error due to the tolerance band of the temperature sensors	m
ΔT_{tol}	Temperature of the tolerance band of the PT100's	K
\dot{Q}_r	Radiant energy leaving the fiber optic interferometer	m
m_r	Number of reflections	-
r	reflection	-
n_1	Refractive index of waveguide material 1	-
n_2	Refractive index of waveguide material 2	-
OP_{Δ}	Difference in OPD for the two arms	m
S_1	Signal 1 measured at the detector system	A
S_2	Signal 2 measured at the detector system	A
S	Sensitivity of the fiber optic interferometer	W/m
P_{photo}	Power incident on the photodiode	W
x	Displacement of the moving mirror	m
e	Internal energy density	J
q_i	Component of the heat flux in direction i	N/m^2
σ_{ij}	Mechanical stresses on surface $i=1,2,3$ in direction $j=1,2,3$	N/m^2
ϵ_{ij}	State of strain on surface $i=1,2,3$ in direction $j=1,2,3$	-
ρ	Density of the material	kg/m^3
c	Specific heat capacity of the material	J/kgK
A_s	Surface	m^2
$Q_{rad,k}$	Radiant heat component k	W
q_{inc}	Incident heat flux	W/m^2
ϵ	Emissivity	-
σ	Stefan Boltzmann constant	J/sm^2K^4
A_i	Pouter surface of element i	m^2
T_i	Temperature of element i	K
$q_{inc,2i}$	Incident heat flux on element i	W/m^2
$Q_{rad,on,i}$	Radiating heat entering element i	W

$Q_{\text{rad,off},i}$	Radiating heat exiting element i	W
n_e	Number of discretized elements	-
k_i	Thermal coefficient of conduction of element i	W/mK
A_c	Cross section of the fiber optic cable	m^2
Δx	Element length	m
O	Circumference of the fiber optic cable	m
$Q_{\text{rad,off},i}$	Radiating heat exiting element i	W
n_e	Number of discretized elements	-
P_{in}	Optical power on the input of a subsystem	W
P_{out}	Optical power on the output of a subsystem	W
A_{IL}	Attenuation of the subsystem due to insertion loss	-
A_{dB}	Attenuation of the subsystem due to insertion loss in dB	dB
P_{loss}	Optical power lost in a subsystem	W
E_0	Amplitude of the harmonic disturbance	N/C
ω	Wave frequency	rad/s
t	Time	s
k	Wave number	-
x_{OPD}	Distance from the from the source of the wave to the emitter	m
ε_i	Initial phase at the emitter	rad
λ	Wavelength	m
ϕ	Phase	rad
n	refractive index of the waveguide	-
A_0	Calibrated current offset	A
V_0	Calibrated visibility or calibrated contrast	-
I_{re}	Real component of the projection	A
I_{im}	Complex component of the projection	A
P_{meas}	Power of the laser returned from the measurement arm	W
P_{ref}	Power of the laser returned from the reference arm	W
P_1	Power of the laser in detector arm 1	W
P_2	Power of the laser in detector arm 2	W
P_3	Power of the laser in detector arm 3	W
$P_{1,\text{meas}}$	Laser power returned from the measurement arm in detector arm 1	W
$P_{1,\text{ref}}$	Laser power returned from the reference arm in detector arm 1	W
Amp	Amplitude of the signal	A
V_{max}	Maximal voltage at the ADC	V
$I_{\text{rms},1}$	Rms current amplitude of the signal	A_{rms}
I_{photo}	Current created in the photodiode	A

G_{trans}	Gain of the transimpedance amplifier	A/V
G_{filter}	Gain of the low pass filter	V/V
U_c	Calibrated voltage signal	V
U	Voltage signal at the ADC	V
A_v	Voltage offset of the voltage signal at the ADC	V
V_v	Visibility of the voltage signal at the ADC	-
v_n	Rms noise voltage	V_{rms}
i_n	Rms noise current	A_{rms}
PSD	Power spectral density	V^2/Hz
VSD	Voltage spectral density	$V/\text{sqrt}(\text{Hz})$
CPS	Cumulative power spectrum	W
f_B	Spectral bandwidth	Hz
M	Number of samples that are averaged	-
n_s	Sample number	-
Ω	Frequency in the digital domain	rad/s
CAS	Cumulative amplitude spectrum	V_{rms}
VSD _{out}	Voltage spectral density on the output of the decimation filter	$V/\text{sqrt}(\text{Hz})$
$v_{n,\text{tot}}$	Total noise contribution on the processed data signal on photodiode n	V_{rms}
v_{therm}	Thermal noise voltage spectral density	$V/\text{sqrt}(\text{Hz})$
k_B	Boltzmann's constant	J/K
T_R	Resistor temperature	K
R	Electrical resistance	Ω
i_{shot}	Shot noise current spectral density	$I/\text{sqrt}(\text{Hz})$
q	Charge of the electron	C
I_{DC}	Average DC diode current	A
v_{adc}	Quantization noise voltage spectral density	$V/\text{sqrt}(\text{Hz})$
$f_{s,\text{adc}}$	Sample frequency of the ADC	Hz
n_{bits}	Number of bits in the ADC	-
U_{signal}	Total peak to peak voltage range of the signal at the ADC	V
v_{amp2}	Amplifier 2 noise voltage spectral density	$V/\text{sqrt}(\text{Hz})$
$e_{\text{int},n}$	Displacement error due to intensity noise	nm
x_{ideal}	Simulated ideal displacement	nm
x_{noise}	Simulated displacement with intensity noise within the signal	nm
$e_{\text{opt},\text{dis}}$	Displacement error due to optical disturbances	nm
$x_{\text{opt},\text{dis}}$	Simulated displacement with optical disturbances within the signal	nm
c	Speed of light in vacuum	m/s
ν	Frequency	Hz

λ_0	Wavelength in vacuum	m
m	Parameter as a measure for the wavelength fraction	-
OPD	Optical path difference	m
x_1	Distance travelled by EM wave 1	m
x_2	Distance travelled by EM wave 2	m
$e_{\text{laser drift}}$	Change of detected position due to laser drift	m
ϕ_{normal}	Ideal phase	rad
ϕ_{drift}	Drifted phase	rad
$\Delta\lambda$	Wavelength deviation from the center wavelength of the laser	m
$\Delta\nu$	Frequency deviation from the center frequency of the laser	m
ν_{laser}	Laser frequency	Hz
α	Wave phase	rad
E	Amplitude	-
$\Delta\lambda_{\text{FWHM}}$	Wavelength deviation due to the FWHM	m
$p_{\text{loss,lens}}$	Percentage of lost light	%
$P_{\text{loss,lens}}$	Power of lost light	W
$P_{\text{no loss,lens}}$	Power coupled back into the lens	W
e_{align}	Displacement error due to angular misalignment	m
$x_{\text{loss,lens}}$	Simulated displacement with optical losses due to angular misalignment	m
d_{offset}	Offset of the light bundle on the grin lens	m
d_{lens}	Diameter of the grin lens	m
T_m	Measured temperature	C
R_m	Measured resistance	Ω
a	Sensitivity of the PT100	K/ Ω
b	Conversion factor	K

Abbreviations

SPICA = Space Infrared telescope for Cosmology and Astrophysics
SAFARI = SpiCA far infrared Instrument
FTS = Fourier Transform Spectrometer
FTSM = Fourier Transform Spectrometer Mechanism
FOI = Fiber Optic Interferometer
ADC = Analogue to Digital Converter
FFT = Fast Fourier Transform
TBC = To Be Considered
OPD = Optical Path Difference
ODL = Optical Delay Line
GBW = Gain Bandwidth product
RMS = Root Mean Square
DTFT = Discrete time Fourier transform
FFT = Fast Fourier transform
ADC = Analogue to digital converter
EM = Electro magnetic
FC APC SM = Fixed connection angled physical contact single mode
FWHM = Full width at half maximum
MZFTS = Mach Zehnder Fourier Transform Spectrometer
TBC = To be considered
LSB = Least significant bit
EOM = Electro Optic Modulator
SPOF = Single Point Of Failure



